Collective effects in networks of negatron elements

L. O. Bartoneva, S. A. Basharin, M. Yu. Bychkov, A. A. Kal'nin, and A. V. Korolev

St. Petersburg State Electrotechnical University, 197376 St. Petersburg, Russia
(Submitted December 29, 1995)
Zh. Tekh. Fiz. **68**, 1–8 (May 1998)

Results are presented from numerical simulations and experimental studies of a network system consisting of elements with negative differential resistance (negatrons). It is shown that systems of this type have valuable functional characteristics owing to a cooperative interaction of the elements and can be used to create information systems for pattern analysis and recognition. A variational principle is introduced which uses the macroscopic positions to determine the direction of evolution of the state of the network under the influence of applied signals. The possibility of integrating negatron networks into engineering systems may eventually lead to the creation of new materials of the synergetic type for use in electronic technology. © *1998 American Institute of Physics.* [S1063-7842(98)00105-6]

INTRODUCTION

In recent years there has been significant progress in creating parallel information processing systems. Besides the rapid development of synergetic computer systems,[1] there is great interest in creating physical adaptive systems with empirical learning of a conditioned response,[2,3] in which the computational adaptation process is replaced by direct physical adaptation. Computational systems have some valuable characteristics, primarily the protection of the transformation event from fluctuations in the power supply, ambient temperature, and other factors, which ensures the operational reliability of these systems. In practical development work, however, the a physical adaptation process has some inherent advantages that should not be overlooked: deep deparallelization of the signal action, address-free adaptive movement, and a large amount of freedom in construction, admitting a random coupling of the active elements, which facilitates the reliable fabrication of physical adaptive systems.

It should, however, be noted that creating physical adaptive systems is quite difficult, owing to functional shortcomings in the available electronic components. Such important requirements for these elements as calibrability of a physical quantity with retention of its value in memory,[2] the capacity for redistribution reactions in collective relationships,[3] and cumulation-threshold reactions under the influence of applied signals[4] must be imitated by circuit solutions. Little work has been done on creating materials (media) with adaptive properties.

Since the ultimate goal of this study is to evaluate the feasibility of creating new electronic materials (media), we have devoted primary attention to studying the macroscopic reactions of a network system resulting from cooperative interactions among the components of which it is made up. Circuit theory (i.e., microscopic analysis of currents and voltages) was used in the computational model to reveal the characteristics of the macroscopic reactions and then to generalize to systems with random connections of elements in a network system.

1. COMPUTATIONAL MODEL OF THE ADAPTIVE REACTION OF A NEGATRON NETWORK TO REGULAR APPLIED SIGNALS

The adaptation process was analyzed using a model consisting of a regular network of negatron elements (Fig. 1a) with coordination number $z=4$ (square network). The current–voltage (I–V) characteristic of a negatron element (negatron) in this model had two symmetric folds; the symmetry point was the coordinate origin (Fig. 1b). This representation of the I–V characteristic corresponds to a simple piecewise linear approximation of the real I–V characteristic of two antiparallel tunnel diodes. An active state of the network was generated by passing fixed currents I_0 through a set of input and output electrodes. The value of the bias current I_0 is indicated on the I–V characteristic shown here. The signal voltages which change the electrical state of the network, u_{ab} and u_{cd}, were applied between the corresponding nodes a, b, c, and d of the network. The format of the two-dimensional model of the network consisted of 7×7 nodes. In the following they were numbered in sequence by row from 1 to 49 and 84 negatron elements were inserted between the nodes.

The equivalent circuits of the negatron element biasing in the three characteristic segments *I–III* (Fig. 1b) consisted of a resistive element with resistance R_2 in segment *II* and resistive elements $R_{1,3}$ with a series source of voltage E_0 having different polarities in segments *I* and *III*. One can set R_2 equal to $R_{1,3}$ in the calculations without loss of generality of the conclusions in this study.

An external signal voltage $E_{p,q}$ could be applied between any pair of nodes p and q. The sequence of signal voltages applied to the nodes and the values of the residual node potentials (currents in the arms) after removal of the external sources are important for determining the final state of the system.

Thus, for the variables describing the state of the network system we have chosen the potentials of 48 of the nodes relative to the 49th, grounded, node. In the starting

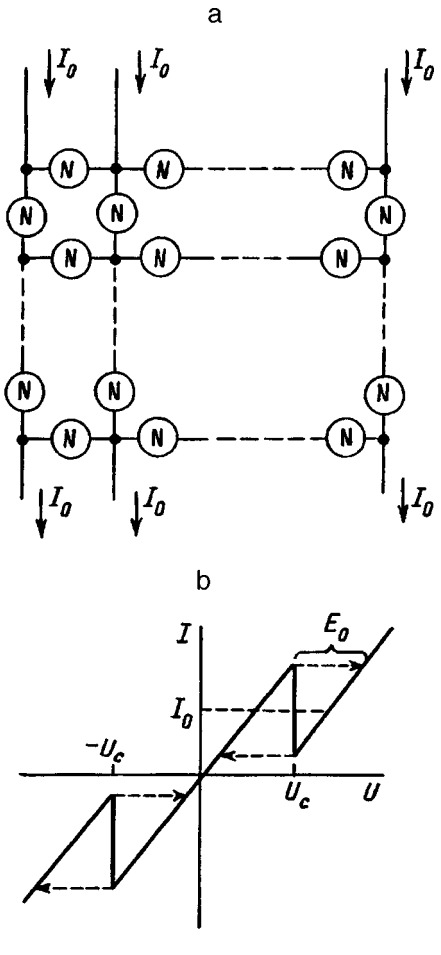

FIG. 1. A sketch of the regular negatron network used in the computational model (a) and an approximate I–V characteristic of a negatron element (b).

state, the network is in an unperturbed state, i.e., the currents in the longitudinal arms are equal to I_0, there are no currents in the transverse arms, and there are no applied voltage sources in the bias circuit for the negatrons.

In developing a program for modeling the potential transitions from various states of the network, the following procedural difficulties are of importance: the system has alternative final adaptive states which depend on the evolutionary path, i.e., the sequence in which the internal voltage sources are turned on (off); the system has alternatives to the evolutionary paths, i.e., it displays a self-organization effect. These difficulties were overcome by using a computational method employing a stepwise gradual growth (reduction) in the external signal voltages and in the internal source voltages which simulate the switching of the negatrons. In cases where alternative internal switchings occur, the conflict was resolved with the aid of a random number generator.

For calculating the potential and current state of the network system after the signal voltages had acted, the method of node potentials was used. The states of the network were represented by points in a 48-dimensional space, i.e., by vectors starting at the coordinate origin and ending at the given point.

For a negatron network system we denote the conductivity matrix of the electrical circuit by A and the conductivity matrix of the circuit with signal voltage sources $E_{p,q}$ between nodes p and q by $\tilde{A}$. Before the signal source is turned on, the state of the network is represented by the point P_0 in an arbitrary coordinate space; the voltage between nodes p and q before the signal source is turned on is $E^{(0)}_{p,q}$. The insertion of a signal source into an unperturbed network represents a displacement from the initial point P_0 by an amount $\tilde{A}^{-1}\cdot b_0$, where b_0 is a column vector which consists of the right-hand sides of the system of equations used in the node potential method[5] and which corresponds to a voltage increase $\Delta E_{p,q}=E_{p,q}-E^0_{p,q}$.

For each negatron the boundaries between regions *I* and *II* and between regions *II* and *III* separating the parts of the I–V characteristic are the hyperplanes

$$u_i-u_j=v_c, \tag{1}$$

$$u_i-u_j=-v_c, \tag{2}$$

where i and j are the numbers of the nodes between which the given negatron lies and v_c is the critical voltage (Fig. 1b).

A gradual stepwise increase in the voltage between nodes p and q from $E^{(0)}_{p,q}$ to $E_{p,q}$ leads to the attainment of a critical voltage at which one or several, at once, of the negatrons undergo a transition from one segment of the I–V characteristic to another. A set of simultaneously switching negatrons is found as follows. The crossing of the point P_1 by one of the hyperplanes of the form (1) or (2) as it moves from the point P_0 along the vector $\tilde{A}^{-1}\cdot b_0$ requires that an internal source be switched on (or off) at the corresponding branch of the network system. This, in turn, requires a modification on the right hand side of the system of equations by adding a term b_1 which accounts for insertion (removal) of the source. Inserting an internal voltage source that symbolizes a transition of the negatron, for example, from segment *II* to segment *III* of the I–V characteristic represents a transition from the point P_1 by an amount $\tilde{A}^{-1}\cdot b_1$. However, during movement from the point P_1 by an amount $\tilde{A}^{-1}\cdot b_1$, hyperplanes of the form (1) and (2) may also be encountered. At each regular (in sequence the kth) crossing of one of the hyperplanes, the motion must be corrected by adding a quantity $\tilde{A}^{-1}\cdot b_k$ to the end of the instantaneous vector. Here motion takes place from the point P_k of the last intersection to the end of the sum vector. This sort of motion in coordinate space leads to the point Q, at which the switching of the negatrons is complete. This point corresponds to the end of the vector

$$\tilde{A}^{-1}\sum_{k=1}^{N} b_k,$$

which begins at the point P_2, where N is the number of negatrons which simultaneously switch on as the point P_1 is reached. After the set of negatrons which switches at the point P_1, the motion along the vector $\tilde{A}^{-1}\cdot b_0$ continues, but already from the point Q with the next critical point, etc.

This computational procedure makes it possible to ascertain all the switchings of the negatrons and the sequences of sets of them when an external signal voltage $E_{p,q}$ is applied.

In modeling the procedure for removal of a signal voltage, the circuit with a voltage source E_{pq} between nodes p and q is replaced by an equivalent circuit with an source of current I_{pq} between these nodes. The source current is gradually reduced, stepwise, from I_{pq} to zero. The computational procedure is completely analogous to the procedure for applying a signal voltage, with the sole difference that now the matrix A is used instead of the matrix $\tilde{A}$.

The above computational model was used to study the behavior of a negatron grid acted on by cyclical potentials. Signal voltage sources were connected to arbitrarily chosen pairs of nodes and then turned off, leaving an ''impression.'' The sequence of turning them on (off) was strictly maintained and was cyclical, i.e., the sequence of turning them on was repeated until evolutionary changes of the network state were observed. When a final (unchanging) state of the network was reached, the ''demonstration'' of voltages was terminated.

In the computational model, primary attention was devoted to studying the possibility of introducing a variational principle for the evolution of the state of the negatron network under the influence of applied signals. To do this, it was necessary to introduce a functional that reflects the macroscopic state of the network and follow its variations during the movement to the limiting adaptive state. Two of the many possible alternative formulations of the functional were subjected to verification in the computational model. The first can be represented in the following way.

A network system of negatron elements which have an N-type fold in their I–V characteristic and are subject to constant current boundary conditions that ensure the electrical multistability of the system evolves under the influence of cyclical potential signals to a limiting state that is characterized by a minimum of the sum of the excess currents in the branches,

$$\Phi=\sum_{m=1}^{M}|I_m^{(s,c)}-I_{m0}|\rightarrow\min, \tag{3}$$

where I_m is the current in the mth branch after application of the signal internode voltage in the sth demonstration of the cth cycle, I_{m0} is the initial current in the mth branch before the signal application corresponding to a completely turned-off internal voltage source, and M is the total number of branches in the network.

In introducing the functional, it was noted that the evolutionary changes take place as a result of attaining extremal currents in the nodes, and that attaining a peak current in some demonstration of signals, which causes turn on of an internal source E_0, reduces the absolute value of the current, while a current dip (turning off an internal source) raises it. Both of these acts cut off extremal currents and make the currents approach the initial bias I_{m0}. Recall that I_{m0} in the vertical branches of the network is equal to the bias current I_0, while that in the horizontal branches is zero.

An alternative formulation of the functional is to state that the sum of the absolute values of the differences in the currents in adjacent branches, both vertically and horizontally,

$$\Phi'=\sum_{m,n=1}^{M}|I_m-I_n|\,\eta(m,n), \tag{4}$$

is a minimum, where

$$\eta(m,n)=\begin{cases}1, & \text{if the } m\text{-branch is adjacent to the } n\text{th branch}\\ & \text{(horizontally or vertically) and } m<n;\\ 0, & \text{if they are not adjacent or } m\geqslant n.\end{cases}$$

The significance of this functional is that cutting off an extremal current, such as a peak, means that it is redistributed under the fixed current boundary conditions with an increase in the adjacent branches. In other words, during the evolution, sharp current dips in the branches or arbitrary current gradients are cutoff.

The efficacy of these variational principles was tested in the model. Here we used the simplest versions of the signal demonstrations and their sequences. During the modeling, there was a limit on the levels of the input signal voltages: these levels should not inhibit compromising adaptation during successive applications of voltages to chosen pairs of nodes in the network, i.e., attainment of the limiting potential state of the network. Otherwise, a cyclical repetition of the potential situations may occur. Note, however, that even in this case these functionals can be used, but it is necessary to compare their values after identical demonstrations in their cyclical sequence.

Figure 2a shows a typical example of the change in state of a negatron network after turning on and subsequent turn-

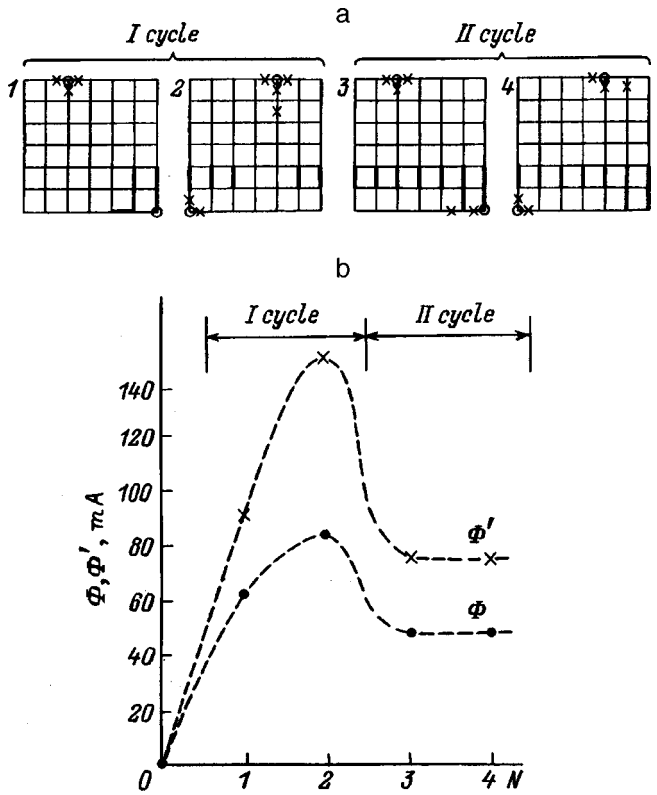

FIG. 2. Changes in the potential state of a negatron network during sequential cyclic switching on (with switching off) of signal voltage sources (a) and the changes in the macroscopic functionals Φ and Φ' as functions of the number of switching events (b).

ing off of sources of signal voltages between the nodes denoted by circles. The thick lines denote branches (negatrons) in which the internal voltage sources were left on, symbolizing switching of the negatrons. The crosses denote negatrons that have switched during the time the signal voltages are applied but return to the ''unperturbed'' state after the influence of the potential is removed. As can be seen from the figure, the network undergoes a change in state, but a demonstration of voltages in the second cycle no longer changes the state of the network, i.e., the final potential distribution has been attained.

Figure 2b shows the change in the Φ-functional calculated after each demonstration. It is clear that there is a rise in the sum of the excess currents during the first and second potentials applied to the network nodes, and then a repeat of these demonstrations reduces the sum of the excess currents. Note that, prior to turning on the signal sources (the starting state), it was equal to zero, i.e., the starting state is also ''attractive'' and a transition through a maximum of Φ is required in order to shift to a new adaptive state.

Experiments confirm that the functionals Φ and Φ' are minimized during the evolution from an arbitrary starting situation. We discuss some of the most important consequences of this conclusion below.

2. CHARACTERISTIC EFFECTS INTRINSIC TO NEGATRON NETWORKS

Further studies were carried out on a specially created negatron network system consisting of gallium arsenide tunnel diodes. The network consisted of negatron elements with a symmetric fold in their I–V characteristics, achieved by sequential parallel–antiparallel installation of pairs of tunnel diodes (Fig. 3), regularly mounted in a two-dimensional system with a coordination number $z=4$. The network format consisted of 6×6 nodes and there were 66 negatron elements. For visual observation of the changes in the potential state of the network, a light emitting diode (LED) screen was built, on which the brightness of the emission from each LED was proportional to the voltage drop across the negatron element located in the column, i.e., in the direction of flow of the bias current. The current in the columns was set with the aid of current generators; here the operating point, as in the computer simulations, was an average between the peak and dip currents.

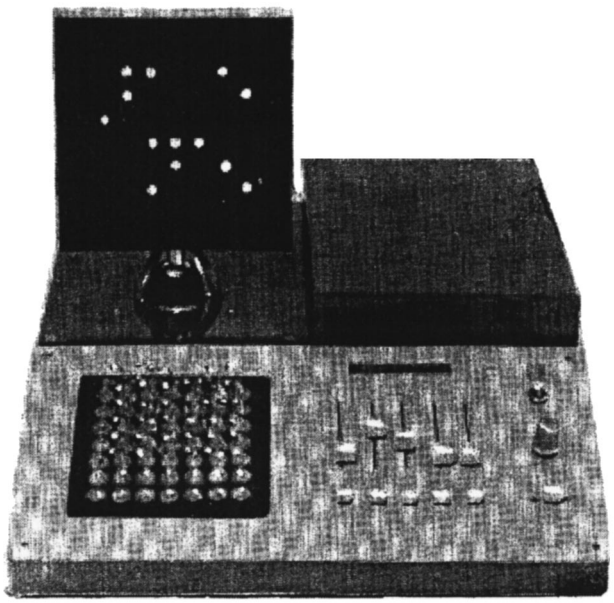

FIG. 3. Overall view of the negatron network assembled from tunnel diodes.

An all-purpose panel permits reassembly of the network with changes in the coordination number z. The apparatus contains five potentially independent sources of variable signal voltages in arbitrary sequence.

The results of the experimental observations made on this physical network system are presented below.

a) *Band structure of the node potentials.* When a bias current[6] passes through a one-dimensional chain of negatron elements, there is a set of $(n+1)$ discrete values of the voltage drops, where n is the number of negatrons in the chain. This kind of system is characterized by a degeneracy of the potential states because of the existence of alternative variants of the voltage distribution among the negatrons which create the same total voltage drop. Adding a second dimension to the possibilities for interelement coupling creates a splitting in the levels with formation of specific bands of allowed node potentials. Since calculating all the possible values of the node potentials is a difficult task, even for a comparatively small network format, we set up an experiment in which the residual values of the node potentials were recorded after the signal was applied. A random signal (noise) generator was used.

Figure 4 shows how the residual (allowed) potentials at the third node (upper row) of the physical negatron network are distributed. The zero reference is taken to be the potential of the third node of the lowest row. As can be seen from this diagram, the values of the node potentials are grouped in specific bands of allowed potentials, $\Delta\varphi'$, which alternate with ''forbidden'' bands $\Delta\varphi$. Here the width of an ''allowed'' potential band decreases as the system moves to the limiting values of the residual potentials (i.e., to the greatest and least).

The transitions between states are selective, which is a valuable functional property of the system, and the entire set of allowed values of the potentials forms a basis for a discrete-analog memory.

b) *Critical size of the potential switching region.* The experiment shows that turning on a single negatron when all the elements in the nearest surroundings are turned off causes it to shut itself off. At higher signal voltages, when adjacent negatrons are also switched on, i.e., a region with changed internode voltages develops, it may be retained when the signal voltage is turned off. There is a critical size (extent in terms of regular network steps) of this region which is capable of retaining a residual potential. In our case, it consists of 3 switched-on negatrons in vertical branches lying horizontally. A similar situation occurs when an attempt is made to turn off a single negatron.

In general, there is a certain size of the region with a set of adjacent switched-on negatrons up to which the system tends to self-turnoff the negatrons, and beyond which it tends

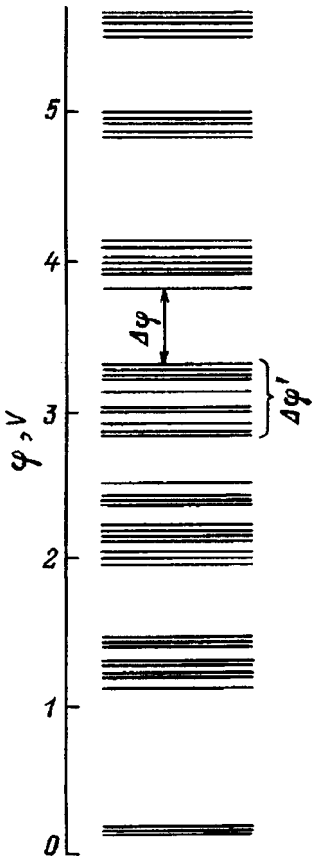

FIG. 4. Typical structure of the residual potentials on one of the nodes of the network after signals have been applied.

to self-growth, if a noise signal which activates switching is acting on the system. Based on the variational principle for the evolution of the negatron system introduced above, we can say that both limiting cases (a fully turned on or turned off row) ensure a zero sum of the excess currents in the branches.

c) *Adaptive variation in the threshold for negatron switch-on.* This valuable property, which can be used for creating neural-net adaptive systems, is manifested as follows. If a negatron switch-on current signal flows between nodes of the network, then there is a certain value of that current at which a negatron, along with its surroundings, is turned on (Sec. 2b). If the voltage between nodes is then brought to zero or a current of the opposite direction is induced, then the negatron switches off. Then, however, an adaptive trace of the negatron's having been in a switched-on state may remain in the system, i.e., not all of the surroundings (adjacent switched-on negatrons) are switched off. This adaptive trace lowers the threshold for turning on the negatron. In other words, if in the general case an element (a fragment) were brought into a certain potential state and then removed from that state, then a subsequent transition to that state will be easier, since the barriers separating the two states have now been lowered.

In practice, the value of the threshold current for the first switching on of a given negatron in the network in our experiments was 6 mA, while a subsequent switch-on occurred at a current of only 2.5 mA. The current for a repeated switch-on depends on the ''strength'' of the adaptant left remaining in the system, i.e., an element can be brought to a sensitive state. This simple effect is essentially the manifestation of an attractor. In the more general case a potential state created in a portion of the nodes with the aid of external signals can be ''fixed'' in the system by means of a noise generator, for example. The resulting adaptant with its complementary properties ensures a reduction in the collective switching barriers, which may bring into effect a selective switching of the state of the network.

d) *Domain formation and reference potential in potential switchings.* This effect shows up in the following experiment. If the potentials at several nodes (in our experiments, at 2–3 nodes) are simultaneously switched while the distribution of the potentials between these nodes is kept unchanged, then a mutual bonding of the potentials of the node fragment takes place. This mutual bonding means that when the potentials of only part of the nodes are changed, so are the potentials of the remaining nodes of the fragment. In doing the experiment we first confirmed that prior to the operation leading to mutual bonding of the potentials, the mutual potentials of the chosen fragment are not maintained when part of its nodes are acted on.

Computational modeling showed that self-bonding (domain formation) is caused by a reduction in the excess currents within the confines of a domain, while in the region surrounding the domain the excess currents are large, causing a predisposition to switching.

Thus, conservation of individual regions of the network system is possible, and this makes switching of fragments possible. It is clear, however, that switching the potentials of a fragment (domain) requires a reference potential on another fragment that does not undergo switching when a signal voltage is applied, i.e., a fragment with high current barriers against switching.

e) *Protective shifting of information units.* This effect is illustrated in Fig. 5, which shows a nominal image of the potential states of the vertical branches of the network. (A lit LED represents the switched-on state of a negatron.) This state (for example, Fig. 5a) ensures that there is some difference in potentials between the upper and lower nodes of the network, which for the given potential distribution was equal to V. If the diodes marked by crosses in the picture are shorted out, then they turn off, but then a vertically adjacent negatron switches on (Fig. 5b), thereby maintaining the controlled internode voltage.

3. ON THE POSSIBILITY OF CREATING MATERIALS WITH ELECTRICAL MULTISTABILITY

The network principle, that is, random interelement coupling, ensures a greater degree of design and engineering freedom. In the limit, this may no longer be a structure made up of negatron elements, but a material (medium) with statistically coupled elements (e.g., grains with negatron properties).

In our studies, we have created a model of a material consisting of random combinations of pairs of parallel–antiparallel GaAs tunnel diodes. On creating quasiuniform

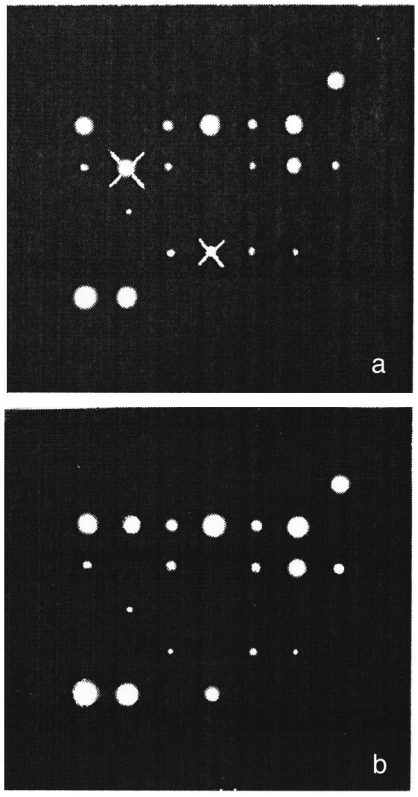

FIG. 5. The protective overflow of information units: (a) initial potential state of the network negatrons; (b) the result of short circuiting.

current conditions at the opposite boundaries of the model and inserting signal electrodes in arbitrary parts of the network, we observed multistability in the potential, adaptive lowering of the excitability threshold, and other properties noted above. We also noticed a cumulative effect resulting from applying numerous current pulses. The parallel–antiparallel tunnel diodes essentially model a semiconductor grain with a shallow surface $p-n$ tunnel junction. In fact, a paper[7] has been published on the possibility of creating $p-n$ tunnel junctions by a diffusion method.

We have also made an engineering study aimed at creating a ceramic material with electrical multistability. The material consists of a grain of n-type silicon with a shallow surface $p-n$ junction which was formed by diffusion of acceptors (boron) from a glassy binder of composition SiO_2 (5 wt %), PbO (80 wt %), and B_2O_3 (15 wt %). The amount of glass forming mixture was chosen subject to the feasibility of electrical contact of the silicon grains and was 10 wt % 0.5-mm-thick tablets with a diameter of 8 mm, produced by compression of n-type silicon powder (average gain diameter ~ 5 μm) with a glass forming filler and an organic binder, were annealed at a temperature of 1200 °C for 5–10 min. A shallow $p-n$ junction is necessary to prevent current flow over the highly conducting p^+-layer at the surface.

A set of metallic contacts, 0.5 mm in diameter and with a gap of ~ 0.1 mm between them, was produced on one of the tablet surfaces in order to study the properties of the ceramic. Typical I–V characteristics obtained by passing a current between two neighboring contacts are shown in Fig. 6a. It can be seen that the material has negatron properties. The peak voltage on the S-fold of the I–V characteristic drops as the gap between the electrodes is reduced. The I–V characteristic is symmetric, that is, it is nonpolar.

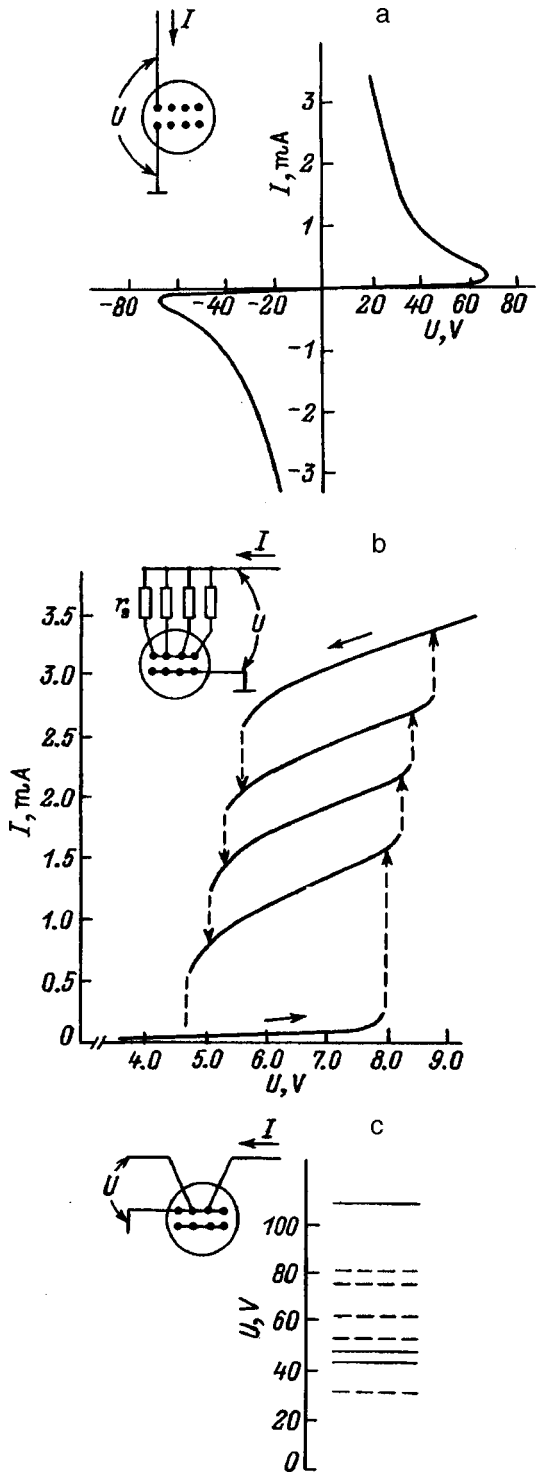

FIG. 6. Electrical properties of the silicon based ceramic material. (a) A typical I–V characteristic obtained by passing a current through two adjacent electrodes on the surface of the tablet; (b) current multistability in a parallel system with resistive current limitation; (c) potential multistability which develops as the current approaches a critical value (the continuous lines denote stable and the dashed lines, relatively unstable potential states).

The presumed mechanism for the appearance of a negative differential resistance is as follows. When there is a point intergrain contact, each grain can be regarded as a p^+-n-p^+ structure which may have transistor properties. Here the ''base'' potential is floating. When a certain voltage is exceeded, breakdown may occur in the neighborhood of the reverse biased $p-n$ junction; then the positive current feedback typical of transistors with a floating base potential may develop. Evidently, a mixed type of breakdown (avalanche–thermal) takes place in this system. At high currents a thermistor effect may occur. There is some evidence of current filamentation in the ceramic. For example, concurrent switching of the current may occur as it flows through one common and two adjacent electrodes.

Electrical current multistability could be ensured by creating folds in the I–V characteristic using resistive current limitation. To do this, resistors were inserted between electrodes or a resistive layer was created by thick film technology. A typical I–V characteristic for this case is shown in Fig. 6b, in which one can see current multistability in 4 parallel-connected elements with resistive current limitation.

A somewhat unexpected effect was the appearance of potential multistability when a voltage was applied between two distant electrodes, between which lay a third electrode at which the potential was recorded. This resulted in a unique voltage divider. When a voltage close to, but not more than, the peak was applied to the outer electrodes, it was possible to vary the potential of the central electrode through an external current interaction. The remaining potentials differed in having a different measure of stability. In a number of cases, a spontaneous transition to a new potential state was noticed. But, perhaps, the most interesting thing was the appearance of an attractor effect, i.e., the spontaneous switching from relatively unstable states into a stable potential state where the system spent a long time (several minutes). One possible explanation of this effect is the injection of hot carriers into the dielectric binder, and may turn out to be an adaptive wake of the current channel. This question, however, requires special study.

CONCLUSION

While the properties of our model studies and material test samples are far from the performance expected for practical use, they may open up a new class of materials– technologically integrated network systems. The predisposition to search for similar materials (media) has, in its time, led to experiments with powders of conducting particles (electrocohesive media). A diode version of an old device, the coherer,[7] was used to receive radio signals. As more detailed studies showed, however, under the influence of current flow in an electrocohesive medium a well formed geometric system of electrocohesion communications develops which is capable of branching and evolutionary adaptive changes.[3] Furthermore, the possibility has been demonstrated of teaching a conditioned response in media of this type.[8]

It is entirely possible that electrocohesive media are the prototype of future materials (''coherites'') in which an information signal participates in establishing a conditional structure, i.e., an internal ordering of the medium, that will provide an ''trainable'' reaction capability. We may expect the appearance of media with a rhythmic activity which greatly enriches the possibility of transferring signals to a medium, with their internal conversion into rhythmic modes. The hierarchical evolutionary dynamics of media of this type,[9] along with the associated development of modalities, the formation of conservative regions of rhythmic action (nuclei), frequency mixing of regions, and other properties in their practical applications[10] may facilitate the establishment of a new discipline of electronic materials science — synergetic materials with adaptive properties.

The authors thank V. M. Pasyut for help in studying the properties of the ceramic material.

[1] H. Haken, in *Neural and Synergetic Computers*, H. Haken, Ed., Springer, Berlin (1988), 215 pp.
[2] T. Kohonen, *Self-Organization and Associative Memory*, Springer, Berlin (1984), 255 pp.
[3] A. A. Kal'nin, Peterburgskiĭ Zhurnal Élektroniki, No. 1, pp. 36–55 (1993).
[4] T. G. Bochkareva and I. A. Mityureva, ''Expert systems based on threshold-cumulation elements'' [in Russian], Izv. SPbGÉTU, No. 471, pp. 61–63 (1994).
[5] P. N. Matkhanov, *Elements of Electrical Circuit Analysis. Linear Circuits* [in Russian], Vysshaya Shkola, Moscow (1972), p. 336.
[6] Yu. L. Ivas'kov, *Principles of Design of Multivalued Physical Systems* [in Russian], Naukova Dumka, Kiev (1971), p. 316.
[7] E. Branly, ''Variations de conductibilité sous diverses influences électriques,'' Comptes Rendus (Gauthier, Paris) V. CXI, No. 21 (1890).
[8] M. Yu. Bychkov, M. Varshburger, and A. A. Kal'nin, Izv. SPbGÉTU, No. 457 (1993).
[9] J. S. Nicolis, *Dynamics of Hierarchical Systems: An Evolutionary Approach*, Springer-Verlag, Berlin (1986), 397 pp.; Mir, Moscow (1989), 486 pp.
[10] D. A. Kabanov, *Functional Devices with Distributed Parameters. Foundations of Theory and Design* [in Russian], Sov. Radio, Moscow (1979), 450 pp.

Translated by D. H. McNeill

Laser-induced transport of atoms from an illuminated region in a gas

A. M. Bonch-Bruevich, T. A. Vartanyan, S. G. Przhibel'skiĭ, and V. V. Khromov

S. I. Vavilov State Optical Institute All-Russian Science Center, 199034 St. Petersburg, Russia
(Submitted January 23, 1997)
Zh. Tekh. Fiz. **68**, 9–13 (May 1998)

A new optical effect in the transport of atoms in dense gases, capillaries, and porous media is predicted. The origin of this effect lies in superelastic collisions of excited atoms, which give rise to thermal diffusion processes. Model estimates are made for the magnitude of the effects in the absence of flows and in the presence of flows in capillary systems. It is shown that under certain assumptions regarding superelastic collisions of atoms with the walls, the optical effect changes the transmission of a capillary. © *1998 American Institute of Physics.* [S1063-7842(98)00205-0]

INTRODUCTION

Several possibilities for stimulating atomic and molecular transport processes in various media by laser radiation have been predicted and are currently being studied. Of these, the most widely known are optically induced drift[1] and the controlled transport of molecular vapor through porous glasses.[2,3] Recently, the optical stimulation of atomic transport through the interface between a condensed medium and a gas has been reported.[4] The origin of these processes lies in the principle of different interactions of excited and unexcited atoms with the surrounding medium. In this paper we examine a new variant of this principle for stimulating a transport process by converting part of the energy of laser radiation into the kinetic energy of atoms through superelastic collisions. Unlike the previously discussed mechanisms, this mechanism for optically stimulated transport is initiated by spatially nonuniform radiation or by the spatially inhomogeneity of a medium under uniform irradiation.

Collisions of electronically excited atoms with molecules are often accompanied by quenching of the excitation and significant conversion of internal energy into translational motion of the particles. Thus, in collisions of excited alkali metal atoms with CO_2 and N_2 molecules, up to 30% of the energy of electronic excitation (on the order of 2 eV) goes into kinetic energy of the products.[5]

The transport stimulation process considered here consists of the following: thermal atoms that have been excited electronically by the light become ''hot'' after superelastic collisions with molecules of the buffer medium. The concentration of the latter is assumed to be so high (compared to the resonant component) that their temperature does not change. Thus, an atomic subsystem is superheated within the illuminated region in a constant-temperature buffer medium. In the steady state, when the fluxes of atoms from the illuminated region and into it are equal, this is accompanied by a drop in the concentration of atoms within the illuminated region.

Laser-induced transport is, to a certain extent, analogous to thermal diffusion,[6] but does not reduce to it. Unlike thermal diffusion, in which one and the same temperature can be ascribed to both components of a gas mixture, during spatially nonuniform illumination the active component of the mixture enters a highly nonequilibrium state, while the state of the buffer component hardly changes. This leads not only to a substantial enhancement in the transport effect, but also to a change in its sign.

The purpose of this paper is to provide a model description of laser-stimulated transport and to estimate the change in the local concentration in the irradiated region.

ELEMENTS OF THE THEORY

Let us consider an unbounded irradiated gas mixture with a plane boundary between the light and shadow regions. We shall assume that the illumination intensity varies smoothly along the x axis. In the illuminated region, collisions of excited atoms with buffer gas molecules lead to quenching of the electronic excitation and to conversion of part of the excitation energy into translational degrees of freedom. As a result, the distribution of the atoms with respect to velocity v strays far from equilibrium. At the same time, if the concentration n_a of atoms is much smaller than that of the buffer particles, n_b, then the changes in the state of the buffer medium will be negligible. Under these conditions, we can write down the following system of two coupled kinetic equations for the distribution functions of the atoms in the ground and excited states, $f(x,v)$ and $f^*(x,v)$:

$$v\frac{\partial f}{\partial x}=St+St^*+[\gamma+P(x)]f^*-P(x)f, \tag{1}$$

$$v\frac{\partial f^*}{\partial x}=P(x)f-[\gamma+P(x)+\nu^*(v)]f^*, \tag{2}$$

where St is the collision integral for the unexcited atoms with the buffer particles and St^* controls the arrival of hot unexcited atoms owing to superelastic collisions with cross section $\sigma^*(v)$ and rate

$$\nu^*(v)=n_b\sigma^*(v)v. \tag{3}$$

The general form of St^* is given by the integral

$$St^*=\int W(v,v')f^*(x,v')dv', \tag{4}$$

in which the kernel $W(v,v')$ is defined in terms of the relative collision velocity, its differential cross section, and the density of the buffer gas in the standard way.[7,8] In Eq. (2) we have omitted the terms describing collisions of excited atoms which are not accompanied by damping, since the cross sections for these processes are much smaller than the quenching cross section. The action of the light is described in Eqs. (1) and (2) in a balance approximation: $P(x)$ represents the rate of absorption of the light, proportional to its intensity at the point x, while γ is the rate of spontaneous relaxation. It should be noted that for buffer gas densities below $n_b \sim 10^{19}$ cm^3, typical values of the quenching collision cross sections of $\sigma^* \sim 10^{-15}$ cm^2, and velocities of the atoms $v \sim 10^4$ cm/s, the collisional relaxation rate is much lower than the spontaneous relaxation rate, which is typically on the order of 10^8 s^1 for allowed optical transitions.

Since the characteristic scale length of the nonuniformity in the light field cannot be less than a few wavelengths, the gradient terms in Eqs. (1) and (2) are small compared to the terms on the right. This makes it possible to neglect the gradient terms and express f^* in terms of f in the first approximation. Equating the right hand side of Eq. (2) to zero, we find

$$f^* = f \frac{P(x)}{\gamma + P(x) + \nu^*(v)}. \tag{5}$$

Substituting Eq. (5) in Eq. (1), we obtain

$$v \frac{\partial f}{\partial x} = St + St^* - \nu^*(v) s(x) f, \tag{6}$$

where

$$s(x) = \frac{P(x)}{\gamma + P(x)} \tag{7}$$

determines the degree of saturation in the atomic excitation at the point x provided $\nu^*(v) \ll \gamma$. With the same degree of accuracy in St^*, we can set $f^* = s(x) f$. Equating the right hand side of Eq. (6) to zero, we find an equation satisfied by the distribution function f_0 for every value of x. In this approximation, f_0 remains isotropic, but may deviate sharply from equilibrium if the rate of relaxation associated with collisions of excited atoms, $\nu^*(v)s(x)$, is comparable to or greater than the rate of relaxation owing to collisions of unexcited atoms, which we shall denote by ν_t. In the latter case, f_0 ceases to depend on x in the depth of the illuminated region and is completely determined by the characteristics of the collisions involving excited atoms.

In the next approximation with respect to the gradient term, the solution of Eq. (6) becomes anisotropic and optically-induced transport sets in. In the case of a small anisotropy, the flux of the active component of the mixture, $j(x)$, is expressed in terms of the gradient of f_0. Following Ref. 7, we then obtain

$$j(x) = -\frac{1}{3} \int l(x,v) v \frac{\partial f_0}{\partial x} dv, \tag{8}$$

where

$$l(x,v) = \frac{v}{s(x)\nu^*(v) + \nu_t}; \tag{9}$$

$l(x,v)$ has the meaning of an effective mean free path for the unperturbed atoms including optical excitation and superelastic collisions.

EQUILIBRIUM CONDITIONS FOR A NONUNIFORMLY ILLUMINATED GAS MIXTURE

To analyze the equilibrium conditions which follow from Eqs. (8), we rewrite $f_0(x,v)$ in the form

$$f_0(x,v) = n(x) \tilde{f}(x,v), \tag{10}$$

where $\tilde{f}(x,v)$ is the velocity distribution function normalized to unit density and $n(x)$ is the particle number density.

Denoting local averaging over the velocities with the function $\tilde{f}(x,v)$ by angle brackets $\langle \ldots \rangle$, we obtain

$$j(x) = -D(x) \frac{\partial n}{\partial x} - n \left[\frac{\partial D(x)}{\partial x} - \delta(x) \right], \tag{11}$$

where

$$D(x) = \frac{1}{3} \langle v l \rangle \quad \text{and} \quad \delta = \frac{1}{3} \left\langle v \frac{\partial l}{\partial x} \right\rangle. \tag{12), (13}$$

Let us consider the case $j = 0$. Then the solution of Eq. (13) determines the following relationship between the densities of atoms n_* and n_0 deep inside the illuminated region and in the shadow regions, respectively:

$$n_* D_* = n_0 D_0 \exp\left\{ \int_{-\infty}^{\infty} \frac{\delta(x)}{D(x)} dx \right\}. \tag{14}$$

Here $D_* = D(\infty)$ and $D_0 = D(-\infty)$ are the diffusion coefficients in the depth of the illuminated and unilluminated regions. In connection with this result, it should be noted that it describes an effect that is caused, not only by the nonuniform heating of the atoms, but also by the spatially nonuniform mean free path. If the explicit dependence of the mean free path on position is written in the factored form $l(x,y) = 1/N(x)\sigma(v)$, as, for example, in a medium with a nonuniform density of scatterers, $N(x)$, then Eq. (14) reduces to the equations of thermal diffusion for a light impurity in a heavy buffer gas.[7] It should be emphasized that, as opposed to thermal diffusion, where the active component and the buffer medium have the same temperature at every point, with optically-induced transport the state of the buffer medium is unchanged over all space. This difference causes a change in the sign of the effect. Whereas in thermal diffusion the light impurity concentrates in places with an elevated temperature, optically-induced transport leads to a drop in the concentration of the active component in the illuminated region. As for the magnitude of the effect, it can be much greater than in the case of thermal diffusion because the resonant component can be ''overheated'' to high temperatures through superelastic collisions. Thus, during collisions of excited lithium atoms with CO_2 molecules, the former obtain an energy of 0.5 eV, which causes their concentration in the illuminated region to change by roughly a factor of 4.

OPTICALLY-INDUCED FLOW ALONG CAPILLARIES

The above discussion of optically-induced transport processes allows us to predict yet another effect. Let us consider the effect of irradiation on the flow of a pure atomic gas in the Knudsen regime through a capillary or porous medium, in which the atoms are excited by the light. Suppose that the collisions of the excited atoms with the walls are superelastic, such as those considered above for atom-molecule collisions. The fact that excited atoms are quenched in collisions with a solid surface with a probability near unity has been established quite reliably,[9,10] and there is also some experimental evidence that part of the electronic excitation energy of the atom is transferred to its translational degrees of freedom during this process.[11] We shall assume that the scattering of atoms at the walls is diffuse and that the mean free path l, which is of the same order of magnitude as the diameter of the capillary, is small compared to the length of the capillary. The motion of an atom under these conditions is similar to its motion in a medium with randomly distributed scatterers. Thus, the description of transport processes in this case reduces to that given above for impurities in a gaseous medium.

For the flux of atoms we use Eq. (11). D_* is determined by the velocity distribution of the atoms heated by collisions with the wall. This heating will increase as an atom moves further into the capillary, until cooling processes stop this rise. In order not to complicate the analysis, without additional information on energy exchange processes during inelastic collisions of excited atoms with solid dielectric surfaces, we shall assume that the heating is stabilized immediately at the entrance of the capillary. In this case. D_* is independent of x and for conservation of the flux in the capillary, Eq. (11) yields

$$D_* \frac{\partial n}{\partial x} = -j = \text{const}. \tag{15}$$

Considering an efflux into free space, we obtain the following concentration distribution of the atoms in a capillary of length L:

$$n(x) = j(L-x)/D_* . \tag{16}$$

The current density j is determined from the condition at the beginning of the capillary, where the flux

$$j = \int v_x f(0, v)dv - \int_{v_x>0} v_x f_>(0,v)dv - \int_{v_x<0} v_x f_<(0,v)dv. \tag{17}$$

Here the first term is determined by the flux in the capillary and the second by the flux outside it. At the beginning of the capillary the velocity distribution of the atoms is highly anisotropic: cold atoms enter the capillary and hot ones leave it. Determining the distribution function at the boundary of randomly scattering media is a complicated Milne problem.[12] Here we give the boundary condition formally without solving this problem, merely noting that, because of the strong anisotropy, the values of $n_>$ and $n_<$, defined by

$$n_> = \int_{v_x>0} f_<(0,v)dv \quad \text{and} \quad n_< = \int_{v_x<0} f_<(0,v)dv, \tag{18}$$

differ substantially. Then, in Eq. (17) for the flux, written in the form $j = n_> v_> - n_< v_<$, where $v_>$ and $v_<$ are the average velocities of the particles entering and leaving the capillary, we set $n_> = n_a/2$ as the volume density of atoms and $n_< = n(0)/2$ as the density of atoms moving diffusively from the beginning of the capillary. The corresponding average velocities will be $v_> = v_T$, where v_T is the average thermal speed, and $v_< = v_*$, where v_* is the average speed of the atoms heated in the capillary as a result of excitation quenching in collisions with the walls. Thus, instead of Eq. (17), we obtain

$$2j = n_0 v_T - n(0) v_* . \tag{19}$$

Solving Eqs. (16) and (19) jointly, we obtain the following expression for the flux through the capillary:

$$j = n_0 v_T D_* / 2L v_* . \tag{20}$$

Calculating the velocity distribution of the atoms along the length of a capillary requires detailed knowledge of the behavior of superelastic collisions of atoms with the walls and cannot be done here. Nevertheless, we point out that heating a resonant gas in the capillary can, in principle, be used to separate multicomponent gas mixtures using an ordinary atomic velocity selector when the capillary is excited by radiation that is resonant with an electronic transition of just one of the components. In addition, it is clear from Eq. (20) that the flux of gas in the capillary can also be changed owing to the effect of the light on the mean free path of atoms in the capillary.

Two possible mechanisms for this effect, which involve a difference in the angular distributions of scattered thermal, hot, and excited atoms at the walls, can be pointed out. The first is simply related to the difference between the temperature of the incident beam and that of the surface. It is known[13] that as a beam of atoms incident on a surface with temperature T_n is heated, ordinary thermal (diffuse) scattering is supplanted by structural scattering, in which the angular distribution of the scattered beam forms a rather sharp lobe in a direction close to that for mirror reflection of the incident beam. This change in scattering regime takes place at beam temperatures of only a few times the surface temperature and can cause a substantial rise in the flux through the capillary of gas that has been ''heated'' by the optical radiation.

The second mechanism through which the light acts on the angular distribution of the scattering may be related to the behavior of superelastic collisions. Recall that diffuse (cosine) scattering is usually related to sequential adsorption and desorption events for particles at the surface, during which any correlation between the initial and final velocities is lost. In superelastic collisions, where part of the electronic excitation energy is released, the particle is not adsorbed, so that a correlation of this type is possible. For example, if the momentum imparted to a particle during a superelastic collision is predominantly normal to the wall,[14] then this causes

a reduction in the mean free path along the capillary and a reduction in the flux in the capillary. The same sort of reduction in the flux occurs when this momentum is in the opposite direction to the velocity vector of the incident particle.

Calculating the velocity distribution in a capillary requires knowledge of the character of atom-wall superelastic collisions. Collisions of excited atoms with dielectrics have hardly been studied, as pointed out specially in the literature.[5] We note that measurements of the parameters of a flow through a laser illuminated capillary and a determination of the distribution of the concentration of atoms along its length might be one of the simplest ways to study the efficiency and angular distribution of collisions of excited atoms with solid surfaces.

CONCLUSION

The processes discussed above are among many examples of the selective effect of laser radiation on the kinetics of phenomena in gaseous media. These processes, as a rule, are of interest in themselves, but their value is greatly enhanced when they can be used successfully in practice. There is no doubt that the changes in the concentration of a resonantly excited system in an illuminated region may serve as a basis for methods of separating gaseous mixtures and should be taken into account in any interaction of bounded laser beams in gases, in particular, in acousto-optic spectroscopy using rather high-power cw lasers.

The question of whether these effects occur in molecular media requires further study. Superelastic collisions of electronically excited molecules with a quenching partner have clearly not been studied adequately. In addition, in dense gaseous mixtures, where the rates of vibrational–rotational equilibration and V–T relaxation are quite high, the above analysis can be carried over to molecular collisions almost entirely.

There is special interest in the possibility of similar phenomena in liquids and in the interior of solids. We have already mentioned the observation of diffusive escape into vacuum of alkali metal atoms adsorbed into the volume of a silane film when irradiated by optical radiation for which silane is transparent. We believe that this effect is directly associated with the drop in the concentration of atoms in an illuminated region discussed above. In fact, if we assume that the energy barrier for volume diffusion of the alkali atoms is lower than the energy of a photon absorbed by them, then the sequence of absorption and quenching of electronic excitation causes the atoms to jump to neighboring positions, ''heats'' them a certain extent, and speeds up their volume diffusion. The escape of an atom from the film at the vacuum interface causes a decrease in the concentration of atoms in the film and an increase in their concentration in the volume, as is observed experimentally.[4] We may, therefore, assume that attempts to find similar effects in solids and weakly concentrated liquids will be successful.

This work was supported by the Russian Fund for Fundamental Research.

[1] F. Kh. Gel'mukhanov and A. M. Shalagin, JETP Lett. **29**, 711 (1979).
[2] N. V. Karlov, I. K. Meshkovskiĭ, R. P. Petrov *et al.*, JETP Lett. **30**, 42 (1979)].
[3] N. V. Karlov, A. N. Orlov, Yu. N. Petrov *et al.*, Pis'ma Zh.Tekh. Fiz. **9**, 69 (1983) [Sov. Tech. Phys. Lett. **9**, 29 (1983)].
[4] M. Meucci, E. Mariotti, P. Bicchi, C. Marinella, and L. Moi, Europhys. Lett. **25**, 639 (1994).
[5] B. M. Smirnov, *Excited Atoms* [in Russian], Énergoizdat, Moscow (1982), 232 pp.
[6] K. E. Grew and T. L. Ibbs, *Thermal Diffusion in Gases*, Gostekhizdat, Moscow (1956), 183 pp.
[7] E. M. Lifshitz and L. P. Pitaevskii, *Physical Kinetics*, Pergamon, Oxford (1981).
[8] V. P. Silin, *Introduction to the Kinetic Theory of Gases* [in Russian], Nauka, Moscow (1971), 331 pp.
[9] A. G. Zajonc and A. V. Phelps, Phys. Rev. A **23**, 2479 (1981).
[10] E. B. Aleksandrov, N. N. Kostin, V. V. Khromov, and Yu. I. Chernaya, Opt. Spektrosk. **67**, 517 (1989) [Opt. Spectrosc. **67**, 302 (1989)].
[11] A. M. Bonch-Bruevich, T. A. Vartanyan, A. V. Gorlanov *et al.*, Zh. Éksp. Teor. Fiz. **97**, 1077 (1990) [Sov. Phys. JETP **70**, 604 (1990)].
[12] K. M. Case and P. F. Zweifel, *Linear Transport Theory* (Addison-Wesley, Reading, Mass. (1967); Mir, Moscow (1972), 384 pp.).
[13] F. O. Goodman and H. Y. Wachman, *Dymamics of Gas–Surface Scattering* (Academic Press, New York (1976); Mir, Moscow (1980), 424 pp.).
[14] V. V. Levdanskiĭ, Zh. Tekh. Fiz. **52**, 826 (1982) [Sov. Phys. Tech. Phys. **27**, 533 (1982)].

Translated by D. H. McNeill

Inversion of the density gradient and the diffusion ''gate'' in isothermal mixing of gases

V. N. Kosov and Yu. I. Zhavrin

Scientific-Research Institute of Experimental and Theoretical Physics, Al-Farabi Kazakh National University, 480078 Alma-Ata, Kazakhstan

V. D. Seleznev

Ural State Technical University, 620002 Ekaterinburg, Russia
(Submitted November 14, 1996)
Zh. Tekh. Fiz. **68**, 14–17 (May 1998)

The stable quasistationary mixing of ternary gas mixtures in a system of two chambers connected by a capillary is described by a theoretical model which predicts the density distribution of the mixture along the length of the diffusion channel. It is demonstrated that inversion of the density gradient can occur due to a nonlinear concentration distribution of the heavy component in a diffusion ''gate'' effect. The results obtained using this model are compared with the experimental data. © *1998 American Institute of Physics.* [S1063-7842(98)00305-5]

1. The onset of convective instability during isothermal binary diffusion in sealed structures was investigated theoretically in Refs. 1 and 2, where it was shown that a condition of breakdown of the diffusion mechanism of mixing is a large positive density gradient of the mixture (where the density above is greater than that below). This fact is confirmed experimentally. However, in ternary (three-component) gas mixtures[3,4] an anomalous convective instability is observed, which arises for negative density gradients of the mixture (the density in the upper part of the structure is less than in the lower part). The reason for this anomalous behavior of ternary mixtures is insufficiently understood, but a comparison of the experimental data on the anomalous convective instability[4–7] and on the diffusion ''gate'' effect[8] shows that these two effects are most strikingly manifested in the same mixtures. On the basis of these facts it may be surmised that during the organization of a diffusion ''gate'' a change in sign of the density gradient can occur on some segment of the channel, and this is the reason for the instability.

The aim of the present paper is to verify the above conjecture and analyze the conditions for inversion of the density gradient. This is done on the basis of solution of the problem of the quasistationary density distribution of a ternary mixture under conditions of mixing of the gases in a system of two chambers connected by a vertical channel.

2. Consider a system of two chambers joined by a capillary (Fig. 1). The upper chamber contains a binary mixture of gases diffusing into a pure component located in the lower chamber. For definiteness, it is convenient to choose the following numbering of the components: *1,2* — the light and heavy gases in the upper chamber (*I*), respectively; *3* — the gas in the lower chamber (*II*). The density of the mixture in the upper part of the apparatus is always less than the density of the pure component in the lower part at any temperature T and pressure P. We assume that the volumes of the chambers V are equal and significantly exceed the volume of the connecting capillary of length L and cross-sectional area $S=\pi r^2$ (r is the radius of the capillary).

Isothermal diffusion is accompanied by the appearance of a pressure difference in the chambers ΔP (the diffusion baro-effect[9]), but for the viscous regime considered in the problem (the Knudsen number $\mathrm{Kn}=\lambda/r\ll 1$, where λ is the mean free path) the quantity $\Delta P/P$ is of the order of Kn^2 and is negligibly small. This allows us to take the pressure P to be uniform throughout the system and constant in time. However, the small pressure difference that arises gives rise

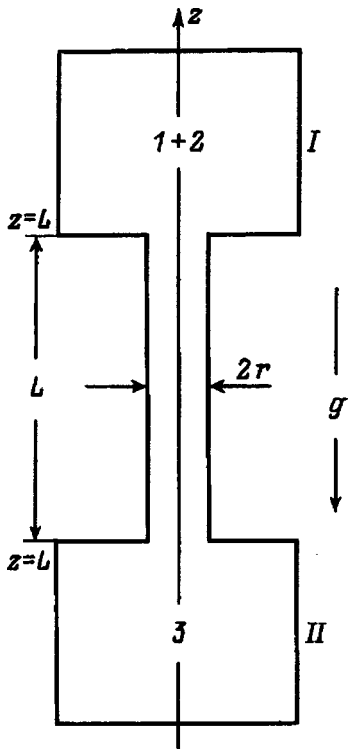

FIG. 1.

to a quasistationary diffusion regime in which the average numerical velocity vanishes[8,10]

$$\omega = c_1 u_1 + c_2 u_2 + c_3 u_3 = 0, \tag{1}$$

where c_i is the concentration of the ith component, u_i is the z-axis projection of the velocity of the ith component in the laboratory coordinate system, averaged over the cross section.

The diffusion velocities $(u_i - u_j)$ can be determined from the Stefan–Maxwell equations, which for a ternary mixture of ideal gases have the form

$$\frac{c_1 c_3}{D_{13}}(u_1-u_3)+\frac{c_1 c_2}{D_{12}}(u_1-u_2)=-\nabla_z c_1,$$

$$\frac{c_1 c_2}{D_{12}}(u_2-u_1)+\frac{c_2 c_3}{D_{23}}(u_2-u_3)=-\nabla_z c_2, \tag{2}$$

where D_{ij} is the binary diffusion coefficient of the binary mixture, $i,j=\overline{1,3}$, and $c_i = n_i/(n_1+n_2+n_3) = n_i/n$.

Equations (1) and (2) define explicit expressions for the component velocities[8]

$$u_1=\frac{1}{c_1}\left\{\frac{c_1 D_{23}(D_{12}-D_{13})\nabla_z c_2 - D_{13}[(c_2+c_3)D_{12}+c_1 D_{23}]\nabla_z c_1}{c_1 D_{23}+c_2 D_{13}+c_3 D_{12}}\right\},$$

$$u_2=\frac{1}{c_2}\left\{\frac{c_2 D_{13}(D_{12}-D_{23})\nabla_z c_1 - D_{23}[(c_1+c_3)D_{12}+c_2 D_{13}]\nabla_z c_2}{c_1 D_{23}+c_2 D_{13}+c_3 D_{12}}\right\},$$

$$u_3=\frac{1}{c_3}\left\{\frac{D_{13}[(c_1+c_2)D_{23}+c_3 D_{12}]\nabla_z c_1 + D_{23}[(c_1+c_2)D_{13}+c_3 D_{12}]\nabla_z c_2}{c_1 D_{23}+c_2 D_{13}+c_3 D_{12}}\right\}. \tag{3}$$

In what follows we assume that the composition equalization time in the system of chambers τ is much longer than the setup time τ_L of the concentration distribution along the length of the capillary. Thus, for times $t > \tau_L$ the mixture of gases can be assumed to be quasistationary. In this case the concentration distributions of the components set up quite rapidly to the assigned values of the composition of the mixture in the chambers and vary slowly as the concentrations in the system equalize. For such conditions it can be assumed that the flow rate of each component across an arbitrary cross section of the capillary is independent of the coordinate z

$$Q_i = n_i(z) u_i(z) \pi r^2 = \text{const}. \tag{4}$$

Substituting expressions (3) into Eq. (4) and employing the assumption of smallness of the molar concentration of the second component ($c_2 \ll 1$) to simplify the resulting expression, we readily obtain the following expressions for $c_i(z)$:

$$-D_{13}\frac{dc_1}{dz}=\frac{1}{\pi r^2}\frac{Q_1}{n},$$

$$-c_2 D_{13}(D_{23}-D_{12})\frac{dc_1}{dz} - D_{12}D_{23}\frac{dc_2}{dz} = \frac{1}{\pi r^2}\frac{Q_2}{n}[D_{12}+c_1(D_{23}-D_{12})]. \tag{5}$$

The solution of system (5) allowing for the boundary conditions

$$z=0,\ c_1=c_2=0,\ a_3=c_{3_{II}},$$

$$z=L,\ c_1=c_{1_I},\ c_2=c_{2_I},\ c_3=0 \tag{6}$$

is written as follows:

$$c_3 = 1-\frac{z}{L},\quad c_1 = 1-c_2-c_3,$$

$$c_2=\left\{c_{2_I}+\frac{Q_2}{Q_1}\left[\frac{D_{12}(D_{13}-D_{23})}{D_{13}(D_{12}-D_{23})}-c_{1_I}\right]\right\}\times\exp\left[-\frac{1}{\pi r^2}\frac{Q_1}{n}\frac{(D_{23}-D_{12})}{D_{12}D_{23}}(L-z)\right]-\frac{Q_2}{Q_1}\times\left[\frac{D_{12}(D_{13}-D_{23})}{D_{13}(D_{12}-D_{23})}-c_{1_I}\right]-\frac{1}{\pi r^2}\frac{Q_2}{D_{13}n}(L-z), \tag{7}$$

where

$$Q_1 = -\frac{nD_{13}}{L}(c_{1_I}-c_{1_{II}})\pi r^2,$$

$$Q_2=-\frac{\dfrac{nD_{13}}{L}\,\pi r^2\left\{c_{2_{II}}-c_{2_I}\exp\left[-\dfrac{D_{13}(D_{12}-D_{23})}{D_{12}D_{23}}(c_{1_I}-c_{1_{II}})\right]\right\}}{\dfrac{1}{(c_{1_I}-c_{1_{II}})}\left[\dfrac{D_{12}(D_{13}-D_{23})}{D_{13}(D_{12}-D_{23})}-c_{1_I}\right]\left\{\exp\left[-\dfrac{D_{13}(D_{12}-D_{23})}{D_{12}D_{23}}(c_{1_I}-c_{1_{II}})\right]-1\right\}-1}. \tag{8}$$

It should be noted that the case $D_{23}\ll D_{12},D_{13}$ corresponds to a substantially nonlinear distribution of the concentration of the heavy component along the capillary. Figure 2 [*a*—0.7He(*1*)+0.3R12(*2*)–Ar(*3*), *b*—0.9He(*1*) +0.1R12(*2*)–Ar(*3*)] plots the distribution $c_i(z)$ for the mixture He(*1*)+R12(*2*)–Ar(*3*) (the numbering of the components is indicated here in parentheses) for different amounts of freon-12 in the mixture ($c_{2_I}\ll 1$). The nonlinearity of the distribution $c_2(z)$ is due to the fact that in the mutual diffusion of helium and argon ($c_2\to 0$) a baro-effect arises with increase in the pressure in the lower chamber. The resulting pressure gradient is the reason for the hydrodynamic flow of the mixture into the upper chamber with velocity $v_0 \sim D_{13}/L$. The characteristic diffusion velocity of freon for the case when the concentration distribution $c_2(z)$ is linear is of the order of $c_{2_I}D_{23}/L$, which is much less than v_0. The resulting freon velocity is directed upwards. In the quasistationary situation the concentration c_2 becomes exponentially small in the lower part of the capillary and the flow-rate Q_2 [formula (8)] becomes much less than the value $n\pi r^2 c_{2_I}D_{23}/L$ corresponding to the case when $c_2(z)$ is linear. The effect of an abrupt decrease in Q_2 in similar situations is called a ''diffusion gate''[7] and takes place in mixtures with a significant diffusion baro-effect for the first and third components for a low value of the diffusion coefficient D_{23}. For small values of Q_2 relations (7) and (8) permit one to obtain simplified approximate expressions for the concentration distributions $c_i(z)$

$$c_1=1-c_2-c_3,\quad c_2=c_{2_I}\exp\left[-\frac{D_{13}(D_{12}-D_{23})}{D_{12}D_{23}}\left(1-\frac{z}{L}\right)\right],$$

$$c_3=1-\frac{z}{L}. \tag{9}$$

Expressions (9) allow one to find the density distribution along the length of the capillary

$$\rho=\rho_1c_1+\rho_2c_2+\rho_3c_3, \tag{10}$$

and also its maximum gradient

$$\frac{1}{n}\frac{d\rho}{dz}=\Delta m_2c_{2_I}\exp[-\varkappa]\frac{\varkappa}{L}\exp\left[\varkappa\frac{z}{L}\right]-\Delta m_3\frac{1}{L},$$

$$\Delta m_2=m_2-m_1,\quad \Delta m_3=m_3-m_1,$$

$$\varkappa=\frac{D_{13}(D_{12}-D_{23})}{D_{12}D_{23}}, \tag{11}$$

where m_i is the mass of a molecule of species i.

For the typical diffusion-gate system He(*1*)+R12(*2*)–Ar(*3*) the density distribution of the mixture over the length of the capillary, calculated according to formulas (9) and (10), is plotted in Fig. 3 and illustrates the possibility of inversion of the density gradient as the concentration distribution $c_i(z)$ adjusts to the boundary conditions with $\rho_I<\rho_{II}$. Such a gradient inversion may be the reason for the convective instability; therefore it would be advisable to investigate the conditions for the appearance of nonmonotonicity of $\rho(z)$ as c_{2_I} varies for $\rho_I<\rho_{II}$. The largest value of the concentration of the second component in chamber I in the interval of interest to us corresponds to the condition $\rho_I=\rho_{II}$, i.e.,

$$m_3=(1-c_{2_I})m_1+c_{2_I}m_2,$$

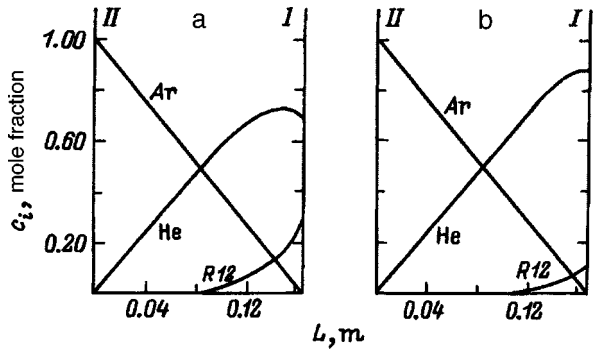

FIG. 2.

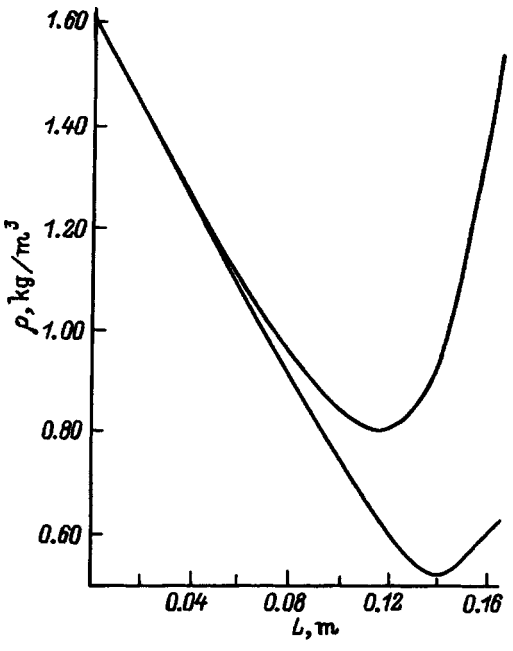

FIG. 3.

whence it follows that

$$c_{2_I}^{\max}=\frac{m_3-m_1}{m_2-m_1}=\frac{\Delta m_3}{\Delta m_2}. \tag{12}$$

The minimum value $c_{2_I}=c_{2_I}^{\min}$ in this interval can be found on the basis of Eq. (11) from the condition

$$\frac{d\rho}{dz}\Big|_{z=L}=0, \quad c_{2_I}^{\min}=\frac{\Delta m_3}{\Delta m_2}\frac{D_{12}D_{23}}{D_{13}(D_{12}-D_{23})}. \tag{13}$$

Thus, inversion of the density gradient and, consequently, anomalous (for $\rho_I<\rho_{II}$) unstable diffusion can take place only in the concentration interval of the heavy component in the upper chamber

$$c_{2_I}^{\min}<c_{2_I}<c_{2_I}^{\max}. \tag{14}$$

3. As an illustration, a comparison of the above results with experimental data obtained with a two-chamber setup can be had for the case of two ternary gas mixtures: $CH_4(1)+Ar(2)-N_2(3)$ and $He(1)+R12(2)-Ar(3)$ for $P=0.101$ MPa and $T=298$ K.[6,11] In the first system the binary diffusion coefficients of the components are comparable with each other. This system exhibits the stable regime of isothermal diffusion over a wide pressure interval and for arbitrary values of the concentration c_{2_I} (Ref. 11). This is because for similar values of D_{12} and D_{23} the quantity $(c_{2_I}^{\max}-c_{2_I}^{\min})\ll 1$ (see formulas (12) and (13)) and therefore in the investigated concentration interval it is impossible to observe the instability. A quasistationary distribution of the component concentrations and the density is shown in Fig. 4, from which it can be seen that linear component concentration distributions for the system $0.55CH_4+0.45Ar-N_2$ lead to a linear distribution of the density.

For the second system the coefficients D_{12} and D_{23} are substantially different (38.5×10^{-6} m^2/s and 6.8×10^{-6} m^2/s, respectively). This leads to the following boundary values of the concentration of the heavy component in the upper chamber (1): $c_{2_I}^{\min}=0.035$, $c_{2_I}^{\max}=0.308$. If we choose c_{2_I} from this interval, we obtain the density distributions shown in Fig. 3. The graphs show that $\nabla\rho$ changes sign. Experiments carried out with this mixture indeed show that for $c_{2_I}\gtrsim 0.105$ the diffusion instability takes place.

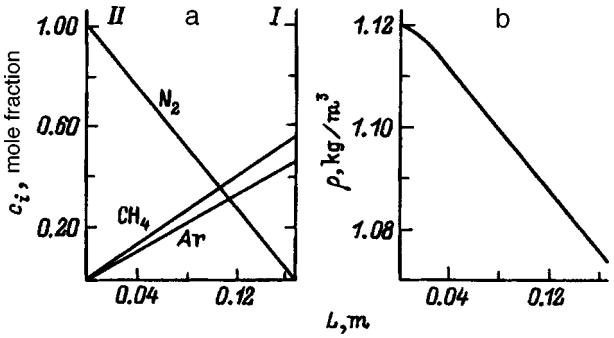

FIG. 4.

Table I lists values of $c_{2_I}^{\min}$ and $c_{2_I}^{\max}$ and experimental data for c_{2_I} for various mixtures for which convective instability was observed. In the calculation of $c_{2_I}^{\min}$ and $c_{2_I}^{\max}$ for the systems H_2+CO_2-air, N_2+R12–R22, and Ar+R12–R22 the binary diffusion coefficients were determined within the framework of the rigorous kinetic theory.[12,13] In all the other cases we used the experimental values of the binary diffusion coefficients in formula (13). Analysis of the concentrations so obtained shows that in all the experiments with anomalous unstable diffusion c_{2_I} is found between $c_{2_I}^{\min}$ and $c_{2_I}^{\max}$. This confirms the validity of the theoretical model.

4. Thus, we have developed a theoretical model of stable quasistationary mixing of three gases in a system of two chambers joined by a capillary that allows one to determine the density distribution along the length of the channel.

We have shown that for the density of the mixture in the upper chamber ρ_I less than the density in the lower chamber ρ_{II}, inversion of the density gradient takes place in the channel due to nonlinearity of the concentration distribution of the heavy component, exhibiting the effect of a diffusion

TABLE I. Boundary values of the concentration of the heaviest component of the mixture for a series of diffusion-unstable systems at $T=298$ K.

Reaction No.	System	Component concentrations, mole fraction: Calculation $c_{2_I}^{\min}$	Calculation $c_{2_I}^{\max}$	Experiment c_{2_I}	Ref.
1	He+Ar—N_2	0.265	0.667	0.30−0.35	4
2	He+R12 — Ar	0.035	0.308	0.08−0.12	5
3	CH_4+R12—n-C_4H_{10}	0.017	0.400	0.10−0.16	5
4	He+R12 — n-C_4H_{10}	0.044	0.462	0.08−0.12	5
5	N_2+R12—n-C_4H_{10}	0.155	0.323	0.16	5
6	$H_2+N_2-CH_4$	0.212	0.538	0.25*	
7	H_4+Ar−N_2	0.230	0.684	0.30−0.35*	
8	H_2+CO_2-air	0.158	0.643	0.16	3
9	N_2+R12—R22	0.387	0.629	0.30−0.50	3
10	Ar+R12 — R22	0.428	0.574	0.29−0.49	3
11	H_2+R12—Ar	0.031	0.319	0.07	5

*Experimental data of the authors.

''gate.'' We have determined the range of concentrations of the heavy component in the upper chamber for which such inversion takes place. Comparison of this range with the experimentally determined interval of concentrations c_{2_I} corresponding to unstable diffusion apparently caused by inversion of the density gradient demonstrates good agreement.

[1] G. Z. Gershuni and E. M. Zhukhovitskiĭ, *Convective Stability of an Incompressible Liquid* [in Russian], Nauka, Moscow (1972).
[2] D. D. Joseph, *Stability of Fluid Motions I* (Springer-Verlag, New York, 1976); *Global Stability of Fluid Motions II* (Springer-Verlag, New York, 1976) [Mir, Moscow, 1981, 638 pp.].
[3] L. Miller, T. H. Spurling, and E. A. Mason, Phys. Fluids **10**, 1806 (1967).
[4] Yu. I. Zhavrin, N. D. Kosov *et al.*, Zh. Tekh. Fiz. **54**, 943 (1984) [Sov. Phys. Tech. Phys. **29**, 561 (1984)].
[5] V. N. Kosov and Yu. M. Zhavrin, in *Thermophysical Properties of Substances and Materials* [in Russian] (Izd. Standartov, Moscow, 1989), No. 28, pp. 112–122.
[6] Yu. M. Zhavrin and V. N. Kosov, Teplofiz. Aeromekh. **2**(2), 145 (1995).
[7] Yu. M. Zhavrin and V. N. Kosov, Pis'ma Zh. Tekh. Fiz. **19**, No. 10, 18 (1993) [Tech. Phys. Lett. **19**, 301 (1993)].
[8] V. D. Seleznev and V. G. Smirnov, Zh. Tekh. Fiz. **51**, 795 (1981) [Sov. Phys. Tech. Phys. **26**, 471 (1981)].
[9] P. E. Suetin and P. V. Volobuev, Zh. Tekh. Fiz. **34**, 1107 (1964) [Sov. Phys. Tech. Phys. **9**, 859 (1964)].
[10] V. D. Seleznev *et al.*, *Thermophysical Properties of Substances and Materials* [in Russian] (Izd. Standartov, Moscow, 1982), No. 17, pp. 24–43.
[11] V. N. Kosov and Yu. I. Zhavrin, *Diffusive and Convective Transport in Gases and Liquids* [in Russian] (Izd. KazGU, Alma-Ata, 1986), pp. 16–18.
[12] J. O. Hirschfelder, C. F. Curtiss, and R. B. Bird, *Molecular Theory of Gases and Liquids* (Wiley, New York, 1954; IL, Moscow, 1961, 931 pp.).
[13] K. M. Aref'ev, *Transport Phenomena in Gases and Plasma* [in Russian] (Énergoatomizdat, Leningrad, 1983), 112 pp.

Translated by Paul F. Schippnick

Relaxation of a hard-sphere gas and criteria of validity of the calculations

A. Ya. Énder and I. A. Énder

A. F. Ioffe Physicotechnical Institute, Russian Academy of Sciences, 194021 St. Petersburg, Russia; St. Petersburg State University, 199034 St. Petersburg, Russia

(Submitted January 17, 1997)
Zh. Tekh. Fiz. **68**, 18–26 (May 1998)

The isotropic Boltzmann equation is solved using the Sonin moment system of equations. The main task here is the construction of a matrix describing the particle interaction. Such a matrix has been constructed analytically for various interaction cross sections in a number of papers [M. Barnsley and G. Turchetti, Lett. Nuovo Cimento **33**, 347 (1982); G. Turchetti and M. Paolilli, Phys. Lett. A **90**, 123 (1982); F. Schürrer and G. Kügerl, Phys. Fluids A **2**, 609 (1990); A. Ya. Énder and I. A. Énder, Tech. Phys. **39**, 997 (1994)]. Calculations of matrix elements arrived at by different methods for the hard-sphere model are compared. Some general properties of the matrix are found that can be used as criteria of the validity of the calculations. With the help of such criteria it is shown that the nonlinear matrix elements were calculated incorrectly by Schürrer and Kügerl (op. cit.). © *1998 American Institute of Physics.* [S1063-7842(98)00405-X]

INTRODUCTION

In this paper we consider the moment method for solving the nonlinear Boltzmann equation for problems of isotropic relaxation, based on expanding the distribution function in Sonin (Laguerre) polynomials.[1–4] The possibility of solving the nonlinear Boltzmann equation numerically by the moment method up to large velocities was first demonstrated in Refs. 1 and 2. To construct the distribution function at large velocities, it is necessary to include many moments, i.e., to know the nonlinear matrix elements describing the particle interaction, at large values of the indices. The formula for the matrix elements in Ref. 2, derived for cross sections isotropic in the velocities, contains six nested sums. This limits the possibilities of increasing the number of terms of the expansion N (in Ref. 2 the calculations were carried out only to $N=13$). In our previous paper[4] using the α representation[5,6] we obtained formulas valid for any power-law potential and dropped the number of nested sums down to four. This enabled us to increase the number of terms to $N=30$ with the same error as obtained in Ref. 2 for $N=13$. The authors of Ref. 3 proposed a simpler algorithm for the particular case of the hard-sphere model that raised the hope of increasing the number of terms significantly higher. Unfortunately, there is an error in their formulas for the nonlinear matrix elements. The derivation of the matrix elements is a quite complicated problem, and errors are possible. In the course of comparison and analysis of the matrix elements calculated by various authors,[2–4,7] we developed some criteria of validity of calculation of nonlinear matrix elements.

1. COMPARISON OF DIFFERENT CALCULATIONS OF THE MATRIX ELEMENTS

In earlier classical works the method of expanding the distribution function in orthogonal polynomials was applied to calculate the first several linear moments needed in problems of transport theory. Later, works appeared in which the polynomial method was applied numerically[2–4] as well as analytically[8] to the isotropic Boltzmann equation (that is, isotropic in the velocities) to construct the distribution function at high energies. In this method the isotropic distribution function is expanded in a series of Sonin (Laguerre) polynomials

$$f(v,t)=M(v,\tilde{T}_0)\sum_{n=0}^{\infty} C_n(t)S_{1/2}^n(v^2/\tilde{T}_0) \tag{1}$$

with weighting function

$$M(v,\tilde{T}_0)=(1/\pi\tilde{T}_0)^{3/2}\exp(-v^2/\tilde{T}_0),\quad \tilde{T}_0=2kT_0/m_0. \tag{2}$$

As a rule, the equilibrium temperature of the gas is chosen for T_0. The Boltzmann equation reduces to the following system of moment equations:

$$dC_n/dt=\sum_{k,m=0}^{\infty} K_{k,m}^n C_k C_m. \tag{3}$$

It should be noted that the method of expanding in Sonin polynomials is applicable only if the distribution function satisfies Grad's criterion

$$\int_0^{\infty} f^2 \exp(v^2/\tilde{T}_0)d^3v<\infty. \tag{4}$$

In Ref. 9 it was shown that if the distribution function is represented in the form of a sum over two Maxwellians with temperatures T_1 and T_2 ($T_1<T_2$) and $T_2/T_0>2$, then this criterion is not satisfied.

The matrix elements $K_{k,m}^n$ are asymmetric relative to transposition of the lower indices. In the case of interaction of particles of one sort it is possible to transform to symmetric matrix elements $\tilde{K}_{k,m}^n=(K_{k,m}^n+K_{m,k}^n)/2$. Such matrix elements are considered in Refs. 1 and 2. We will not write out

the complicated formula given in Ref. 2 for $\tilde{K}^n_{k,m}$, which consists of six nested sums. Its derivation is laid out in detail in Ref. 1. It should be noted that this formula is valid only for the model of power-law potentials under the assumption that the cross section does not depend on the scattering angle.

When calculating series (1) on a computer, it is always necessary to truncate at some finite N, and the sum (3) becomes finite. The great achievement of the authors of Refs. 1 and 2 is that they were the first who were able to systematically calculate the nonlinear matrix elements up to $N=13$, which made it possible to advance into the region of high velocities. However, the huge number of terms in the formula in Ref. 2 has limited the possibility of increasing the number of terms N.

In Ref. 4, using the α method, we constructed the matrix $K^n_{k,m}$ for anisotropic cross sections as well and showed that it is possible to treat equations involving up to 25–30 moments with guaranteed accuracy.

The Boltzmann equation in the α representation ($\alpha = m_0/2kT$) has the form[5,6]

$$n_0 \frac{\partial \varphi}{\partial t} = n_0^2 \int_0^\infty A(\tilde{T},\tilde{T}_1,\tilde{T}_2)\varphi(\tilde{T}_1,t)\varphi(\tilde{T}_2,t)d\tilde{T}_1 d\tilde{T}_2. \quad (5)$$

Here n_0 is the particle number density, and the distribution function in the v-representation is related to $\varphi(T,t)$ by the following equation:

$$f(v,t) = \int_0^\infty M(v,\tilde{T})\varphi(\tilde{T},t)d\tilde{T}. \quad (6)$$

The kernel $A(\tilde{T},\tilde{T}_1,\tilde{T}_2)$ is a transform of the collision integral of two Maxwellians $J^m(\tilde{T}_1,\tilde{T}_2,v)$ in α space

$$J^m(\tilde{T}_1,\tilde{T}_2,v) = n_0^2 \int_0^\infty M(v,\tilde{T})A(\tilde{T},\tilde{T}_1,\tilde{T}_2)d\tilde{T}. \quad (7)$$

The orthogonal system of Sonin polynomials $S^r_{1/2}$ with Maxwellian weight corresponds to a biorthogonal system of functions s_L and s_R in α space

$$s^r_R(\tilde{T},\tilde{T}_*) = (\tilde{T}_*)\delta^{(r)}(\tilde{T}-\tilde{T}_*)/r!, \quad (8)$$

$$s^r_L = (1-\tilde{T}/\tilde{T}_*)^r. \quad (9)$$

Here $\delta^{(r)}(\tilde{T}-\tilde{T}_*)$ is the rth derivative of the δ function. Here

$$M(v,\tilde{T}_*)S^r_{1/2}(v^2/\tilde{T}_*) = \int_0^\infty M(v,\tilde{T})s^r_R(\tilde{T},\tilde{T}_*)d\tilde{T}, \quad (10)$$

$$\int_0^\infty s^i_L s^j_R d\tilde{T} = \delta_{ij}. \quad (11)$$

The function $\varphi(T)$ on the right-hand side of Eq. (5) can be represented in the form

$$\varphi(\tilde{T},t) = \sum_{n=0}^\infty C_n(t)s^n_R(\tilde{T},\tilde{T}_0), \quad (12)$$

$$C_n(t) = \int_0^\infty \varphi(\tilde{T},t)s^n_L(\tilde{T},t)d\tilde{T} = \int_0^\infty (1-\tilde{T}/\tilde{T}_0)^n \varphi(\tilde{T},t)d\tilde{T}. \quad (13)$$

In order to obtain system (3), we multiply both sides of Eq. (5) by $s^n_L(T,T_0)$ and integrate over T. We obtain for the matrix $K^n_{k,m}$

$$K^n_{k,m} = n_0^2 \tilde{T}_0^{k+m}(-1)^{k+m}\frac{d^{k+m}}{d\tilde{T}_1^k d\tilde{T}_2^m} \times \left(\frac{\tilde{T}_1^k \tilde{T}_2^m}{k!m!}\int_0^\infty d\tilde{T}(1-\tilde{T}/\tilde{T}_0)^n A(\tilde{T},\tilde{T}_1,\tilde{T}_2)\right)\Bigg|_{\substack{\tilde{T}_1=\tilde{T}_0,\\ \tilde{T}_2=\tilde{T}_0}} \quad (14)$$

In the case of a power-law dependence of the potential V on distance r ($V\sim 1/r^\kappa$) we have

$$g\sigma(g,z) = B_\gamma g^\gamma \chi(z)/4\pi, \quad z=\sin^2\theta/2. \quad (15)$$

Here $\sigma(g,z)$ is the differential scattering cross section, $\gamma = (\kappa-4)/\kappa$, B_γ=const, and $\chi(z)$ is the angular part of the cross section. In this case the kernel $A(T,T_1,T_2)$ and the matrix $K^n_{k,m}$ have the form

$$A(\tilde{T},\tilde{T}_1,\tilde{T}_2) = \sum_{l=1}^\infty d_l(\tilde{T}_1,\tilde{T}_2)s^l_R(\tilde{T},\tilde{T}_1), \quad (16)$$

$$d_l = \frac{4\pi l!}{\Gamma(-\mu)\Gamma(l+3/2)} \times \sum_{q=1}^l \frac{(-\Delta)^q \tilde{T}_1^{(l-2q)}\Gamma(l-q-\mu)\Gamma(q+3/2+\mu)}{q!(l-q)!\lambda^{l-q-\mu}}J_q, \quad (17)$$

$$K^n_{k,m} = n_0^2\left(\frac{4kT_0}{m_0}\right)^\mu \frac{4\pi(-1)^{n+k}n!\Gamma(\mu+5/2)}{2^m} \times \sum_{q=1}^n \frac{(\mu+5/2)_{q-1}}{q!}J_q \sum_{i=\max(0,q-k)}^{\min(m,q)}\left(\frac{q}{i}\right)\frac{2^i}{(m-i)!} \times \sum_{l=\max(q,n-k+q-i)}^n \frac{(2l-2q-1)!!(-1)^l}{\Gamma(l+3/2)(n-l)!} \times \sum_{j-\max(0,m_2)}^{m_1}\frac{(-1)^j(-\mu)_{j+m_3}}{j!2^j(m_1-j)!(j-m_2)!}, \quad (18)$$

where $\mu=\gamma/2$, $\Delta=\tilde{T}_2-\tilde{T}_1$, $m_1=k-n+i+l-q$, $m_2=k-n+i-l+q$, $m_3=l-q+m-i$.

Here we have made use of the following relations:

$$(a)_k = a(a+1)\ldots(a+k-1) = \frac{\Gamma(a+k)}{\Gamma(a)},$$

$$J_q = B_\gamma/4\pi\int_0^1 \chi(z)z^q dz.$$

A similar derivation of formulas (16)–(18) is given in Ref. 4.

For isotropic cross sections (and it was specifically this case that was considered in Refs. 1 and 2 $\chi(z)=1$ and J_q

$=B_\gamma/(q+1)/4\pi$. For the hard-sphere model $\mu=0.5$, $B_1=\pi d^2$, where d is the particle diameter, and $J_q=d^2/(4(q+1))$.

Formula (18), like the formulas from Ref. 2, is suitable for arbitrary values of the indices k, m, n. In the particular case in which one of the lower indices k, m vanishes, we obtain expressions for the linear elements. In this case the number of summations is substantially decreased. Thus, in formula (18) only one summation remains.

Unsystematic calculations of nonlinear matrix elements were also carried out in earlier works. Thus, Ref. 7 gives formulas for the symmetrized matrix elements $\tilde{K}^n_{k,m}$ in the case of power-law potentials, but only for $N\leqslant 4$.

Reference 3 calculates nonlinear matrix elements up to $N=64$ for the hard-sphere model. The expressions for the matrix elements in Ref. 3 have the form

$$K^n_{k,m}=\beta^n_{k,m}-\alpha^n_{k,m}, \tag{19}$$

$$\alpha^n_{k.m}=-\frac{n!}{2^{1/2}\Gamma(n+3/2)}\times\left(\frac{1}{m}\{\Lambda^1_{k,m-1,n}\}+\frac{1}{m(m-1)}\sum_{r=0}^{m-2}\{\Lambda^2_{k,r,n}\}\right),\quad m\geqslant 2, \tag{20}$$

$$\beta^n_{k,m}=\frac{2^{1/2}n!}{\Gamma(n+3/2)}\left(\frac{\{\Lambda^3_{k-1,m-1,n}\}}{km}-\frac{\{\Lambda^3_{k-2,m-1,n}\}}{(k-1)m}-\frac{\{\Lambda^3_{k-1,m-2,n}\}}{k(m-1)}+\frac{\{\Lambda^3_{k-2,m-2,n}\}}{(k-1)(m-1)}+\frac{k+1/2}{k}\{\Lambda^1_{k-1,m,n}\}+\frac{m+1/2}{m}\times\{\Lambda^1_{m-1,k,n}\}-(n+1)\{\Lambda^0_{k,m,n+1}\}\right),$$

$$k,\ m\geqslant 2. \tag{21}$$

Here $\{\Lambda^0_{k,m,n}\}$, $\{\Lambda^1_{k,m,n}\}$, $\{\Lambda^2_{k,m,n}\}$, and $\{\Lambda^3_{k,m,n}\}$ are various combinations of the gamma functions. Note that the linear elements $\alpha^n_{k,0}$, $\beta^n_{k,0}$, and $\beta^n_{0,m}$ are calculated according to separate formulas. These formulas, after some simple analytical transformations, coincide with the corresponding formulas obtained from formula (18).

TABLE I.

k/m	0	1	2	3	4	5
0	.00000	−.13333	.50000	−.14583	−.02188	−.00645
1	.13333	.53333	−.14583	−.02708	−.01100	−.00540
2	−1.03333	.01250	−.01667	−.00872	−.00513	−.00332
3	.27917	.02708	.00039	−.00260	−.00235	−.00186
4	.03854	.01517	.00382	.00007	−.00085	−.00096
5	.01061	.00801	.00377	.00117	.00002	−.00038
6	.00363	.00417	.00288	.00145	.00050	.00001
7	.00138	.00216	.00198	.00134	.00070	.00026

Note: The values of K^n_{km} for $n=2$ are taken from Ref. 4.

The most complicated formula for calculation, as was noted in Ref. 3, is the triple sum $\{\Lambda^3_{k,m,n}\}$, whose calculation requires a special recursive procedure.

Whereas the calculations of the linear elements are simple and have been carried out by many authors, the formulas for the nonlinear elements are significantly more complicated. Note that in Ref. 3 there is no comparison with Refs. 2 and 7, nor does it give a detailed derivation of formulas (19)–(21). Therefore we had to perform an additional study.

Since our results, like the results of Refs. 2 and 7, are valid not only for the hard-sphere model, it is possible to make a wider comparison. We compared our results with the results of Ref. 2. The values of the linearized matrix elements given in the table in Ref. 2 for $\mu=0.25$ and calculated according to formula (18), completely coincide. Our formulas, like the formulas from Ref. 2, in the particular case of pseudo-Maxwellian molecules reduce to the well-known simple form. In Ref. 4 we compared the errors involved in calculating according to the formulas from Ref. 2 and from formula (18). We showed that for pseudo-Maxwellian molecules the error incurred in the first case for $N=13$ is incurred in the second case only for $N=30$. In addition, in order to compare the results, we programmed up the formula from Ref. 2 and calculated the matrix elements for the hard-sphere model. It turns out that up to $N=5$ the results coincide with the results of formula (18) out to 13 significant figures. For large N we proposed a special method in Ref. 4 for error determination based on calculating with a different degree of accuracy and showed that going from six sums in Ref. 2 to four in formula (18) decreases the error at large N by several orders of magnitude. Thus it can be said that if sufficient accuracy is provided in the calculations the formulas from Ref. 2 and formula (18) give the same result, i.e., they are equivalent. For the hard-sphere model we carried out a comparison for $N=2$ with the results of Ref. 7. Most of the 12 symmetrized matrix elements calculated there coincide with the values we calculated. The linear element $K^2_{3,0}$ differs in sign from the corresponding element in Refs. 2–4, which is clearly a typographical error. Among the various nonlinear elements, $K^2_{2,1}$ differs (it has opposite sign), as does $K^2_{4,1}$ (it is two times larger than in Ref. 4). However, comparing with the results of Ref. 3 and calculating the problems presented there using our formulas leads to qualitatively different results (see Sec. III). In order to ensure that there are no typographical errors in Ref. 3, upon coding up their formulas we calculated the nonlinear matrix elements according to formulas (19)–(21) for N up to 16 and repeated the calculations of the relaxation processes with the initial data from Ref. 3. Comparing the results of our calculations with the graphical results presented in Ref. 3, we convinced ourselves that the formulas for $K^n_{k,m}$ in Ref. 3 correspond to their final results.

Table I displays the matrix elements calculated according to formula (18) for $n=2$ and $0\leqslant k\leqslant 7$, $0\leqslant m\leqslant 5$. In our calculations we chose as our unit of time the same quantity as used in Ref. 3: $\tau_0=(\pi m/16kT_0)^{1/2}/n_0\sigma$, where σ is the total cross section. Corresponding calculations according to formulas (19)–(21) showed that all the nonlinear elements

TABLE II.

	$k=0$	$k=1$	$k=2$	$k=3$	$k=4$	
n	$m=4$	$m=3$	$m=2$	$m=1$	$m=0$	K_{22}^n, Ref. 3
1	-5.2083×10^{-3}	-1.0417×10^{-2}	.00000	1.0417×10^{-2}	5.2083×10^{-3}	-3.7109×10^{-2}
2	-2.1875×10^{-2}	-2.7083×10^{-2}	-1.6667×10^{-2}	2.7083×10^{-2}	3.8542×10^{-2}	1.7578×10^{-2}
3	$-.12891$	$-.13281$	$-.12500$	1.8527×10^{-2}	.36819	4.2480×10^{-2}
4	.37240	.36979	.37500	.41751	-1.5347	4.0039×10^{-2}
5	$-.10579$	$-.10742$	$-.10417$	-8.5940×10^{-2}	.40332	2.7466×10^{-2}
6	-1.6602×10^{-2}	-1.7578×10^{-2}	-1.5625×10^{-2}	-7.0639×10^{-3}	5.6869×10^{-2}	1.5015×10^{-2}
7	-5.2572×10^{-3}	-5.8268×10^{-3}	-4.6875×10^{-3}	-5.0573×10^{-4}	1.6277×10^{-2}	6.1951×10^{-3}
8	-2.0616×10^{-3}	-2.3872×10^{-3}	-1.7361×10^{-3}	3.4867×10^{-4}	5.8362×10^{-3}	1.0986×10^{-3}
9	-8.9333×10^{-4}	-1.0764×10^{-3}	-7.1023×10^{-4}	3.4141×10^{-4}	2.3386×10^{-3}	-1.3046×10^{-3}
10	-4.0904×10^{-4}	-5.1076×10^{-4}	-3.0731×10^{-4}	2.2699×10^{-4}	1.0001×10^{-3}	-2.0981×10^{-3}
11	-1.9367×10^{-4}	-2.4962×10^{-4}	-1.3772×10^{-4}	1.3496×10^{-4}	4.4605×10^{-4}	-2.0771×10^{-3}
12	-9.3707×10^{-5}	-1.2422×10^{-4}	-6.3189×10^{-5}	7.6367×10^{-5}	2.0475×10^{-4}	-1.7281×10^{-3}

Note: The values of K_{km}^n for $k+m=4$ are taken from Ref. 4 and of K_{22}^n from Ref. 3.

differ significantly both in magnitude and in sign.

It is of interest to display the values of $K_{k,m}^n$ calculated according to formula (18) and over a wider range of k, m, n. This is done in Tables II and III for $1\leqslant n\leqslant 12$ for k and m such that $k+m=4$ and $k+m=5$, respectively. The last column of Table II for comparison gives the values of $K_{2,2}^n$ calculated in Ref. 3. For Maxwellian molecules the matrix elements $K_{k,m}^n$ are nonzero only if $m+k=n$. The authors of Refs. 2 and 4 draw attention to the fact that the matrix elements have a sharp peak at $m+k=n$ for other values of μ as well, in particular for hard spheres, and fall off rapidly with growth of $|m+k-n|$. One can convince oneself of this by close inspection of Tables I, II, and III. Comparing the elements $K_{2,2}^n$ from Table II, calculated according to formulas (18) and (19)–(21), it is clear that the matrix elements calculated according to the formulas from Ref. 3 do not possess this property. This proved also to be the case for other values of the indices. Note that despite the fact that all three derivations of the matrix elements in Refs. 2, 4, and 7 were reached by completely different paths, they coincide with each other, apart from some minor typographical errors in Ref. 7, but not with the results of Ref. 3. On the basis of the above-said we may conclude that the calculation of the nonlinear matrix elements in Ref. 3 is erroneous.

Nevertheless it would be desirable to have criteria that would provide a direct check on the validity of one formula or another. In the following section we derive two relations that the matrix elements $K_{k,m}^n$ must satisfy.

2. PROPERTIES OF THE MATRIX ELEMENTS

We choose as our initial distribution function the Maxwellian distribution with temperature T_1. The collision integral of such a distribution function is equal to zero. If, as is customary, we expand this function in Sonin polynomials about the same temperature T_1, then only the zeroth-order coefficient C_0 will be nonzero, and $dC_0/dt=0$ since $K_{0,0}^0=0$. Say, however, that we expand this same distribution function in Sonin polynomials about a different temperature T_2. In α space the Maxwellian with temperature T_1 has the transform $\delta(T-T_1)$. Then, using formula (13), we obtain for the expansion coefficients C_n

$$C_n=(1-T_1/T_2)^n. \tag{22}$$

TABLE III.

	$k=0$	$k=1$	$k=2$	$k=3$	$k=4$	$k=5$
n	$m=5$	$m=4$	$m=3$	$m=2$	$m=1$	$m=0$
1	-1.6276×10^{-3}	-4.8828×10^{-3}	-3.2552×10^{-3}	3.2552×10^{-3}	4.8828×10^{-3}	1.6276×10^{-3}
2	-6.4453×10^{-3}	-1.1003×10^{-2}	-8.7240×10^{-3}	3.9063×10^{-4}	1.5169×10^{-2}	1.0612×10^{-2}
3	-20947×10^{-2}	-2.5342×10^{-2}	-2.3145×10^{-2}	-1.4355×10^{-2}	2.9806×10^{-2}	5.3983×10^{-2}
4	$-.11637$	$-.11995$	$-.11816$	$-.11100$	2.1839×10^{-2}	.44336
5	.33722	.33457	.33590	.34119	.38352	-1.73240
6	-9.8572×10^{-2}	$-.10040$	-9.9487×10^{-2}	-9.5825×10^{-2}	-7.6583×10^{-2}	.47087
7	-1.6100×10^{-2}	-1.7311×10^{-2}	-1.6705×10^{-2}	-1.4284×10^{-2}	-4.7772×10^{-3}	6.9177×10^{-2}
8	-5.3345×10^{-3}	-6.1076×10^{-3}	-5.7210×10^{-3}	-4.1748×10^{-3}	6.8368×10^{-4}	2.0654×10^{-2}
9	-2.1935×10^{-3}	-2.6741×10^{-3}	-2.4338×10^{-3}	-1.4725×10^{-3}	1.0513×10^{-3}	7.7225×10^{-3}
10	-9.9702×10^{-4}	-1.2895×10^{-3}	-1.1433×10^{-3}	-5.5833×10^{-4}	7.6385×10^{-4}	3.2242×10^{-3}
11	-4.7867×10^{-4}	-6.5351×10^{-4}	-5.6609×10^{-4}	-2.1641×10^{-4}	4.7938×10^{-4}	1.4353×10^{-3}
12	-2.3742×10^{-4}	-3.4042×10^{-4}	$-2\ .8892\times10^{-4}$	-8.2926×10^{-5}	2.8405×10^{-4}	6.6563×10^{-4}

Note: The values of K_{km}^n for $k+m=5$ are taken from Ref. 4.

In general, the collision integral can be written as

$$J(f,f)=M(v,\tilde{T}_2)\sum_{n=0}^{\infty} S_{1/2}^{n}(v^2/\tilde{T}_2)\frac{dC_n}{dt}. \tag{23}$$

Obviously, re-expanding the Maxwellian about a different temperature cannot lead to a nonzero collision integral, i.e., the collision integral of the Maxwellian is invariant with respect to choice of basis.

From the identity $J(f,f)=0$, using Eq. (23) and the properties of completeness and orthogonality of the Sonin polynomials, we obtain

$$\frac{dC_n}{dt}=0,\ \ n=0,\ldots,\infty. \tag{24}$$

Hence, substituting expression (22) into Eq. (3) we obtain

$$\sum_{k,m} K_{k,m}^{n}(1-T_1/T_2)^{k+m}=0. \tag{25}$$

Denoting $k+m$ as m' and transforming to new summation indices, we obtain

$$\sum_{m=1}^{\infty}(1-T_1/T_2)^m\sum_{k=0}^{m} K_{k,m-k}^{n}=0. \tag{26}$$

This expression is a power series in $(1-T_1/T_2)$. Since the identity (26) is satisfied for all values of T_2, it follows that

$$\sum_{k=0}^{m} K_{k,m-k}^{n}=0,\quad n,m=0,\ldots,\infty. \tag{27}$$

Note that this property is valid for arbitrary scattering cross section and imposes additional constraints on the matrix elements. Let us write out in explicit form relations (27) for $m=0,\ 1,\ 2$

$$K_{0,0}^{n}=0,\quad n=0,\ldots,\infty \tag{28}$$

$$K_{0,1}^{n}+K_{1,0}^{n}=0,\quad n=0,\ldots,\infty \tag{29}$$

$$K_{0,2}^{n}+K_{1,1}^{n}+K_{2,0}^{n}=0,\quad n=0,\ldots,\infty. \tag{30}$$

For the matrix elements calculated according to formula (18) (and consequently according to the formulas from Ref. 2) relations (27) are fulfilled with high accuracy, limited by the accuracy of calculation of the matrix elements themselves. Thus, calculating according to formula (18), for $k,\ m,\ n<12$ the error does not exceed 10^{-10}. Note that for large m and n errors accumulate in the calculation of $K_{k,m}^{n}$ and deviations from relation (27) can be used as an estimate of the magnitude of this calculational error.

As for Ref. 7, relations (27) are fulfilled there fore $m=0,\ 1,\ 2$, and 4. Since it was demonstrated above that the sign of the linear element $K_{3,0}^{2}$ in Ref. 7 was given incorrectly, equality (27) for $m=3$ confirms the fact that the sign of the element $K_{2,1}^{2}$ was also given incorrectly. Properties (27) can also be useful in the deciding where to truncate in the numerical solution of system (3). Usually, one chooses some number N and then sweeps through the region of $k,\ m,\ n$ values

$$k,\ m,\ n\leqslant N. \tag{31}$$

However, when $k+m>N$, not all the matrix elements entering into equality (27) are used, i.e., the truncated matrix $K_{k,m}^{n}$ does not satisfy the above relations. As follows from the preceding discussion, expanding the Maxwellian with temperature T_1 about the temperature T_2 leads to a deviation from the equilibrium Maxwellian distribution. In our view, it is much more natural to truncate the matrix in such a way that after this procedure properties (27) remain in force, i.e., to sum over k and m such that

$$k+m\leqslant N,\ \ n\leqslant N. \tag{32}$$

It is impossible to check whether relation (27) is satisfied if we substitute the expressions for $K_{k,m}^{n}$ from Ref. 3 since Ref. 3 does not give any matrix elements having even one of the lower indices equal to unity (in this case the denominators of the formulas for the nonlinear elements tend to infinity). In each of relations (27) starting with the second, one encounters at least one such element. The authors of Ref. 3 rightly note that for the nonlinear and linearized problems they considered when expanding the distribution function about the equilibrium Maxwellian the matrix elements having at least one index equal to unity are not needed. However, when expanding about a Maxwellian with temperature different from the equilibrium temperature or when considering a mixture of gases knowledge of all these elements is necessary. The fact that formula (18) satisfies relation (27) is a sufficiently serious argument in favor of its validity. However, since an analogous check of formulas (19)–(21) is impossible, an additional check is necessary.

We will make use of the circumstance that for the hard-sphere model an analytical formula is given in Ref. 10 for the collision integral of two Maxwellians with arbitrary temperatures

$$J^m(\tilde{T}_1,\tilde{T}_2,v)=R_+-R_-,$$

$$R_+=\left(\frac{\alpha_1\alpha_2}{\pi}\right)^{3/2}\frac{n_0^2\sigma}{\alpha_1\alpha_2(\alpha_1-\alpha_2)v}$$
$$\times(e^{-\alpha_2 v^2}\mathrm{erf}(v\sqrt{\alpha_1})-e^{-\alpha_1 v^2}\mathrm{erf}(v\sqrt{\alpha_2})),$$

$$R_-=\left(\frac{\alpha_1\alpha_2}{\pi}\right)^{3/2}\frac{n_0^2\sigma}{\alpha_2^2}e^{-\alpha_1 v^2}\left(\frac{e^{-\alpha_2 v^2}}{\pi}+\mathrm{erf}(v\sqrt{\alpha_2})\right.$$
$$\left.\times\left(v\sqrt{\alpha_2}+\frac{1}{2v\sqrt{\alpha_2}}\right)\right),$$

$$(\alpha_j=m/(2kT_j),\quad j=1,\ 2). \tag{33}$$

A more general formula is given in Ref. 11 for the collision integral, which accommodates two Maxwellians with arbitrary temperatures and mean velocities. In the particular case of isotropic relaxation these formulas reduce to formula (33).

Let us consider the nonlinear case in which the distribution function is a sum of two Maxwellians

$$f(v)=M(v,\tilde{T}_1)+M(v,\tilde{T}_2). \tag{34}$$

TABLE IV.

v	$\overline{J^m}(33,35)$ exact	$\overline{J^m}(37)$ (Ref. 3) $N=15$	$\overline{J^m}(37)$ (Ref. 4) $N=15$	$\overline{J^m}(37)$ (Ref. 4) $N=30$
0.2	-1.7552290×10^{-1}	-1.7525095×10^{-1}	-1.7555138×10^{-1}	-1.7552291×10^{-1}
0.4	-1.2497906×10^{-1}	-1.2544142×10^{-1}	-1.2497804×10^{-1}	-1.2497906×10^{-1}
0.6	-6.5744483×10^{-2}	-6.6418029×10^{-2}	-6.5736926×10^{-2}	-6.5744484×10^{-2}
0.8	-1.8434685×10^{-2}	-1.8628521×10^{-2}	-1.8435320×10^{-2}	-1.8434685×10^{-2}
1.0	7.7167202×10^{-3}	8.0490871×10^{-3}	7.7138033×10^{-3}	7.7167068×10^{-3}
1.2	1.5360482×10^{-2}	1.5683595×10^{-2}	1.5360751×10^{-2}	1.5360481×10^{-2}
1.4	1.2729115×10^{-2}	1.2637250×10^{-2}	1.2730204×10^{-2}	1.2729119×10^{-2}
1.6	7.2240132×10^{-3}	6.8289308×10^{-3}	7.2239580×10^{-3}	7.2240154×10^{-3}
1.8	2.7475941×10^{-3}	2.4073228×10^{-3}	2.7472289×10^{-3}	2.7475944×10^{-3}
2.0	2.5189258×10^{-4}	1.5935936×10^{-4}	2.5187636×10^{-4}	2.5189266×10^{-4}
2.2	-7.0711916×10^{-4}	-6.0972001×10^{-4}	-7.0701226×10^{-4}	-7.0711916×10^{-4}
2.4	-8.3763687×10^{-4}	-6.9330519×10^{-4}	-8.3761446×10^{-4}	-8.3763689×10^{-4}
2.6	-6.5391938×10^{-4}	-5.5003966×10^{-4}	-6.5394481×10^{-4}	-6.5391937×10^{-4}
2.8	-4.2204328×10^{-4}	-3.7263742×10^{-4}	-4.2205553×10^{-4}	-4.2204328×10^{-4}
3.0	-2.4043828×10^{-4}	-2.2664423×10^{-4}	-2.4043422×10^{-4}	-2.4043820×10^{-4}

Note: Comparison of $\overline{J^m}$ $(v,0.5,1.5)$ calculated according to different formulas.

Then the collision integral has the form

$$J(f,f)=J^m(\tilde{T}_1,\tilde{T}_2,v)+J^m(\tilde{T}_2,\tilde{T}_1,v)=\overline{J^m}(\tilde{T}_1,\tilde{T}_2,v). \tag{35}$$

We expand the distribution function (34) in Sonin polynomials about the equilibrium temperature $T_0=(T_1+T_2)/2$. Employing formula (13), we obtain for the expansion coefficients

$$C_{2n}=2\left(\frac{T_2-T_1}{T_2+T_1}\right)^{2n}=2\tilde{\Delta}^{2n},$$

$$C_{2n+1}=0, \quad n=0,\ldots,\infty. \tag{36}$$

Knowing the coefficients C_n, we can construct the expansion of the collision integral in Sonin polynomials. From Eq. (23) invoking Eqs. (3) and (36) for the case under consideration we obtain

$$\overline{J^m}(\tilde{T}_1,\tilde{T}_2,v)=M(v,\tilde{T}_0)\sum_{n=0}^{\infty} S^n_{1/2}(v^2/\tilde{T}_0)D_n(\tilde{T}_1\tilde{T}_2), \tag{37}$$

$$D_n(\tilde{T}_1,\tilde{T}_2)=4\sum_{m=1}^{\infty}\sum_{k=0}^{m}\tilde{K}^n_{2k,2m}(2-\delta_{k,m})\tilde{\Delta}^{2(k+m)}. \tag{38}$$

The properties of coefficients (36) together with equality (28) allow us in expression (38) to carry out the sum over m starting from unity. Thus, matrix elements for which expressions are absent in Ref. 3 do not figure in the expansion of the function $\overline{J^m}(T_1,T_2,v)$ in Sonin polynomials.

If we substitute the correct values of the matrix elements $K^n_{k,m}$ in expressions (37) and (38), we obtain a function that should coincide with $J^m(T_1,T_2,v)$ as given by formulas (33) and (35). This gives one more criterion for the validity of the calculations.

It would also be useful to compare the expressions for the expansion coefficients of the collision integral in Sonin polynomials D_n (38) with the exact formula obtained by integrating $\overline{J^m}(T_1,T_2,v)$ with the corresponding Sonin polynomial,

$$D_n(\tilde{T}_1,\tilde{T}_2)=\sum_{l=0}^{n}\left(\frac{n}{l}\right)\tilde{\Delta}^{n-l}\left(d_l(\tilde{T}_1,\tilde{T}_2)\left(\frac{T_1}{T_0}\right)^l+(-1)^{n-l}d_l(\tilde{T}_2,\tilde{T}_1)\left(\frac{T_2}{T_0}\right)^l\right). \tag{39}$$

Here $d_l(T_1,T_2)$ is given by formula (17). Let us avail ourselves of the obtained criteria to check the validity of formulas (19)–(21). The degree of deviation from equilibrium is characterized in formulas (37) and (38) by the single parameter $\tilde{\Delta}$. For small deviations from equilibrium ($\tilde{\Delta}\ll1$) the collision integral is determined chiefly by its linear terms and hardly any difference is observed between the calculations in Refs. 3 and 4. If $\tilde{\Delta}$ is chosen large enough, Grad's criterion is violated and series (37) does not converge. In view of this, we chose an intermediate value ($\tilde{\Delta}=1/2$, $T_1/T_0=0.5$, $T_2/T_0=1.5$) for comparison.

Table IV compares the exact values of $\overline{J^m}$ calculated from formulas (33) and (35) and the expansion (37). The calculations of expansion (37) used the matrices from Refs. 3 and 4. In the calculations using the formulas from Ref. 3 for $N=15$ the error is significant and in some cases exceeds 10%: for example, for $v=1.8$ it is 12.4%, and for $v=2$ it reaches 35%. Using the matrix from Ref. 4, again for $N=15$, the error does not exceed 0.01%. To show that when using $K^n_{k,m}$ from Ref. 4 the error is associated only with convergence of the series for large deviations from equilibrium, the calculation was checked for $N=30$. The value in this case coincides with the exact value to seven significant figures.

The difference between the calculations according to Refs. 3 and 4 is made especially clear in Table V, which displays values of the moments $D_l(T_1,T_2)$ calculated according to formula (38) using the formulas for $K^n_{k,m}$ from Refs. 3 and 4 for $N=15$, and calculated using the exact formula (39). While the second, third, and fourth moments calculated according to formula (18) coincide with the exact moments to seven figures beyond the decimal point, the cal-

TABLE V.

l	$D_l(\tilde{T}_1,\tilde{T}_2)(38)$ (Ref. 3)	$D_l(\tilde{T}_1,\tilde{T}_2)(38)$ (Ref. 4)	$D_l(\tilde{T}_1,\tilde{T}_2)(39)$ exact
2	-5.2590077×10^{-1}	-5.3333333×10^{-1}	-5.3333333×10^{-1}
3	1.8491582×10^{-1}	1.4285714×10^{-1}	1.4285714×10^{-1}
4	-2.6368847×10^{-1}	-1.8333333×10^{-1}	-1.8333333×10^{-1}
5	1.1192430×10^{-1}	6.3356775×10^{-2}	6.3356782×10^{-2}
6	-8.1335949×10^{-2}	-5.3578599×10^{-2}	-5.3578582×10^{-2}
7	4.3118543×10^{-2}	2.1906036×10^{-2}	2.1906072×10^{-2}
8	-2.2503093×10^{-2}	-1.4720030×10^{-2}	-1.4719954×10^{-2}
9	1.4152822×10^{-2}	6.8945086×10^{-3}	6.8946644×10^{-3}
10	-6.1439616×10^{-3}	-3.9044694×10^{-3}	-3.9041520×10^{-3}
11	4.1044116×10^{-3}	2.0687224×10^{-3}	2.0693780×10^{-3}
12	-1.8663395×10^{-3}	-1.0107704×10^{-3}	-1.0093606×10^{-3}

Note: Comparison of $D_l(\tilde{T}_1,\tilde{T}_2)$ calculated according to different formulas.

culations according to formulas (19)–(21) give an error already in the third moment of the order of 30%.

Thus, it can be asserted that the formulas for the nonlinear matrix elements in Ref. 3 are in error.

3. DISCUSSION OF THE RESULTS OF CALCULATIONS OF RELAXATION PROCESSES

Reference 3 investigated the question of the convergence of the Laguerre series (1) in the instance of two problems of isotropic relaxation: the first with initial conditions corresponding to the BKW mode

$$C_n(0)=(0.4)^n(1-n) \tag{40}$$

and the second with initial conditions

$$C_n(0)=0.8\delta_{n,2},\quad n\geqslant 2. \tag{41}$$

Expanding the initial BKW mode in Sonin polynomials, the authors of Ref. 3, Schürrer and Kügerl, demonstrated a connection between the number of terms in the expansion N and the maximum velocity $v_{\max}$ out to which the expansion is valid. Thus, for $N=8$, 16, 32, and 64 $v_{\max}$ took the values 2.6, 3.6, 5.1, and 6.6, respectively. To find $v_{\max}$ from the known moments (40) they constructed a segment of the series and compared it with the known analytical distribution function. In the case of Maxwellian molecules such a comparison can be made for any time τ ($\tau=t/\tau_0$), where for each τ there exists a maximum value of the velocity $v_{\max}$ such that for $v\leqslant v_{\max}$ series (1) converges and with approach to equilibrium the convergence improves, i.e., $v_{\max}$ increases.

A comparison of calculations of the first problem is given in Figs. 1 and 2. Figure 1 plots the distribution function constructed according to the formulas from Ref. 3 for $N=16$ at the same times $\tau/\sqrt{2}=0,1,2,5$ as were used in Ref. 3. The results of linear calculations, i.e., those in which the nonlinear terms were set to zero, are also shown. The first thing that catches the eye is the abrupt fallout of the distribution function into negative values in the vicinity of velocities near four for $\tau=\sqrt{2}$ and $2\sqrt{2}$. Reference 3 gives the solution of the first problem for $N=64$. Comparison shows that this solution essentially coincides with the solution shown in Fig. 1, i.e., the abrupt falloff into negative values is preserved for $N=64$. As is well known, the exact solution of the nonlinear Boltzmann equation for a positive initial distribution function cannot become negative.

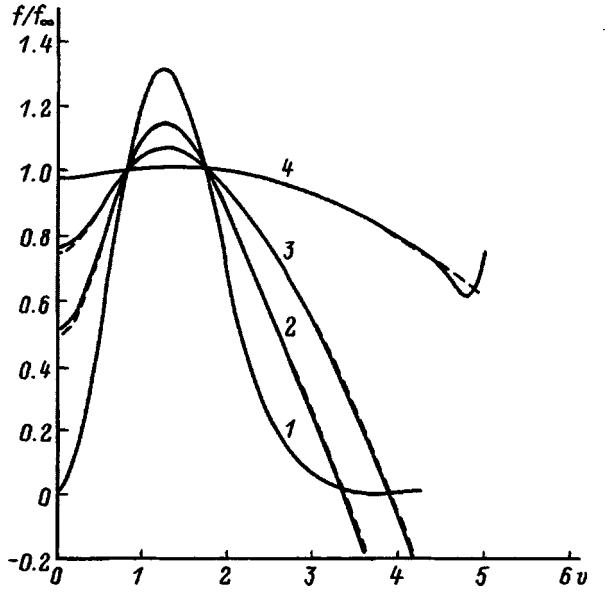

FIG. 1. Solutions of the linear (dashed curves) and nonlinear (solid curves) Boltzmann equation for initial conditions (40). Matrix elements from Ref. 3 ($N=16$) were used in the nonlinear solutions, and matrix elements with $N=30$ were used in the linear solutions; *1–4* — times $\tau/\sqrt{2}=0$, 1, 2, 5.

The second thing that strikes the eye when looking at Fig. 1 is the very small difference between the linear and nonlinear processes in the tails. The fact that the linear solution goes negative is no cause for wonder. The absence of a noticeable correction to the linear solution after including the nonlinear elements is explained by the strong depression of the values of the maximum nonlinear matrix elements (see Sec. I) which largely determine the nonlinear process.

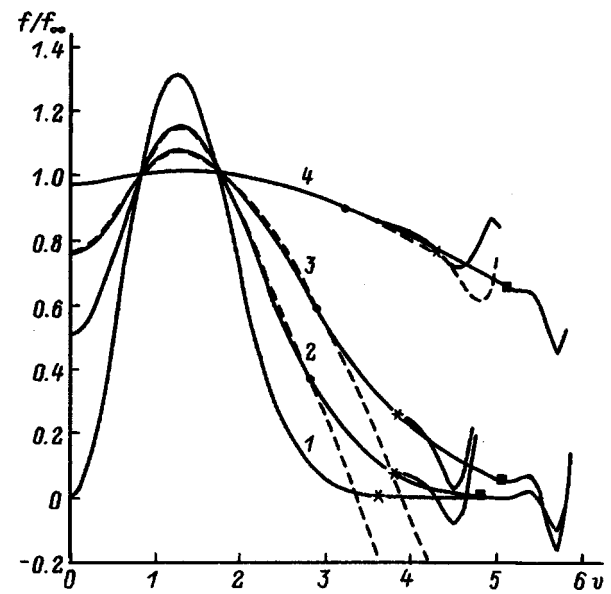

FIG. 2. Solutions of the nonlinear Boltzmann equation for initial conditions (40), using the matrix from Ref. 4. The dashed curves plot the analogous solution, but using the matrix from Ref. 3 ($N=16$); *1–4* — same as in Fig. 1; * — $v_{\max}$ for $N=16$, ■ — for $N=30$.

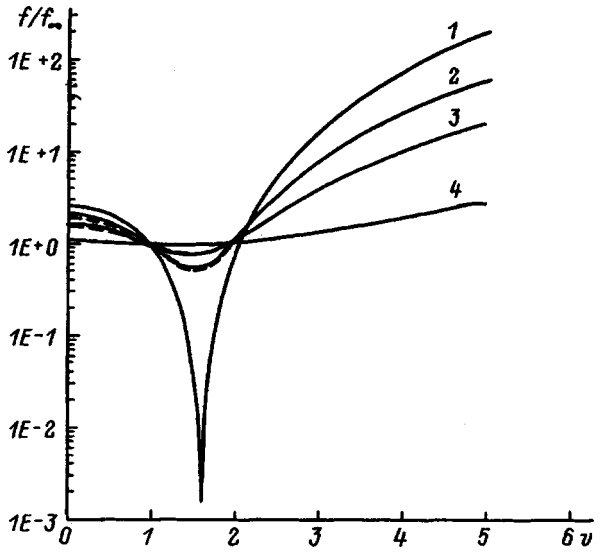

FIG. 3. Solutions of the linear (dashed curves) and nonlinear (solid curves) Boltzmann equation for initial conditions (41). Matrix elements from Ref. 3 ($N=16$) were used in the nonlinear solutions, and matrix elements with $N=30$ were used in the linear solutions; *1–4* — same as in Fig. 1.

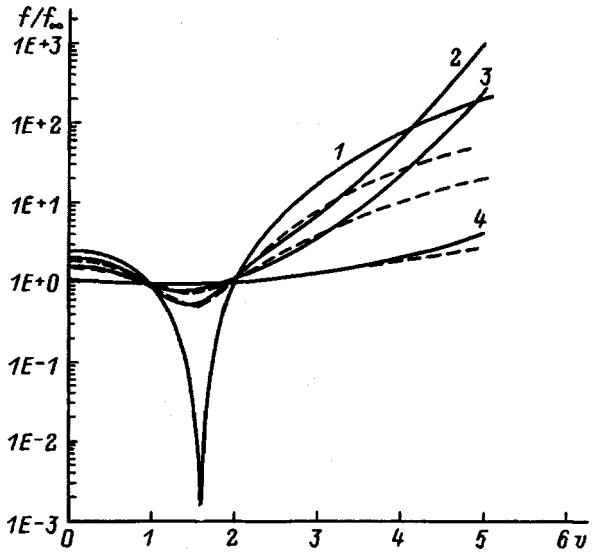

FIG. 4. Same as in Fig. 3 except that matrix elements from Ref. 4 ($N=16$) were used in the nonlinear solutions, and in the linear solutions again matrix elements with $N=30$.

Figure 2 depicts the same process with initial conditions (40), but calculated with the correct matrix (18) for $N=16$ and 30. The dashed curves here are the solution calculated with the matrix from Ref. 3 for $N=16$. On each solid curve the corresponding maximum velocity $v_{\max}$ is indicated, to the left of which series (1) converges. The convergence limit is clearly visible from the onset of perturbations in the curve. In contrast to Fig. 1, whereas for $N=16$ in the time interval $1 \leqslant \tau/\sqrt{2} \leqslant 2$ the maximum velocity $v_{\max}$ approaches four, for $N=30$ it is already greater than five, i.e., as in the case of Maxwellian molecules, adding new moments makes the distribution function positive for increasingly larger velocities. It is clear from Fig. 2 that in the interval $1 \leqslant \tau/\sqrt{2} \leqslant 2$ the values of the maximum velocity $v_{\max}$ are close to the values read off for zero time. Consequently, it can be asserted that for the same times for $N=64$ the value of $v_{\max}$ will be around 6.5.

The solid circles in Fig. 2 indicate where the calculations using the formulas from Ref. 3 begin to differ from the calculations using the correct matrix (18). These velocities lie in the interval $2.5 \leqslant v \leqslant 3$, which is significantly less than 6.5. Thus, in the region $v>3$ a large systematic error arises in Ref. 3, which cannot be corrected by simply adding more terms.

The authors of Ref. 3, recognizing the paradoxicality of their results and attempting to explain the appearance of negative solutions regardless of the value of N, came to the invalid conclusion that it was due to poor convergence of the series and even inapplicability of the method of expansion in Laguerre polynomials in the given case.

Figures 3 and 4 plot the distribution functions with initial conditions (41), calculated using the formulas from Refs. 3 and 4, respectively. The different character of relaxation of the tails is noteworthy; even their curvature changes. Here, as in the previous problem, the linear and nonlinear curves calculated using the formulas from Ref. 3 are observed essentially to coincide. Again, this is due to an incorrect calculation of the maximum nonlinear matrix elements. As can be seen from Fig. 4, the tails of the linear and nonlinear distribution functions should actually have different curvature.

The small difference between the nonlinear and linearized solutions noted in Ref. 3 is indeed the case in the region of not too large velocities, but in the tail region the difference is significantly greater.

CONCLUSION

In the present paper we have compared different approaches to calculating the interaction matrix in the moment method of solving the isotropic Boltzmann equation. Because the formulas they used for the nonlinear matrix elements are incorrect, the authors of Ref. 3 arrived at invalid conclusions about the course of the relaxation process and generally about the possibilities of application of the moment method. We arrive at a different conclusion: the moment method can be used to construct the distribution function at large velocities, but it is necessary to include a large number of terms.

Our analysis of calculations of the matrix $K^n_{k,m}$ revealed some of its properties, which we then used as criteria of validity of the calculations. The first of these properties is quite general and is valid for arbitrary interaction cross sections. It is based on conditions of invariance of the collision integral of the Maxwellian distribution function with respect to choice of the basis functions. If we develop this idea further, then it is possible to construct nonlinear matrix elements for the nonisotropic Boltzmann equation, which is especially important for many physical-chemical processes and in studies of transport processes in which the particles interact via the Coulomb interaction.

This work was carried out with the partial support of the Russian Fund for Fundamental Research (Project No. 97-02-

18080) and the Federal Special Program ''State Support for Integration of Higher Education and Fundamental Science'' (Contract No. 326.53).

[1] M. Barnsley and G. Turchetti, Lett. Nuovo Cimento **33**, 347 (1982).
[2] G. Turchetti and M. Paolilli, Phys. Lett. A **90**, 123 (1982).
[3] F. Schürrer and G. Kügerl, Phys. Fluids A **2**, 609 (1990).
[4] A. Ya. Énder and I. A. Énder, Zh. Tekh. Fiz. **64**, 38 (1994) [Tech. Phys. **39**, 997 (1994)].
[5] I. A. Énder and A. Ya. Énder, Dokl. Akad. Nauk SSSR **193**, 61 (1970) [Sov. Phys. Dokl. **15**, 1 (1970)].
[6] I. N. Kolyshkin, A. Ya. Énder and I. A. Énder, Zh. Vychisl. Mat. Mat. Fiz. **28**, No. 6, 901 (1988).
[7] C. A. Word and D. Mintzer, Phys. Fluids **14**, 499 (1971).
[8] M. H. Ernst, Phys. Rep. **78**, 1 (1981).
[9] I. A. Énder and A. Ya. Ender, Zh. Tekh. Fiz. **54**, 1671 (1984) [Tech. Phys. **29**, 978 (1984)].
[10] I. N. Kolyshkin, A. Ya. Énder, and I. A. Énder, Izv. Akad. Nauk SSSR, Mekh. Zhidk. Gaza No. **5,** 132 (1977).
[11] E. M. Deshpande and R. Narasimha, J. Fluid Mech. **36**, 3 (1969).

Translated by Paul F. Schippnick

Study of the characteristics of a non-self-sustaining atmospheric-pressure discharge in a CO_2: N_2: He mixture with oxygen and water impurities

M. F. Danilov and A. N. Malinin

Scientific-Research Institute of Comprehensive Testing of Opto-Electronic Devices and Systems, S. I. Vavilov State Optical Institute All-Russia Science Center, 188537 Sosnovyĭ Bor, Leningrad District, Russia

(Submitted November 12, 1996)
Zh. Tekh. Fiz. **68**, 27–32 (May 1998)

Results of experimental and numerical studies of a non-self-sustaining discharge in an atmospheric-pressure electron-beam-controlled CO_2 laser medium are reported. The main focus of the paper is a numerical analysis of the effect of an oxygen impurity on the nature of the ionic–molecular processes determining the ionic composition of the discharge plasma and its conductivity. © *1998 American Institute of Physics.* [S1063-7842(98)00505-4]

STATEMENT OF THE PROBLEM

Non-self-sustaining discharges maintained by a fast electron beam are widely used to excite high-pressure laser media.[1,2] Electron-beam-controlled (''electroionization'') CO_2 lasers usually operate in CO_2: N_2: He mixtures which are prepared using commercial-grade gases containing electronegative impurities (O_2, H_2O). As a result of various plasma-chemical reactions in the gas mixture, many secondary species are formed which have a substantial effect on the operating characteristics of the active medium.[2–4]

A number of publications[5–11] have been dedicated to a study of the effect of impurities and additives on the kinetics of plasma-chemical processes and the characteristics of a CO_2-laser discharge. In Ref. 5 it was shown that addition of H_2 and CO to the starting gas mixture can lead to stable equilibrium of the chemical composition of the mixture in sealed systems. CO is commonly used in laser mixtures in conjunction with efforts to activate CO_2 regeneration reactions. Under such conditions, oxygen, which may be contained in the starting gases as an impurity and can decrease the stability of the plasma, ''ignites.''[6] The addition of H_2 and H_2O lowers the degree of dissociation of CO_2 in the discharge. The authors of Refs. 7 and 8 ascribe the main role in this process to the OH radical which regenerates the CO_2.

Besides their effect on chemical processes, additives act on the vibrational kinetics, the charged particle balance, and the stability and limiting energy characteristics of the discharge.[9–11] The behavior of charged particles in the plasma, in particular their participation in numerous reactions, has a decisive influence on its conductivity. In an electron-beam-controlled CO_2 laser the electron balance is determined mainly by ionization processes initiated by the electron beam, attachment of electrons to electrically negative molecules, electron recombination with positive ions and electron detachment from negative ions.[12] For the working electric field intensities E and densities N in CO_2 lasers ($E/N \sim 2\times10^{-16}$ V/cm^2) ionization by discharge electrons does not play a substantial role. The authors of Ref. 12 investigated the influence of oxygen impurity on the energy characteristics of an electric discharge and found the maximum permissible O_2 concentrations in the laser mixtures. They showed that the effective rate of attachment of the electrons to the oxygen molecules in the electron density range $3\times10^{12}-5\times10^{13}$ cm^{-3} is 6.7 times greater than their rate of attachment to the CO_2 molecules.

The ionic composition and the effective electron recombination and detachment rate constants which depend on it are to a significant degree determined by ion conversion processes.[13] A mass-spectrometric analysis of the composition of the plasma in CO_2 laser mixtures showed[4] that small impurities play a large role in the formation of the ionic component. In particular, the ionic composition is substantially determined by oxygen, water vapor, and nitrogen oxides.

Most of the published works which discuss the various aspects of the effect of impurities on the characteristics of a laser discharge report unrelated results obtained under dissimilar discharge conditions. The published results are insufficient for an understanding of the extent of the influence of impurities on the characteristics and stability of the discharge, and on the gain of the active medium.[6] Given the complicated makeup of the plasma and the large number of reactions between its components considering the inadequate amount of information on reaction rates, questions about mechanisms by which the impurities affect the characteristics of the discharge remain unresolved.

The aim of the present paper is an experimental and numerical study of the characteristics of a non-self-sustaining atmospheric-pressure discharge in a CO_2: N_2: He mixture with O_2 and H_2O impurities. The main focus of this work is a numerical analysis of the effect of an oxygen impurity on the nature of the ionic–molecular processes controlling the ionic composition of the plasma and its conductivity.

DESCRIPTION OF THE EXPERIMENT

The experiments were carried out on the setup described in Refs. 14 and 15, which allows one to excite up to 10 liters of working gas mixture by means of an electric discharge. The gas was ionized with the help of an electron accelerator

with a thermal-emission directly-heated (filamentary) cathode. The beam was directed into the discharge gap, which was 10 cm in height, through a foil partition 40 μm in thickness. The beam cross section was 10×100 cm, and the energy of the fast electrons at the entrance to the discharge gap was 180 keV. Regulation of the heating of the cathode made it possible to smoothly vary the beam current density from 5 to 70 mA/cm^2. Power to the main discharge was provided by a double line former, which made it possible to send a pulse with variable duration from 5 to 30 μs and deposit up to 250 J of energy per liter to the discharge gap. A space discharge was created in the mixture of molecular gases in the ratio CO_2: N_2: He = 1 : 2 : 3. During the course of the experiment we measured the voltage and current of the main discharge, and also the electron beam current. The voltage was measured by a resistor–capacitor divider, and the current by a Rogowski loop.

To determine the concentrations of the O_2 and H_2O impurities in the working mixture, we used standard-product-line devices: a ''Flyuorit'' oxygen analyzer and a ''Baĭkal'' Coulomb hygrometer. The relative measurement error for O_2 and H_2O concentrations in the range 10 to 1000 ppm did not exceed 5%.

MATHEMATICAL MODEL OF THE DISCHARGE

The mathematical model of the plasma-chemical and charge kinetics of a non-self-sustaining discharge in a CO_2: N_2: He laser mixture was described in detail in Refs. 15 and 16. In all, the model takes into account $\sim$300 reactions for 67 plasma components: e, CO_2, N_2, He, O_2, H_2O, CO_2^+, N_2^+, He^+, OH, H^-, O, O^-, CO, O_2^+, $N_2(A^3\Sigma_u^+)$, $N_2(a'^1\Sigma_u^-)$, $N_2(v)$, N, NO, H, O_2^-, H_2O^+, C, NO^+, CO^+, N^+, O^+, H_2, HO_2, NO_2, O_3, $O_2(^1\Delta_g)$, O_3^-, N_2O, NO_2^-, C^+, H_3O^+, He_2^+, N_4^+, $C_2O_4^+$, CO_4^-, CO_3^-, O_4^+, H^+, OH^+, $N_2(C^3\Pi_u)$, $N_2(B^3\Pi_g)$, N_2O^+, H_2^+, NO_3, NO_3^-, NH^+, N_2H^+, COH^+, $O_2^+\cdot H_2O$, H_3^+, N_3^+, $NO^+\cdot NO$, $H_3O^+\cdot H_2O$, $NO^+\cdot H_2O$, $NO_2^-\cdot H_2O$, OH^-, $CO_3^-\cdot H_2O$, HNO, HO_2^+, $H_3O^+\cdot OH$.

The quantity $N_2(v)$, representing the total reservoir of vibrational energy of the nitrogen molecule, controls the extent to which vibrational processes interact with processes of electronic excitation of the nitrogen molecule and with processes of chemical and charge kinetics.[17] A list of the components and reactions included in the model is created automatically at the step in which the right-hand sides of the plasma-chemical balance equations are calculated. It is defined by the initial composition of the gas mixture augmented by the new reaction products included in the model.[16] Ionization of neutral components of the discharge plasma CO_2, N_2, He, O_2, H_2O, CO, O, and N by the electron beam is represented in the model by monomolecular reactions of the type

$$CO_2\rightarrow CO_2^+ + e. \tag{1}$$

The external ionization frequency ν_i serves as the constant of these reactions and was chosen in such a way as to ensure that the calculated electron concentration corresponded to that obtained from the experimentally measured resistance of the discharge with allowance for the actual geometry of the discharge gap. Estimates give the conductivity ≈ 0.05 S/m, the electron concentration $n_e\approx 2\times 10^{12}$ cm^{-3}, and the ionization rate $\nu_i\approx 0.09$ s^{-1}. The increase in the external ionization rate in the model by a factor of two in comparison with Ref. 15 is the result of increasing the number of recombination processes taken into account in this model.

The experimentally monitored electrode voltage $U(t)$, the time delay between the start-up time of the electron gun and the start of the voltage pulse, the external ionization rate ν_i, and the gas temperature T_g are parameters of the model and define the external conditions of the problem. The initial conditions are assigned by the initial composition of the gas mixture $CO_2:N_2:He = 1:2:3$ with addition of 0.005–0.25% O_2 and 0.005% H_2O, which are usually present in the gas used as the working medium of CO_2 lasers. The average total current density $\overline{j_0(t)}$ and the average electric field intensity $\overline{E(t)}$ used in the model to calculate the rate constants of the reactions in which the electrons participate were determined from measurements of the current pulse, the voltage, and the overall dimensions of the discharge gap $\overline{j_0(t)} = I_0(t)/S$; $\overline{E}(t) = U(t)/h$, where S is the cross-sectional area of the discharge and h is the distance between the electrodes.

For the rate constants of the plasma-chemical reactions between the components of the plasma we used the data from Refs. 3, 13, and 18–31. The electron-impact ionization cross sections of the CO_2, He, N_2, O_2, CO, H_2, and NO molecules and the cross sections of dissociative attachment to molecules of O_2, H_2O, CO, NO, CO_2, and N_2O as well as the excitation cross sections of the metastable levels of the nitrogen molecule $N_2(A^3\Sigma_u^+)$ and $N_2(a'^1\Sigma_u^-)$ were taken from Refs. 21–24 and 26. The direct ionization cross sections of the H, N, O, and C atoms and the stepped ionization with metastable levels of N_2 and He were calculated according to Thomson's formula.[25] The model uses the dependence of the dissociative recombination rate constants of the ions O_2^+, N_4^+, $C_2O_4^+$, O_4^+, H_2O^+, H_3O^+, N_3^+, and N_2O^+ on the electron temperature given in Refs. 25 and 28. In all, 30 processes are taken into account whose rates depend on the field intensity in the discharge and the electron temperature. In line with Refs. 13 and 28, we assumed that the recombination rates for the ionic clusters $H_3O^+\cdot H_2O$, $O_2^+\cdot H_2O$, and $H_3O^+\cdot OH$ do not depend on the electron temperature and have values $\sim 10^{-6}$ cm^3/s. Processes involving the electron levels of the nitrogen molecule $N_2(A^3\Sigma_u^+)$, $N_2(a'^1\Sigma_u^-)$, $N_2(C^3\Pi_u)$, and $N_2(B^3\Pi_g)$ were represented by a set of reactions taken from Refs. 29 and 30. The cross section of the process of excitation of the vibrational levels $N_2(v)$ was taken from Ref. 26. For the process of relaxation of the vibrational energy represented by the monomolecular reaction

$$N_2(v)\rightarrow N_2 \tag{2}$$

we assigned the rate constant $\sim 10^6$ s^{-1}. Primary attention in the development of the model was devoted to a description of the processes of chemical and charge kinetics; a detailed description of processes involving vibrational levels of the molecules goes beyond the scope of this work.

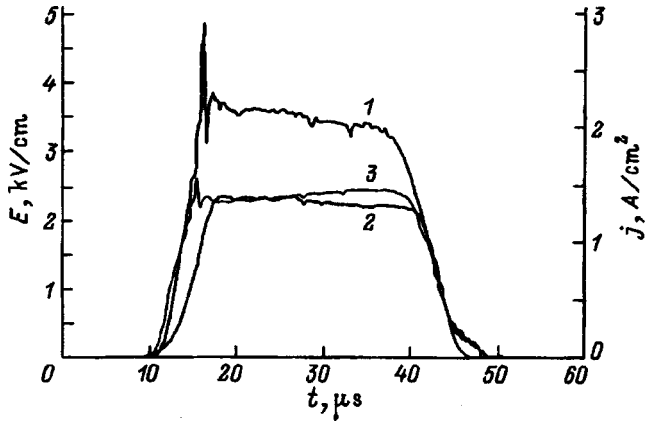

FIG. 1. Experimental and calculated time dependence of the electric field intensity and current density in the discharge.

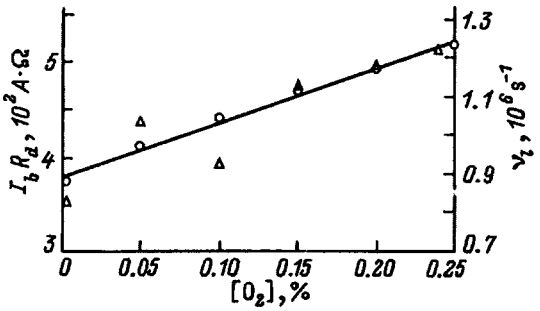

FIG. 2. Experimental and calculated dependence of discharge characteristics on the oxygen concentration; △ — experiment, ○ — calculation.

The system of differential balance equations for the plasma components was solved by the Gear method. As estimates show, the method we used to mathematically model the processes of plasma-chemical and charge kinetics ensures that the relative error in the balance of the charged particle concentrations not exceed 10^{-4} at any point in the calculation and that the elemental composition of the plasma agree with the stoichiometric coefficients of the initial chemical composition of the gas mixture with a relative error of $\sim 10^{-2}$ (Ref. 32).

RESULTS AND DISCUSSION

Figure 1 plots the experimentally observed time dependence of the mean field intensity (curve *1*) and current density (curve *2*), and the calculated time dependence of the current density (curve *3*). The duration of the pump pulse at seven-tenths maximum was 25 μs. For electron beam density 22 mA/cm^2 the mean field intensity in the discharge gap was 3.5 kV/cm, and the current density was 1.4 A/cm^2. The electron beam current pulse has the shape of a trapezoid with duration at its base 8 μs longer than the voltage pulse and the main discharge current pulse. The duration of the leading and trailing edges of the pulse is 5 μs. The rate of ionization of the gas molecules by the electron beam grows linearly with rise of the leading edge of the pulse and falls linearly with falloff of the trailing edge. In the calculations the rate of ionization of the gas mixture by the electron beam remains constant during the duration of the discharge. This fact explains the differences between the experimental and calculated current pulses on the leading edge. Until the external ionization rate reaches its maximum, the magnitude of the experimental current remains considerably less than that of the calculated current. Small differences are also observed in the quasistationary segment of the discharge. This may be due to the fact that lowering the voltage on this segment leads to a decrease in the energy of the electron beam and, consequently, in the external ionization rate.[33] For constant external ionization rate in the model the electron concentration grows, which leads for a small drop in the field intensity in the discharge to growth of the current in comparison with the experimental value of the current. On the basis of the above comparison of the calculated and experimental time dependence of the current it is possible to conclude that in general the model gives a satisfactory description of the kinetics of electron processes determining the conductivity of a discharge plasma.

In our experiments the oxygen concentration in the starting gas mixture was varied from 0.0024 to 0.25%. For constant external ionization rate and increasing oxygen concentration the resistance of the discharge grew on average by $\approx 40\%$. Under stationary conditions of a non-self-sustaining discharge the condition

$$\nu_i N_0 / n_e = k_a N_a + k_r N^+ - k_d N^- \equiv \nu_l ,$$

is fulfilled, where N_0 is the neutral particle density of the gas; N_a is the density of electronegative molecules, and n_e, N^+, and N^- are the densities of the electrons and positive and negative ions, respectively; k_a, k_r, and k_d are the rate constants of attachment, recombination, and detachment, respectively; and ν_l is the effective electron loss rate in the discharge.

It is easy to show that the product of the electron beam current I_b and the discharge resistance R_d is proportional to the effective electron loss rate in the discharge $I_b R_d \sim \nu_i N_0 / n_e = \nu_i$. Figure 2 plots the dependence of the experimentally determined value of $I_b R_d$ and the calculated value of the effective electron loss rate ν_l on the relative oxygen volume concentration in the starting gas mixture. Comparison of these two dependences demonstrates that the model correctly predicts changes in conditions in the discharge controlling the charge-kinetics processes as a function of the oxygen concentration.

Numerical analysis revealed the following characteristic features of the development of a non-self-sustaining discharge in a $CO_2 : N_2 : He$ mixture with O_2 and H_2O impurities. After a time $t < 10^{-9}$ s conversion of the ionic composition determined by the initial composition of the gas mixture takes place. At this early stage the CO_2^+, N_2^+, and He^+ ions are replaced by the secondary ions N_4^+ and $C_2O_4^+$ formed in the reactions

$$He^+ + N_2 \rightarrow N_2^+ + He, \quad k = 1.7 \times 10^{-9} \text{ cm}^3/\text{s} \text{ (Ref. 3)}, \quad (3)$$

$$N_2^+ + 2N_2 \rightarrow N_4^+ + N_2, \quad k = 7.2 \times 10^{-29} \text{ cm}^6/\text{s} \text{ (Ref. 3)}, \quad (4)$$

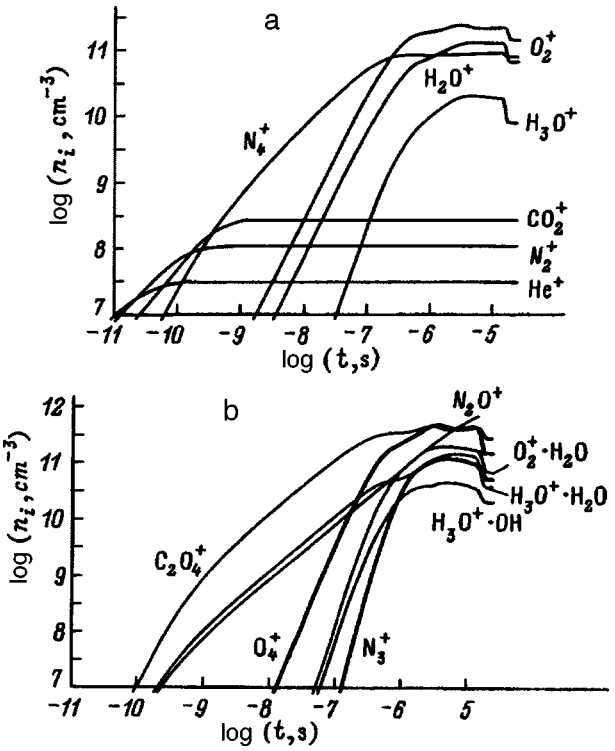

FIG. 3. Calculated time dependence of the concentrations of the main positive ions in the discharge.

$$CO_2^+ + 2CO_2 \rightarrow C_2O_4^+ + CO_2,$$

$$k = 3.0\times10^{-28}\ \text{cm}^6/\text{s}\ \text{(Ref. 3)}. \quad (5)$$

Their concentration at the end of the first nanosecond after initiation of the discharge exceeds the total concentration of the primary ions, which remains stationary at the level 10^8 cm^{-3} during the duration of the discharge (Fig. 3a and b). At a time 10–100 ns later, this concentration level is reached by the $H_3O^+ \cdot H_2O$, N_2O^+, O_2^+, H_2O^+, O_4^+, $O_2^+ \cdot H_2O$, $H_3O^+ \cdot OH$, H_3O^+, and N_3^+ ions, whose appearance is due both directly to ionization by the electron beam of the O_2 and H_2O molecules and to the chain of ionic–molecular reactions

$$He^+ + CO_2 \rightarrow O^+ + CO + He,$$

$$k = 1.2\times10^{-9}\ \text{cm}^3/\text{s}\ \text{(Ref. 3)}, \quad (6)$$

$$O^+ + N_2 + He \rightarrow N_2O^+ + He,$$

$$k = 5.4\times10^{-29}\ \text{cm}^6/\text{s}\ \text{(Ref. 3)}, \quad (7)$$

$$O_2^+ + O_2 + He \rightarrow O_2^+ + He,$$

$$k = 3.1\times10^{-29}\ \text{cm}^6/\text{s}\ \text{(Ref. 3)}, \quad (8)$$

$$O_4^+ + H_2O \rightarrow O_2^+ \cdot H_2O + O_2,$$

$$k = 1.2\times10^{-9}\ \text{cm}^3/\text{s}\ \text{(Ref. 3)}, \quad (9)$$

$$O_2^+ + H_2O + He \rightarrow O_2^+ \cdot H_2O + He,$$

$$k = 9.\times10^{-29}\ \text{cm}^6/\text{s}\ \text{(Ref. 13)}, \quad (10)$$

$$O_2^+ \cdot H_2O + H_2O \rightarrow H_3O^+ \cdot OH + O_2,$$

$$k = 1.0\times10^{-9}\ \text{cm}^3/\text{s}\ \text{(Ref. 3)}, \quad (11)$$

$$H_2O + H_2O \rightarrow H_3O^+ + OH,$$

$$k = 1.0\times10^{-9}\ \text{cm}^3/\text{s}\ \text{(Ref. 3)}, \quad (12)$$

$$H_3O^+ + H_2O + He \rightarrow H_3O^+ \cdot H_2O + He,$$

$$k = 7.0\times10^{-28}\ \text{cm}^6/\text{s}\ \text{(Ref. 13)}. \quad (13)$$

Changes in the ionic composition cause the effective recombination rate constant $\overline{k_r} = \Sigma_i n_i k_{ri} / \Sigma_i n_i$ (n_i and k_{ri} are the concentration and recombination rate constant of ions of type i, respectively) to vary from 1.7×10^{-7} cm^3/s at $t = 10^{-10}$ s to 1.5×10^{-6}cm^3/s at $t = 5.\times10^{-7}$ s, which corresponds to the onset of the voltage pulse acting on the discharge gap. As the voltage increases, the electron temperature grows and the effective recombination rate constant begins to decrease. At the maximum electron temperature T_c, which in the given case is approximately equal to 0.7 eV, it becomes approximately equal to 4×10^{-7}cm^3/s. An important factor here is the fact that the recombination rate constants of the ionic clusters $H_3O^+ \cdot H_2O$, $O_2^+ \cdot H_2O$, and $H_3O^+ \cdot OH$ adopted in the model do not depend on the electron temperature and have values $\sim10^{-6}$ cm^3/s. As the oxygen concentration in the initial gas mixture is increased, the fraction of complex ions $O_2^+ \cdot H_2O$, $H_3O^+ \cdot OH$, and O_4^+ grows, and along with it the effective recombination rate constant.

The negative ions are initially formed in three-body attachment reactions

$$O_2 + e + N_2 \rightarrow + O_2^- + N_2, \quad k = 1.\times10^{-31}\ \text{cm}^6/\text{s}\ \text{(Ref. 3)}, \quad (14)$$

$$O_2 + e + O_2 \rightarrow + O_2^- + O_2,$$

$$k = 2.5\times10^{-30}\ \text{cm}^6/\text{s}\ \text{(Ref. 3)}, \quad (15)$$

$$O_2 + e + H_2O \rightarrow + O_2^- + H_2O,$$

$$k = 1.4\times10^{-29}\ \text{cm}^6/\text{s}\ \text{(Ref. 3)}, \quad (16)$$

and processes of dissociative attachment

$$CO_2 + e \rightarrow CO + O^-, \quad k = k(E/N), \quad (17)$$

$$O_2 + e \rightarrow O + O^-, \quad k = k(E/N). \quad (18)$$

Ionic–molecular processes

$$O_2^- + 2CO_2 \rightarrow CO_4^- + CO_2,$$

$$k = 9.0\times10^{-30}\ \text{cm}^6/\text{s}\ \text{(Ref. 3)}, \quad (19)$$

$$O^- + 2CO_2 \rightarrow CO_3^- + CO_2,$$

$$k = 8.0\times10^{-29}\ \text{cm}^6/\text{s}\ \text{(Ref. 3)}, \quad (20)$$

$$CO_3^- + NO \rightarrow NO_2^- + CO_2,$$

$$k = 9.0\times10^{-12}\ \text{cm}^6/\text{s}\ \text{(Ref. 3)}, \quad (21)$$

then lead to conversion of the negative-ion composition with predominance of the complex ions CO_4^-, CO_3^-, and NO_2^-. Figure 4 shows that the dynamics of variation of the concentration of the O^- ions and the related ions CO_3^- and NO_2^- is driven by the strong dependence of the dissociative attach-

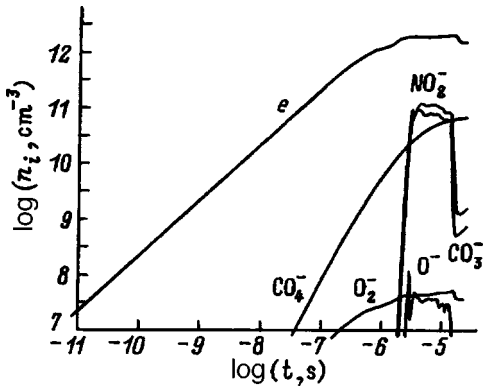

FIG. 4. Calculated time dependence of the concentration of the main negative ions in the discharge.

ment rate constant on the field intensity in the discharge. The rate constant of three-body electron attachment depends on the electron temperature and the field intensity much more weakly.[25] We took it to be constant in our calculations; therefore changes in the concentration of the O_2^- ions and the related CO_4^- ions are driven mainly by changes in the electron concentration.

Analysis of the contributions of the various processes to the process of electron loss under our experimental conditions ($E/N \approx 1.5\times 10^{-16}$ V·cm^2, $[O_2]=0.005\%$) shows that the recombination fraction amounts to approximately 95%, and the attachment fraction, to approximately 5%. Increasing the oxygen concentration in the starting mixture from 0.005 to 0.25% increases the electron loss rate by 40%. In this event, the total attachment rate constant grows by a factor of two. This causes the electron loss rate to grow by 5%. The remaining 35% of the growth of this rate is due to the increase in the effective recombination rate constant. The buildup of nitrogen oxides after $\sim 10^{-5}$ s in our case reaches $\sim 10^{12}$ cm^{-3}, which does not a significant effect on the attachment rate.

Thus, the increase in the resistance of the discharge with growth of the oxygen concentration for the electric field intensity ≈ 3.5 kV/cm can be explained by an enhancement of ion conversion processes with formation of ionic clusters having in comparison with other types of ions a large recombination rate constant. The situation is substantially different if the field intensity is increased to 4–5 kV/cm. Increasing the field intensity causes the effective rate constant of dissociative attachment to decrease as a consequence of the resulting increase in the electron temperature. However, the exponential growth of the attachment rate constants leads to the result that attachment becomes the dominant process leading to electron loss. As was shown in Ref. 15, when a critical value of the field intensity is reached $E_* \approx 4$ kV/cm an instability develops in a non-self-sustaining discharge in the mixture $CO_2 : N_2$: He leading to filamentation. The main role in the proposed instability mechanism is played by processes of electron attachment to CO_2 molecules and stepped and associative ionization with participation of metastable states of the nitrogen molecule. For the external ionization rate constant, the critical value of the field intensity is determined by the relative predominance of recombination and attachment processes. Calculation of this quantity in the range of conditions necessary for efficient operation of an electron-beam-controlled CO_2 laser requires additional study with the goal of attaining a detailed account of ionic–molecular reactions involving small impurities and the corresponding nascent ionic clusters.

In conclusion, we would like to express our gratitude to I. V. Arkanova for assistance with the processing of the experimental data.

[1] N. G. Basov, É. M. Belenov, V. A. Danilychev, and A. F. Suchkov, Usp. Fiz. Nauk **114**, 213 (1974) [Sov. Phys. Usp. **17**, 705 (1974)].
[2] G. A. Mesyats, V. V. Osipov, and V. F. Tarasenko, *Pulsed Gas Lasers* [in Russian] (Nauka, Moscow, 1991), 272 pp.
[3] K. Smith and R. M. Thompson, *Computer Modeling of Gas Lasers* (Plenum Press, New York, 1978; Mir, Moscow, 1981, 516 pp.).
[4] V. S. Golubev and S. V. Pashkin, *High-Pressure Glow Discharge* [in Russian] (Nauka, Moscow, 1990), 335 pp.
[5] D. S. Stark, P. H. Cross, and H. Foster, IEEE J. Quantum Electron. **QE-11**, 774 (1975).
[6] G. A. Baranov, Yu. B. Butaev, A. P. Vorob'ev, and A. K. Zinchenko, Zh. Tekh. Fiz. **64**(5), 49 (1994) [Tech. Phys. **39**, 483 (1994)].
[7] W. J. Witteman, Appl. Phys. Lett. 1967. **11**, 337 (1967).
[8] A. L. S. Smith and P. G. Brown, J. Phys. D **7**, 1652 (1974).
[9] A. L. S. Smith, T. H. Bett, and P. G. Brown, IEEE J. Quantum Electron. **QE-11**, 335 (1975).
[10] W. J. Witteman, *The CO_2 Laser* (Springer-Verlag, Berlin, 1987; Mir, Moscow, 1990, 360 pp.).
[11] G. A. Mesyats, V. M. Orlovskiĭ, V. V. Osipov *et al.*, Dokl. Akad. Nauk SSSR **303**, 850 (1988) [Sov. Phys. Dokl. **33**, 922 (1988)].
[12] E. P. Glotov, V. A. Danilychev, and I. V. Kholin, Tr. Fiz. Inst. Acad. Nauk SSSR **116**, 188 (1980).
[13] V. Dzh. Vigand, in *Applied Atomic Collision Physics*, Vol. 3 (*Gas Lasers*), edited by E. W. McDaniel and W. Nigan [Academic Press, New York (1982); Mir, Moscow (1986), 552 pp.].
[14] M. F. Danilov, E. A. Zobov, A. N. Malinin, and Yu. P. Nikonov, Zh. Tekh. Fiz. **61**, No. 12, 36 (1991) [Sov. Phys. Tech. Phys. **36**, 1347 (1991)].
[15] M. F. Danilov and A. N. Malinin, Zh. Tekh. Fiz. **66**, No. 2, 74 (1996) [Tech. Phys. **41**, 153 (1996)].
[16] M. F. Danilov, ''Software package for data processing and numerical simulation of plasma-chemical reactions'' [in Russian], Dep. VIMI No. Do-8502 (1992).
[17] Yu. S. Akishev, A. A. Deryugin, V. B. Karal'nik *et al.*, Fiz. Plazmy **20**, 571 (1994) [Plasma Phys. Rep. **20**, 511 (1994)].
[18] H. Hokazono and H. Fujimoto, J. Appl. Phys. **62**, 1585 (1987).
[19] V. N. Kondrat'ev, *Rate Constants of Gas-Phase Reactions* [in Russian], (Nauka, Moscow, 1970), 351 pp.
[20] V. P. Agafonov, V. K. Vertushkin, A. A. Gladkov, and O. Yu. Pol'yanskiĭ, *Nonequilibrium Physical-Chemical Processes in Aerodynamics* [in Russian] (Mashinostroenie, Moscow, 1972).
[21] J. J. Lovke, A. V. Phelps, and B. W. Irwin, J. Appl. Phys. **44**, 4664 (1973).
[22] D. Rapp and P. J. Englander-Golden, J. Chem. Phys. **43**, 1464 (1965).
[23] D. Rapp and D. D. Briglia, J. Chem. Phys. **43**, 1480 (1965).
[24] H. S. W. Massey, *Negative Ions* (Cambridge University Press, Cambridge, 1976), 756 pp.
[25] Yu. P. Raĭzer, *Physics of Gas Discharges* [in Russian] (Nauka, Moscow, 1987), 592 pp.
[26] A. G. Engelhardt, A. V. Phelps, and C. G. Risk, Phys. Rev. A **135**, 1566 (1964).
[27] A. V. Berdyshev, I. V. Kochetov, and A. P. Napartovich, Fiz. Plazmy **14**, 741 (1988) [Sov. J. Plasma Phys. **14**, 438 (1988)].
[28] M. A. Biondi, in *Applied Atomic Collision Physics*, Vol. 3 (*Gas Lasers*), edited by E. W. McDaniel and W. Nigan [Academic Press, New York (1982); Mir, Moscow (1986), 552 pp.].
[29] A. V. Berdyshev, A. S. Golovin, A. V. Gurashvili *et al.*, Fiz. Plazmy **15**, 335 (1989) [Sov. J. Plasma Phys. **15**, 195 (1989)].
[30] A. A. Deryugin, I. V. Kochetov, A. F. Pal' *et al.*, Fiz. Plazmy **17**, 1138

(1991) [Sov. J. Plasma Phys. **17**, 661 (1991)].
[31] R. Kummler, C. Leffert, K. Im *et al.*, Phys. Chem. **81**, 2451 (1977).
[32] M. F. Danilov and E. V. Kalashnikov, Teplofiz. Vys. Temp. **39**, 663 (1995).
[33] Yu. D. Korolev and G. A. Mesyats, *Physics of Pulsed Breakdown of Gases* [in Russian] (Nauka, Moscow, 1991), 224 pp.

Translated by Paul F. Schippnick

Study of the limiting energy characteristics of a combined discharge in a gas flow

V. V. Osipov, M. G. Ivanov, and V. V. Lisenkov

Institute of Electrophysics, Ural Branch of the Russian Academy of Sciences, 620219 Ekaterinburg, Russia
(Submitted November 27, 1996)
Zh. Tekh. Fiz. **68**, 33–38 (May 1998)

A combined method of excitation of a gaseous medium is used in an investigation of the energy characteristics of a non-self-sustaining discharge as functions of the capacitance of the capacitor bank, the number of pulses per burst, and the burst repetition rate for different time intervals between the pulses in a burst and different flow velocities of the gas. It is shown for infrared lasers that under optimal pumping conditions the average discharge power can reach 8.5 W/cm^3 for a pulse power of 25 W/cm^3. © *1998 American Institute of Physics.* [S1063-7842(98)00605-9]

INTRODUCTION

The creation of a new generation of CO_2 and CO lasers capable of generating radiation with an average power density of 2–3 W/cm^3 for a quantum yield of 15–20% in active media occupying a volume of tens to hundreds of liters is an extremely important problem, especially in that its potential solution is based on the existence of lasers in which the medium is pumped by a non-self-sustaining discharge controlled by an electron beam.[1,2] However, new-generation lasers, beyond and above the advantages of electron-beam-controlled (''electroionization'') lasers, should possess important additional qualities: a long service life and reliable operation, the absence of radiation danger, and small dimensions. The main hope of solving this problem probably rests in replacing the electron beam by a short-duration self-sustaining discharge creating a plasma with prescribed concentration.[3] The main part of the energy is injected into the gas by a non-self-sustaining discharge in a decaying plasma. As an analog of such lasers we may cite electron-beam-controlled lasers excited by an electron-beam–initiated non-self-sustaining discharge.[4] Such lasers yield little to other types of electron-beam-controlled lasers.

Discharges combining successive, clearly defined stages of self-sustaining and non-self-sustaining discharge have come to be called combined discharges. A number of methods have been proposed to excite them[3,5,6] which differ among themselves in the means employed to decouple the self-sustaining and non-self-sustaining discharge circuits. Testing of the possibility of realization of these methods has been carried out, as a rule, under conditions of absence of gas flow-through, in the single-pulse[3] or burst modes[5,6] and has demonstrated the possibility of realization of space discharges with power densities greater than 10 W/cm^3 (Ref. 3) and even 100 W/cm^3 (Ref. 6). In these studies it was assumed that if the gas were refreshed during one pulse of the non-self-sustaining discharge, then such characteristics could be realized in the continuous mode. However, attempts to realize this goal went for a long time without success since gas flow-through brings with it substantial changes in the energetics of the discharge. Only recently, thanks to the efforts of Nikumb *et al.*[7] and Nagai *et al.*[8] has the hope been raised of solving this problem.

In particular, Nikumb *et al.*[7] report the creation of a 12-module CO_2 laser with a channel volume (volume of the active medium) of 40 liters and average radiation power equal to 10 kW, where pumping of the medium was realized by a combined discharge. The laser of Nagai *et al.*,[8] having a channel volume of 10 liters and pumped by a self-sustaining discharge with intense pre-ionization of the medium, achieved a still greater radiation power — 20 kW. Unfortunately, neither[7,8] of these groups was able to avoid the necessity of using resistive stabilization of the discharge, which, as is well known, lowers the total efficiency of the laser by not less than twofold.

In the present work, we have developed a new method for exciting a combined discharge, in which current-limiting elements are absent in the circuits of the self-sustaining and non-self-sustaining discharges. The main focus of this work is a study of the effect on the limiting energy characteristics of the discharges of the medium parameters, the elements of the power-supply circuit, and their arrangement relative to the discharge zone.

EXPERIMENTAL TECHNIQUE

The basic scheme for combined discharge excitation is analogous to that presented in Ref. 9. The overall volume of the discharge zone was $4.2\times2\times80$ cm and the height of each of the interelectrode gaps was 2.1 cm. The middle electrode was fashioned in the shape of a plate 1 cm in thickness, and the main electrodes had a large-radius cylindrical surface. The auxiliary discharge electrodes whose purpose it was to pre-ionize the medium and where this auxiliary discharge had the form of a series of spikes, were located near the main electrodes at different locations in the gas channel. The total capacitance of the auxiliary-discharge capacitors did not exceed 1.5 nF. The repetition rate and amplitude of the high-voltage pulses igniting the self-sustained discharge could be regulated within the limits 0.1–20 kHz and 6–15 kV, respectively. To study the pumping burst mode we devised a scheme allowing us to vary the burst repetition rate,

the number of pulses per burst, and the time between these pulses. Correspondingly, by varying these parameters we were able to obtain a quasicontinuous pulsing regime with constant repetition rate. The capacitance of the capacitors of the self-sustaining discharge was 2 nF. The power supply to the non-self-sustaining discharge, which provided power levels up to 7.5 kW, could maintain a constant voltage on the electrodes of 1–2.5 kV. The capacitance of the capacitor block of the non-self-sustaining discharge varied during the course of the experiment from 1 to 11 μF.

The gas flow-rate through the discharge chamber could be varied within the limits 0–50 m/s. The gas mixture for most of the experiments had the composition $CO_2:N_2:He = 2:14:44$ Torr.

The limiting energy characteristics of the space discharge were determined by recording and analyzing oscillograms of the discharge current and electrode voltage. Characteristic oscillograms of the current pulses of the self-sustaining discharge (a), ionizing the working medium, and the non-self-sustaining discharge (b), delivering the main fraction of the energy to the gas at the stage of plasma decay, are shown in Fig. 1. The duration of the self-sustaining discharge current was 10^{-7} s, while that of the non-self-sustaining discharge current varied from 10^{-4} to 1.5×10^{-4} s during the course of the experiment. Analysis of the ratio of the energies delivered to the gas at the stage of the self-sustaining (W_s) and non-self-sustaining discharge (W) shows that under typical conditions it is $\sim 5\%$. It is also clear that despite the constant amplitude of the current pulses of the self-sustaining discharge, the amplitude of the burst of current pulses of a non-self-sustaining discharge at first grows and then drops off. If the growth of the amplitude is associated with peculiarities of the implemented excitation scheme, then its decay, in our opinion, is due to a buildup in the medium of electronegative components of the type O_2, NO_2, N_2O, and NO, increasing the rate of attachment processes and lowering the discharge current.[10]

The energy delivered to the active medium at the stage of the non-self-sustaining discharge was determined by graphically integrating the product of the current and voltage

$$W=\int_0^\infty I(t)U(t)dt.$$

Here $I(t)$ and $U(t)$ are the current and voltage of the non-self-sustaining discharge.

RESULTS

Throughout the course of the experiments we tracked the limiting electrical power and energy delivered to the gas by the burst of pulses as functions of the capacitance of the capacitor bank feeding the non-self-sustaining discharge, the burst repetition frequency, the number of pulses per burst, and the time interval between them, i.e., we found the optimum values of these parameters under conditions of stable burning of the space discharge.

First we elucidated the optimal location of the auxiliary discharge pre-ionizing the medium. The system of electrodes for its excitation was emplaced upstream or downstream in the gas flow at a distance of 0.5–10 and 4–10 cm, respectively, from the electrodes of the main discharge or below them. In the latter case there were slits in the electrodes to transmit the auxiliary discharge radiation. The dependence of the electron concentration in the self-sustaining discharge on the capacitance of the capacitors feeding the auxiliary discharge is given in Ref. 9 for different locations of the auxiliary discharge. Here it may be noted that the best stability of the discharge and the corresponding maximum energy transfers to the non-self-sustaining discharge were obtained when the auxiliary discharge was located upstream and as close as possible to the main discharge. This was especially noticeable in mixtures with CO_2, since the emitted ultraviolet radiation is strongly absorbed by CO_2 molecules. It is also noteworthy that the best results were obtained when maximum illumination was directed on the cathode since photoemission of electrons from the cathode is of great importance for ignition of a uniform discharge. At the same time, for ignition of the auxiliary discharge under the main-discharge electrodes the nonuniform structure of the electrodes shows up strongly in the nonuniformity of the main discharge. On the basis of these results, the pins of the auxiliary-discharge electrode were emplaced 5 mm in front of the main-discharge electrodes upstream relative to the gas flow. Since an intermediate plate served as the cathode in the self-sustaining discharge, a special effort was made to ensure maximum illumination of this plate.

One of the most important parameters influencing the energy delivered to the gas as well as the overall dimensions

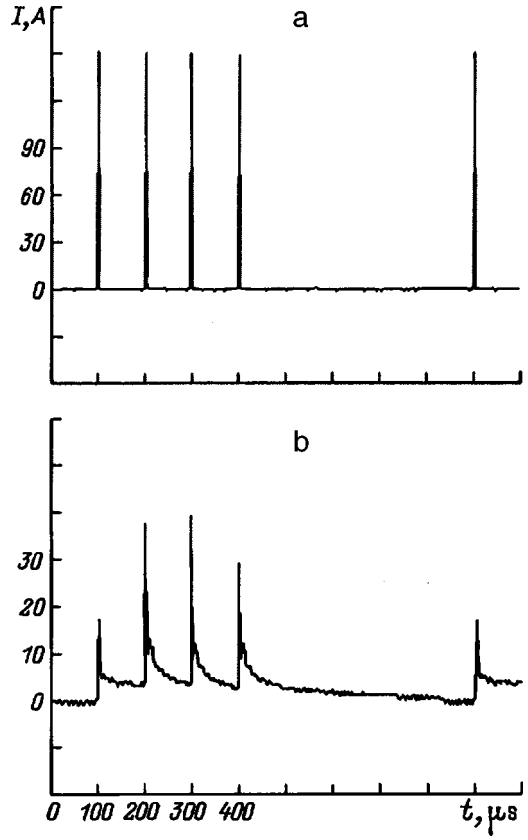

FIG. 1. Oscillograms of current pulses of a self-sustaining (a) and a non-self-sustaining (b) discharge.

of the laser is the capacitance of the capacitor bank feeding the non-self-sustaining discharge. Its value was optimized for the electron-beam-initiated non-self-sustaining discharge excited in the single-pulse mode.[11] Since in our case excitation was realized by a burst of pulses under threshold conditions from the point of view of contraction of the discharge, it is logical to expect a deviation of our data from those obtained in Ref. 11.

Results of choosing the optimal capacitance of the capacitor bank for preserving the spatial nature of the discharge are displayed in Fig. 2 in the form of curves of the energy transfer to the discharge as a function of the capacitance. The experiments were performed for a burst repetition rate of 100 Hz and gas flow velocity of 50 m/s, i.e., the gas was refreshed 25 times between pulses. This, given a large supply of gas, ensured fulfillment of the condition of absence of any effect of the preceding pulse. Therefore it may be asserted that contraction of a space discharge is due only to processes taking place during the burst.

It can be seen that when the number of pulses per burst is not more than two, curve *4* saturates in the range 4–6 μF and the energy delivered to the gas by the burst does not depend on the capacitance C of the capacitor bank. It may be noted that to obtain this dependence the initial voltage U_0 on the electrodes was kept fixed while the capacitance C was varied. Curves *5* and *6* for the number of pulses per burst equal to three or more have a quite pronounced maximum at C_m equal to 2–4 μF. In the latter case, simultaneous with increase of the capacitance beyond 3 μF (beyond the maximum) the initial voltage on the capacitor bank (U_0) was lowered to a level ensuring absence of contraction of the discharge. In order to explain such behavior of the curves and to determine the optimum value of C, we analyzed decay of the plasma and its effect on the limiting energy characteristics of a space discharge. Toward this end, we considered a system of equations taking into account discharging of the capacitor bank as a consequence of passage of the current of the non-self-sustaining discharge and decrease of the electron concentration due to processes of attachment and recombination

$$\frac{dU}{dt}=-\frac{S}{Cd}e\mu U n_e,$$

$$\frac{dn_e}{dt}=(\nu_t-\nu_D)n_e-\beta n_e^2, \tag{1}$$

where S is the area of the electrodes, C is the capacitance, μ is the electron mobility, d is the interelectrode spacing, ν_i and ν_D are the ionization and dissociative recombination rates, respectively, and β is the electron–ion recombination coefficient.

The values of the kinetic coefficients (rate constants), with the exception of β, were obtained by numerical solution of the Boltzmann equation. The value of β was taken from Ref. 12.

Solving system of equations (1), it is possible to obtain the following expression for the residual voltage on the capacitor:

$$U_{\text{res}}=U_0\ \exp\left[-\frac{eS\mu}{Cd}\left((K-1)\int_0^{\tau_{\text{pul}}}\frac{dt}{Y}+\int_0^{\infty}\frac{dt}{Y}\right)\right], \tag{2}$$

where

$$Y=\left(\frac{1}{n_0}+\frac{\beta}{\nu_D-\nu_i}\right)\exp((\nu_D-\nu_i)t)-\frac{\beta}{\nu_D-\nu_i},$$

U_0 is the initial voltage on the capacitor bank and K is the number of pulses per burst. The energy per unit volume delivered to the gas may be written as

$$w=\frac{C}{2Sd}(U_0^2-U_{\text{res}}^0), \tag{3}$$

where U_{res} is calculated from formula (2).

For the case of two pulses per burst, the dependence of w on C was calculated according to formula (3) assuming constant U_0 (Fig. 2, curve *1*). Reasonable agreement with experiment is observed (curve *4*).

It can be seen that at small C the value of w grows linearly with C. At large C the growth of w becomes insignificant as a consequence of a decrease in the degree of discharging of the capacitor, and w tends toward its limiting value

$$w_{\max}=\left(\frac{U_0}{d}\right)^2 e\mu\int_0^{\infty}n_e dt.$$

Obviously, the optimum value of the capacitance will be the value at which growth of w saturates.

As the number of pulses per burst is increased, the nature of the dependence of w on C is fundamentally altered. The growth of w for small C gives way to a falloff at large C. The reason for this is the appearance of instabilities. As a result, to obtain a sparkless regime, as was already noted, it was necessary in the course of the experiments to lower the

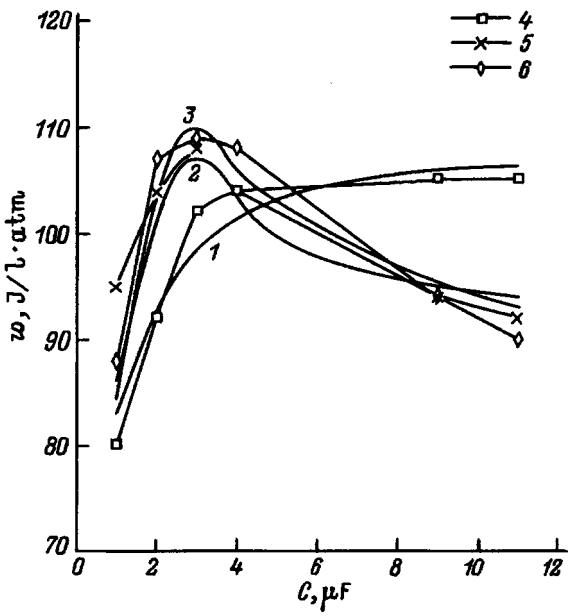

FIG. 2. Dependence of the specific energy transfer on the capacitance of the capacitor bank of a non-self-sustaining discharge. Time between pulses in a burst 100 μs; *1,4* — 2 pulses; *2,5* — 3 pulses; *3,6* — 4 pulses per burst; *1–3* — calculation, *4–6* — experiment.

initial voltage of the non-self-sustaining discharge while increasing the capacitance, which then led to a decrease of w.

To explain these results we assumed the following. As a result of thermal expansion of the heated gas, its number density N decreases, which leads to an increase in the ratio E/N in the interelectrode gap. If during the duration of the burst $\tau_n = K\tau_{\text{pul}}$ the gas heats up so much that E/N exceeds some critical value $(E/N)_k$, then as a consequence of the development of a thermal instability of the discharge a spark channel is formed.

Indeed, in the case of small capacitances a decrease in N is compensated by a decrease in E as a consequence of discharging of the capacitor. With increase of the capacitance the degree of discharging of the capacitor is decreased and cannot compensate growth of E/N due to thermal expansion of the gas. As a result, for the capacitance greater than $C_m \approx 3\mu F$ the value of E/N at the end of the burst exceeds its starting value. It is precisely for $C > C_m$ that the falloff of the experimental curves $w = w(C)$ is observed.

Thus, for $C > C_m$, using the condition

$$\frac{U_{\text{res}}}{dN_d} = (E/N)_k, \tag{4}$$

where N_d is the gas number density at the end of the burst.

Employing relations (2) and (4), it is possible to obtain the following expressions for U_{res} and U_0:

$$U_{\text{res}} = (E/N)_k dN_d, \tag{5}$$

$$U_0 = (E/N)_k dN_d \exp\left[\frac{eS\mu}{Cd}\left((K-1)\int_0^{\tau_{\text{pul}}}\frac{dt}{Y} + \int_0^{\infty}\frac{dt}{Y}\right)\right]. \tag{6}$$

The value of N_d is given by

$$N_d = N_0 \frac{T_0}{T_d}, \tag{7}$$

where T_0 and N_0 are the initial values of the temperature and number density of the gas, respectively; T_d is the temperature of the gas at the time τ_d

$$T_d = T_0 + \xi \frac{w}{c_p}, \tag{8}$$

where c_p is the specific heat of the gas and ξ is the fraction of the energy converted to heat as of the time τ_d.

To determine ξ, we performed a numerical analysis of the population kinetics and thermal relaxation of the main vibrationally excited states of the CO_2 and N_2 molecules. The necessary constants were taken from Ref. 13. For bursts of two, three, and four pulses the values of ξ are respectively 0.35, 0.4, and 0.47. As a result, the expressions for U_{res} and U_0 take the form

$$U_{\text{res}} = (E/N)_k dN_0 \frac{T_0}{T_0 + \xi \dfrac{w}{c_p}}, \tag{9}$$

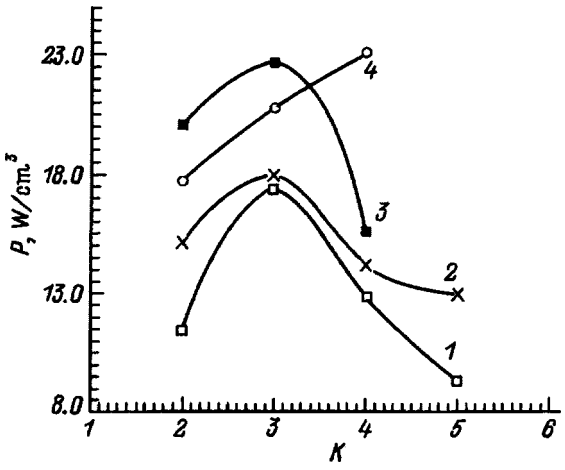

FIG. 3. Dependence of the specific power of a non-self-sustaining discharge versus the number of pulses per burst. C, μF: *1* — 11, *2* — 4, *3* — 2, *4* — 1.

$$U_0 = (E/N)_k dN_0 \frac{T_0}{T_0 + \xi \dfrac{w}{c_p}} \times \exp\left[\frac{eS\mu}{Cd}\left((K-1)\int_0^{\tau_{\text{pul}}}\frac{dt}{Y} + \int_0^{\infty}\frac{dt}{Y}\right)\right]. \tag{10}$$

The values of $(E/N)_k$ were determined from an analysis of the experimental data.

As was noted above, the authors associate the presence of a critical value of $(E/N)_k$ with the development of a heating–ionization instability and offer the following justification for their position. It is well known[14] that the increment of the heating–ionization instability is proportional to $\Omega \sim E^2/N \sim (E/N)^2 N$. The quantity Ωt characterizes the degree of development of the instability after the time t. If we calculate the product $(E/N)_k^2 N_d \tau_d$ for two, three, and four pulses per burst, then we find out that for all three cases the given quantity is constant (to within $\sim 5\%$). This proves that under our conditions contraction of the discharge is due to development of precisely the thermal (heating–ionization) instability.

Thus, to determine the optimal capacitance of the capacitor bank, $w = w(C)$ must be calculated according to formula (3), observing the following conditions: for the number of pulses per burst $K = 2$, and also for $K = 3-4$ and $C \leqslant C_m$, one uses $U_0 = \text{const}$ and the value of U_{res} found from formula (2); for $K = 3-4$ and $C > C_d$ one uses U_0 from formula (10) and U_{res} from formula (9). The calculated curves *1–3* in Fig. 2, obtained in this way, are in reasonable agreement with the experimental curves *4–6* in Fig. 2.

During the course of this study we also investigated the dependence of the limiting power of the non-self-sustaining discharge on the number of pulses per burst and the burst repetition rate. We found that the chosen value of the capacitance of the non-self-sustaining discharge capacitors has its own optimum number of pulses per burst (Fig. 3). Thus, for the number of pulses per burst less than three maximum power of the discharge is not achieved, and for more than

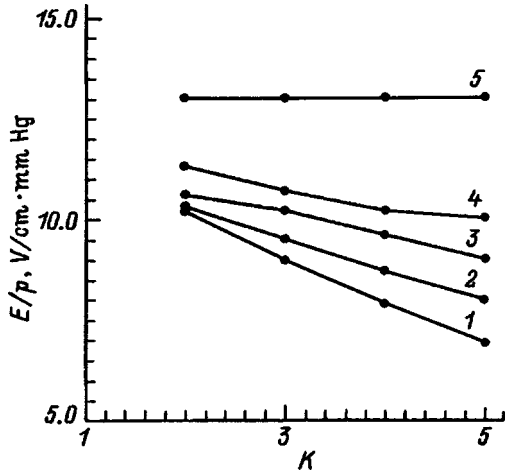

FIG. 4. Dependence of the ratio E/p for a non-self-sustaining discharge on the number of pulses per burst. C, μF: *1* — 11, *2* — 9, *3* — 4, *4* — 3, *5* — 1.

three its stability is lowered and it is correspondingly necessary to lower the initial voltage on the storage capacitance of the non-self-sustaining discharge. At the same time, the small capacitance makes it possible to raise the initial voltage on the discharge and increase the energy transfer during the first pulses, but for a large number of pulses it is substantially discharged and during subsequent pulses the rate of energy delivery to the gas is abruptly diminished. Values of the initial field intensity E_0/p of the non-self-sustaining discharge are plotted in Fig. 4 versus number of pulses per burst for different values of the capacitance of the capacitor bank.

Figures 5 and 6 plot the dependence of the average power of the non-self-sustaining discharge P on the burst repetition rate for different intervals between pulses in the burst, gas flow velocities, and number of pulses per burst. As can be clearly seen, as long as the influence of the preceding pulse is insignificant, P grows as the burst repetition rate is increased, and vice versa. It can be seen that for the same flow velocity at the lower burst repetition rate (<700 Hz) the

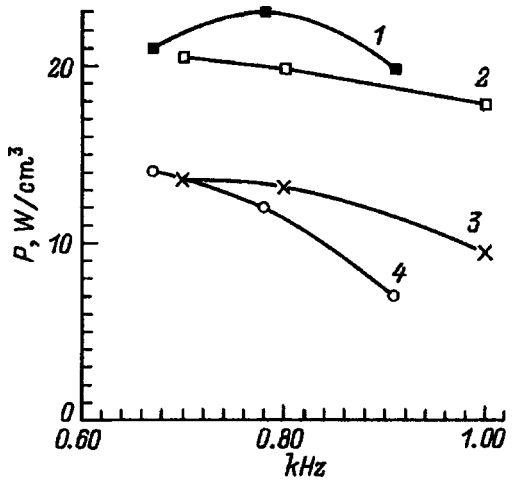

FIG. 5. Dependence of the specific power of a non-self-sustaining discharge on the burst repetition rate for different gas-flow velocities *1,2* — 50; *3,4* — 40 m/s; τ_{pul}, μs: *1,3* — 100; *2,4* — 150.

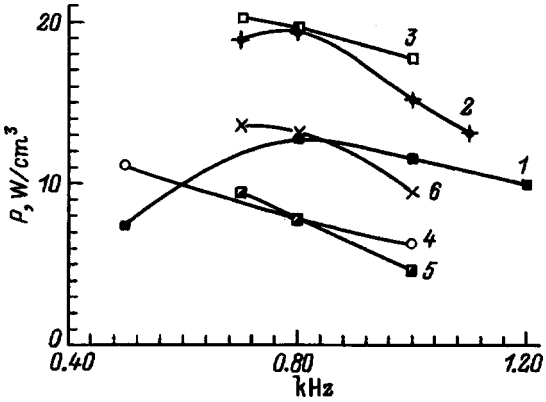

FIG. 6. Dependence of the specific power of a non-self-sustaining discharge on the burst repetition rate for different gas-flow velocities and different number of pulses per burst; $\tau_{pul}=100\mu$s; *1–3* — 50, *4–6* — 40 m/s; *1,4* — 1 pulse; *2,5* — 2 pulses; *3,6* — 3 pulses per burst.

regime with a large time between the pulses is efficient, but for large burst repetition rates it becomes necessary to decrease either the time between pulses in a burst (Fig. 5) or the number of pulses per burst (Fig. 6). At the lower flow velocity it is necessary to lower the repetition rate or decrease the duration of the burst.

This conclusion is in good agreement with the results of Nikumb *et al.*,[7] who, unfortunately, did not indicate the apparent reasons for this behavior. In their experiments they noted a stable maximum of the energy transfer to the non-self-sustaining discharge at burst repetition rates of $\sim$800 Hz both in the pulsed and in the quasicontinuous modes although the self-sustaining discharge burned stably at pulser frequencies up to 15 kHz.

We are inclined to associate this with processes of energy release in the least stable part of the discharge—the cathode layer, and correspondingly with the development of a thermal instability in the near-cathode region. Consequently, the effective duration of the burst is limited by the onset time of the thermal instability at the cathode, but the time between bursts (greater than is necessary for a single flush of the gas) is dictated by the necessity of cooling the gas in the poorly flushed near-electrode boundary layer. Our calculations showed that for the conditions of our experiment the length of the cathode fall is practically equal to the thickness of the Prandtl boundary layer.

At the same time, it appears that acoustic processes[15] develop as well. At the onset of current flow through the discharge gap a shock wave sets out in both directions relative to the gas flow, becoming more intense in the region of the non-self-sustaining discharge.

Accordingly, the duration of the burst is limited by the time for return of the shock wave to the dischange zone. In addition, an interruption between bursts is necessary in order that all the nonuniformities of the gas density that have been created will be swept out with the flow.

During the course of our experiments we found the optimal composition and pressure of the working mixture for obtaining the maximum energy transfer to the active medium during stable operation of the laser (without contraction of the space discharge). In the gas mixture CO_2:N_2:He

$=1:7:22$ at a pressure of 60 Torr and a burst repetition rate (burst of pump pulses) of 800 Hz with three pulses per burst, one every 100 μs, 5.2 kW average power was dissipated in the non-self-sustaining discharge. When the pulse frequency was increased to 20 kHz and the number of pulses per burst to 6, at a burst repetition rate of 600 Hz the average dissipated power was increased to 6 kW, which corresponds to an average power density of 8.5 W/cm^3, or during the time of a burst of pulses during which pumping takes place, 25 W/cm^3. This exceeds the analogous value of available commercial lasers. It should be noted that to obtain these results it was not necessary to employ sectioned electrodes or resistive decoupling, which significantly enhanced the uniformity of the discharge and the efficiency of energy delivery to the gas.

CONCLUSION

In conclusion, let us recapitulate our main results.

We have shown that the energy parameters of a combined discharge can be close to those realized in an electron-beam–driven non-self-sustaining discharge.

We have determined the limiting energy characteristics of a non-self-sustaining discharge as functions of the capacitance of the capacitor bank, the number of pulses per burst, the burst repetition rate for various time intervals between the pulses in a burst, and the gas flow velocity.

We have proposed a technique for calculating the optimal capacitance of the capacitor bank feeding a non-self-sustaining discharge.

[1] S. P. Bugaev, Yu. I. Bychkov, E. K. Karlova *et al.*, Pis'ma Zh. Tekh. Fiz. **1**, 492 (1975) [Tech. Phys. Lett. **1**, 226 (1975)].
[2] Yu. I. Bychkov, E. K. Karlova, N. V. Karlov *et al.*, Pis'ma Zh. Tekh. Fiz. **2**, 212 (1976) [Tech. Phys. Lett. **2**, 81 (1976)].
[3] J. R. Reilly, J. Appl. Phys. **43**, 3411 (1972).
[4] Yu. I. Bychkov, I. N. Konovalov, Yu. A. Kurbatov *et al.*, Prib. Tekh. Eksp. No. **3**, 165 (1974).
[5] A. E. Hill, Appl. Phys. Lett. **22**, 670 (1973).
[6] Yu. J. Bychov, V. V. Osipov, V. A. Telnov, J. Phys. (France) **40**, 161 (1979).
[7] S. K. Nikumb, H. J. J. Seguin, V. A. Seguin *et al.*, IEEE J. Quantum Electron. **QE-25**, 1725 (1989).
[8] H. Nagai, M. Hishii, M. Tanaka *et al.*, IEEE J. Quantum Electron. **29** 2898 (1993).
[9] M. G. Ivanov, S. V. Mukhachev, and V. V. Osipov, Opt. Atmos. Okeana **8**, 1616 (1995).
[10] V. M. Karpov, Yu. G. Konev, V. M. Orlovskiĭ *et al.*, Kvantovaya Elektron. (Moscow) **15**, 465 (1988) [Sov. J. Quantum Electron. **18**, 294 (1988)].
[11] Yu. I. Bychkov, Yu. D. Korolev, Yu. A. Kurbatov, and G. A. Mesyats, Zh. Tekh. Fiz. **44**, 791 (1974) [Sov. Phys. Tech. Phys. **19**, 499 (1974)].
[12] H. Hokazono and H. Fujimoto, J. Appl. Phys. **62**, 1987. 1585 (1987).
[13] R. L. Taylor and S. Bitterman, Rev. Mod. Phys. **41**, 26 (1969).
[14] Yu. P. Raĭzer, *Physics of Gas Discharges* [in Russian] (Nauka, Moscow, 1987), 592 pp.
[15] G. S. Dzacowic and S. A. Waztke, J. Appl. Phys. **46**, 5061 (1973).

Translated by Paul F. Schippnick

Charge-state distribution of ions in a vacuum arc discharge plasma in a high magnetic field

A. G. Nikolaev, E. M. Oks, and G. Yu. Yushkov

Tomsk State Academy of Control Systems and Radio Electronics, 635050 Tomsk, Russia
(Submitted December 16, 1996)
Zh. Tekh. Fiz. **68**, 39–43 (May 1998)

It is shown that the fraction of multiply charged metal ions generated in a vacuum arc discharge plasma grows substantially in a high magnetic field. This effect was observed for more than 30 different cathode materials. A relation is established between growth of the mean charge of the ions and increases in the burning voltage of the arc. It is demonstrated that the burning voltage of the vacuum arc can be ultimately increased to 160 V. © *1998 American Institute of Physics.* [S1063-7842(98)00705-3]

INTRODUCTION

The heightened interest that has been shown in recent years in processes taking place in the cathode spot of a vacuum arc discharge and the adjacent region[1,2] has been occasioned not only by the development of vacuum switches[3] but also with the use of vacuum arc discharges in ion-plasma deposition devices[4] and high-current metal ion beam sources.[5] In the last case the charge distribution of the ions extracted from the plasma is of great significance, since it determines the average energy of the ion beam. Multiple ionization in a vacuum arc discharge plasma ensures an enhanced mean ion charge state, which upon their extraction leads to an increase in the ion beam energy at a given accelerating voltage. Under ordinary vacuum arc burning conditions with a discharge current of hundreds of amperes and discharge pulse duration of tenths of milliseconds depending on the cathode material, ions are present in the plasma with charge states from 1^+ to 5^+ with a mean charge state from 1 (carbon cathode) to $2.5-3.0$ (heavy-metal cathodes).[6,7] Besides the cathode material, the ion charge-state distribution depends to a significant degree on the duration of the arc pulse and the residual gas pressure. The fraction of multiply ionized particles can substantially decrease when the duration of the discharge pulse is increased on a time scale of tens and even hundreds of microseconds[8] or the pressure is increased from 10^{-6} to 10^{-5} Torr (Ref. 9).

A plasma-forming medium arises in a vacuum arc discharge, as is well known,[10] as a result of evaporation of the electrode material at the cathode spot and its ionization in a relatively small region near the spot. It is precisely in this region that all processes take place that define the parameters of the vacuum arc discharge plasma. At the boundary of this region ionization essentially ceases and ''freezing'' of the plasma parameters, so to speak, takes place.[11] Beyond this region the plasma simply expands into the volume of the discharge chamber.[12]

Since creation of a high magnetic field in a local region does not present great difficulties, it is possible to investigate the influence of such a field on the conditions of formation of the steady-state parameters of a vacuum arc discharge plasma. Here by high magnetic field we mean a field that influences not only the electron component, but also the ionic component of the plasma. Obviously, a high magnetic field is capable of increasing the fraction of multiply ionized atoms since by containing the ions it at least ensures that they will be found for a longer time in the intense ionization region. The influence of a high magnetic field on the ion charge-state distribution in a vacuum arc discharge plasma is the object of research efforts, whose results are presented in this paper.

EXPERIMENTAL TECHNIQUE

A schematic of the discharge system is shown in Fig. 1. A vacuum arc discharge ($0.1-4$ kA, $0.25-1$ ms) between the cathode *1* and anode *4* is initiated by an auxiliary discharge on a ceramic surface when a short-duration (10μs) positive high-voltage (12 kV) pulse is fed to the trigger electrode relative to the cathode.[3] The cathode–anode separation was varied from a few millimeters to 10 cm. In experiments on stabilization of the arc and achieving a higher arc burning voltage in analogy with the discharge stabilization system in the high-current proton source of the Institute of Nuclear Physics of the Siberian Branch of the Russian Academy of Sciences[13] the interelectrode gap was overlapped with a system of flat electrodes with central coaxial openings with diameters of 6 and 12 mm.

The magnetic field was created by a short solenoid (average diameter of the coil 35 mm, length 30 mm), creating at the center of the coil a pulsed magnetic field of 10 kG. The solenoid was powered by a separate power supply or it was connected in series to the discharge gap. In the latter case, increases in the magnetic field were accompanied by a corresponding increase in the arc current.

A study of the ion charge-state distribution was carried out at the experimental facilities of the Association for Heavy Ion Research (GSI, Darmstadt, Germany) and also at the Lawrence Berkeley National Laboratory (LBNL, Berkeley, USA) within the framework of joint research projects with these laboratories. A vacuum arc discharge was triggered in the electrode system of the high-current wide-

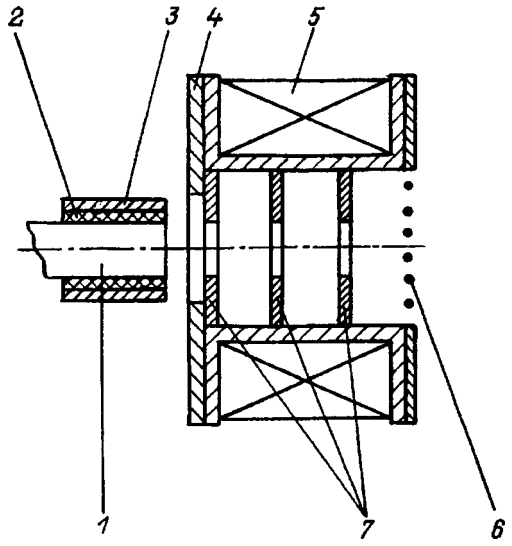

FIG. 1. Schematic of the experimental setup: *1*—cathode, *2*—insulator, *3*—trigger electrode, *4*—anode, *5*—solenoid, *6*—grid, *7*—electrodes of the arc stabilization system.

aperture ion beam sources MEVVA-4 (Ref. 14) and MEEVVA-5 (LBNL).[15] Identical in their principle of operation, these devices have only minor design differences. Measurement of the ion charge-state distribution were realized with the help of a magnetic mass–charge separator (GSI)[16] and a time-of-flight spectrometer (LBNL).[17] In both cases the extracted ions were accelerated by a voltage of 30−60 kV with the help of a three-electrode multi-aperture extraction system.[18] In order to preclude any effects of the duration of the arc pulse, all measurements of the ion charge-state distribution were made 100μs after initiation of the discharge. During the measurements the residual gas pressure in the discharge system and drift tube was kept at a level of 10^{-6} Torr.

EXPERIMENTAL RESULTS

Results of measurements of the ion charge-state distribution in a high magnetic field by two independent methods essentially coincided. This may also be taken as convincing proof of the reliability of the measurements. Therefore, the experimental results presented below are combined results and were confirmed by measurements on both setups.

The ion charge-state distributions under ordinary discharge conditions without a magnetic field are given on the left side of Table I for a wide range of cathode materials. Comparison with previously published data[19] unambiguously reveals essentially complete coincidence of the measured results. Characteristic points of comparison can be, for example, the 100%-fraction of singly charged ions in the carbon plasma or essentially the same fraction of doubly charged ions in the case of a barium cathode. As a rule, the mean charge state of the ions, Q, grows with increase of the atomic mass. Note should also be made of the relatively

TABLE I.

Cathode material	No magnetic field						Magnetic field							Parameters	
	Charge distribution, %													B,	I_{arc},
	1^+	2^+	3^+	4^+	5^+	$\langle Q\rangle$	1^+	2^+	3^+	4^+	5^+	6^+	$\langle Q\rangle$	kGs	kA
C	96	4				1.0	29	58	13				1.8	3.20	3.20
Mg	51	49				1.5	5	95					1.9	3.75	0.22
Al	38	51	11			1.7	5	11	85				2.8	1.20	1.20
Se	23	66	11			1.9	16	53	59	2			2.5	3.75	0.22
Ti	11	76	12	1		2.0	1	6	15	58	20		3.9	10.0	1.30
V	11	72	15	2		2.1	13	31	48	8			2.5	3.75	0.22
Cr	14	70	15	1		2.0	4	9	20	53	12	2	3.7	6.20	0.80
Mn	48	52				1.5	26	47	25	2			2.0	3.75	0.22
Fe	28	68	6			1.8	6	20	34	38	2		3.7	2.20	2.20
Ni	43	50	7			1.6	1	9	19	32	27	12	3.5	3.40	3.44
Co	34	59	7			1.8	5	46	47	2			2.5	6.00	0.40
Cu	28	53	18	1		1.9	10	22	32	32	4		3.0	4.60	0.60
Y	7	63	29	1		2.2	6	9	77	8			2.9	3.75	0.22
Nb	3	40	39	16	2	2.7	–	6	11	29	51	3	4.3	1.20	1.20
Mo	7	30	40	20	3	2.8	–	10	19	32	27	12	4.1	5.40	1.70
Ba	3	97				2.0	2	41	53	3	1		2.6	3.75	0.22
La	4	65	31			2.3	3	16	61	20			3.0	3.75	0.22
Gd	8	81	11			2.0	1	43	41	15			2.7	3.75	0.22
Er	8	62	30			2.2	2	12	70	16			3.0	3.75	0.22
Ag	13	61	25	1		1.9	7	23	37	30	3		3.0	5.40	0.70
Hf	7	26	48	18	1	2.8	1	5	11	39	41	3	4.2	4.60	0.60
Ta	1	17	39	39	4	3.3	1	5	13	40	41	2	4.2	3.75	0.22
W	1	17	35	35	12	3.4	1	5	16	39	32	7	4.2	3.75	0.22
Pt	12	70	18			2.1	1	16	34	46	3		3.3	10.0	1.2
Pb	40	60				1.6	1	75	24				2.2	3.75	0.22
Bi	89	11				1.1	7	27	57	9			2.7	4.60	0.60
U	20	40	32	8		2.3	1	20	32	28	16	3	3.5	4.6	0.60

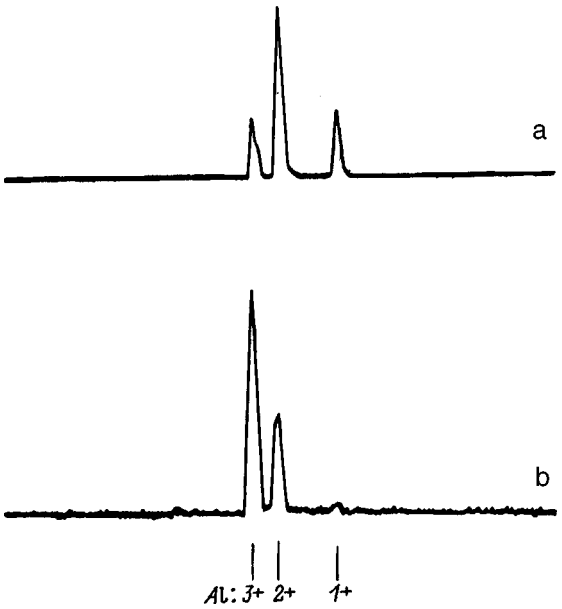

FIG. 2. Oscillograms of collector current of time-of-flight mass-spectrometer; a—$B=0.12$ T, b—$B=0$. Delay of measurement time 100μs relative to onset of current pulse of the arc discharge.

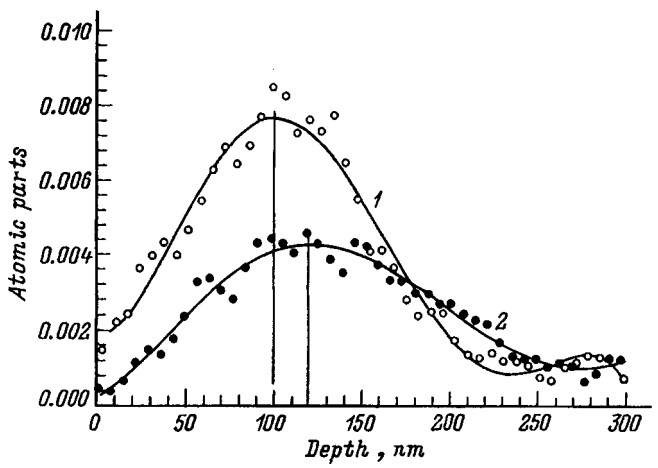

FIG. 3. Depth profile of implanted titanium ions in silicon for ion extraction from plasma; *B*, T: *1*—0, *2*—0.4.

large value of Q (close to three) in the vacuum arc discharge plasma for cathodes of niobium, molybdenum, hafnium, tantalum, tungsten, and uranium.

Creation of a high magnetic field in a vacuum arc discharge plasma leads to a substantial change in the ion charge-state distribution, consisting in an abrupt drop in the fraction of singly and doubly charged ions with a simultaneous noticeable increase in the multiply charged ionic component. This observed experimental fact is illustrated by the current pulses shown in Fig. 2 of the ion collector of the time-of-flight mass-spectrometer in the case of an aluminum cathode. Similar dependences were observed using a magnetic mass–charge separator. Additional evidence of an increase in the mean charge state in a high magnetic field is provided by measurements of the depth profile of implanted titanium ions in silicon, where these ions were extracted from a vacuum arc plasma and accelerated by the same accelerating voltage (55 kV, Fig. 3). It can be seen that in a high magnetic field the position of the maximum of the implanted ion profile is shifted deeper into the silicon surface. This unambiguously indicates an increase in the energy of the ions, which for a constant accelerating voltage can be achieved only by increasing the mean charge state of the extracted ions.

The right side of Table lists the charge-state distributions in a magnetic field. The ion fractions of given charge state shown in the Table were calculated by dividing the ion current of given charge state, measured with a Faraday cup, by that charge state (multiplicity of ionization). This gives information about the actual fraction of ions of the given charge state in the total flux, which is important, for example, for industrial applications associated with ion implantation. It is important to note that in the presence of a high magnetic field noticeable fractions of previously unobserved components (C^{3+}, Ti^{5+}, Cr^{5+}, Ni^{5+}, Ni^{6+}, Mo^{6+}, Ba^{3+}, Ba^{4+}, Pb^{3+}, U^{5+}, etc.) show up in the charge-state spectrum of the ions in a vacuum arc discharge. The fraction of highly charged components is also sharply increased. Thus, without a magnetic field in a vacuum discharge plasma with a uranium cathode quadruply charged ions constitute 8% of the total number of ions in the plasma. In a high magnetic field the fraction of U^{4+} ions grows fourfold. This yields a 30 mA current of quadruply charged uranium ions over a duration of 1 ms (Fig. 4). This result is extraordinarily important for using a vacuum arc discharge to create a high-current metal-ion injector for heavy-ion accelerators.

Increasing the arc current to approximately 1 kA did not affect the ion charge-state distribution. However, at high arc currents increasing the current led to a substantial change in this distribution. Figure 5 plots the fraction of doubly charged aluminum ions as a function of arc current for serial connection of the solenoid to the discharge circuit and without. It can be seen that the influence of the arc current on the variation of the ion fraction of one or another charge state is almost identical to the effect of a magnetic field, but without a magnetic field such an effect takes place at larger current

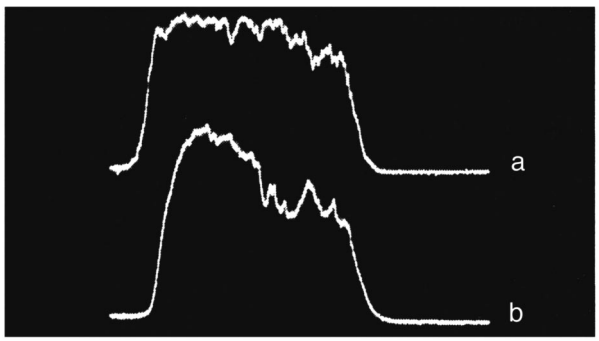

FIG. 4. Oscillograms of the total uranium ion current and its quadruply charged component after separation at $B=0.4$ T, start-up level of oscillograph 0.208 V, delay relative to start-up zero, scanning rate 0.2 ms/cm. a—channel 2, b—channel 1; sensitivity of oscillograph per channel 10 (a), 4 mV/cm (b); current of quadruply charged uranium ions 40 (a), 8 mA/cm (b); load 25 (a), 50Ω (b).

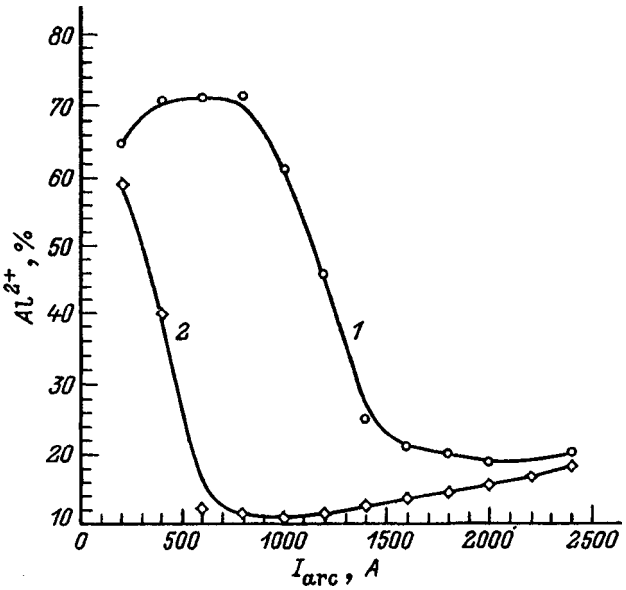

FIG. 5. Percent fraction of doubly charged aluminum ions as a function of arc discharge current: *1*—without solenoid, *2*—with solenoid.

values. Simple estimates indicate that at such current values the magnitude of the self magnetic field of an arc column is on the order of 1 kG and is commensurate with values of the external magnetic field at which it is observed to have an effect on the ion charge-state distribution.

In the experiments we observed a precise correlation between increasing the mean charge state and growth of the arc burning voltage. Thus, at maximum values of the magnetic field and the arc current yielding the largest fraction of highly charged ions the arc burning voltage reached values of 100−120 V and exceeded by five to sixfold the initial value of the arc burning voltage setting up in an arc discharge at relatively low values of the arc current in the absence of a magnetic field. Comparison of the later, set-up value of the arc burning voltage with the ionization potentials showed that to achieve a noticeable fraction with the required ionization multiplicity it is necessary that the arc burning voltage reach a value near the desired ionization potential. Therefore to increase the mean charge state of the ions it is necessary to provide conditions for corresponding growth of the burning voltage. One possible way of increasing the burning voltage is to trigger the arc in a high magnetic field in an extended discharge gap stabilized by a system of flat electrodes with central openings. As experiments have shown, increasing the cathode–anode separation to 10 cm and partitioning it with nine equally spaced electrodes provides an arc burning voltage of 160−180 V in a magnetic field of 0.6 T. Such values of the arc burning voltage will provide further growth of the ionization multiplicity in a vacuum arc discharge and an enhanced mean charge state.

CONCLUSION

The creation of a detailed physical model and the determination of the main mechanism responsible for the ion charge-state distribution in a vacuum arc discharge plasma in a high magnetic field will be the subject of further research. However, it is already evident that growth of the fraction of multiply charged ions is due to an increase in the electron temperature in the plasma. Calculations performed in Refs. 20 and 21 show that to achieve the growth of the mean charge state observed in experiment it is sufficient to increase the electron temperature by 25−30%, or 1−2 eV. Such an increase in the electron temperature is entirely achievable.

The authors assume their customary duty to thank Ian G. Brown, leader of the Plasma Applications Group of Lawrence Berkeley National Laboratory, and the group leaders of the Ion Injector Laboratory of the Association for Heavy Ion Research, Bernhard H. Wolf and Peter Spädtke, for making it possible to carry out measurements of the ion charge-state distribution in a vacuum arc discharge plasma.

This work is being carried out with the support of the Russian Fund for Fundamental Research (Grant No. 96-02-16669).

[1] *Proceedings of the Seventeenth International Symposium on Discharge and Electrical Insulation in Vacuum*. Berkeley, California, 1996. Vol. 1–2.
[2] G. A. Mesyats, *Ectons*, Parts I–III [in Russian] (UIF ''Nauka,'' Ekaterinburg, 1993).
[3] V. I. Rakhovskiĭ, *Physical Principles of Electric Current Switching in Vacuum* [in Russian] (Nauka, Moscow, 1970).
[4] *Abstracts of the Fourth All-Russia Conference on Modification of the Properties of Construction Materials by Charged-Particle Beams* [in Russian], Tomsk, 1996.
[5] I. G. Brown, IEEE Trans. Plasma Sci. **PS-21**, 537 (1993).
[6] W. D. Davis and H. C. Miller, J. Appl. Phys. **40**, 2212 (1969).
[7] I. G. Brown, B. Feinberg, and J. E. Galvin, J. Appl. Phys. **63**, 4889 (1988).
[8] A. Anders, S. Anders, B. Jüttner, and I. G. Brown, IEEE Trans. Plasma Sci. **PS-21**, 305 (1993).
[9] P. Spaedtke, H. Emig, B. H. Wolf, E. Oks, Rev. Sci. Instrum. **65**, 3113 (1994).
[10] J. M. Lafferty (Ed.), *Vacuum Arcs: Theory and Application* (Wiley, New York, 1980; Mir, Moscow, 1982).
[11] S. Anders and A. Anders, J. Phys. D **21**, 213 (1988).
[12] A. Anders, S. Anders, A. Forster, I. G. Brown, Plasma Sources Sci. Technol. **1**, 263 (1992).
[13] V. I. Davydenko, G. I. Dimov, I. I. Morozov, and G. V. Roslyakov, Zh. Tekh. Fiz. **53**, 258 (1983) [Sov. Phys. Tech. Phys. **28**, 160 (1983)].
[14] B. H. Wolf, H. Emig, P. Spaedtke, and D. Ruck, Rev. Sci. Instrum. **65**, 3091 (1994).
[15] I. G. Brown, Rev. Sci. Instrum. **65**, 3061 (1994).
[16] I. G. Brown, P. Spaedtke, H. Emig *et al.*, Nucl. Instrum. Methods A **295**, 12 (1990).
[17] I. G. Brown, J. E. Galvin, R. A. MacGill, and R. T. Wright, Rev. Sci. Instrum. **58**, 1589 (1987).
[18] E. Oks, P. Spaedtke, H. Emig, and B. H. Wolf, Rev. Sci. Instrum. **65**, 3109 (1994).
[19] I. G. Brown and X. Godechot, IEEE Trans. Plasma Sci. **PS-19**, 713 (1991).
[20] E. Oks, A. Anders, I. G. Brown, *et al.*, IEEE Trans. Plasma Sci. **PS-24**, 1174 (1996).
[21] A. Anders, Preprint N LBL 38672. UC-427, University of California, Berkeley, 1996.

Translated by Paul F. Schippnick

Choosing an adequate mathematical model in problems with high pulsed energy deposition

T. A. Andreeva and S. N. Kolgatin

St. Petersburg State Technical University, 195251 St. Petersburg, Russia

K. V. Khishchenko

Scientific-Research Center of Thermal Physics of Pulsed Actions, 111250 Moscow, Russia
(Submitted January 15, 1997; resubmitted September 30, 1997)
Zh. Tekh. Fiz. **68**, 44–47 (May 1998)

The problems of choosing the optimal mathematical model for a prescribed range of parameters of a pulsed action are discussed. A preliminary analysis performed by similarity and dimensional-analysis methods using interpolation equations of state of the matter shows that the complete system of equations of gasdynamics can be simplified by dropping individual terms which are not important in a given parameter range. The results of an analysis are presented in the form of nomograms, which also make it possible to identify the class of fast and energy-intensive gasdynamic processes more accurately than at an intuitive level. © *1998 American Institute of Physics.* [S1063-7842(98)00805-8]

It is well known that a simple mathematical model of a process is more convenient to study than a complicated one. A simple model is easier to study, contains fewer parameters, can sometimes be solved analytically, and so on. In the present paper we shall discuss pulsed (characteristic time $\tau_0 < 10$ ms) and quite powerful (increases in the specific internal energy ε by an amount one or more orders of magnitude greater than the heat of sublimation λ) processes of energy deposition in a material. Such processes occur when charged-particle or radiation beams impinge against a solid wall, in powerful electric discharges in condensed media, and in explosions of different physical nature. Since such problems are of practical importance, it is important to give some a priori recommendations on choosing a mathematical model of such processes, for example, whether or not the spatial nonuniformity of the pressure should be taken into account, whether or not heat conduction should be taken into consideration, and how important transfer processes between phases at interfaces are. These questions can be solved completely when the characteristics of the thermophysical properties of real media are taken into account correctly.

To investigate in the one-dimensional approximation processes in the class of interest we shall employ the system of gasdynamic equations that, after the Euler coordinate x is replaced by the Lagrangian variable

$$s=\int_0^x \rho(\xi)\,d\xi$$

(ρ is the density) can be written in the following form:

$$\frac{\partial(1/\rho)}{\partial t}=\frac{\partial v}{\partial s}, \tag{1}$$

$$\frac{\partial s}{\partial t}=v, \tag{2}$$

$$\frac{\partial v}{\partial t}=-\frac{\partial p}{\partial s}, \tag{3}$$

$$\frac{\partial \varepsilon}{\partial t}=-p\frac{\partial v}{\partial s}-\frac{\partial W}{\partial s}+Q(s,t), \tag{4}$$

$$p=f_p(\rho,T), \tag{5}$$

$$\varepsilon=f_\varepsilon(\rho,T), \tag{6}$$

$$W=-\kappa\frac{\partial T}{\partial s}, \tag{7}$$

$$\kappa=\rho\cdot f_\lambda(\rho,T). \tag{8}$$

Here t is the time, v is the velocity, p and ε are, respectively, the pressure and specific internal energy, W is the heat flux due to heat conduction, Q is the specific energy release, κ and λ are, respectively, the mass and standard thermal conductivities, and f_p, f_s, and $f_\lambda(\rho,T)$ are, respectively, the functional dependences of p, ε, and λ as given by the equation of state and model of heat conduction which are adopted for the material.

We choose as the independent scaling parameters ρ_*, T_*, p_*, and x_*. Then the scaling parameters for the remaining variables are

$$s_*=\rho_*\cdot x_*, \quad \varepsilon_*=p_*/\rho_*, \quad v_*=\sqrt{\frac{p_*}{\rho_*}},$$

$$t_*=x_*\sqrt{\frac{\rho_*}{p_*}}, \quad Q_*=\frac{1}{x_*}\left(\frac{p_*}{\rho_*}\right)^{3/2}, \quad \kappa_*=\frac{p_*\rho_* x_*^2}{t_* T_*}.$$

The scaling parameters presented above describe the character of the gasdynamic behavior of the medium. These scaling parameters should be compared with the parameters of the problem at hand, which include, first and foremost, τ_0 — the duration of the pulse (or characteristic time of energy

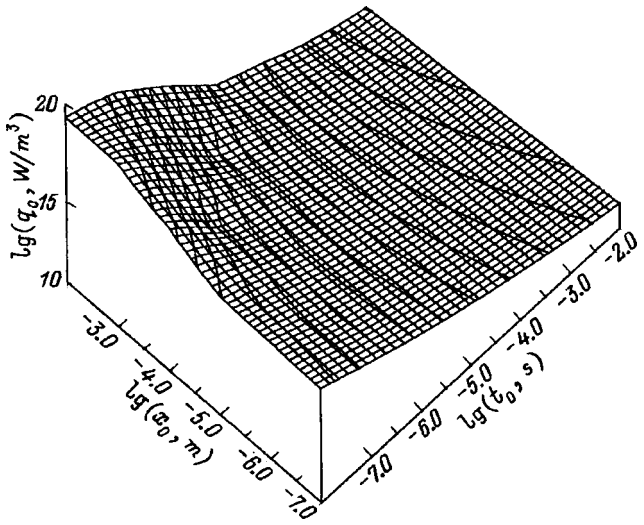

FIG. 1. Suddenness criterion.

deposition), $Q_0=q_0/\rho_*$ — the characteristic intensity of energy deposition per unit mass (q_0 is the same per unit volume), and Λ_0 is the specific heat of sublimation of the material from the initial state (its value is close to the heat of vaporization). So, dividing τ_0 by t_0 we obtain a suddenness criterion

$$K_M=\frac{\tau_0}{t_*}=\frac{\tau_0}{x_*}\sqrt{\frac{p_*}{\rho_*}}. \tag{9}$$

The case $K_M \ll 1$ corresponds to quite rapid energy deposition, when the absorption of energy and the gasdynamic unloading of the heated region (of characteristic size x_*), where the pressure at the end of the pulse reaches values of the order of $p_{\max}\simeq\gamma\rho\varepsilon\approx\gamma\rho Q$ (γ is the Gruneisen constant), can be separated in time. As an example of an analytical analysis of the problem of instantaneous heat release we call attention to Ref. 1.

In the opposite case, $K_M \gg 1$, there is enough time for waves of unloading to traverse repeatedly the heated region during the time the perturbation acts on the medium and energy absorption occurs practically at constant pressure with no formation of discontinuous flows of the shock-wave type.

The case $K_M \sim 1$ is more complicated. In this case the energy deposition and gasdynamic relaxation processes cannot be separated: It is necessary to solve the momentum conservation equation (3), which, as a rule, it is impossible to do in an analytical form. Integrating the closed system of equations (1)–(8) numerically it is not difficult to estimate the suddenness criterion, for example, for prescribed characteristic process duration t_u, length scale x_0, and volume energy deposition q_0. Figure 1 displays the computational results obtained for the surface $K_M=1$ for copper using a wide-range multiphase equation of state.[2] An instantaneous energy deposition regime obtains in the region beneath the surface; far above the surface it can be assumed that the corresponding processes occur at a constant (along the coordinate x) pressure.

The following temporal parameter characterizing the thermal conductivity can be constructed from the scaling parameters:

$$\tau_T=\frac{p_*\rho_*x_*^2}{\kappa_*T_*}. \tag{10}$$

This is essentially the ratio of the squared characteristic length to the effective thermal diffusivity

$$a_*=\frac{\lambda_*}{\varepsilon_*/T_*},$$

where $\lambda_*=\kappa_*/\rho_*$ is the scale parameter for the thermal conductivity λ.

Comparing τ_T with t_*, we obtain a heat conduction criterion

$$K_T=\frac{t_*}{\tau_T}=\frac{\lambda_*T_*\rho_*^{1/2}}{x_*p_*^{3/2}}. \tag{11}$$

This criterion shows how gasdynamic relaxation and heat propagation are related. It can also be expressed as

$$K_T=\left(\frac{V_T}{C_*}\right)^3,$$

where $C_*=\sqrt{p_*/\rho_*}$ is the characteristic sound velocity, the rate at which pressure relaxes, and

$$V_T=\sqrt[3]{\frac{\lambda_*T_*}{\rho_*x_*}}$$

is the scaling parameter for the propagation velocity of the temperature-equalizing heat wave.

The regime $K_T \ll 1$ can be called purely gasdynamic. In this case the gasdynamic processes (i.e., passage of shock waves and pressure equalization) unfold much more quickly than heat propagation by means of heat conduction. In consequence, the term $\partial W/\partial s$ in Eq. (4) can be neglected.

The regime $K_T \gg 1$ corresponds to rapid heat transfer, when pressure and density equalization lag substantially behind the temperature. A simple numerical analysis shows that this case can occur only for radiant heat conduction.[3] Gasdynamic relaxation of the medium in this case proceeds isothermally.

The most complicated regime requiring a complete analysis arises when $K_T \sim 1$. In this case the gasdynamic and heat-conduction processes cannot be separated and the corresponding equations must be solved simultaneously.

To estimate K_T it is necessary to know the radiative component of heat conduction. It can be taken into account by the following simple method. It is known[3] that radiant heat conduction occurs when the size x_* of the region of energy deposition becomes much greater than the characteristic photon mean free path l_0. The latter quantity in turn can be estimated using the formulas for hydrogen-like atoms.[3]

The main energy losses are observed in the continuous radiation spectrum. It is necessary to take account of the fact that electron bremsstrahlung in the Coulomb field of an ion gives rise to photon absorption. The photon mean free path as a result of this process is[3]

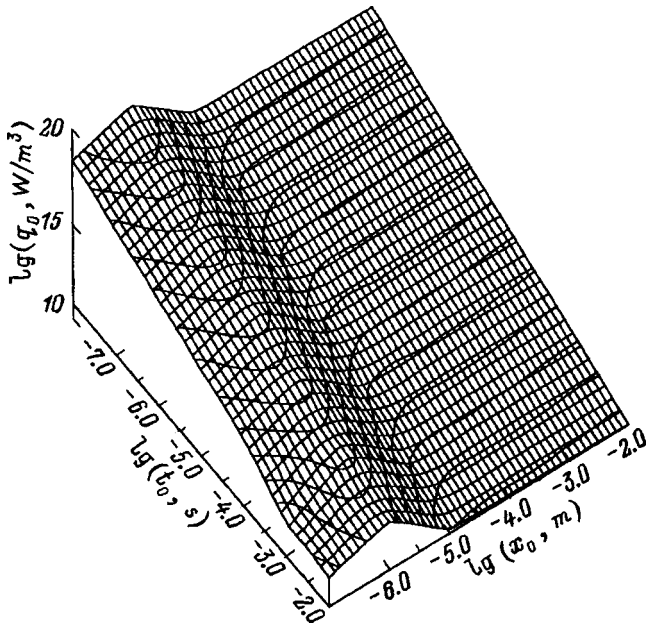

FIG. 2. Heat conduction criterion.

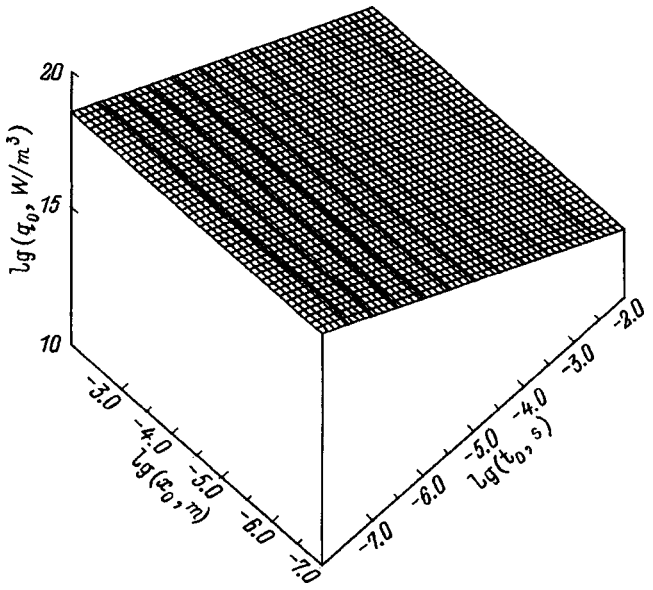

FIG. 3. Regime criterion.

$$l_1 = 4.8\times 10^{24}\frac{T^{1/2}}{Z^2 N_+ N_e}(\text{cm}), \tag{12}$$

where T is the temperature (in K), Z is the ion charge, and N_e and N_+ are, respectively, the electron and ion densities (cm^{-3}).

Next, for estimates we neglect the less likely process of free-bound electron capture with emission of a photon in the first-ionization region. Then at high temperatures (above 50000 K) and at the onset of multiple ionization the photon mean free path length is given by[3]

$$l_2 = 4.4\times 10^{22}\frac{T^{1/2}}{N^2\bar{m}(\bar{m}+1)^2}(\text{cm}), \tag{13}$$

where $\bar{m}$ is the average charge of a hydrogen-like ion, $\bar{x}_1 = \bar{I}/kT$ is the reduced average degree of ionization, and for low degrees of ionization $l_2 >> l_1$.

We now select the smallest of the quantities (12) and (13) as follows:

$$\frac{1}{l_0} = \frac{1}{l_1} + \frac{1}{l_2}.$$

The radiative thermal conductivity λ_R is determined in terms of the characteristic photon mean free path l_0 as

$$\lambda_R = \frac{16}{3}\sigma_{\text{St}} l_0 T^3, \tag{14}$$

where σ_{St} is the Stefan–Boltzmann constant; for $l_0 > x_*$ we can set $\lambda_R = 0$.

To estimate the effect of the thermal conductivity it is sufficient to add $\lambda = \lambda_R + \lambda_e$, where λ_e is the standard (electronic) thermal conductivity.[4] The corresponding result obtained by solving the system of equations (1)–(8) is shown in Fig. 2. The surface where $K_T = 1$ is distinguished. Below this surface heat conduction is not important over characteristic gasdynamic times. Above the surface the temperature in the heated region can be assumed to be approximately constant.

Finally, an important parameter for the problems that we are studying is the characteristic time at which the material starts to fly apart:

$$\tau_p = \frac{\Lambda}{Q_0}. \tag{15}$$

Dividing by this quantity the duration of the physical process of interest we obtain the regime criterion

$$K_P = \frac{\tau_0}{\tau_p} = \frac{\tau_0 Q_0}{\Lambda}. \tag{16}$$

The regime criterion actually shows how complicated the equation of state must be when investigating any problem. For $K_P \ll 1$ the process occurs without formation of a phase boundary at all. Such problems can be solved in the thermoelasticity approximation; they do not require a complicated thermodynamic model. An example of such a problem that can be solved analytically is the action of a defocused relativistic electron beam on an aluminum target.[5] For $K_P \gg 1$ the material passes very quickly into the gas (or plasma) phase. In most cases, when the details of the development of this process at the initial stage are of no interest, phase transitions can be neglected and a simplified equation of state can be used. The variant where $K_P \sim 1$ is one of the most complicated cases. In this case the equation of state must describe condensed and gaseous states as well as the transitional region (see Ref. 3 for a more detailed discussion). Interphase transfer will play a large role in these processes. The surface $K_P = 1$, which separates processes according to the regime criterion, is displayed in Fig. 3.

In summary, our analysis has shown that the system of gasdynamic equations for a specific range of initial parameters can be substantially simplified on the basis of preliminary estimates.

[1] L. A. Kalmykova, V. N. Kondrat'ev, and I. V. Nemchinov, Prikl. Mekh. Tekh. Fiz. **5**, 2 (1966).
[2] A. V. Bushman, G. I. Kanel', A. L. Ni, and V. E. Fortov, *Thermophysics and Dynamics of Intense Pulsed Actions* [in Russian], OIKhF AN SSSR, Chernogolovka, 1988, pp. 200.
[3] Ya. B. Zel'dovich and Yu. P. Raĭzer, *Physics of Shock Waves and High-Temperature Hydrodynamic Phenomena*, Academic Press, New York, Vol. 1, 1966; Vol. 2, 1967 [Russian original, Nauka, Moscow, 1966, pp. 686].
[4] I. M. Bespalov and A. Ya. Polishchuk, ''Methods of calculation of transport coeffecients of plasmas over a wide range of parameters'' [in Russian], IVTAN Preprint No. 1-257, Institute of High Temperatures, Russian Academy of Sciences, Moscow, 1988.
[5] S. N. Kolgatin, A. M. Stepanov, and A. V. Khachatur'yants, Vopr. At. Nauk Tekh. Ser. Termoyad. Sintez (Kharkov), No. 2(10), pp. 87–91 (1982).

Translated by M. E. Alferieff

Characteristics of a multielectrode corona discharge in the working media of periodic-pulse XeCl* and KrCl* lasers

A. K. Shuaibov

Uzhgorod State University, 294000 Uzhgorod, Ukraine
(Submitted March 3, 1997)
Zh. Tekh. Fiz. **68**, 48–51 (May 1998)

Results are reported from an investigation of the electrical and optical characteristics of a multielectrode negative-polarity corona discharge in He/Xe(Kr)/CCl_4 mixtures, which are used as the working media in inert-gas chloride lasers operating in the periodic-pulse mode. The corona discharge is studied in a needle–grid electrode system which is approximately as long as the active medium in a laser. Such a corona discharge is of interest for use in electrical modules for blowing the working media through XeCl* and KrCl* lasers, the working media of which contain vapors of liquid hydrocarbons of the CCl_4 type. © *1998 American Institute of Physics.* [S1063-7842(98)00905-2]

INTRODUCTION

Inert-gas chloride (RCl*) electric-discharge lasers with working mixtures containing the complex chlorine-containing molecules[1–4] BCl_3 and CCl_4, have superior energy and lifetime characteristics in some operating regimes as compared to the case when hydrogen chloride molecules are used. The mechanical systems employed in this case for the transverse blow-through of the working mixtures are characterized by high energy consumption, vibration, and noise, in addition to introducing contaminants into the working mixture.

In periodic-pulse XeCl* lasers operating on a He/Xe/HCl mixture with repetition frequencies $f \leqslant 70$ Hz it is possible to use electrical blowing, with an average transverse flow velocity of the gas mixture $\leqslant 3$ m/s.[5] For hot, corrosive, high-pressure gas mixtures this method of change-out, which utilizes a multielectrode corona discharge (CD) uniformly distributed along the length of the transverse discharge of a periodic-pulse excimer laser, is free of some of the drawbacks of mechanical blowers.

The results of an investigation of some characteristics of such a corona discharge in the working media of electric-discharge RCl* lasers where HCl molecules are used as the chlorine carrier, are reported in Ref. 6.

The present paper reports the results of an investigation of the characteristics of a multielectrode CD in the mixtures He/Kr(Xe)/CCl_4. The discharge is ignited in a system of needle–grid electrodes and is intended for use in the emitters of miniature periodic-pulse RCl* lasers through which the working medium is blown electrically.

EXPERIMENTAL PROCEDURE

The CD was ignited in a stainless steel high-pressure discharge chamber. The system of electrodes for the CD was placed on the dielectric flange of the discharge chamber and consisted of one row of needles and a nickel grid. The system of electrodes was 12 cm long, and the distance between the needle points and the grid was equal to 2 cm. The radius of curvature of a needle point was equal to 0.5 mm, and the diameter of the grid wires was equal to 0.3 mm. A negative dc voltage ($U \leqslant 12$ kV, $I_{mid} \leqslant 15$ mA) was applied to the needles through an external limiting resistance. The electrical and optical characteristics of the CD were measured with the registering system described in Refs. 6 and 7. The optical investigations of the plasma radiation were performed with a full view of the entire interelectrode gap through the input slit of the monochromator. Control experiments showed that hot zones near the needle points make the main contribution to the plasma radiation. Therefore it can be assumed, to within 5–10%, that the characteristics of the hot zones of a CD are being investigated.

In the present experiments a multielectrode CD was observed in the form of bright hot zones (near the needle points), very small hot zones at the grid, and a dark or weakly-luminescing exterior region of the CD between the needles and the grid.

ELECTRICAL CHARACTERISTICS

Compared with similar CDs in binary mixtures (no additives consisting of chlorine-containing molecules), in the media investigated there is no intense glow discharge in the exterior region and the maximum discharge current at the noncontracted stage is one to two orders of magnitude lower. The CD current in this case is determined not by the magnitude of the ballast resistance but rather by the density of electronegative molecules in the mixture.[6] When the voltage on the needles exceeds a definite, critical value, the CD contracts. This is manifested as the formation of an anodic streamer near one of the needles.

The average current-voltage characteristics (AIVCs) of CDs in mixtures of inert gases with CCl_4 molecules are presented in Fig. 1. The AIVCs obtained cannot be described by relations of the type $I = \alpha(U - U_0)^2$ (where α is a constant and U_0 is the discharge ignition voltage), which are most typical for CDs.[8] Two different stages of the CD, character-

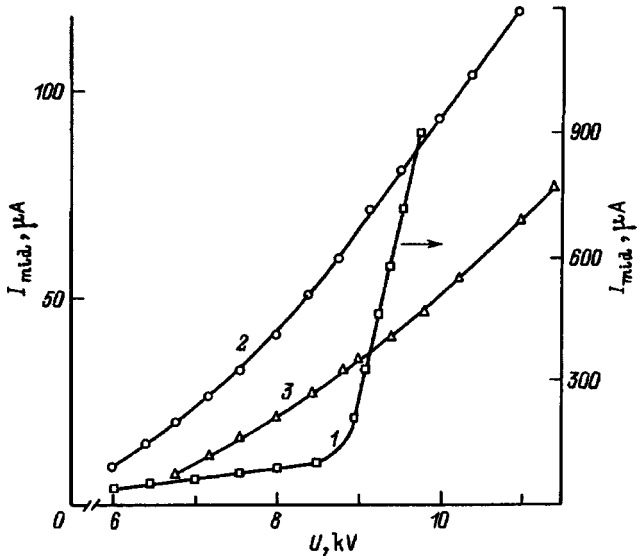

FIG. 1. Current–voltage characteristics of a negative corona discharge in mixtures of inert gases with CCl_4 molecules. *1*—He/CCl_4=220/0.13 kPa; *2*—He/He/CCL_4=220/2, 8/0, 13 kPa; *3*—He/Kr/CCl_4=220/16/0, 13 kPa.

ized by their own threshold voltages and CD current growth rates, can be seen in the AIVCs of a CD in the mixture He/CCl_4. These stages are distinguished by linear dependences of the type $I_{mid}=\beta(U-U_0)$. The values of U_0 and β for the low- and high-current stages of a CD in the mixture He/CCl_4 are, respectively, $U_0^1=5.5$ kV, $\beta^1=50$ μA/kV, and $U_0^2=8.75$ kV, $\beta^2=1000$ μA/kV. Only a low-current stage was observed in ternary mixtures, and in this case the AIVC was more linear.

The differences of the AIVCs obtained here from the typical AIVCs for CDs are due to nonlinearities of CDs in inert gases.[9] Thus, in the present media it is possible to obtain a discharge whose properties fall between coronal and glow discharges. In contrast to the AIVCs of CDs in the mixtures He/Kr(Xe), the AIVCs show virtually no hysteresis, possibly because of quenching of the metastable atoms $R(m)$ by the halogen-containing molecules.[10,11]

The velocity at which the gases are blown through the CD goes as $v\sim I^{1/2}$ (Ref. 12), so that it will be higher in xenon-containing media with the minimum content of CCl_4 molecules. It is undesirable to increase the CCl_4 content above 0.13 kPa because the operating efficiency of the excimer laser decreases.[3,4] As the pressure of a ternary mixture decreases to 100 kPa, the voltage range of where a stable CD exists decreases, while the CD current increases by a factor of 1.5. The dependences $I_{mid}=f(U)$ become quadratic.

Figure 2 shows the shape of the CD current pulse and the dependence of the pulse repetition frequency on the voltage applied to the needles. For a CD in ternary mixtures the current pulse duration at half height equals 0.3–0.5 μs. The CD current pulses were observed against a dc background. As one can see from Fig. 2b, the current pulses of a CD in ternary mixtures appear only at the precontraction stage of the discharge and their repetition frequency, just as in media based on HCl molecules,[6] reaches 30–40 kHz. For a CD in a binary mixture the current pulses reached 1.5 μs and were

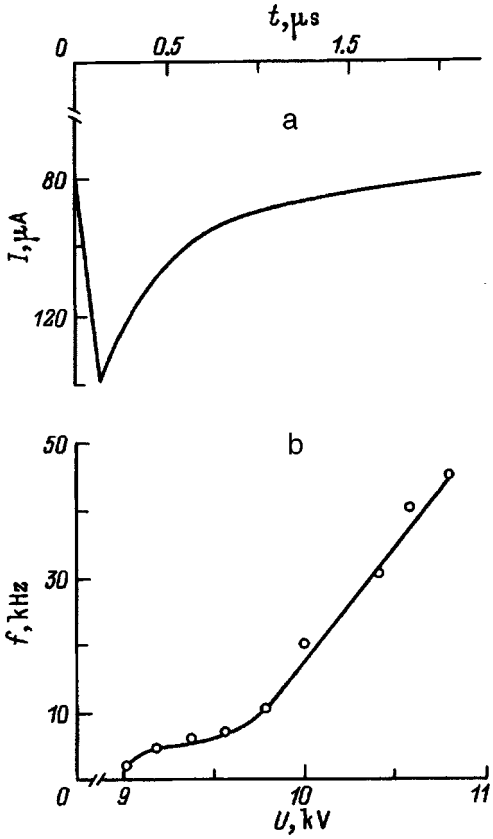

FIG. 2. Form of the current pulses (a) and dependence of the pulse repetition frequency on the voltage applied to the needles (b) for a CD in the mixture He/Xe/CCl_4=220/2, 8/0, 13 kPa.

observed only in the region $\Delta U=6-8$ kV, while at the high-current stage of the CD the current was continuous.

OPTICAL CHARACTERISTICS

The plasma emission spectra of the hot zones of a CD in binary and ternary mixtures are displayed in Fig. 3. For a CD in the mixture He/CCl_4, the formation of Cl_2^* molecules (λ 258 nm) and CCl* radicals (λ 278 nm) is observed in the UV region of the spectrum. The most intense band is the Cl_2 emission band. The continuum in the region λλ 450–850 nm due to the decomposition of CCl_3 or C_2Cl_4 radicals, which

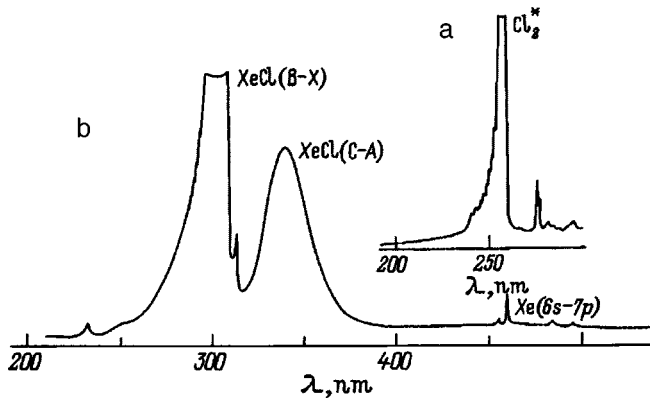

FIG. 3. Plasma emission spectra of a CD in the mixtures He/CCl_4 (a) and He/Xe/CCl_4 (b).

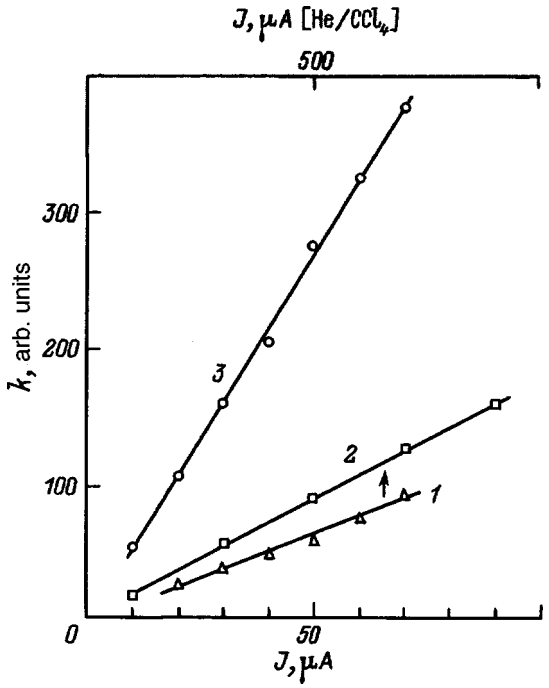

FIG. 4. Relative intensity of the emission bands of molecules versus the average CD current. *1* — λ = 258 nm Cl_2^*, He/CCl_4; *2*—308 nm XeCl ($B-X$), He/Xe/Ccl_4; *3*—λ = 222 nm KrCl ($B-X$), He/Kr/CCl_4.

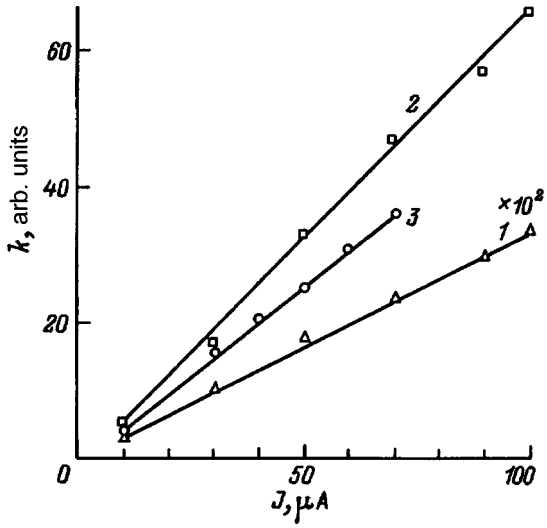

FIG. 5. Relative intensity of Xe* and Kr* emission lines versus the average CD current. *1*—λ = 467 nm Xe ($6s-7p$); *2*—λ = 823 nm Xe ($6s-6p$); *3*—λ = 810 nm Kr ($5s-5p$).

have been observed[13,14] in a low-pressure dc discharge, is absent. According to the data of Ref. 13, predominantly the radicals CCl_2, CCl_3, and Cl_2^* and atoms Cl* form in the primary electron-induced decomposition reactions of CCl_4 molecules, while the radicals CCl* form as a result of secondary reactions. The low intensity of the CCl* emission band (as compared with Cl_2^* radiation) is due to the rapid reactions leading to its annihilation in collisions with other radicals or Cl_2^* molecules.

Investigation of the panoramic spectra of a CD plasma in a ternary mixture (Fig. 3b) in the range λλ 200–1000 nm showed that the main bands are the emission bands λ 308 nm XeCl ($B-X$), λ 222 nm KrCl ($B-X$) and the weaker, wide bands λ 330 nm XeCl ($C-A$) and λ 230 nm KrCl ($C-A$). The most intense emission lines in the near-IR and visible regions of the spectrum were observed on the transitions Kr ($5s-6p$, $5p$) and Xe ($6s-7p$, $6p$). Emission lines from states lying above the first vibrational state of the molecular ions R_2^+ and excited ions of heavy inert gases were absent.

This character of the intensity distribution in the emission line spectrum could be due to population of p states of Kr and Xe atoms in dissociative-recombination reactions[15] and as a result of excitation by electron impact.[16,17]

Typical curves showing the average intensities of the radiation in molecular bands and in the lines of Kr and Xe atoms as a function of the average CD current are displayed in Figs. 4 and 5. These curves are all linear. The excimer molecules KrCl (B) are formed most efficiently from the molecules and the molecules Cl_2^* are formed least efficiently. The emission intensity on the transitions Xe ($6s-6p$) and Kr ($5s-5p$) is more than two orders of magnitude higher than that from higher-lying states (Fig. 5). The emission intensity from Xe and Kr atoms in IR transitions in CDs in the mixtures He/Xe(Kr) (comparable in magnitude to those presented in Fig. 5) was obtained in pure inert gases only with average CD currents of 1 mA. The CD current was mainly continuous. This shows that in CDs in ternary mixtures Xe ($6s$) and Kr ($5s$) metastables are efficiently removed by collisions. The quench rate constants for Xe ($6p$) by CCl_4 molecules lies in the range $(7.3-7.8)\times10^{-10}$ cm^3/s, while for Xe ($6s$) metastables the quench rate equals 6.3×10^{-10} cm^3/s (Ref. 11).

The plasma in the hot zone of a CD is strongly enriched with metastable inert-gas atoms. This is due to the specific form of the electron energy distribution function in the CD: The distribution is clipped at high energies. The ion density in the CD is much lower than the density of metastable atoms and atoms excited into low-lying energy levels.[18] For this reason, the predominant reaction leading to the formation of excimer molecules in the hot zones of the CD could be the ''harpoon'' reaction

$$R(np,ns)+CCl_4\rightarrow RCl(B,C)+CCl_3. \quad (1)$$

For xenon atoms the branching ratio for the reaction in which Xe ($6p,6s$) is quenched by CCl_4 molecules and XeCl (B,C) is formed in a process with participation of Xe ($6p$) is much higher ($0.6-0.7$) than for Xe ($6s$) (0.24). The formation of an excimer molecule in a ''harpoon'' reaction also indirectly confirms that the dependences of the emission intensity in the XeCl ($B-X$) band and Xe ($6s-6p$) transition lines are of the same character.

The increase in RCl* emission intensity during operation of a discharge apparatus operating on mixtures of inert gases and CCl_4 molecules that is characteristic for a pulsed transverse discharge is not observed in a CD. This is due to the fact that CCl_4 molecules in the plasma of RCl* lasers do not participate directly in the formation of excimer molecules. The reaction leading to the decomposition of CCl_4 occurs first:

$$CCl_4 + H_2 + \eta\nu \rightarrow 2HCl + Cl_2, \quad (2)$$

after which excimer molecules are formed according to the kinetic chain of RCl* lasers operating on working media to which HCl molecules are added.[3]

CONCLUSIONS

Our investigation of the characteristics of a multielectrode corona discharge in the working media of periodic-pulse lasers operating on inert-gas chlorides showed that it is characterized by low energy consumption ($W \leqslant 1$ W) and it is stably ignited in mixtures of the type He/Xe(Kr)/CCl_4. The discharge current and the rate at which the gas mixtures are blown through the system are limited by the development of an instability when the voltage on the needles is high. To increase the blow-through rate it is necessary to use CCl_4-depleted gaseous media and several blower modules connected in parallel. The electrical characteristics and the form of the CD are largely determined by the electron attachment to CCl_4 molecules and the mobility of the corresponding negative ions. Excimer molecules in the hot zones of the CD can form predominantly in direct ''harpoon'' reactions with the participation of CCl_4 molecules and Xe $(6p,6s)$ and Kr $(5p, 5s)$ atoms. CCl_4 molecules efficiently depopulate the metastable states of Xe and Kr atoms and increase the intensity in IR transitions Xe $(6s-6p)$ and Kr $(5s-5p)$.

[1] V. E. Peet, A. B. Treshalov, and E. B. Slivinski, Appl. Phys. B **52**, 234 (1991).
[2] A. N. Malinin, L. L. Shimon, V. M. Dobosh, and B. Ya. Khomyak, Kvant. Elektron. (Moscow) **21**, 1174 (1994).
[3] R. Salimbeni, M. Matera, M. Vannini, and P. Burlamachi, Opt. Commun. **39**, 75 (1981).
[4] A. Luches, V. Nassisi, and M. R. Perrone, Opt. Commun. **51**, 315 (1984).
[5] A. I. Baranov, K. V. Gurkov, M. I. Lomaev, Prib. Tekh. Éksp., No. 4, 108 (1994).
[6] A. K. Shaibov, L. L. Shimon, and I. V. Shevera, Kvant. Elektron. (Moscow) **24**, No. 2 (1997).
[7] A. K. Shuaibov, A. I. Minya, V. V. Zvenigorodskiĭ, and V. S. Shevera, Pis'ma Zh. Tekh. Fiz. **22**(13), 73 (1996) [Tech. Phys. Lett. **22**, 551 (1996)].
[8] P. L. Henson, J. Appl. Phys. **52**, 709 (1981).
[9] A. A. Belevtsev *et al.*, in *Abstracts the 4th All-Union Conference on the Physics of Gas Discharges* [in Russian], DGU, Makhachkala, 1988, Pt. 1, pp. 15–16.
[10] J. E. Velazco, J. H. Kolts, and D. W. Setser, J. Chem. Phys. **65**, 3468 (1976).
[11] J. K. Ku and D. W. Setser, Appl. Phys. Lett. **48**, 689 (1986).
[12] I. P. Vereshchagin, *Corona Discharge in the Devices of Electron–Ion Technology* [in Russian], Énergoatomizdat, Moscow, 1985.
[13] Yu. S. Kravchenko, V. S. Osadchuk, D. I. Slovetskiĭ, and V. N. Korovyanko, Khim. Vys. Énerg. **23**, 444 (1989).
[14] Yu. S. Kravchenko, V. S. Osadchuk, D. I. Slovetskiĭ, and S. V. Taranov, Khim. Vys. Énerg. **23**, 539 (1989).
[15] V. A. Ivanov, Usp. Fiz. Nauk **162**, 35 (1992) [Sov. Phys. Usp. **35**, 17 (1992)].
[16] P. V. Fel'tsman and I. P. Zapesochnyĭ, Ukr. Fiz. Zh. **13**, 205 (1968).
[17] N. J. Mason and W. R. Nevel, J. Phys. B **20**, 1357 (1987).
[18] V. D. Peskov, Zh. Tekh. Fiz. **45**, 2544 (1975) [Sov. Phys. Tech. Phys. **20**, 1584 (1975)].

Translated by M. E. Alferieff

Features of the $\alpha-\gamma$ transition in a low-pressure rf argon discharge

V. A. Lisovskiĭ

Kharkov State University, 310077 Kharkov, Ukraine
(Submitted December 9, 1996)
Zh. Tekh. Fiz. **68**, 52–60 (May 1998)

It is found that the region for the stable existence of the α regime of a radio-frequency (rf) discharge is bounded not only on the moderate-pressure side, but also on the low-pressure side. One feature of the $\alpha-\gamma$ transition in a low-pressure rf discharge is that the criterion for breakdown of the electrode sheath is not satisfied. It is shown that at low pressures the $\alpha-\gamma$ transition of an rf argon discharge takes place abruptly and exhibits hysteresis. At intermediate pressures the $\alpha-\gamma$ transition is continuous and lacks jumps; negative differential conductivity appears, double layers form, and nonmonotonic behavior of the plasma density is observed at the center of the discharge. The role of stochastic (collisionless) electron heating in sustaining an rf discharge at intermediate gas pressures is discussed. © *1998 American Institute of Physics.* [S1063-7842(98)01005-8]

INTRODUCTION

Industrial plasma processes which employ radio-frequency (rf) capacitive gas discharges play a major role in the production of microcircuits (etching of semiconductor substrates) and in modifying the surfaces of materials (the deposition of oxide and diamond-like thin films).[1,2] Radio-frequency discharges are also often used to pump gas lasers.[3,4] Therefore, the experimental investigation of the characteristics of rf discharges is of great importance. As we know,[4–6] an rf discharge can burn in two different regimes: a low-current (α) regime and a high-current (γ) regime. In the α regime electrons acquire energy for ionizing gas atoms in the rf field in a quasineutral plasma, and the emission of electrons from the electrode surfaces does not play a major role in sustaining the discharge. The conductivity of the electrode sheaths is small, and the circuit between the plasma and the electrodes is closed mainly by the bias current. In the γ regime electron avalanches develop in the electrode sheaths, ionization of the gas atoms by electron impact takes place mainly near the boundaries between the electrode sheaths and the quasineutral plasma, and the emission of electrons from the electrode surfaces has a significant influence on the electron multiplication process and on sustaining the discharge.[4–15] The electrode sheaths have considerable conductivity in the γ regime, and their characteristics are similar to those of the cathode sheath of a dc glow discharge. The experiments in Refs. 6, 11, and 14 and the numerical calculations in 8 show that an rf discharge passes abruptly from the α regime into the γ regime at moderate pressures and that the plasma density in the discharge volume and the amplitude of the rf current increase severalfold. At moderate gas pressures the $\alpha-\gamma$ transition is accompanied by complete reorganization of the spatial structure of an rf discharge (while the plasma density reaches a maximum at the center of the discharge in the α regime, in the γ regime plasma-density maxima are observed near the boundaries between the electrode sheath and quasineutral plasma, and a minimum is observed in the central portion of the discharge with an axial distribution of the plasma density). At intermediate pressures ($p\sim 1$ Torr) an rf discharge passes smoothly from the α form to the γ form without abrupt jumps.[7,9,16–19] In addition, when the distance between the electrodes is sufficiently large (>1 cm), rf discharges in inert gases exhibit negative differential conductivity[16] and nonmonotonic behavior of the plasma density in the central portion of the discharge[17] (the conduction current in the electrode circuit and the plasma density at the discharge center decrease with increasing rf voltage until complete conversion of the discharge into the γ form occurs), low-frequency plasma noise and oscillations appear in the quasineutral plasma,[17] and plasma double layers form.[18,19]

The region for the stable existence of the α regime of an rf discharge is bounded on the moderate-pressure side ($p\sim 10$ Torr): for a fixed distance between the electrodes L there is a pressure p_{cr}, which is such that at $p\geqslant p_{cr}$ the rf discharge can burn only in the high-current γ regime.[6] The curves describing the $\alpha-\gamma$ transition of rf discharges are similar to the ignition curve of a discharge in a constant electric field.[7,8,13]

EXPERIMENTAL METHOD

The experiments were carried out at the argon pressures $p=10^{-2}-10$ Torr, in the range of rf voltages $U_{rf}\leqslant 1000$ V, and at the field frequency $f=13.56$ MHz. The distance between the flat parallel stainless steel electrodes with a diameter of 100 mm was varied in the range $L=6-54$ mm. An rf voltage was supplied to one electrode, and the other electrode was grounded. To eliminate the constant self-bias voltage between the electrodes, a choke coil with an inductance of 4 mH was included. The measurements of the discharge current were performed using a Rogowski loop located on the bus grounding one of the electrodes (a grounded bus). The signal from the Rogowski loop was fed into an FK2-12 phase-difference meter. The signal supplied to the other in-

put of the FK2-12 meter was from a capacitive divider connected to the rf electrode, permitting measurement of the amplitude of the rf voltage U_{rf} and the discharge current I_{rf}, as well as the phase angle between them φ.

The plasma parameters (the electron temperature T_e, the plasma density n_i, and the constant component of the plasma potential ϕ_{pl}) were measured using single cylindrical Nichrome probes with a length of 5 mm and a diameter of 0.18 mm. All three operating regimes of the probes (the collisionless, transitional, and collisional regimes) can be observed in the range of pressures investigated, i.e., depending on the pressure, ions can traverse the near-probe layer without collisions (at low pressures, $p \leqslant 0.05$ Torr), collide with gas atoms a few times (at intermediate pressures), or collide with neutral gas particles many times ($p > 1$ Torr). Therefore, the plasma density n_i was calculated from the ion branch of the probe current and the measured electron temperature T_e using the method described in Refs. 20–22. The plasma potential ϕ_{pl} was determined from the zero value of the second derivative of the probe current with respect to the voltage, as well as from the measured values of the probe floating potential ϕ_f and the electron temperature T_e using the formula $\phi_{\mathrm{pl}} = \phi_f + CT_e[B]$, where C is a constant, which depends on the kind of gas.[15] The electron temperature T_e was calculated from the linear portions of the probe current–voltage characteristic and the second derivative of the current in the probe with respect to the constant voltage on the probe (which were plotted in semilogarithmic coordinates). The values of T_e determined by these two methods differed by no more than 10–20%. The second derivative of the current in the probe with respect to the voltage $d^2I_{\mathrm{pr}}/dU_{\mathrm{pr}}^2$ was measured by the second-harmonic technique, i.e., the probe current was modulated by a low-frequency voltage (the frequency was $f_{\mathrm{lf}} \sim 1-3$ kHz), the signal being detected at $2f_{\mathrm{lf}}$. A measuring system for determining $d^2I_{\mathrm{pr}}/dU_{\mathrm{pr}}^2$ similar to ours was described in Ref. 23.

Let us ascertain the changes in the parameters of an rf discharge which must be taken as criteria for the $\alpha-\gamma$ transition at low and intermediate gas pressures. On the one hand, the value of U_{rf} at which there is a jump in the derivative $dI_{\mathrm{rf}}/dU_{\mathrm{rf}}$ is often taken as the voltage of the $\alpha-\gamma$ transition of an rf discharge.[7,13] In this case electron avalanches develop in the electrode sheaths, and the plasma density increases rapidly as the rf voltage increases in the entire discharge gap. On the other hand, it was assumed in Ref. 5 that at low pressures the $\alpha-\gamma$ transition curve coincides with a portion of the ignition curve for an rf discharge burning at once in the γ regime after breakdown of the gas. We note that these two criteria for the $\alpha-\gamma$ transition of an rf discharge at low gas pressures are not always consistent with one another. In addition, visual observations show that at low and intermediate gas pressures the structure of an rf discharge becomes very similar to the structure of a dc glow when the rf voltage applied to the electrodes is still clearly inadequate for breakdown of the electrode sheaths. It can also be concluded from the current–voltage characteristics of rf discharges in Ref. 16 that smaller rf voltages are needed to go from the α regime to the γ regime as the argon pressure is lowered. Therefore, in the present work the following

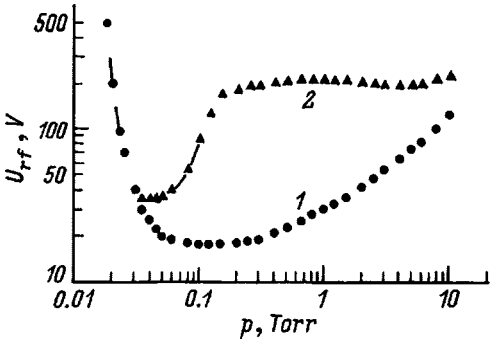

FIG. 1. Extinguishing curve of an rf discharge (*1*) and $\alpha-\gamma$ transition curve (*2*) for $L = 22$ mm.

changes in the rf discharge parameters were taken as criteria for the transition from the α regime to the γ regime. At argon pressures $p > 0.5$ Torr the $\alpha-\gamma$ transition is continuous and lacks jumps and is accompanied by a decrease in the rf conduction current in the electrode surface $I_{\mathrm{rf}}\cos(\varphi)$ and by a decrease in the plasma density n_i at the discharge center.[17] It was assumed in this pressure range that the $\alpha-\gamma$ transition occurs at the value of the rf voltage at which $I_{\mathrm{rf}}\cos(\varphi)$ and n_i reach a maximum. At $p \approx 0.05-0.5$ Torr the $\alpha-\gamma$ transition is accompanied by restructuring of the rf discharge: the uniform glow of the positive column in the α regime abruptly transforms into two negative glows and two Faraday dark spaces of a glow discharge, which intersect at the center of the discharge gap. The appearance of a dark region at the discharge center is well detected visually. At low pressures the $\alpha-\gamma$ transition is accompanied by abrupt decreases in the plasma density n_i and the electron temperature T_e in the central portion of the discharge and an increase in the phase angle φ between the rf current and the voltage, which permit reliable detection of the occurrence of the $\alpha-\gamma$ transition. The $\alpha-\gamma$ transition is also accompanied by a change in the visible glow of the discharge: the white (reddish at intermediate pressures) glow acquires a violet tint, which apparently indicates the appearance of fast electrons in the discharge.

EXPERIMENTAL RESULTS

Existence region of the α regime. Figure 1 presents the extinguishing curve of an rf discharge and the $\alpha-\gamma$ transition curve. It is seen from the figure that at moderate pressures ($p \sim 10$ Torr) the $\alpha-\gamma$ transition curve tends toward the extinguishing curve of the rf discharge. As the pressure is lowered, the value $U_{\alpha\gamma}$ of the rf voltage across the electrodes at which the $\alpha-\gamma$ transition is observed at first decreases and reaches a minimum (a minimum which is similar to the Paschen curve for the ignition of a glow discharge), after which $U_{\alpha\gamma}$ increases slightly and then goes out onto a plateau which extends over the range of argon pressures $p \approx 0.5-1$ Torr. Further lowering of the pressure leads to a rapid decrease in $U_{\alpha\gamma}$, and in the pressure range $p \leqslant 0.03$ the $\alpha-\gamma$ transition curve coincides with the extinguishing curve of the rf discharge.

Figure 2 shows plots of the dependence of the conduction current in the electrode circuit $I_{\mathrm{rf}}\cos(\varphi)$ on the rf volt-

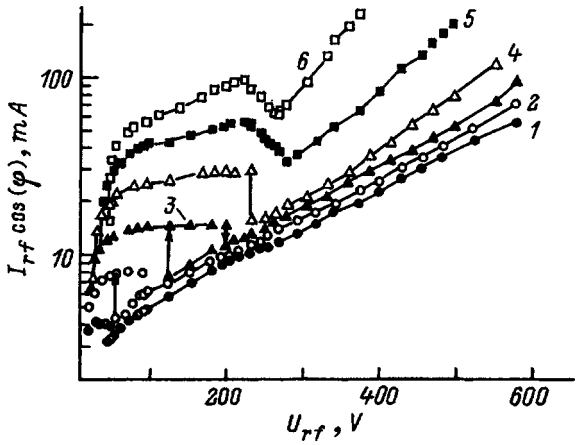

FIG. 2. Dependence of the rf conduction current in the electrode circuit on the applied rf voltage. $L=22$ mm. p, Torr: *1*—0.06, *2*—0.1, *3*—0.2, *4*—0.5, *5*—1, *6*—2.

age. It is seen from the figure that at argon pressures $p\leqslant 0.5$ Torr the $\alpha-\gamma$ transition occurs abruptly and exhibits hysteresis (until $U_{\alpha\gamma}$ reaches a plateau). At higher pressures the $\alpha-\gamma$ transition is smooth and lacks jumps, and negative differential conductivity is observed in the rf discharge. After the transformation of the discharge into the γ form is completed, the conduction current in the electrode circuit increases monotonically with increasing rf voltage.

Let us consider the processes taking place during the transition of an rf discharge from the α regime to the γ regime at different gas pressures. At low pressures ($p<0.05$ Torr) the secondary electrons emitted from the electrode surfaces under the action of bombardment by ions and metastable atoms traverse the electrode sheath with virtually no collisions, gaining energy in an amount up to $\varepsilon_e\approx eU_{\rm sh}$ over the entire thickness of the sheath ($U_{\rm sh}$ is the rf voltage on the sheath). When $U_{\rm sh}\geqslant U_i$ ($U_i=15.8$ V is the ionization potential of an argon atom upon electron impact), a beam of fast electrons from the sheath, which ionize gas atoms along their path, penetrates the plasma. The rf discharge passes into the γ regime, and, according to its characteristics, the region of the quasineutral plasma becomes an analog of two negative glows of a glow discharge, which intersect at the discharge center. We note that the electrons gain energy in the sheath and ionize gas atoms in the quasineutral plasma comparatively far from the sheath boundary. If the gas pressure is sufficiently low (in Fig. 1, $p<0.03$ Torr), the rf discharge can burn only in the γ regime, since the voltage on the electrode sheath $U_{\rm sh}$ exceeds the ionization potential of the gas atoms U_i over the entire existence region of the discharge. In this pressure range the γ regime of the rf discharge is visually very similar to the α regime and can thus easily lead to a mistaken impression.

Let us verify whether the familiar breakdown criterion[15] for an electrode sheath

$$\mu=\gamma\{\exp(\alpha d_{\rm sh})-1\}=1 \qquad (1)$$

holds for the $\alpha-\gamma$ transition of a low-pressure rf discharge (α and γ are the first and second Townsend coefficients, respectively, and $d_{\rm sh}$ is the thickness of the electrode sheath). When the argon pressure $p=0.1$ Torr, the rf discharge passes from the α regime to the γ regime at $U_{\rm rf}\approx 85$ V. The sheath thickness is then equal to $d_{\rm sh}\approx 0.6$ cm. We assume that the rf field is distributed uniformly within an electrode sheath and that all of the applied rf voltage falls on one sheath (the latter assumption is valid for the cathodic phase of the sheath under consideration). Then it is easy to show that $\mu\approx 0.018$ under the present conditions, i.e., the breakdown criterion (1) does not hold for the $\alpha-\gamma$ transition of a low-pressure rf discharge (even at clearly overestimated values of μ). An rf voltage $U_{\rm rf}\approx 850$ V must be applied to satisfy the criterion (1) when $pd_{\rm sh}=0.06$ Torr·cm. Therefore, breakdown of the sheath occurs at rf voltages significantly greater than $U_{\alpha\gamma}$ when a large ion flux, which causes intense ion–electron emission, impinges on the electrode and electron avalanches develop in the sheath. Thus, the electrode sheath does not break down in the γ regime over a broad range of rf voltages and thus continues to be one of the main sources of fast electrons.

At the pressures $p\sim 0.05-0.5$ Torr the secondary electrons crossing an electrode sheath manage to collide elastically and inelastically once or several times with gas atoms and, for this reason, gain less energy over the thickness of the sheath than in the collisionless case. Therefore, when the pressure is raised, the $\alpha-\gamma$ transition occurs at higher rf voltages on the sheath $U_{\rm sh}>U_i$ and on the electrodes. Near an electrode the electrons are accelerated in a strong rf field and acquire most of their energy in just that region. Electrons which have collided elastically and inelastically with gas atoms as they move through the sheath can be further accelerated in the relatively weak field near the sheath boundary and form a high-energy beam. Since the electron ionization path length λ_e exceeds the sheath thickness $d_{\rm sh}$ in this pressure range, a considerable portion of the ionizing collisions will take place not only near the sheath boundary, but also in the quasineutral plasma. According to its characteristics, the quasineutral plasma becomes analogous to two negative glows and two Faraday dark spaces of a glow discharge, which intersect at the discharge center. The electric field in these parts of the discharge is known to be small.[15] Consequently, during the $\alpha-\gamma$ transition the rf voltage drop on the electrode sheaths increases, and the reverse $\gamma-\alpha$ transition occurs at small rf voltages, and hysteresis is, therefore, observed.

At higher gas pressures ($p>0.5$ Torr) the two Faraday dark spaces do not intersect, and an equivalent positive column is observed in the central region at the beginning of the $\alpha-\gamma$ transition. An increase in the rf voltage leads to an increase in the length of the Faraday dark spaces, the region occupied by the positive column narrows, and at higher rf voltages the two Faraday dark spaces intersect at the discharge center. While the $\alpha-\gamma$ transition took place abruptly with manifestations of hysteresis at low pressures, here the rf discharge passes into the γ regime continuously, and the hysteresis vanishes. Negative differential conductivity is observed in the discharge, nonmonotonic behavior of the plasma density appears in the central portion of the discharge gap, plasma double layers form, and low-frequency oscillations and noise appear.[16–19] At $p>1$ Torr, the $\alpha-\gamma$ transi-

tion is similar in its characteristics to the ignition of a dc glow discharge: each electrode sheath is in the prebreakdown state, and the $\alpha-\gamma$ transition curve is similar to the Paschen curve.[6–8,13]

When the $\alpha-\gamma$ transition is considered, it must be taken into account that the rf field is distributed nonuniformly across the electrode sheath (it is strongest near the electrode and very weak on the sheath-plasma boundary); therefore a correct analogy cannot always be drawn between the $\alpha-\gamma$ transition of an rf discharge and the ignition of a glow discharge in a uniform constant electric field. In the collisionless case such a distribution of the rf field in the sheath does not play any special role in the $\alpha-\gamma$ transition. However, the situation changes in the highly collisional case. Secondary electrons knocked out of the electrode surface are accelerated from the electrode to the sheath boundary and gain most of their energy in the region of the strong rf field (near the electrode surface). After a certain distance $d^*<d_{\mathrm{sh}}$ the electrons enter a region of a relatively weak rf field and cease to be accelerated, since they gain less energy from the rf field than they lose in collisions with gas atoms. If the electrons do not manage to acquire energy sufficient for ionizing gas atoms along their path from the electrode to d^*, the $\alpha-\gamma$ transition does not occur at that value of the applied rf voltage. A flux of electrons (it can contain electrons with energies of the order of 10 eV), which move from the electrode sheath into the plasma and excite gas atoms along their path, is observed. Therefore, at intermediate and moderate pressures the fluorescence can be brighter in the α regime on the of the electrode sheath boundaries than in other regions of the discharge (this was also noted in Refs. 6 and 11). If the rf voltage is raised to a value at which the secondary electrons enter the region of the weak rf field with an energy sufficient for ionizing gas atoms, the $\alpha-\gamma$ transition is observed. At moderate gas pressures the electrode sheath thickness decreases abruptly to $d_{\mathrm{sh}}\leqslant d^*$ and becomes comparable in value to the normal sheath thickness of a dc glow discharge.[8]

2. Phase angle between the rf current and the voltage. Figure 3a shows plots of the dependence of the phase angle between the rf current and the voltage on the amplitude of the rf voltage. As is seen from the figure, at low pressures the phase angle φ increases with increasing rf voltage, φ increases abruptly during the $\alpha-\gamma$ transition, and φ reaches a maximum and then slowly decreases as the rf voltage is increased further. At intermediate pressures and low values of U_{rf}, the phase angle φ at first decreases, passes through a minimum, and then increases as the rf voltage is increased; during the $\alpha-\gamma$ transition the phase angle φ increases more rapidly then in the α regime, reaches a maximum, and decreases monotonically in the γ regime.

Unlike the authors of Refs. 9, 24, and 25, we did not observe a situation in which $\varphi\approx 0$, i.e., in which the active rf current in the electrode circuit is equal in value to the amplitude of the rf current and the discharge transforms from a capacitive to an inductive discharge under any conditions over the entire range of pressures, interelectrode distances, and rf voltages investigated. This refers not only to argon, but also to the other gases that we investigated (hydrogen, oxygen, nitrogen, air, CF_4, SF_6, etc.). The disparities between the values of the phase angle φ that we measured and the results in Refs. 9, 24, and 25 are apparently attributable to the difference in the location of the Rogowski loops. We measured the rf current using a Rogowski loop located on a grounded bus, while in Refs. 9, 24, and 25 the Rogowski loop was located on the bus which conducts electricity from the rf generator to the potential electrode. If the Rogowski loops (or a similar measuring device with a grounded housing) are placed on the bus which conducts the rf voltage to the potential electrode, the value of I_{rf}^* measured in this way depends on the location of the measuring device relative to the electrode and does not describe the real value of the discharge current I_{rf}. This is because part of the rf current escapes from the bus and the electrode into the grounded housing of the measuring device, and the rf current partially escapes from the potential electrode into the grounded parts of the experimental apparatus (housings of devices, metal parts of the vacuum system, etc.); therefore the value of the measured rf current $I_{\mathrm{rf}}=\psi(U_{\mathrm{rf}})$ depends on the distance from the measuring device to the rf electrode. The readings from a Rogowski loop located on a grounded bus do not depend on the distance to the grounded electrode. Therefore, such a location for the measuring device permits more accurate determination not only of the value of the discharge current, but also of the phase angle between the rf current and the voltage. We note that our measured values of φ are

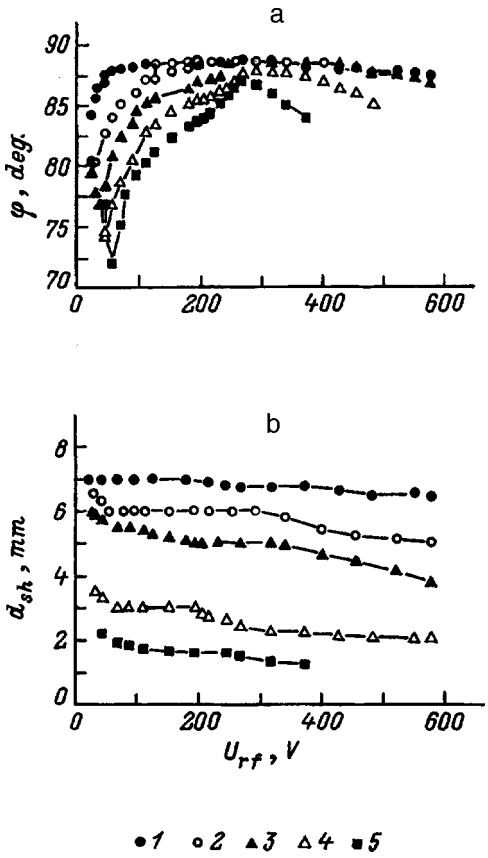

FIG. 3. a — Dependence of the phase angle between the rf current and the voltage on the applied rf voltage; p, Torr: *1* — 0.06, *2* — 0.2, *3* 0.5, *4* — 1, *5* — 2. b — Dependence of the electrode sheath thickness on the rf voltage; p, Torr: *1* — 0.06, *2* — 0.1, *3* — 0.2, *4* — 1, *5* — 2; $L=22$ mm.

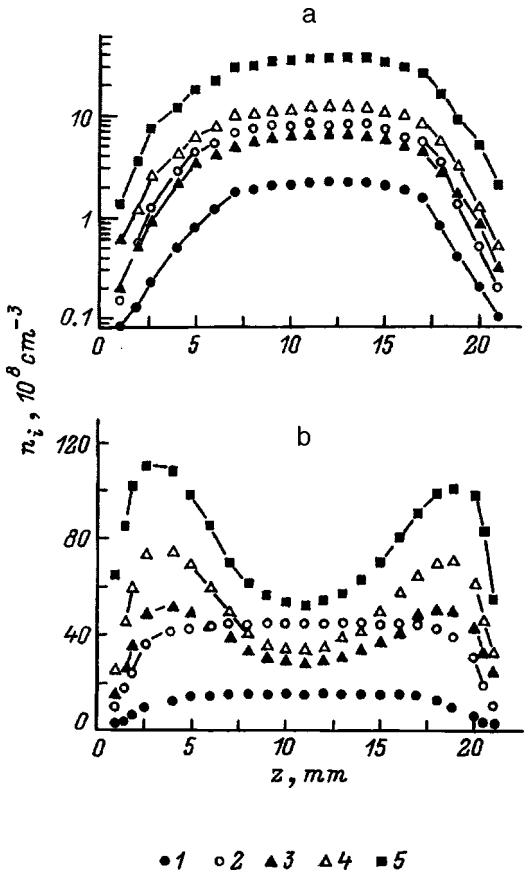

FIG. 4. Axial profiles of the plasma density for argon pressures equal to 0.1 Torr (a) and 1 Torr (b) and various applied rf voltages. a—U_{rf}, V: *1*—25, *2*—65 (α regime), *3*—65 (γ regime), *4*—100, *5*—200; *b*—U_{rf}, V: *1*—100, *2*—225, *3*—275, *4*—325, *5*—350.

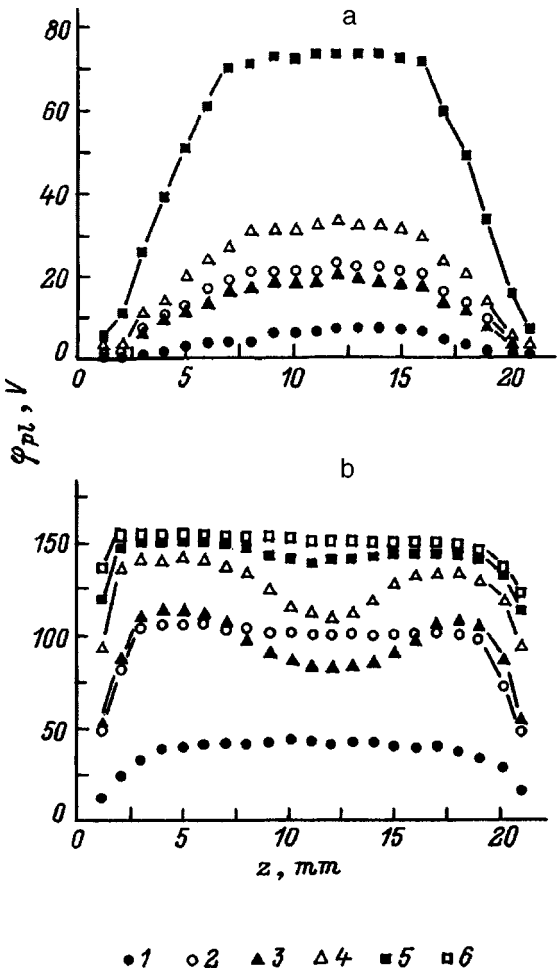

FIG. 5. Axial profiles of the constant plasma potential for argon pressures equal to 0.1 Torr (a) and 1 Torr (b) and various applied rf voltages. a — U_{rf}, V: *1*—25, *2*—65 (α regime), *3*—65 (γ regime), *4*—100, *5*—200; b—U_{rf}, V: *1*—100, *2*—238, *3*—263, *4*—325, *5*—350, *6*—365.

in satisfactory agreement with the experimental and theoretical values of φ in Refs. 12,14, and 26–29.

3. Axial structure of an rf discharge. Figures 4–6 show axial profiles of the plasma density n_i, the constant component of the plasma potential ϕ_{pl}, and the electron temperature T_e, respectively, at various rf voltages for argon pressures equal to 0.1 and 1 Torr.

At low pressures the axial profiles of n_i and ϕ_{pl} have a ''bell-shaped'' form with a maximum at the center of the discharge gap in the α discharge regime. As the rf voltage is increased, the plasma density and the constant plasma potential increase throughout the entire discharge. However, at a certain value of the rf voltage the α regime transforms abruptly into the γ regime, and sharp decreases in n_i and ϕ_{pl} are observed in the discharge volume. As the rf voltage is increased further, the plasma density and the constant plasma potential monotonically increase over the entire discharge gap. At intermediate pressures n_i and ϕ_{pl} have maxima at the discharge center and monotonically decrease as the electrodes are approached in the α regime of the rf discharge. The transition from the α to the γ regime is accompanied by continuous increases in n_i and ϕ_{pl} in the electrode sheaths and near the sheath/quasineutral-plasma boundaries, while in the central portion of the discharge n_i and ϕ_{pl} decrease with increasing rf voltage. Two plasma double layers form in the discharge volume. Their ''cathode'' parts come into contact at the discharge center, and their ''anode'' parts are located near the sheath/quasineutral-plasma boundaries. After the discharge has passed completely into the γ regime, the double layers disappear, and the density and constant potential of the plasma increase monotonically with increasing rf voltage throughout the entire discharge gap.

In the α regime at a low pressure the axial profile of the electron temperature has maximum values in the central part of the discharge; as the rf voltage is increased, T_e decreases throughout the entire discharge. After passage into the γ regime, the axial profile of the electron temperature is altered: the values of T_e are highest near the electrode sheath boundaries and have a maximum in the central portion of the discharge. As the rf voltage is increased further, the electron temperature decreases monotonically throughout the entire discharge. At intermediate pressures (Fig. 5b) the axial distribution of the electron temperature has maxima near the electrode sheath boundaries and a minimum in the central portion of the discharge not only in the γ regime, but also in the α regime. Such profiles of the electron temperature were also obtained experimentally in Ref. 30 and were theoretically predicted in Ref. 31. Sommerer and Kushner[31] attribute them to stochastic (collisionless) electron heating, which oc-

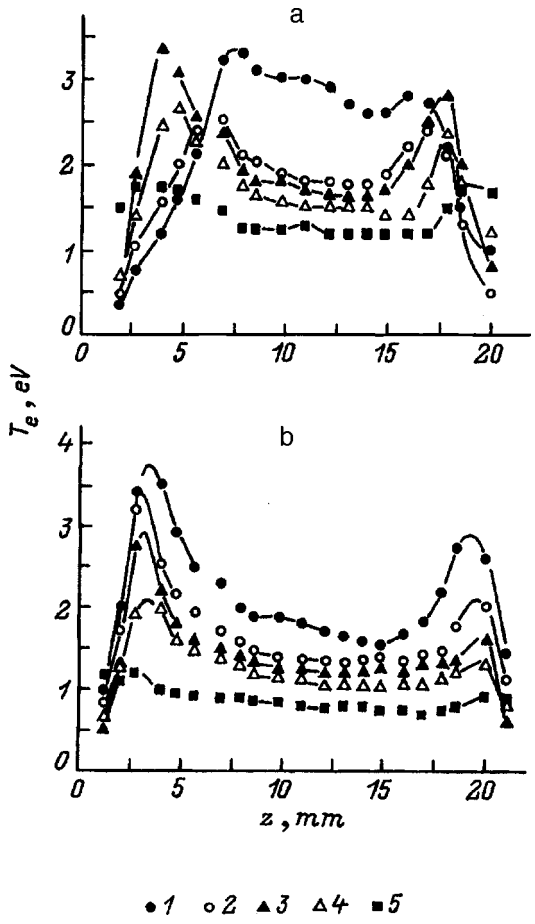

FIG. 6. Axial profiles of the electron temperature for argon pressures equal to 0.1 Torr (a) and 1 Torr (b) and various applied rf voltages. a—U_{rf}, V: *1*—25, *2*—65 (α regime), *3*—65 (γ regime), *4*—200, *5*—400; b—U_{rf}, V: *1*—50, *2*—200, *3*—225, *4*—250, *5*—350.

curs upon collisions of electrons with the oscillating electrode sheath boundaries.[13,32–34]

The behavior of the electron temperature and the plasma density during the $\alpha-\gamma$ transition at low argon pressures can be explained in the following manner. In the α regime at low rf voltages electrons are accelerated both in the rf field in the central region and upon collisions with the oscillating sheath boundary, as is evidenced by the axial profiles of T_e. As the rf voltage is increased, the plasma density increases, and, as a result, the rf voltage drop on the electrode sheath increases, and the voltage drop on the quasineutral plasma decreases. Therefore, the electron temperature decreases with increasing rf voltage in the α regime. When the rf voltage drop on the electrode sheath reaches a certain critical value, a flux of fast electrons begins to enter the plasma from the sheath. When high-energy electrons appear in the quasineutral plasma, the equivalent of the positive column in the α regime transforms into the negative glow of the γ regime. The field in the negative glow is appreciably weaker than in the positive column, electrons in the quasineutral plasma are accelerated in a weaker rf field, and the electron temperature in the central portion of the discharge decreases. Therefore, the axial distribution of T_e in the γ regime has a maximum on the electrode sheath boundaries (owing to collisionless electron heating) and a minimum at the discharge center. At that moment the flux of fast electrons capable of ionizing gas atoms is still not sufficiently large to ensure a high ionization rate; therefore, the decrease in the electron temperature during passage of the discharge into the γ regime leads to a decrease in the plasma density in the discharge volume. As the rf voltage is increased further, the flux of fast electrons increases, the ionization rate of the gas atoms by fast electrons increases, and the plasma density in the entire discharge volume rises. The rf voltage drop on the electrode sheaths increases, and the voltage drop on the quasineutral plasma decreases; therefore, the electron temperature also decreases.

Let us now consider the case of intermediate pressures. As we know,[15] the frequency of electron–atom collisions ν for argon depends strongly on the electron temperature $\nu/p \sim T_e^{3/2}$. Therefore, at intermediate argon pressures and the characteristic electron temperatures $T_e \approx 2$ eV a fairly large part of the rf voltage falls on the quasineutral plasma in the α discharge regime. During the $\alpha-\gamma$ transition beams of fast electrons emerge from the electrode sheaths, and the region of the quasineutral plasma transforms into two negative glows and two Faraday dark spaces of a glow discharge. As a result, the rf field in the discharge volume decreases. This leads to a decrease in the electron temperature and, consequently, in an appreciable decrease in the plasma density in the central portion of the discharge. The plasma density at the discharge center decreases with increasing rf voltage until the diffusion fluxes of charged particles moving from the electrode sheath boundaries (regions with increased ionization) into the central region compensate the decreasing ionization of the argon atoms by the plasma electrons. When the rf voltage is increased further, the nonmonotonic behavior of the plasma density in the central portion of the discharge gap vanishes, and the rf discharge burns in a full-fledged γ regime.

4. Stochastic heating of electrons. There is still no unanimous opinion regarding the conditions under which the stochastic heating of electrons must be taken into account. It was stated in Ref. 35 that the dark (thermal) electron velocity V_{te} considerably exceeds the velocity of an oscillating sheath boundary V_{sh}; therefore, only ''cold'' electrons with energies $\varepsilon < 0.1$ eV can acquire a considerable fraction of the energy during a collision with a sheath boundary, while the bulk of the electrons scarcely acquire energy during collisions with a sheath boundary. At the same time, the opposite case, in which $V_{sh} > V_{te}$, was also treated in Ref. 33 with consideration of a two-temperature Maxwellian distribution.

Let us estimate the velocity of an oscillating sheath boundary V_{sh} on the basis of the conclusion from Ref. 6 that the electrode sheath thickness is approximately equal to the amplitude of the oscillations of electrons in an rf electric field equal in strength to the rf field on the sheath boundary E_b. For the sheath velocity we can write $V_{sh}(t) = eE_b \cos(\omega t)/m\nu$, where e and m are the charge and mass of an electron. We use $V_{sh,0}$ to denote the maximum sheath boundary velocity corresponding to the amplitude of E_b. Then for the electrode sheath thickness we have $d_{sh} = eE_b/m\nu\omega = V_{sh,0}/\omega$.[6] The electrode sheath thickness

varies as a function of the gas pressure and the applied rf voltage: at low pressures $d_{sh} \sim 1$ cm, and at intermediate pressures $d_{sh} \approx 1-3$ mm (Fig. 3b). Taking $d_{sh}=3$ mm, $f=13.56$ MHz, and an argon pressure $p=1$ Torr, for the sheath boundary velocity we obtain $V_{sh,0} \approx 3\times 10^7$ cm/s. The thermal velocity of electrons with a temperature $T_e=2$ eV is $V_{te} \approx 9.4\times 10^7$ cm/s. Thus, it follows from this estimate that the electron thermal velocity is several times greater than the sheath boundary velocity, especially at intermediate pressures and small rf voltages. This means that at intermediate pressures stochastic (collisionless) electron heating should not play a decisive role in sustaining an rf discharge. However, it is seen from Fig. 6b that the electron temperature T_e near the electrode sheath boundaries decreases with increasing rf voltage (both in the α regime and after passage of the rf discharge into the γ regime). Apparently, this effect can be reasonably attributed specifically to the mechanism of collisionless electron heating. If, for example, secondary electron emission from the electrode surfaces played a significant role in the behavior of T_e near a sheath boundary, the electron should have increased with increasing rf voltage, since the number of fast electrons passing from the electrode sheaths into the plasma would have increased. Since the sheath thickness decreases with increasing rf voltage (Fig. 3b), the velocity of the electrode sheath boundary should decrease, and, therefore, the electrons should acquire less energy in collisions with an oscillating sheath boundary. We also see this in Fig. 6b. Therefore, the estimates presented above for the velocity of an electrode sheath boundary are apparently underestimated.

Let us examine several analytical models of other investigators, from which the sheath boundary velocity can be evaluated. Godyak and Sternberg[36] obtained the time dependence of the position of a sheath boundary

$$\lambda(\Theta)=\lambda_1-\rho-\frac{3}{4}\rho^2+\left(\rho+\rho^2+\frac{\rho^3}{8}\right)\sin(\Theta)+\frac{\rho^3}{12}\sin^3(\Theta)-\frac{5\rho^3}{12\pi}\cos(\Theta)+\frac{11\rho^3}{36\pi}\cos^3(\Theta)+\frac{\rho^2}{4}\cos(2\Theta)-\frac{\rho^3}{4\pi}\Theta\sin(\Theta)-\frac{\rho^3}{6\pi}\Theta\sin^3(\Theta), \quad (2)$$

where $\lambda=d(t)/\lambda_D$, $\lambda_1=d_{sh}/\lambda_D$, $\rho=a_1/\lambda_D$, $a_1=eE_p/m\nu\omega$, $\Theta=\omega t$, $d(t)$ is the coordinate of the sheath boundary, λ_D is the Debye radius for the values of T_e and n_i corresponding to the sheath boundary, and E_p is the ohmic part of the rf field near the sheath boundary.

Differentiating (2) with respect to time, we obtain the maximum value of the sheath boundary velocity $V_{sh,0} \approx 3.6\times 10^7$ cm/s. Budyanskiĭ[37] obtained the expression for the maximum velocity of the electron cloud in an rf discharge

$$V_0=\frac{eU_{rf}}{m\omega L}\left\{\left(\frac{\omega_0^2}{\omega^2}-1\right)^2+\frac{\nu^2}{\omega^2}\right\}^{-1/2}, \quad (3)$$

where $\omega_0^2=(4\pi e^2 n_0/m)(2d_{sh}/L)$, and n_0 is the plasma density on the sheath boundary.

Since the oscillating of an electron cloud as a single unit in an rf field was considered in Ref. 37, it is clear that $V_0=V_{sh,0}$. Then the estimates based on formula (3) give $V_{sh,0} \approx 5.4\times 10^7$ cm/s. From Ref. 38 we can easily obtain the expression for the sheath boundary velocity

$$v_{sh}(t)=\omega\frac{d_0}{u_b}\left(\frac{2e\lambda_i}{\pi M}\right)^{1/2}\sqrt{E^*}\sin\omega t, \quad (4)$$

where $d_0=J_0/e\omega n_0$, J_0 is the amplitude of the rf current density, $u_b=(eT_e/M)^{1/2}$, M is the mass of an ion, λ_i is the mean free path of the ions, and

$$E^*=\frac{4J_0}{\omega}(\sin\omega t-\omega t\cos\omega t). \quad (5)$$

The maximum value of the sheath boundary velocity obtained from (4) is equal to $V_{sh,0}=2\times 10^8$ cm/s. Finally, Raĭzer and Shneĭder[8] obtained the expression for the motion of an electrode sheath boundary in the cathodic phase

$$d(t)=\frac{d_0}{1+\xi^2}\left\{\xi\cos\omega t+\sin\omega t+\exp\left(-\xi\left(\omega t+\frac{\pi}{2}\right)\right)\right\}, \quad (6)$$

where $\xi=(1+\gamma)4\pi e n_0\mu_+/\omega$ and μ_+ is the mobility of the ions.

Differentiating (6) with respect to time, we obtain $V_{sh,0} \approx 2.7\times 10^8$ cm/s. Therefore, using the same set of experimentally measured values of U_{rf}, J_0, n_0, and T_e on the sheath boundary, we can obtain completely different estimates of the ratio between the thermal velocity of the electrons and the velocity of the electrode sheath boundary from the existing discharge models. Therefore, additional investigations of both the experimental and theoretical types are needed to ascertain the role of stochastic (collisionless) electron heating at intermediate gas pressures.

5. Conditions for the existence of plasma double layers in an rf discharge. As is seen from Fig. 5b, at intermediate pressures the $\alpha-\gamma$ transition is accompanied by the formation of two stationary double layers in the quasineutral plasma, so that maxima are observed near the electrode sheath boundaries on the axial profile of the constant component of the plasma potential, while a minimum is observed in the central portion of the discharge. This is apparently caused by the simultaneous decreases in the plasma density and the electron temperature at the discharge center during the $\alpha-\gamma$ transition (Figs. 4b and 6b). The conductance of the plasma decreases, and in order to conduct the increasing rf current, plasma double layers appear in the quasineutral plasma. It is seen from Figs. 4 and 6 that during the $\alpha-\gamma$ transition the plasma regions with the highest values of the electron temperature and the plasma density are concentrated near the electrode sheath boundaries, and minima are observed in the central portion of the discharge on the axial profiles of T_e and n_i. Therefore, both diffusive and thermal-diffusive fluxes of charged particles, as well as a flux of fast electrons moving from the electrode sheath boundaries to the discharge center, exist during the $\alpha-\gamma$ transition and in the

γ regime proper. Since the axial profile of the constant plasma potential during the $\alpha-\gamma$ transition has maxima near the electrode sheath boundaries and a minimum at the discharge center, fluxes of positive ions from the sheath boundaries to the discharge center will be observed. The existence of stationary double layers in an rf discharge requires that the excess of incoming positive ions be removed from the central region. Since the radial diffusion of charged particles is hardly of great significance under our conditions (in Fig. 5 the diameter of the discharge chamber is almost five times greater than the distance between the electrodes), the main mechanism for the depletion of positive ions in the central region must apparently be ion–electron recombination. As was shown in Refs. 39 and 40, apart from the Ar^+ ions, a fairly significant number of Ar_2^+ ions is observed at $p\sim 0.5-1$ Torr (from fractions of a percent to tens of percent of the total number of positively charged particles). The coefficient of dissociative recombination decreases rapidly with increasing electron temperature[41] ($\beta\sim T_e^{-0.67}$); therefore, there will be little dissociative ion–electron recombination near the electrode sheath boundaries (since T_e is maximal in these regions), while Ar_2^+ will recombine effectively with electrons at the discharge center.

The stationary existence of plasma double layers in an rf discharge also requires that the excess of electrons in the central region be maintained continually at a low level. Beside the intrinsic plasma (cold) electrons, fluxes of fast secondary electrons, which have gained energy in the electrode sheaths, arrive at the discharge center. The flux of fast electrons also contains electrons which were accelerated in the increased rf field in the electrode sheaths in the plasma phase.[34] Clearly expressed double layers are observed at pressures and applied rf voltages at which the positive column observed in the central region at the beginning of the $\alpha-\gamma$ transition gradually disappears and two Faraday dark spaces intersect at the discharge center. As we know,[42,43] the length of a Faraday dark space is determined by the distance over which the thermalization (Maxwellization) of secondary electrons takes place: on the boundary between a Faraday dark space and the positive column the directed velocity of the electrons produced by secondary emission becomes equal to the thermal velocity of the plasma electrons. When the two Faraday dark spaces intersect, the electrons moving from both electrodes are stopped at the discharge center, and a region with a small excess of negative charge forms. The maximum drop in the constant potential across the double layer is observed under just these conditions. At higher rf voltages the flux of secondary electrons emerging from one electrode sheath is stopped already between the discharge center and the opposite electrode sheath. Therefore, the double layers disappear as the rf voltage is increased.

Thus, the transition of an rf discharge from the low-current (α) burning regime to the high-current (γ) regime has been investigated experimentally in the present work at low and intermediate argon pressures. It has been shown that the region for the existence of the α regime is bounded not only on the moderate-pressure side, but also on the low-pressure side. At low gas pressures ($p<0.5$ Torr) the $\alpha-\gamma$ transition of an rf discharge is abrupt and exhibits hysteresis. At intermediate argon pressures the $\alpha-\gamma$ transition is continuous and lacks abrupt jumps, but nonmonotonic behavior of the plasma density appears in the central portion of the discharge, plasma double layers form, and negative differential conductivity is observed in the discharge.

[1] D. L. Flamm, V. M. Donnelley, and D. E. Ibbotson, J. Vac. Sci. Technol. **1**, 23 (1983).
[2] J. M. Coburn and E. Kay, IBM J. Res. Dev. **23**, 33 (1979).
[3] V. I. Myshenkov, and N. A. Yatsenko, Kvantovaya Élektron. (Moscow) **8**, 2121 (1981) [Sov. J. Quantum Electron. **11**, 1297 (1981)].
[4] Y. P. Raizer, M. N. Shneider, and N. A. Yatsenko, *Radio-Frequency Capacitive Discharges*, CRC Press, Boca Raton (1995).
[5] S. M. Levitskiĭ, Zh. Tekh. Fiz. **27**, 970 (1957) [Sov. Phys. Tech. Phys. **2**, 887 (1957)].
[6] N. A. Yatsenko, Zh. Tekh. Fiz. **50**, 2480 (1980) [Sov. Phys. Tech. Phys. **25**, 1454 (1980)]; Zh. Tekh. Fiz. **51**, 1195 (1981) [Sov. Phys. Tech. Phys. **26**, 678 (1981)]; Zh. Tekh. Fiz. **58**, 294 (1988) [Sov. Phys. Tech. Phys. **33**, 180 (1988)].
[7] V. A. Godyak and A. S. Khanneh, IEEE Trans. Plasma Sci. **PS-14**, 112 (1986).
[8] Yu. P. Raĭzer and M. N. Shneĭder, Fiz. Plazmy **13**, 471 (1987) [Sov. J. Plasma Phys. **13**, 267 (1987)]; Fiz. Plazmy **14**, 226 (1988) [Sov. J. Plasma Phys. **14**, 128 (1988)]; Fiz. Plazmy **18**, 1476 (1992) [Sov. J. Plasma Phys. **18**, 762 (1992)].
[9] V. A. Godyak, R. B. Piejak, and B. M. Alexandrovich, IEEE Trans. Plasma Sci. **PS-19**, 660 (1991).
[10] I. D. Kaganovich, L. D. Tsendin, and N. A. Yatsenko, Zh. Tekh. Fiz. **64**(12), 25 (1994) [Tech. Phys. **39**, 1215 (1994)].
[11] P. Vidaud, S. M. A. Durrani, and D. K. Hall, J. Phys. D: Appl. Phys. **21**, 57 (1988).
[12] T. Makabe, N. Nakano, and Y. Yamaguchi, Phys. Rev. A **45**, 2520 (1992).
[13] C. Bohm and J. Perrin, J. Phys. D: Appl. Phys. **24**, 865 (1991).
[14] P. P. Vitruk, H. J. Baker, and D. K. Hall, J. Phys. D: Appl. Phys. **25**, 1767 (1992).
[15] Yu. P. Raizer, *Gas Discharge Physics*, Springer-Verlag, Berlin–New York (1991); Nauka, Moscow (1987), 592 pp.
[16] N. Yu. Kropotov, V. A. Lisovskiĭ, Yu. A. Kachanov *et al.*, Pis'ma Zh. Tekh. Fiz. **15**(21), 17 (1989) [Sov. Tech. Phys. Lett. **15**, 836 (1989)].
[17] V. A. Lisovskiĭ, V. D. Egorenkov, and O. V. Krasnikov, Pis'ma Zh. Tekh. Fiz. **19**(21), 90 (1993) [Sov. Tech. Phys. Lett. **19**, 701 (1993)].
[18] V. A. Lisovskiĭ and O. V. Krasnikov, Pis'ma Zh. Tekh. Fiz. **21**(22), 57 (1995) [Sov. Tech. Phys. Lett. **21**, 931 (1995)].
[19] V. A. Lisovskiy and O. V. Krasnikov, in *22nd IEEE International Conference on Plasma Science. Conference Record, Abstracts*, Madison, Wisconsin (1995), p. 144.
[20] V. A. Nemchinskiĭ, Zh. Tekh. Fiz. **40**, 416 (1970) [Sov. Phys. Tech. Phys. **15**, 314 (1970)].
[21] G. J. Schulz and S. C. Brown, Phys. Rev. **98**, 1642 (1955).
[22] S. V. Dudin, in *23rd IEEE International Conference on Plasma Science. Conference Record, Abstracts*, Boston (1996), p. 45.
[23] S. V. Dudin, Prib. Tekh. Éksp (4), 78 (1994).
[24] V. A. Godyak and A. Kh. Ganna, Fiz. Plazmy **6**, 676 (1980) [Sov. J. Plasma Phys. **6**, 372 (1980)].
[25] O. A. Popov and V. A. Godyak, J. Appl. Phys. **57**, 53 (1985).
[26] C. Beneking, J. Appl. Phys. **68**, 4461 (1990).
[27] F. Tochikudo, T. Kokubo, S. Kakuta *et al.*, J. Phys. D: Appl. Phys. **23**, 1184 (1990).
[28] T. Kokubo, F. Tochikubo, and T. Makabe, Appl. Phys. Lett. **56**, 818 (1990).
[29] S. Kakuta, T. Kitajima, Y. Okabe, and T. Makabe, Jpn. J. Appl. Phys. **33**, 4335 (1990).
[30] K. Terai, Y. Ohsone, T. Kaneda, and T. Kubota, in *Proceedings of the 20th International Conference on Phenomena in Ionized Gases, Contributed Papers*, Pisa (1991), pp. 1151–1152.
[31] T. J. Sommerer and M. J. Kushner, J. Appl. Phys. **71**, 1654 (1992).

[32] V. A. Godyak, Fiz. Plazmy **2**, 141 (1976) [Sov. J. Plasma Phys. **2**, 78 (1976)].
[33] B. P. Wood, M. A. Lieberman, and A. J. Lichtenberg, IEEE Trans. Plasma Sci. **PS-23**, 89 (1995).
[34] I. D. Kaganovich and L. D. Tsendin, IEEE Trans. Plasma Sci. **20** (2), 66, 86 (1992).
[35] P. W. May, D. F. Klemperer, and D. Field, J. Appl. Phys. **73**, 1634 (1993).
[36] A. V. Godyak and N. Sternberg, Phys. Rev. A **42**, 2299 (1990).
[37] A. M. Budyanskiĭ, Pis'ma Zh. Tekh. Fiz. **18**(1), 17 (1992) [Sov. Tech. Phys. Lett. **18**, 6 (1992)].
[38] M. A. Lieberman, Philos. Trans. R. Soc. London, Ser. B **17**, 338 (1989).
[39] P. F. Knewstubb and A. W. Tickner, J. Chem. Phys. **36**, 674 (1962).
[40] R. L. Fitzwilson and L. M. Chanin, J. Appl. Phys. **44**, 5337 (1973).
[41] F. J. Mehr and M. A. Biondi, Phys. Rev. **176**, 322 (1968).
[42] V. L. Granovskiĭ, *Electric Current in a Gas (Steady-State Current)* [in Russian], Nauka, Moscow (1971), 544 pp.
[43] Yu. P. Raĭzer and M. N. Shneĭder, Teplofiz. Vys. Temp. **29**, 1041 (1991) [High Temp. (USSR) **29**, 833 (1991)].

Translated by P. Shelnitz

Kinetic electron reflection coefficient in a low-voltage Knudsen arc

N. I. Alekseev

A. F. Ioffe Physicotechnical Institute, Russian Academy of Sciences, 194021 St. Petersburg, Russia
(Submitted May 5, 1997)
Zh. Tekh. Fiz. **68**, 61–64 (May 1998)

The influence of the escape of fast plasma electrons on the electron distribution function (EDF) in a low-voltage cesium Knudsen arc is discussed. It is shown that even with a large Knudsen parameter $l_e/h \sim 5-10$ (where h is the gap and l_e is the mean free path of electrons with energy of the order of the anode barrier) the electron flux from the plasma to the anode is virtually identical to that calculated with a Maxwellian EDF. © *1998 American Institute of Physics.* [S1063-7842(98)01105-2]

The question of the magnitude of the thermal plasma electron current to the anode is important for calculations of a cesium thermionic converter operating in the Knudsen regime[1] (when the mean free path of electrons with energies of the order of the positive anode drop φ_2 (Fig. 1a) is several times greater than the gap width h) and plasma switching elements.[2] Calculations of both types of devices[1–3] have assumed that this current can be determined by the standard expression $(1/4)nv_{Te}\exp(-\varphi_2/T)$ (n and T are the electron density and temperature), written as if the EDF were Maxwellian, despite the constant depletion of the electron distribution function (EDF) as a result of the escape of fast particles to the anode. The basis for this simplification is that for energy slightly less than the barrier φ_2 the EDF should not differ much from the Maxwellian function because such electrons undergo repeated reflections from the cathode and anode barriers (the effect of fast-particle depletion of the EDF on the thermal-electron current to the electrode is ordinarily described by the so-called reflection coefficient k_{refl}, determined from the relation $j=(1/4)nv_T\exp(-\varphi_2/T)\times(1-k_{\text{refl}})$ (Ref. 4)). However, it is quite difficult to give quantitative estimates because there is no concrete small parameter in the problem: As will become evident from the analysis below, the ratio of the gap width h to the mean free path l_e of a near-barrier electron (in the present problem this ratio equals 0.2–0.5) as such a parameter should be so small that the calculation has virtually no relation to a real Knudsen arc. In the present work the calculation is performed for the conditions of a stationary conducting state of a Knudsen diode with a quite high plasma density $\bar{n} \geqslant 10^{13}$ cm^{-3} and gas pressure $P_{\text{Cs}} \sim 10^{-2}$ Torr (which for fixed n and typical $T \sim 0.3-0.5$ eV corresponds to cesium atom density $N_{\text{Cs}} \sim 3\times10^{13}$ cm^{-3}). Such conditions are also realized in a stationary state of the cathode and anode regions of a switching element.[3,5] Then barrier is $\varphi_2 = 1.5-2$ eV and Coulomb collisions predominate for electrons with energy $E \sim \varphi_2$: The characteristic electron mean free path $l_e = \varphi_2^2/4\pi q^4 n\Lambda$ equals 1.5–3 mm, which is several times shorter than the mean free path l_{ea} for electron–atom collisions ($l_{ea} = 1/\sigma_{ea}N_a$, where $\sigma_{ea} = 3.5\times10^{-14}$ cm^{-3}). The cathode barrier φ_1, exceeding φ_2 by the amount of the arc voltage (Fig. 1a), is assumed to be infinitely high. The parameter ratio $l_{ea} \ll l_e$ characteristic for a nonstationary transient process in the anode region of a plasma switching element with a negative grid pulse applied to the grid[6] will not be studied here, since to calculate the EDF at energies $E \leqslant \varphi_2$ the interaction of electrons with nonresonant Langmuir plasmons is substantial,[7] which makes it much more difficult to obtain a solution but does not change the qualitative results.

Some approximations made in the solution process are similar to calculating k_{refl} in the case $h \gg l_e \gg l_{ea}$ (Ref. 8); specifically, collisions with plasma electrons are described by a Planckian collision integral, which contains, however, two velocity components — longitudinal and transverse (we shall call the velocity component along the discharge axis longitudinal and the velocity component in the plane of the electrodes transverse). The Planckian integral can be used for electrons with energy of the order of φ_2 much greater than T (the factor ''much greater'' equals, it is true, 4–5).

The effect of the electric field in the gap on the electrons moving with such longitudinal velocities is neglected, since the voltage drop across the Knudsen gap is no more than several tenths of a volt, which is an order of magnitude lower than the anode barrier. In these approximations the kinetic equation has the form

$$v_x \partial f/\partial x - (v_T^2/2)\nabla\cdot(\nu_e(\nabla f + (m\vec{v}f/T))) + (v/l_{ea})f = 0, \quad (1)$$

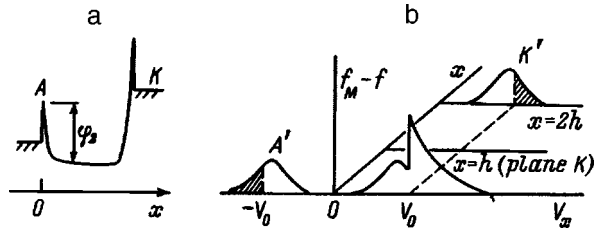

FIG. 1. a: Variation of the potential in the Knudsen gap from the cathode K to the anode A; b: variation of the function $\delta f = f_M - f$: A and A' — in a real gap at $x=0$ (in the anode plane); from A at $x=0$ and K' at $x=2h$ — in an equivalent formulation of the problem at $x=2h$. The velocity range contributing to the current at the anode is hatched.

where ν_e is the frequency of Coulomb collisions of fast above-barrier electrons with thermal plasma electrons, the coordinate x is measured from the anode, and the coordinate of the cathode, from which the electrons are reflected specularly, is $x=h$.

Expanding the divergence operator and taking account of the velocity dependence $\nu_e(v)=(2q^4n\Lambda/m^2v^3)$, we obtain

$$\nabla\cdot(\nu_e(\nabla f+(m\vec{v}f/T))) = \nu_e(\Delta f+(\vec{v}\nabla f)(m/T-3/|v|^2)).$$

Then we rewrite Eq. (1) in the form

$$v_x\partial f/\partial x-(\nu_e v_T^2/2)(\partial^2 f/\partial v_x^2 + v_x\partial f/\partial v_x(m/T-3/|v|^2)+(\partial^2 f/\partial v_\perp^2) + (1/v_\perp)(\partial f/\partial v_\perp)(1+v_\perp^2(m/T-3/|v|^2))) + (v/l_{ea})f=0. \quad (2)$$

The spatial boundary conditions are: At $x=0$ the EDF f is symmetric as a function of v_x for $|v_x|<v_0=(2\varphi_2/m)^{1/2}$ and $f=0$ for $v_x>v_0$; f is symmetric at $x=h$ for any v_x (Fig. 1b). Total reflection at $x=h$, the absence of an interaction between fast particles, and the weakness of the field make it possible, in addition, to study the change in the EDF only for particles with positive velocities at $x=0$, to assume that the velocity at $x=h$ does not change, and to formulate the boundary condition $f(v_x)=f(-v_x)$ for $|v_x|<v_0$, $x=0$ in the form $f(v_x>0,\ x=2h)=f(v_x>0,\ x=0)$.

We shall assume at first that $l_e\gg l_{ea}$ and the last term in Eq. (2) can be dropped. Then it is obvious that the Maxwellian EDF $f_M=\exp(-(v_x^2+v_\perp^2)/v_T^2)$ is a trivial solution of Eq. (2) and can be regarded as a boundary condition for the desired solution for small v_x. The function $\delta f=f_M-f$ likewise satisfies Eq. (2).

Just as in Ref. 8, we shall assume that δf drops off rapidly to the right and left of the point $v_x=v_0$; the ''emergence cone'' $v_\perp/v$ of particles to the anode, where the main depletion of the EDF occurs, is small. In this case in Eq. (2) $|v|$, v_x can be replaced by v_0.

For $T/\varphi_2\sim 1/4$ it is legitimate to replace v by $v_x\simeq v_0$ for $v_\perp/v_T\ll 1/2^{1/2}$. However, the range of velocities $v_\perp$ covered by Eq. (2) can be approximately doubled by switching from δf to

$$g(v_\perp,v_x)=\delta f\ \exp((2-3T/\varphi_2)u_\perp^2/4),$$

where $u_\perp=v_\perp/v_T$.

The function g satisfies the relation

$$(\partial^2 g/\partial u_\perp^2)+(1/u_\perp)(\partial g/\partial u_\perp)\sim(\partial^2 f/\partial u_\perp^2)+(1/u_\perp) \times(\partial f/\partial u_\perp)(1+Xu_\perp^2)+f(X/4)(4+Xu_\perp^2),$$

where $X=v_T^2(m/T-3/|v|^2)\approx 2-3T/\varphi_2$. In this equation the first two terms on the right-hand side appear in the ''transverse'' part in Eq. (2), while the last term can be added and subtracted, with $Xu_\perp^2$ neglected in comparison with 4.

The conditions on δf follow from the conditions for f for $v_x<v_0$

$$\delta f(x=2h)=\delta f(x=0), \quad (3)$$

at $x=0$

$$v_x>v_0:\quad \delta f=f_M=\exp(-v_x^2/v_T^2-u_\perp^2). \quad (4)$$

We shall assume, as we have already stated, that $\delta f\to 0$ as $v_x\to v_T$. The point v_T is chosen completely arbitrarily, and the effectiveness of the choice is determined by how well δf is localized near $v=v_0$ (especially since for $v\sim v_T$ Coulomb collisions cannot be described by a Planckian collision integral).

For $v_\perp\ll v_x\simeq v_0$ electron–atom collisions can also be included in this scheme. Replacing v by v_x in the collision integral $(v/l_{ea})f$, we can see that the function $\tilde{f}_M(v_x,v)=f_M(v)\exp(-x/l_{ea})$ is the solution of Eq. (2), but it is not suitable as a limiting solution of Eq. (2) for $v\sim v_T$. Indeed, if we write the analog of the condition (3) $\delta f(x=2h)=\delta f(x=0)+f_M(v)(1-\exp(-2h/l_{ea}))$, then $\delta f(x=2h)-\delta f(x=0)\neq 0$ increases with decreasing v_x, which is incorrect. In this case the problem requires a more accurate analysis, which should, however, introduce only small changes in the qualitative result obtained below.

Switching from $g(u_\perp)$ to its Fourier–Bessel transform $g_q\equiv g(q_\perp,v_x)=\int_0^\infty g(v_\perp)J_0(u_\perp q_\perp)u_\perp du_\perp$, taking as the longitudinal variable the energy E_x instead of v_x (the relative error arising when E_x is replaced by by $E_0=\varphi_2$ is smaller than when v_x is replaced by v_0), and using instead of E_x and the coordinates x the dimensionless variables $\varepsilon_x=E_xT_e$ and $\xi=x/h$, we obtain for $g(q_\perp)$

$$\partial g_q/\partial\xi-a^2(\partial^2 g_q/\partial\varepsilon_x^2+\Xi\,\partial g_q/\partial\varepsilon_x-g_q\gamma)=0, \quad (5)$$

where $\varepsilon_0=\varphi_2/T$, $a^2=2\varepsilon_0 h\nu_e(v_0)/v_0$, $\gamma=(q_\perp^2+X)/4\varepsilon_0$, and $\Xi=(\varepsilon_0-1)/\varepsilon_0$.

Switching from the function g_q to $F(\xi,\eta,q_\perp)=g_q\times\exp(-\lambda\xi-\mu(\eta+\varepsilon_0))$, where $\lambda=-a^2(\gamma+\Xi^2/4)$, $\mu=-\Xi/2$, and $\eta=\varepsilon_x-1$, we obtain for F the heat-conduction equation in the standard form $\partial F/\partial\xi-a^2\partial^2F/\partial\eta^2=0$. As one can see from Eq. (3), the boundary condition for F is

$$F(\xi=2)=\exp(-2\lambda)F(\xi=0). \quad (6)$$

The variable η is used instead of ε_x on the basis of the form of the condition $F(\varepsilon_x\to 1)\to 0$.

The function $F(\xi)$ is determined by the well-known propagator for the equation of heat conduction on a semi-infinite axis $G(\eta,\eta')=(1/2a(\pi\xi)^{1/2})[\exp(-(\eta-\eta')^2/4a^2\xi)-\exp(-(\eta+\eta')^2/4a^2\xi)]$ and the function by the function $F(\eta,\xi=0)$

$$F=\left(\int_0^{\eta_0}+\int_{\eta_0}^{\infty}\right)G(\eta,\eta')F(\eta',\xi=0)\,d\eta'. \quad (7)$$

As follows from Eq. (4), for $\eta>\eta_0=\varepsilon_0-1$ the function $F(\xi=0,\eta)$ equals $F=F_M=\delta\cdot\varphi_M$, where

$$\delta=\exp\{-q_\perp^2/(4-X)\}/[2(1-X/4)],$$

$$\varphi_M=\exp\{-(\mu+1)(\eta+1)\}. \quad (8)$$

Substituting expressions (6) and (8) into Eq. (7) we obtain for the region $\eta<\eta_0$

$$F(\xi=0,\eta)=\alpha(\hat{K}F(\xi=0,\eta)+\delta\hat{K}_2\varphi_M), \quad (9)$$

where

$$\alpha = C\ \exp(-a^2 q_\perp^2/2\varepsilon_0),$$

$$C = (1/2a(2\pi)^{1/2})\exp[-a^2/(2(\Xi^2 + X/\varepsilon_0))],$$

$$\hat{K}_2\varphi_M = \int_{\eta_0}^{\infty} \exp(-(\eta'+1)(\mu+1))[\exp(-(\eta - \eta')^2/8a^2) - \exp(-(\eta+\eta')^2/8a^2)]d\eta',$$

$$\hat{K}F = \int_0^{\eta_0} F(\eta', \xi=0)[\exp(-(\eta-\eta')^2/8a^2) - \exp(-(\eta+\eta')^2/8a^2)]d\eta'.$$

Writing the solution (9) as a series $F = \delta\Sigma_{n=0}\alpha^{n+1}(\hat{K}^n\hat{K}_2)\varphi_M$, switching to g_q, taking the inverse Fourier–Bessel transform, and returning to the desired function $\delta f(\varepsilon_x)$, we obtain in the region $\eta < \eta_0$

$$\delta f(\varepsilon_x) = C\ \exp(\mu(\eta+1))\left[\exp(-u_\perp^2/d_1)\hat{K}_2\varphi_M/\zeta_1 + \sum_{n=1} C^n \exp(-u_\perp^2/d_n)\hat{K}^n\hat{K}_2\varphi_M/\zeta_n\right], \qquad (10)$$

where $\zeta_n = 1 + a^2 n(4-X)/2\varepsilon_0$ $(n>0)$, $d_n = (1 + Xa^2 n(4 - X)/8\varepsilon_0)/\zeta_n$.

Knowing $F(\xi=0,\eta)$ in the region $[0,\eta_0]$, $F(\xi=2,\varepsilon_x > \varepsilon_0)$, which determines the current through the barrier φ_2, and hence δf can be reconstructed according to the general formula of the theory of heat conduction with propagator G. It is easy to show that $\delta f(\varepsilon_x > \varepsilon_0)$ is determined by the same expression (10).

The series solution constructed converges rapidly even for $h/l_e \sim 0.01$, which corresponds to an extremely weakly ionized plasma (actually, however, for such rare Coulomb collisions, collisions with atoms must be taken into account). Then the small parameter is C.

Figure 2 shows the change $\delta f(\xi=0, \varepsilon_x = \eta+1)$ with $u_\perp = 0$ for several values of the parameter h/l_e. One can see

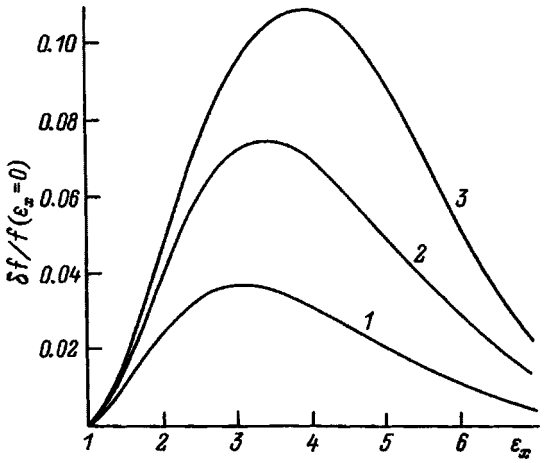

FIG. 2. Difference $\delta f = f_M - f$ of the EDF from the Maxwellian function as a function of longitudinal energy ε_x with $u_\perp = 0$ for several values of the parameter h/l_e. *1* — 0.2, *2* — 0.1, *3* — 0.05. The ratio $\varepsilon_0 = \varphi_2/T = 4$, $u_\perp = 0$.

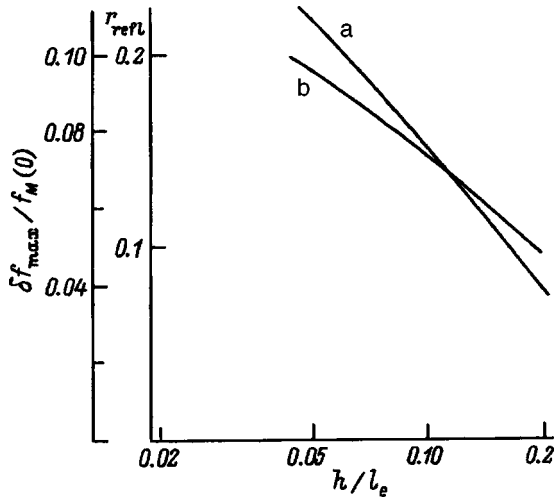

FIG. 3. Maximum of the function δf versus h/l_e for $u_\perp = 0$ and $\varepsilon_0 = \varphi_2/T = 4$ (a) and the analogous dependence of the reflection coefficient (b).

that $\delta f(\varepsilon_x)$ changes at $\varepsilon_x = \varepsilon_0$ smoothly and continuously, just as the function $f(u_x)$ at $u_x = -u_0$. At $u_x = u_0$ the function f undergoes a jump in the plane $\xi = 0$, since $f(u_x = u_0 + 0) = 0$, while $f(u_x = u - 0) = f(u_x = -u_0 + 0) \neq 0$ (Fig. 1b) and determines the electron current escaping to the anode. We note that the maximum of the function δf is shifted somewhat to the left of the point ε_0. As h/l_e decreases, the maximum shifts rightward, the half-width of the curve decreases somewhat, but the degree of localization of the solution near the point $\varepsilon_x = \varepsilon_0$, unfortunately, could be better, even for $h/l_e \sim 0.1$.

Nevertheless, the solution presented above gives a qualitative estimate of the reflection coefficient, equal to, as follows from the definition given,

$$k_{\text{refl}} = \int_{u_0}^{\infty} du_x u_x \int_0^{\infty} \delta f(u_x, u_\perp) u_\perp du_\perp \Big/ \int_{u_0}^{\infty} du_x u_x \times \int_0^{\infty} f_M(u_x, u_\perp) u_\perp du_\perp .$$

The dependence of k_{refl} on the parameter h/l_e is shown in Fig. 3 together with the dependence of the maximum of the function δf at the point $u_\perp = 0$. One can see that the curves correspond qualitatively to one another.

The main result is that even for a very large ratio $l_e/h \sim 10$ the reflection coefficient remains small and does not exceed 20%, which makes it possible, when calculating the plasma parameters in the gap, to use a very simple expression for the escaping thermal electron current over a wide range of values of the plasma parameters.

I am grateful to L. D. Tsendin, who pointed out the need for an examination of this problem, for fruitful discussions.

[1] F. G. Baksht, G. A. Dyuzhev, A. A. Kostin *et al.*, Zh. Tekh. Fiz. **47**, 263 [Sov. Phys. Tech. Phys. **22**, 153 (1977)].
[2] S. Murray, M. El-Genk, B. Wernsman, and V. Kaibyshev, J. Appl. Phys. **74**, 68 (1993).
[3] F. G. Baksht, V. B. Kaplan, A. A. Kostin *et al.*, Zh. Tekh. Fiz. **48**, 2273 (1978) [Sov. Phys. Tech. Phys. **23**, 2301 (1978)].

[4] F. G. Baksht, G. A. Dyuzhev, A. M. Martsinovskiĭ *et al.*, *Thermionic Converters and Low-Temperature Plasma* [in Russian], Énergoatomizdat, Moscow, 1973, 324 pp.
[5] N. I. Alekseev, V. B. Kaplan, and A. M. Martsinovskiĭ, Zh. Tekh. Fiz. **62**, 70 (1992) [Sov. Phys. Tech. Phys. **37**, 930 (1992)].
[6] F. G. Baksht and A. A. Kostin, Zh. Tekh. Fiz. **44**, 1 (1984) [Sov. Phys. Tech. Phys. **29**, 1 (1984)].
[7] F. G. Baksht, A. A. Kostin, A. M. Martsinovskiĭ, and V. G. Yur'ev, Pis'ma Zh. Tekh. Fiz. **5**, 905 (1979) [Sov. Tech. Phys. Lett. **5**, 374 (1979)].
[8] F. G. Baksht, B. Ya. Moĭzhes, and V. A. Nemchinskiĭ, Zh. Tekh. Fiz. **37**, 729 (1967) [Sov. Phys. Tech. Phys. **12**, 522 (1967)].

Translated by M. E. Alferieff

Parametric excitation of spin waves in uniaxial ferrites

A. V. Nazarov and A. G. Gurevich

A. F. Ioffe Physicotechnical Institute, Russian Academy of Sciences, 194021 St. Petersburg, Russia
(Submitted May 26, 1997)
Zh. Tekh. Fiz. **68**, 65–71 (May 1998)

Parametric excitation of spin waves in uniaxial ferrites with large anisotropy is investigated theoretically. First-order processes in a sphere with arbitrary orientation of an external static magnetic field, in which case the pumping is oblique, are studied. The threshold field and the parameters of the excited spin waves are calculated numerically for two ferrites — easy-axis and easy-plane. © *1998 American Institute of Physics*. [S1063-7842(98)01205-7]

INTRODUCTION

Parametric excitation of spin waves has been investigated[1] in detail for the case of transverse pumping: Energy transfer from uniform precession of magnetization (excited by an ac magnetic field perpendicular to the constant magnetization $\mathbf{M}_0$) to pairs of spin waves was studied. Somewhat later parametric excitation of spin waves with longitudinal pumping was investigated.[2,3] In this case energy was transferred to pairs of spin waves directly by an ac magnetic field parallel to $\mathbf{M}_0$. Parametric excitation of spin waves with longitudinal pumping in an easy-plane ferromagnet was investigated in Refs. 4 and 5. The results obtained were confirmed experimentally.[6–8] In the calculations in Refs. 4 and 5 as well as in the experiments of Refs. 6–8 and subsequent works the constant magnetization $\mathbf{M}_0$ was oriented in the same direction as the external static magnetic field $\mathbf{H}_{e0}$. However, this is realized (for easy-plane substances) only for the field $\mathbf{H}_{e0}$ lying in the easy plane or (for a sufficiently strong field) with $\mathbf{H}_{e0}$ directed along the hard axis; in the latter case this direction is very critical. Thus if the ac field $\mathbf{h}$ is parallel to $\mathbf{H}_{e0}$, then the pumping is longitudinal only in the particular cases indicated, while in the general case pumping is oblique, i.e., parametric excitation of spin waves is produced simultaneously by uniform precession and an ac magnetic field parallel to $\mathbf{M}_0$. In substances with a large anisotropy it is difficult to realize purely longitudinal or purely transverse pumping in an experiment. Parametric excitation of spin waves in a uniaxial anisotropic ferromagnet without assuming $\mathbf{M}_0$ and $\mathbf{H}_{e0}$ are parallel to one another was investigated in Ref. 9. However, in this work cases of purely longitudinal or purely transverse pumpings were investigated and, moreover, the threshold field was not minimized.

Parametric excitation of spin waves with oblique pumping in an isotropic ferromagnet was studied in Ref. 10, and in Refs. 11 and 12 the theory was extended to the case of weak cubic anisotropy. The interest being shown in magnetic materials with large anisotropy, specifically, hexagonal ferrites (see, for example, Ref. 13), is making the problem of parametric excitation of spin waves in strongly anisotropic ferrites with arbitrary, oblique pumping topical. The solution of this problem would make possible better use of measurements of the threshold fields of parametric excitation for studying relaxation processes in these materials.

The present work is a first step in this direction. The threshold fields for parametric excitation of spin waves with oblique pumping in ferrite single crystals with large uniaxial anisotropy with both an easy axis and an easy plane have been calculated. We have confined our investigation to first-order processes (the spin-wave frequency $\omega_k = \omega/2$, where ω is the pump frequency) in a spherical sample, while the ferrite was treated as a nonconducting ferromagnet. In what follows, some results of numerical calculations of the threshold field, specifically, the ratio of the threshold field to the spin-wave dissipation parameter as well as the parameters of the excited spin waves are presented for this case.

1. EQUATIONS FOR THE SPIN-WAVE AMPLITUDES

Consider a sphere consisting of uniaxial single-crystal ferromagnet placed in a static external magnetic field $\mathbf{H}_{e0}$. Let us choose the coordinates so that the equilibrium magnetization $\mathbf{M}_0$ is parallel to the z axis, while the anisotropy axis z' lies in the zy plane (Fig. 1). We take into account only the first anisotropy constant K_1, which can be both positive and negative. The effective anisotropy field can be represented in the form[14]

$$\mathbf{H}_{A1} = -\overleftrightarrow{N}^a \mathbf{M}, \tag{1}$$

where $\mathbf{M}$ is the magnetization, and the nonzero components of the anisotropy tensor $\overleftrightarrow{N}^a$ are

$$N^a_{22} = -\frac{2H_{A1}}{M_0}\sin^2\theta_0, \quad N^a_{23} = \frac{2H_{A1}}{M_0}\sin\theta_0\cos\theta_0,$$

$$N^a_{33} = -\frac{2H_{A1}}{M_0}\cos^2\theta_0. \tag{2}$$

Here $H_{A1} = K_1/M_0$ and θ_0 is the angle between the anisotropy axis and the constant magnetization (the z axis). The angle θ_0 can be determined from the transcendental equation[14]

$$\sin 2\theta_0 = \frac{H_{e0}}{H_{A1}}\sin(\theta_H - \theta_0), \tag{3}$$

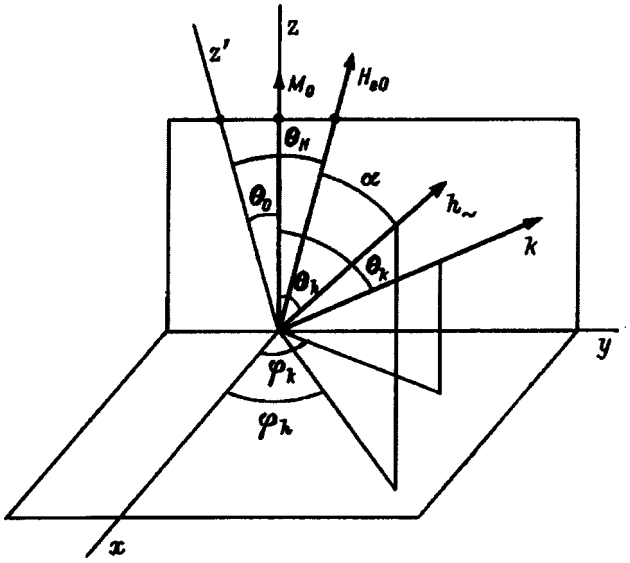

FIG. 1. Coordinate axes.

where θ_H is the angle between $\mathbf{H}_{e0}$ and the anisotropy axis (Fig. 1).

Let us examine a sphere magnetized to saturation. The condition for there to be no domain structure has the form

$$H_{e0}\cos(\theta_H-\theta_0)\geqslant 4\pi M_0/3. \tag{4}$$

Following Ref. 1, first we write the equation of motion for the magnetization neglecting dissipation

$$\frac{\partial \mathbf{M}}{\partial t}=-\gamma \mathbf{M}\times \mathbf{H}_{\text{ef}}, \tag{5}$$

where $\mathbf{M}=\mathbf{M}_0+\mathbf{m}$ is the magnetization including the constant and ac components, while the effective field

$$\mathbf{H}_{\text{ef}}=\mathbf{H}_{e0}+\mathbf{H}_{\text{ex}}+\mathbf{H}_a+\mathbf{H}_d+\mathbf{h}_\sim \tag{6}$$

consists of an external static magnetic field, the exchange field, the effective anisotropy field, the demagnetizing field, and the external ac field. We shall assume that the exchange interaction and the gyromagnetic ratio γ are isotropic. The exchange field in the case at hand can be written in the form

$$\mathbf{H}_{\text{ex}}=\frac{\eta}{\gamma M_0}\nabla^2\mathbf{m}, \tag{7}$$

where η is the inhomogeneous exchange constant.

The external ac field $\mathbf{h}_\sim=\mathbf{h}\cos\omega t$ is linearly polarized. Changing to circular variables $m_\pm=m_x\pm im_y$, $H_{\text{ef}\pm}=H_{\text{ef}x}\pm iH_{\text{ef}y}$, we obtain from Eq. (5)

$$-i\dot{m}_+=\gamma m_+H_{\text{ef}z}-\gamma M_zH_{\text{ef}+} \tag{8}$$

and a similar equation for m_-. We shall study small oscillations of the magnetization and assume that the length of the vector $\mathbf{M}$ is conserved. Then

$$M_z=M_0\left(1-\frac{m_+m_-}{2M_0}\right). \tag{9}$$

Let us expand the variables $m_\pm$ in Fourier series

$$m_+=M_0\sum_{\mathbf{k}} a_k\exp(i\mathbf{k}\cdot\mathbf{r}),$$

$$m_-=M_0\sum_{\mathbf{k}} a^*_{-k}\exp(i\mathbf{k}\cdot\mathbf{r}). \tag{10}$$

In these expansions the terms with $k=0$ correspond[1] to uniform magnetization oscillations, while the remaining terms correspond to spin plane waves. The expressions with are obtained in this case for $\mathbf{H}_{\text{ex}}$ and $\mathbf{H}_d$ are presented in Ref. 1. Let us write Eq. (8) and the equation for m_- in the variables a_k and a^*_{-k} and equate the terms multiplying $\exp(i\mathbf{k}\cdot\mathbf{r})$ on both sides of the equations. Let $a_{k\neq 0}\ll a_0\ll 1$. Then from Eq. (8) we obtain for $k=0$, neglecting small terms,

$$-i\dot{a}_0=a_0(\omega_H+\xi_a)-a_0^*\eta_a-\gamma h_{\sim\perp}, \tag{11}$$

where

$$\omega_H=\gamma H_{e0}\sin(\theta_H-\theta_0),\quad \xi_a=\frac{\omega_M}{8\pi}(N^a_{22}-2N^a_{33}),$$

$$\eta_a=\frac{\omega_M}{8\pi}N^a_{22},\quad \omega_M=4\pi\gamma M_0,$$

$$h_{\sim\perp}=h\sin\theta_h\exp(i\varphi_h)\cos\omega t. \tag{12}$$

Here h is the amplitude of the external ac field and θ_h and φ_h are its polar and azimuthal angles (Fig. 1). The solution of the system of equations (11) and the conjugate equation can be written in the form

$$a_0=a_0^+\exp(i\omega t)+a_0^-\exp(-i\omega t), \tag{13}$$

where

$$a_0^+=\frac{\gamma h\sin\theta_h}{\sqrt{2\omega_a}}\left(\frac{\sqrt{\omega_a+\omega_1}}{\omega_a-\omega}\exp(i\psi_h)\right.$$
$$\left.-\frac{\sqrt{\omega_1-\omega_a}}{\omega_a+\omega}\exp(-i\psi_h)\right),$$

$$a_0^-=\frac{\gamma h\sin\theta_h}{\sqrt{2\omega_a}}\left(\frac{\sqrt{\omega_a+\omega_1}}{\omega_a+\omega}\exp(i\psi_h)\right.$$
$$\left.-\frac{\sqrt{\omega_1-\omega_a}}{\omega_a-\omega}\exp(-i\psi_h)\right), \tag{14}$$

$$\omega_a^2=\omega_1^2-\eta_a^2,\quad \omega_1=\omega_H+\xi_a,$$

$$\tan\psi_h=\frac{h_y}{h_x}\frac{\omega_1+\omega_a}{\omega_a}. \tag{15}$$

In the expressions obtained the substitution $\omega_a\to\omega_a+i\gamma\Delta H_0/2$, where ΔH_0 is the dissipation parameter of uniform precession, must be made near resonance ($\omega=\omega_a$).

We now write Eq. (8) for $k\neq 0$, using the expressions for $\mathbf{H}_{\text{ex}}$ and $\mathbf{H}_d$ presented in Ref. 1, and retaining terms which contain a_0 in powers of no higher than first,

$$-i\dot{a}_k=(A_k+\xi_a+\lambda h_z+D_1)a_k$$
$$+[B_k\exp(2i\varphi_k)-\eta_a+D_2]a^*_{-k}. \tag{16}$$

A similar (adjoint) equation is obtained for a^*_{-k}. In Eq. (16) we introduced the following notation:

$$A_k=\omega_H-\gamma\frac{4\pi M_0}{3}+\eta k^2+\frac{\omega_M}{2}\sin^2\theta_k,\quad B_k=\frac{\omega_M}{2}\sin^2\theta_k,$$

$$D_1=-\frac{\omega_M}{2}\left(\frac{k_+k_z}{k^2}a_0^*+\frac{k_+^*k_z}{k^2}a_0\right)-\frac{\omega_M}{4\pi}N_{23}^a(a_0-a_0^*),$$

$$D_2=-\frac{\omega_M}{2}\frac{k_+k_z}{k^2}a_0-\frac{\omega_M}{4\pi}N_{23}^a a_0,\quad k_+=k_x+ik_y, \tag{17}$$

where θ_k and φ_k are the polar and azimuthal angles of the wave vector $\mathbf{k}$.

The coefficients D_1 and D_2 reflect the coupling between uniform precession and spin waves. They depend strongly on the magnitude and direction of the anisotropy field $\mathbf{H}_a$. The equation (16) and its adjoint are coupled even in the linear approximation. Let us switch to the amplitudes of the normal oscillations b_k and b^*_{-k}, performing a transformation similar to the third Holstein–Primakoff transformation,

$$a_k=\lambda_k b_k-\mu_k b^*_{-k},\quad a^*_{-k}=\lambda_k b^*_{-k}-\mu_k^* b_k, \tag{18}$$

$$\lambda_k=\sqrt{\frac{A_k+\xi_a+\omega_k}{2\omega_k}},$$

$$\mu_k=\sqrt{\frac{A_k+\xi_a-\omega_k}{2\omega_k}}\frac{[B_k\exp(2i\varphi_k)-\eta_a]}{|B_k\exp(2i\varphi_k)-\eta_a|}, \tag{19}$$

$$\omega_k^2=(A_k+\xi_a)^2-|B_k\exp(2i\varphi_k)-\eta_a|^2. \tag{20}$$

In Eq. (20) ω_k is the frequency of the spin waves. The equations which are obtained for the variables b_k and B^*_{-k} from Eq. (16) and its adjoint are coupled only as a result of the nonlinearity. Their solution can be sought in the form

$$b_k=b_k^0\exp(i\omega_k t),\quad b^*_{-k}=b^{0*}_{-k}\exp(-i\omega_k t), \tag{21}$$

where b_k^0 and b^{0*}_{-k} are slowly varying functions of time.

The equation for b_k^0 has the form

$$\begin{aligned}-i\dot b_k^0=&[\lambda_k^2(\gamma h_z+D_1)-\lambda_k(\mu_k^*D_2+\mu_kD_2^*)\\&+|\mu_k|^2(\gamma h_z+D_1^*)]b_k^0-[\lambda_k^2D_2+\mu_k^2D_2\\&-\lambda_k\mu_k(2\gamma h_z+D_1+D_1^*)]b^{0*}_{-k}\exp(2i\omega_k t).\end{aligned} \tag{22}$$

The second (adjoint) equation differs from Eq. (22) by the substitution $b_k^0\rightleftarrows b^{0*}_{-k}$ and complex conjugation.

2. THRESHOLD FIELD FOR FIRST-ORDER PROCESSES

Let us examine the case $\omega\approx 2\omega_k$. Following Eq. (1), we neglect in Eq. (20) and its adjoint all terms that vary rapidly in time. Such terms merely lead to a small high-frequency modulation. The equations obtained can be written in the form

$$\begin{aligned}i\dot b_k^0&=b^{0*}_{-k}\exp(i(\omega-\omega_k)t)Y_k,\\-i\dot b^{0*}_{-k}&=b_k^0\exp(-i(\omega-\omega_k)t)Y^*_{-k},\end{aligned} \tag{23}$$

where

$$\begin{aligned}Y_k=&\lambda_k^2\left(-\frac{\omega_M}{2}\frac{k_+k_z}{k^2}-\frac{\omega_M}{4\pi}N_{23}^a\right)a_0^+\\&+\mu_k^2\left(-\frac{\omega_M}{2}\frac{k_+^*k_z}{k^2}-\frac{\omega_M}{4\pi}N_{23}^a\right)a_0^{-*}\\&-\lambda_k\mu_k\left(\gamma h_z-a_0^+\omega_M\frac{k_+^*k_z}{k^2}-a_0^{-*}\omega_M\frac{k_+k_z}{k^2}\right).\end{aligned} \tag{24}$$

We shall now take account of the damping of the spin waves by making the substitution

$$\omega_k\rightarrow\omega_k+i\omega_{rk}, \tag{25}$$

where ω_{rk} is the relaxation rate of the spin waves.

It is not difficult to show that the amplitude of pairs of spin waves with wave vectors $\mathbf{k}$ and $-\mathbf{k}$ will grow for $|Y_k|>\omega_{rk}$. As the amplitude h of the ac field increases, at some point the energy transferred by the ac field to a pair of spin waves specified by the parameters k, θ_k, φ_k will exceed the damping described by the relaxation parameter $\Delta H_k=2\omega_{rk}/\gamma$. The threshold field $h_{\rm thr}$ can be obtained by minimizing the expression for h following from the condition $Y_k=\omega_{rk}$ taking account of expressions (19), (20), (23), and (24). The quantity $h_{\rm thr}$ can be expressed as

$$h_{\rm thr}=\min\left\{\frac{\omega_k\Delta H_k}{\omega_M|W_k|}\right\}, \tag{26}$$

where

$$\begin{aligned}W_k=&\frac{1}{4}(A_k+\xi_a+\omega_k)\left(\exp(i\varphi_k)\sin 2\theta_k+\frac{N_{23}^a}{\pi}\right)a_{01}\\&+\frac{1}{4}(A_k+\xi_a-\omega_k)\frac{[B_k\exp(2i\varphi_k)-\eta_a]^2}{|B_k\exp(2i\varphi_k)-\eta_a|^2}\\&\times\left(\exp(-i\varphi_k)\sin 2\theta_k+\frac{N_{23}^a}{\pi}\right)a_{02}\\&+[B_k\exp(2i\varphi_k)-\eta_a]\left[\frac{\cos\theta_h}{\omega_M}-\frac{a_{01}}{2}\exp(-i\varphi_k)\right.\\&\left.\times\sin 2\theta_k-\frac{a_{02}}{2}\exp(i\varphi_k)\sin 2\theta_k\right],\end{aligned} \tag{27}$$

$$\begin{aligned}a_{01}=&\frac{\sin\theta_h}{\sqrt{8\omega_a}}\left(\frac{\sqrt{\omega_a+\omega_1}}{\omega_a-\omega}\exp(i\psi_h)\right.\\&\left.-\frac{\sqrt{\omega_1-\omega_a}}{\omega_a+\omega}\exp(-i\psi_h)\right),\\a_{02}=&\frac{\sin\theta_h}{\sqrt{8\omega_a}}\left(\frac{\sqrt{\omega_a+\omega_1}}{\omega_a+\omega}\exp(i\psi_h)\right.\\&\left.-\frac{\sqrt{\omega_1-\omega_a}}{\omega_a-\omega}\exp(-i\psi_h)\right).\end{aligned} \tag{28}$$

We note that for the particular case of oblique pumping in an isotropic ferromagnet expressions (26)–(28) are iden-

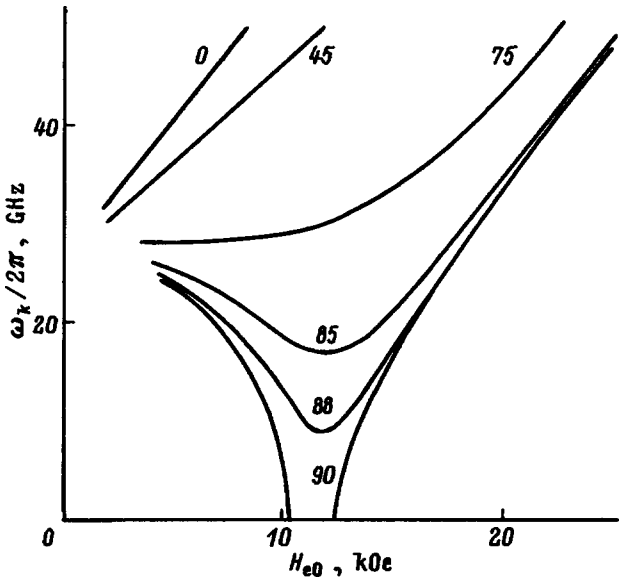

FIG. 2. Spectrum of spin waves with $k=0$ and $\theta_k=0$ for an easy-axis ferrite with $2H_{A1}=11$ kOe, $4\pi M_0=4500$ G. The numbers on the curves are the values of θ_H in degrees.

tical to the results obtained in Ref. 10, while in the case when the ac and static magnetic fields are oriented in the same direction and lie in the easy plane they agree with the results obtained in Ref. 5.

3. EXISTENCE REGIONS OF FIRST-ORDER PROCESSES

To determine the values of ω, H_{e0}, and θ_H for which parametric excitation of spin waves with frequency $\omega_k=\omega/2$ is possible it is necessary to take into consideration expression (20) for the spin-wave spectrum. As an example, we shall study two ferrites of practical interest: $BaFe_{11.4}Sc_{0.6}O_{19}$ and $Ba_2Zn_2Fe_{12}O_{22}(Zn_2Y)$. Figures 2 and 3 show the curves ω_k versus H_{e0} for these materials with different angles θ_H between the external field and the anisotropy axis. In the calculation of these curves for given values of H_{e0} and θ_H the angle θ_0 was found numerically using Eq. (3) and the value so obtained was then substituted into Eq. (20). The calculation was performed for $k=0$. As k increases, ω_k increases. Thus the curves $\omega_k(H_{e0})$ for different values of θ_H in Figs. 2 and 3 represent the limits above which spin wave excitation is possible by an ac magnetic field at the doubled frequency. The value of the angle θ_k was taken to be zero because the frequency ω_k assumes its lowest value (independent of φ_k) for this value.

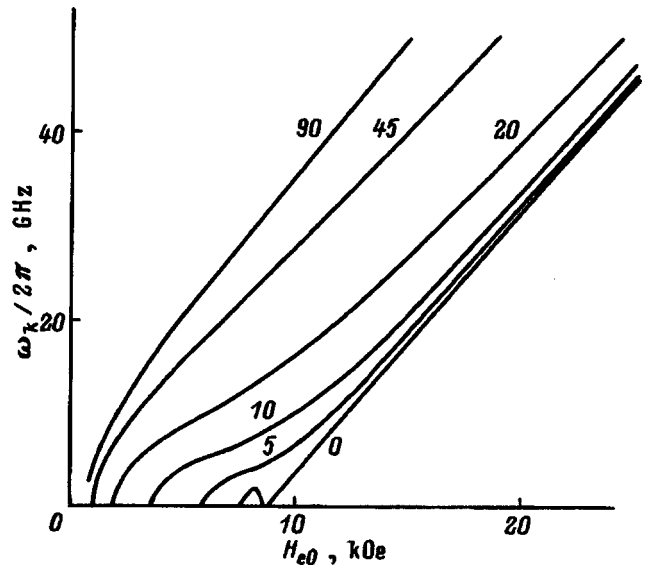

FIG. 3. Same as Fig. 2 for an easy-plane ferrite with $2H_{A1}=-8$ kOe, $4\pi M_0=2000$ G. The numbers on the curves are the values of θ_H in degrees.

One can see in Fig. 2 that for easy-axis ferrites and a high anisotropy field first-order processes leading to the parametric excitation of spin waves can exist (for not very high frequencies) only in a narrow range of angles θ_H (for example, with a pump frequency of 36 GHz the range of angles is $\theta_H=84.5$–$90°$). For $\theta_H=90°$ the first-order parametric spin wave excitation process is possible for any pump frequencies in an external field $H_{e0}=2H_{A1}$, but the value of θ_H in this case is very critical.

For easy-plane ferrites (Fig. 3) spin-wave excitation can occur for arbitrary values of the angle θ_H in a wide range of static magnetic fields.

4. COMPUTATIONAL METHOD

The calculation consisted of minimizing expression (26), taking account of Eqs. (27) and (28). The dissipation parameter ΔH_k appearing in Eq. (26) undoubtedly depends on k, θ_k, and φ_k, which, generally speaking, must be taken into account in the minimization procedure. If this dependence is unknown, then ΔH_k must be taken as constant in the minimization procedure. The quantities k, θ_k, and φ_k are related by the condition $\omega_k(k,\theta_k,\varphi_k)=\omega/2$. For this reason, in the minimization procedure it is sufficient to vary the parameters θ_k and φ_k. In the general case of high anisotropy and oblique pumping it is difficult to perform minimization analytically, but numerical methods can be used, equating the threshold field for different values of (θ_k, φ_k).

The quantities ω, H_{A1}, and M_0 and also ΔH_0 were taken as the constant parameters (ΔH_0 in reality depends on θ_0, but we neglected this dependence). It was assumed that $\varphi_h=90°$, which is usually the case in parametric spin-wave excitation experiments. The variable parameters were θ_H, H_{e0}, and the angle α between $\mathbf{H}_{e0}$ and $\mathbf{h}_{\sim}$ (Fig. 1), which for $\varphi_h=90°$ equals

$$\alpha=\theta_h-\theta_H+\theta_0. \tag{29}$$

The field H_{e0} ranged from 0 to 20 kOe, and the angles θ_H and α ranged from 0 to 90°. The angles θ_0 and θ_h were calculated for each value of H_{e0} using Eqs. (3) and (29), respectively. Next, the threshold field was found for each pair of values (θ_k, φ_k). The number of these pairs determined the computational accuracy. Neighboring values of θ_k and φ_k were equal to 0.25°. The pair (θ_k, φ_k) for which the threshold field assumed its lowest value was found. For this pair a check was made to determine whether or not the value of k corresponding to it is real. As a result, the program output for all values of θ_H and α the values of $h_{\text{thr}}/\Delta H_k$ as

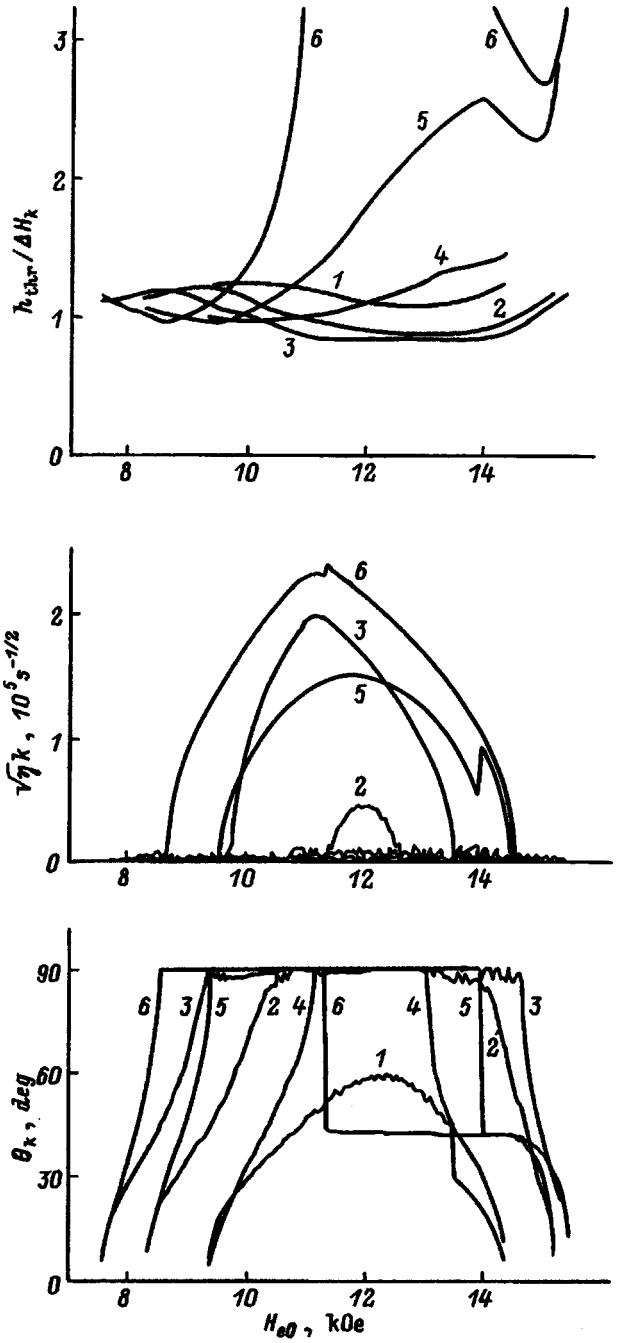

FIG. 4. Threshold field and parameters of the excited spin waves versus the static external magnetic field H_{e0} for an easy-axis ferrite with $2H_{A1}=11$ kOe, $4\pi M_0=4500$ G at pump frequency 36 GHz. α: *1–3* — 0; *4–6* — 90°; θ_H: *1,4* — 86, *2,5* — 88, *3,6* — 90°.

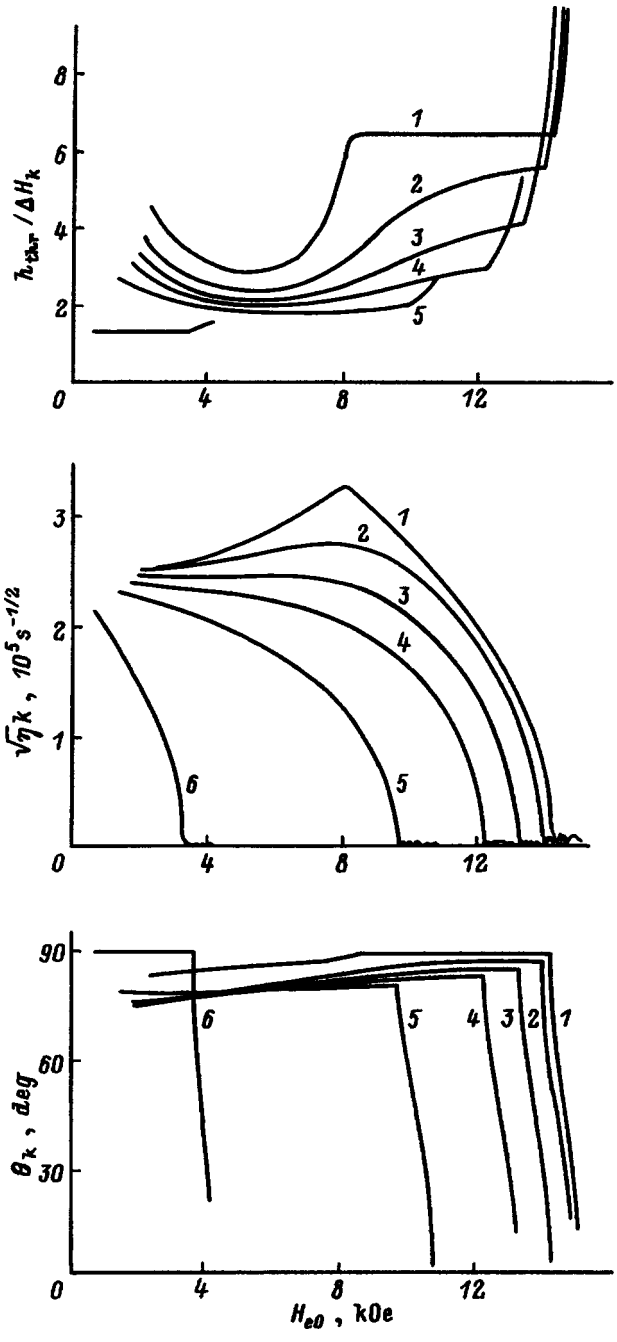

FIG. 5. Same as Fig, 4 for an easy-plane ferrite with $2H_{A1}=-8$ kOe, $4\pi M_0=2000$ G. θ_H: *1* — 0, *2* — 4, *3* — 8, *4* — 12, *5* — 88, *6* — 90°.

well as the parameters θ_k, φ_k, and $\sqrt{\eta}k$of the excited spin waves as a function of the intensity of the static external field H_{e0}.

5. COMPUTATIONAL RESULTS

Figures 4 and 5 show some results of calculations performed by the above-described method for the two ferrites mentioned in Sec. 3 and the pump frequency $\omega/2\pi=36$ GHz. Curves of $h_{\rm thr}/\Delta H_k$, $\sqrt{\eta}k$, and θ_k versus the static external magnetic field H_{e0} for different values of θ_H and two values of the angle α between the ac field and H_{e0} — $\alpha=0$ and 90° — are shown. These values correspond to quasilongitudinal and quasitransverse pumping, but as underscored above the pumping (for arbitrary values of θ_H) is oblique in both cases. We did not know the exact values of η for the ferrites studied. For this reason it was necessary to give the values of $\sqrt{\eta}k$. To estimate k for the excited spin waves the value $\eta\simeq 0.1$ of the exchange constant for yttrium iron garnet (YIG) can be used. The error arising in so doing will not be very large, since the Curie point and the average distances between the Fe^{3+} ions for these substances do not differ much.

It is evident from Fig. 4 that, as noted above, for the

easy-axis ferrite parametric excitation of spin waves considered is possible only in a narrow interval of angles θ_H. For $\alpha=0$ (quasilongitudinal pumping) the threshold field is virtually independent of H_{e0} and θ_H. The ratio $h_{\text{thr}}/\Delta H_k$ is close to 1, in contrast to weakly anisotropic ferrites, for example, YIG, where for longitudinal pumping at such frequencies it is much greater than 1. If $\alpha=90°$ (quasitransverse pumping), then the ratios $h_{\text{thr}}/\Delta H_k$ depend strongly on H_{e0} and the closer the field $\mathbf{H}_{e0}$ is to the hard direction $\theta_H=90°$, the more the they exceed 1. For $\alpha=90°$ and $\theta_H=90°$ the maximum threshold field is reached at $H_{e0}=11.3$ kOe and $h_{\text{thr}}/\Delta H_k$ equals 9.9. We note that the amplitude of uniform precession assumes its minimum value in such a field.

The curves of the wave numbers of the excited spin waves versus H_{e0} have wide ''humps'' where the values of k reach quite large values (of the order of 10^6 cm^{-1}, if the estimate mentioned above is used). For the case $\alpha=0$ these humps lie in the regions of H_{e0} where $\theta_k=90°$. The heights of the humps decrease as θ_H deviates away from 90°. We note that low values of k ($\sqrt{\eta}k\leqslant 10^4$) obtain on both sides of a hump, while for $\theta_H=86°$ (near the limiting value $\theta_H=84.5°$) they are obtained in the entire interval of admissible values of H_{e0}.

The polar angle θ_k of excited spin waves (Fig. 4) equals 90° in a quite wide range of values of H_{e0} for both quasilongitudinal and quasitransverse pumping and decreases as the limits of the intervals of H_{e0} where first-order parametric excitation is possible are approached. Without presenting the values obtained for φ_k, we note only that they depend strongly on H_{e0}. The sharp changes in the dependences $\varphi_k(H_{e0})$ and $\theta_k(H_{e0})$, as a rule, occur at the same values of H_{e0}, and these changes themselves are of an inverse character (as φ_k increases, θ_k decreases and vice versa).

For the easy-plane ferrite we present the computational results only for the case of quasilongitudinal pumping ($\alpha=0$). Turning to Fig. 5, we can see that for such a ferrite parametric excitation of spin waves is possible in a wide range of values of the external field H_{e0}, where (Fig. 2) spin waves with $\omega_k=\omega/2$ exist (we do not study the region of magnetic fields where domain structure exists). As θ_H decreases, i.e., as $\mathbf{H}_{e0}$ (and therefore $\mathbf{M}_0$ also) approaches the hard axis, the highest value of H_{e0} increases, and in the process h_{thr} also increase. As H_{e0} increases, the values of h_{thr} vary evenly, until they start to grow rapidly at some value $H_{e0}=H_c$, when the values of the wave vector k become very small; the rate of growth of h_{thr} increases as θ_H decreases. At this value of H_{e0} the angles θ_k, which were close to 90° in the entire range of high values of k, start to decrease rapidly. This behavior of h_{thr}, k, and θ_k as functions of H_{e0} is also qualitatively characteristic of purely longitudinal pumping.[4,6] The question of which oscillations or waves are excited, when the calculation in the plane wave approximation gives $k\simeq 0$, has been discussed in detail for purely longitudinal pumping (see, for example, Ref. 14) in ferrites with weak anisotropy. In our case this question requires a special analysis. The quantities φ_k for an easy-plane ferrite, in contrast to the easy-axis case, are essentially independent of H_{e0} and for large values of k they lie in the range 90–112°. The main features of the dependences obtained for $\alpha=0$ can be qualitatively explained if the contribution of the uniform precession of the magnetization is neglected. Then expression (26) can be put into the form

$$h_{\text{thr}}=\min\left\{\frac{\Delta H_k}{|4\pi M_0\sin^2\theta_k\,\exp(2i\varphi_k)+2H_{A1}\,\sin^2\theta_0|}\right\}\times\frac{\omega_M}{\gamma\,\sin\,\theta_h}. \tag{30}$$

It follows from this formula that the field h_{thr} can become infinite only when $\theta_0=0$. This happens for $\theta_H=0$: For all H_{e0} in the case $H_{A1}>0$ and for $H_{A1}<0$ in the case $H_{e0}>|2H_{A1}|$. For this reason, in all other cases the threshold field assumes finite values at the limits of the excitation region. It is also evident from expression (30) that for uniaxial ferrites with large anisotropy the threshold field is lower than for isotropic ferrites at such frequencies, since $|2H_{A1}|$ is much great than $4\pi M_0$. Moreover, formula (30) explains the increase in h_{thr} with decreasing θ_H for $H_{A1}<0$, so that for the same values of H_{e0} the value of θ_0, according to Eq. (3), decreases with θ_H. The condition for a minimum (30) requires that the angle $\theta_k=90°$; it is also necessary that $\varphi_k=0$ for $H_{A1}>0$ and $\varphi_k=90°$ for $H_{A1}<0$.

CONCLUSIONS

The parametric excitation of spin waves in a sphere consisting of a uniaxial ferrite (viewed as a ferromagnet) with a high anisotropy field was studied theoretically for first-order processes with arbitrary orientation of the static and ac magnetic fields relative to the anisotropy axis. The values of the threshold field and characteristics of the excited spin waves were found by numerical minimization. It is significant that very low threshold fields are possible for sufficiently high values of H_{A1}. The results obtained can be used to find the damping parameters of spin waves for different values of k, θ_k, and φ_k from experiments on parametric excitation of spin waves in strongly anisotropic materials.

A similar calculation can also be performed for an ellipsoid, specifically, films, as well as for second-order parametric spin wave excitation processes in strongly uniaxial ferrites.

We thank V. A. Bokov, S. S. Starobints, and O. A. Chivileva for helpful remarks made in a discussion of this work.

[1] H. Suhl, Phys. Chem. Solids **1**, 209 (1957).
[2] E. Schlömann, J. J. Green, and U. Milano, J. Appl. Phys. **31**, 386S (1960).
[3] E. Schlömann and R. I. Joseph, J. Appl. Phys. **32**, 1006 (1961).
[4] I. Bady and E. Schlömann, J. Appl. Phys. **33**, 1377 (1962).
[5] E. Schlömann, R. I. Joseph, and I. Bady, J. Appl. Phys. **34**, 672 (1963).
[6] J. J. Green and B. J. Healy, J. Appl. Phys. **34**, 1285 (1963).
[7] S. Dixon, J. Appl. Phys. **34**, 3441 (1963).
[8] S. Dixon, A. Bauber, and R. O. Savage, J. Appl. Phys. **36**, 873 (1965).
[9] V. V. Gann, Fiz. Tverd. Tela (Leningrad) **10**, 2177 (1968) [Sov. Phys. Solid State **10**, 1705 (1968)].
[10] Yu. M. Yakovlev, Fiz. Tverd. Tela (Leningrad) **10**, 2431 (1968) [Sov. Phys. Solid State **10**, 1911 (1968)].

[11] Yu. M. Yakovlev and Yu. N. Burdin, Fiz. Tverd. Tela (Leningrad) **16**, 466 (1974) [Sov. Phys. Solid State **16**, 299 (1974)].
[12] C. E. Patton, Phys. Status Solidi B **92**, 211 (1979).
[13] H. J. Kwon, J. Y. Shin, and J. H. Oh, J. Appl. Phys. **75**, 6109 (1994).
[14] A. G. Gurevich and G. A. Melkov, *Magnetic Oscillations and Waves* [in Russian], Nauka, Moscow, 1994, 462 pp.

Translated by M. E. Alferieff

Photoelectric properties of ITO/p^+–p^--InP solar cells in linearly polarized light

V. M. Botnaryuk, L. V. Gorchak, S. D. Raevskiĭ, and D. A. Sherban

State University, Kishinev, Moldova

V. Yu. Rud'

St. Petersburg State Technical University, 195251 St. Petersburg, Russia

Yu. V. Rud'

A. F. Ioffe Physicotechnical Institute, Russian Academy of Sciences, 194021 St. Petersburg, Russia
(Submitted November 27, 1996; resubmitted November 28, 1997)
Zh. Tekh. Fiz. **68**, 72–76 (May 1998)

Indium phosphide heterostructures and transparent conducting films of wide-gap oxides have previously been used in the development of highly efficient solar cells, making it possible to bring their efficiencies up to 18% [M. M. Koltun, *Optics and Metrology of Solar Cells* [in Russian], Nauka, Moscow (1985); V. M. Botnaryuk, L. S. Gagara, L. V. Gorchak et al., Geliotekhnika **23**, 37 (1990); V. Botnariuc, L. Gagara, E. Negru et al., Solar Energy in Romania **2**(1), 53 (1993)]. In the present paper results are reported from the first studies of the photoelectric properties, in linearly polarized light, of solar cells consisting of a heterojunction between single crystal indium phosphide and a mixed indium and tin oxide film (ITO film, $E_g \cong 3.6$ eV [G. Check and A. Genis, Solid State Techol. **23**(1), 102 (1980)]). © *1998 American Institute of Physics.* [S1063-7842(98)01305-1]

1. The design features of the solar cells used for these polarization studies are shown in Fig. 1. Physical and engineering studies have shown that the maximum efficiency can be realized reproducibly if an additional epitaxial layer of indium phosphide is deposited on single crystal slabs of indium phosphide. p^+–p^--InP structures were grown at temperatures of 720–750 °C in an In–PCl_3–H_2 chloride gas transport system on (100) oriented slabs of InP with free hole concentrations $p^+ \cong 2\times10^{18}$ cm^{-3} at $T=300$ K and misorientations of the order of 3–4° relative to the [110] direction. The InP was uniformly doped with zinc during the epitaxy process to yield layers with hole concentrations $p^- \cong 10^{16}$–10^{17} cm^{-3} and Hall mobilities $\mu_p \cong 90-120$ cm^2/(V·s) at $T=300$ K.

Single-layer ITO brightening coatings (with a geometric film thickness of roughly 500 Å) were deposited on the free, mirror surface of an epitaxial p-InP layer (Fig. 1) using pulverized alcohol solutions of the chlorides of indium ($InCl_3:3H_2O$) and tin ($SnCl_4:5H_2O$). The coatings were deposited on InP substrates heated to temperatures $T_s=400-500$ °C in an oxygen atmosphere for 40-60 s. The ITO films with the highest transparency in the visible and a transmission $T=95\%$ were obtained at $T_s=450$ °C with solutions having components in the proportion $InCl_3:SnCl_4 \cong 9:1$. Then the ITO films had a free electron concentration $n=10^{21}$ cm^{-3} and a Hall mobility $\mu_n \cong 30$ cm^2/(V·s). The films had a uniform dark-lilac color and high adhesion to the InP surface.

The polarization studies of the photosensitivity were conducted with an SPM-2 prism monochromator and polarizing filters that had nearly 100% polarization in the spectral region being studied. The structures were mounted on an STF-1 Fedorov stand, which made it possible to vary the angle of incidence Θ of the radiation in the plane of the detector and the azimuthal angle φ between the electric vector **E** of the light wave and the plane of incidence of the light with an accuracy of better than 30′.

2. Measurements of the dark current–voltage characteristics (Fig. 2, curve *1*) showed that these solar cells, with areas of 1–2 cm^2, had a reproducible rectification of 10^3–10^4 at bias voltages $U \cong 0.5$ V. The forward branch of these characteristics in the region $U>0.5$ V is approximated by the formula

$$U = U_{\text{cutoff}} + R_{\text{res}} i,$$

where $U_{\text{cutoff}}=0.42$–0.45 V and $R_{\text{res}}=400$–500 Ω for the different solar cells.

The reverse current at $U=1$ V for these solar cells is usually less than 10^{-7} A at $T=300$ K. The polarities of the rectification and photovoltage correspond to the energy diagram of ITO/p-InP. The current photosensitivity reached a maximum of $S_i=0.14$ A/W at $T=300$ K with illumination of the solar cells from the ITO side and turned out to be a technically reproducible parameter. A typical spectral plot of the relative quantum efficiency η, calculated as the ratio of the short-circuit photocurrent i to the number of incident photons, for one of the solar cells irradiated by unpolarized light along the normal to the plane of the ITO film is shown in Fig. 2 (curve *2*). It is clear that the ''window effect'' for the intensity of unpolarized light characteristic of real heterojunctions[5–7] exists here in the interval between the widths of the band gaps of the contact materials. The long-wavelength edge of η is exponential and is characterized by

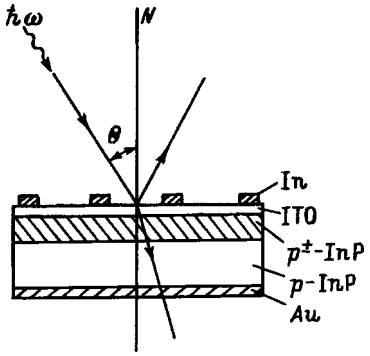

FIG. 1. The design of the ITO/InP heterojunction structures and the scheme for illuminating them.

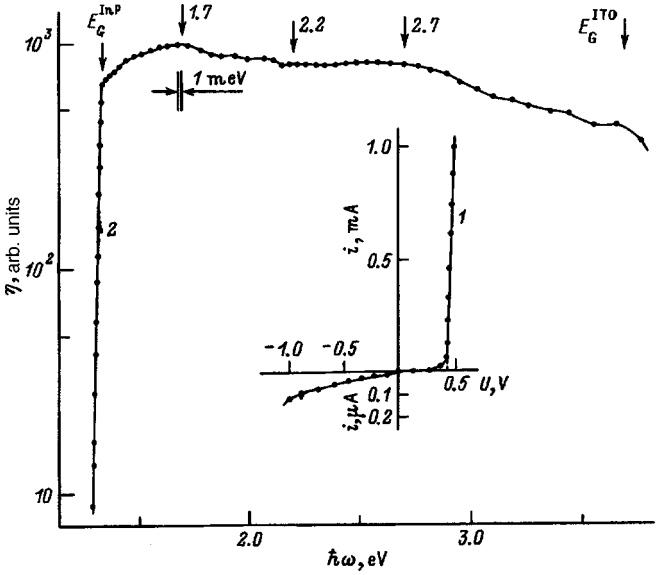

FIG. 2. Steady-state current–voltage characteristic (*1*) and the spectral variation in the relative photoconversion quantum efficiency (*2*) of an ITO/InP structure. $T=300$ K, illumination by unpolarized light, $\Theta=0$.

a steep slope $s=120$ eV^{-1}, which is typical of direct-gap materials, of which InP is one. The energy of the long-wavelength edge and the sharp step in the spectrum of η of the different solar cells at $\hbar\omega\cong1.335$ eV indicates that these features are ascribable to interband absorption of the radiation by a narrow-gap component of the ITO/InP heterojunction. The full width at half maximum (FWHM) of the spectral profile of η is as high as 1.9 eV, which characterizes these solar cells as wide-gap photoelectric converters in the spectral region of greatest interest for solar cells. The reproducible peaks at 1.7 and 2.7 eV and minimum at 2.2 eV in the region of maximum photosensitivity of the solar cells when illuminated by unpolarized light can apparently be attributed to interference of natural light in the ITO brightening coating. In fact, the thickness $d=480$ Å of the interference film estimated from the spectral position of these peaks and the known refractive index of ITO[8] is consistent with its geometric thickness.[1,8–10] However, the ratio of the values of η at the peaks and at the minimum is rather low (~1.15), which makes it impossible to interpret unambiguously the appearance of interference in the spectral η curves in natural light.

3. We now examine the data from our polarization photoelectric spectroscopy[11] studies of the ITO/InP solar cells. The major assumption in these studies reduces to the following. When solar cells are illuminated by linearly polarized light along the normal to the ITO plane (Fig. 2, angle of incidence $\Theta=0$), the short-circuit photocurrent is independent of the position of the electric field vector of the light wave relative to the principal crystallographic axes of the InP throughout the entire photosensitive region. Thus, there is no natural photopleochroism in these structures because of the isotropic nature of photoactive absorption.[11] A change to oblique incidence of the linearly polarized light ($\Theta\neq0$) is accompanied by unequal photocurrents when the electric vector **E** of the light wave is oriented parallel (i^p) and perpendicular (i^s) to the plane of incidence of the light, with $i^p>i^s$. As examples, Figs. 3a and 3b show typical plots of the photocurrents as functions of the angle of incidence (curves *1* and *2*). Clearly, as the angle of incidence Θ is increased, the photocurrents for both polarizations behave similarly: a rise, passage through a maximum, and a subsequent drop at large Θ. This is a new effect. In fact, it has been shown before that, in accordance with the Fresnel formulas for the transmission amplitude coefficients for a light wave at the boundary of two media (air–semiconductor), only for **E** parallel to the plane of incidence does the photocurrent have this behavior for sufficiently high surface quality, and the peak in i^p is associated with the elimination of reflection losses.[11–14] At the same time, the photocurrent i^s is observed to fall off monotonically with increasing Θ, which is also consistent with the Fresnel formulas, according to which an increase in Θ for **E** perpendicular to the plane of incidence is accompanied by increased reflection. In cases of degraded surface quality, both i^s and i^p fell monotonically with rising Θ.[15–18] In this case, the test object contains an ITO brightening coating, which may also be the cause of these features of $i^s(\Theta)$, which indicate reduced reflection losses for **E** parallel to the plane of incidence of the ITO film. Measurements of the polarization curves $i^p(\Theta)$ and $i^s(\Theta)$ over the entire photosensitive range of the solar cells showed that the inequality $i^p>i^s$ holds in the range $0\leqslant\Theta<90°$ studied here. For this reason, the polarization difference of the photocurrents $\Delta i=i^p-i^s$ retains a positive sign over the range of angles Θ and photon energies studied here, but its magnitude has a rather strong spectral variation for $\Theta=$ const (Fig. 3). Thus, for light with a photon energy $\hbar\omega=2.25$ eV (Fig. 3a), the value of Δi at similar angles Θ is much larger than for $\hbar\omega=1.72$ eV (Fig. 3b). In the latter case, the $i^p(\Theta)$ and $i^s(\Theta)$ curves tend to coincide, so $\Delta\rightarrow0$. Turning now to the spectral variation in the quantum efficiency of photon conversion (Fig. 2, curve *2*), it should be noted that the low polarization difference Δi at $\Theta\approx55°$ (where the light of both polarizations undergoes weak reflection and the photoactive absorption is high) accompanies a photocurrent peak, which is indicative of transparency. At the same time, we note that the high polarization difference Δi at $\hbar\omega=2.25$ eV (Fig. 3b), when the rise in the photocurrent predominates only for the polarization with **E** parallel to

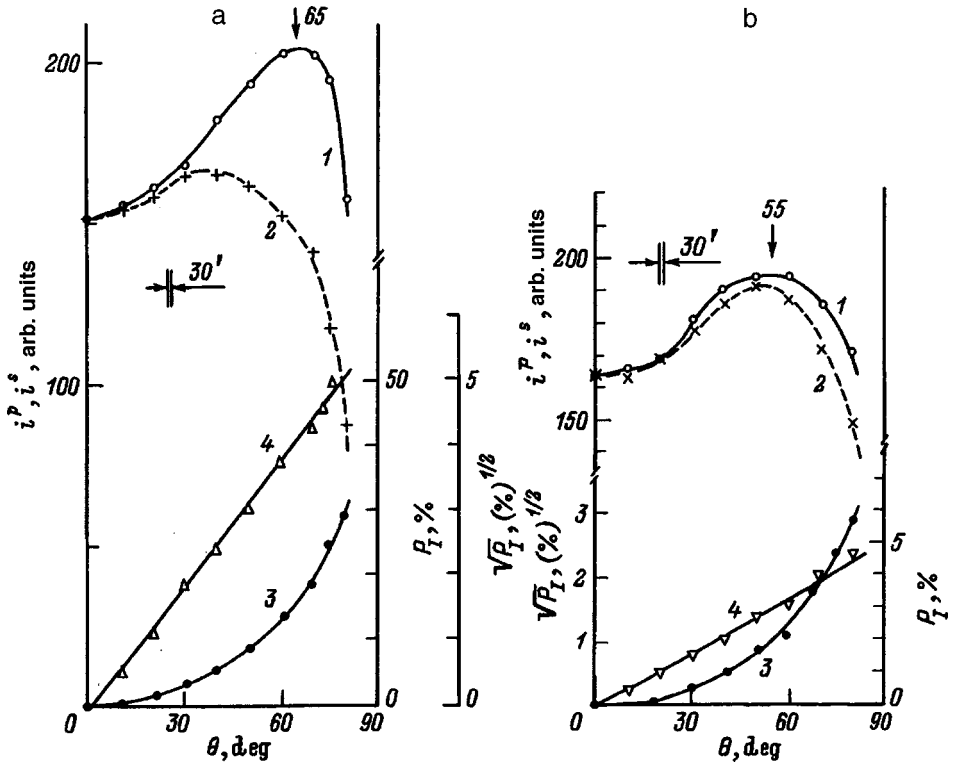

FIG. 3. The variations in the short-circuit photocurrents [(*1*) i^p, **E** parallel to the plane of incidence, (*2*) i^s, **E** perpendicular to the plane of incidence] and induced photopleochroism coefficient (*3*,*4*) of an ITO/InP structure. $T=300$ K; $\hbar\omega=2.25$ eV (a), 1.72 eV (b).

the plane of incidence, occurs at photon energies corresponding to the minimum in the photocurrent i^s near 2.2 eV (Fig. 2, curve *2*). Thus, as the contribution from transparency of the ITO film decreases, the $i^p(\Theta)$ and $i^s(\Theta)$ curves begin to approach those expected from the Fresnel formulas.[9,10]

Some typical examples of the variation in the coefficient of induced photopleochroism,[11]

$$P_i=\left(\frac{i^p-i^s}{i^p+i^s}\right)\cdot 100\%,$$

are shown in Figs. 3a and b (curves *3* and *4*).

Throughout the photosensitive region the induced photopleochroism of the solar cells is positive, and its sign agrees with the Fresnel formulas. For a fixed photon energy, the coefficient of photopleochroism obeys $P_i\sim\Theta^2$. At the same time, it should be emphasized that the coefficient of induced photopleochroism, like Δi, has a marked dependence on the photon energy. This last point conflicts with earlier analyses[19,20] and experimental data.[11–13] This is also related to the fact that in Ref. 20 the transparency effect has been neglected, while this effect essentially did not occur in the objects investigated in the previous studies.

Some typical spectral variations in the short-circuit photocurrents for the orthogonal polarizations at $\Theta=$const for one of the solar cells are shown in Fig. 4 (curves *1* and *2*). As with normal incidence of natural light on the frontal plane of the solar cell (Fig. 2, curve *2*), with oblique incidence of linearly polarized light in both polarizations the spectral variation in the photocurrent has a wide-gap character. The difference $\Delta i>0$ over the entire photosensitive spectral range, but its magnitude depends on the photon energy. This is because the photocurrents i^p and i^s oscillate over the spectrum in opposite phase. In fact, a maximum in i^p accompanies a minimum in i^s, and vice-versa. The energy separation between the peaks, as in the case of unpolarized light (Fig. 2), may be ascribed to interference of linearly polarized light in the ITO. Here it should be emphasized that the depth of modulation of the photocurrent over the spectrum for obliquely incident linearly polarized light is greater than for unpolarized light (Fig. 2).

Figure 4 also shows a typical spectral plot of the induced photopleochroism coefficient $P_i(\hbar\omega)$ of an ITO/InP cell for $\Theta=$const. This curve illustrates the pronounced oscillatory character of the photopleochroism. The energies of the maxima and minima correlate with those determined from the spectral plots of η, but it is evident that the reliability with which they are determined from the $P_i(\hbar\omega)$ curves for $\Theta=$const is certainly greater. This happens, first of all, because as the transparency effect sets in, light of both polarizations undergoes strong absorption, because of which $i^p\cong i^s$ and $P_i\to 0$. Both the minima in the $P_i(\hbar\omega)$ curve at 1.8 and 2.8 eV are related to this. The onset of the transparency effect is controlled by the optical thickness of the ITO film. The peaks in the $P_i(\hbar\omega)$ curves occur when Δi reaches a maximum during the scan over the spectrum. This situation evidently arises when i^p attains a maximum and i^s, a minimum. The latter accompanies transparency for the p-wave and reflection of the s-wave and is most distinct under conditions of pseudo-Brewster reflection.[9,10] This effect is completely controlled by the state of the air–film boundary and is determined solely by the refractive index of the ITO. This latter point is confirmed by the fact that the refractive index determined[20] from the values of the induced photopleochroism coefficient at the peaks (28% for 1.3 eV and 25% for 2.3 eV; Fig. 4, curve *3*), is $n=1.8$–2.0, which agrees with the known value for ITO.[8]

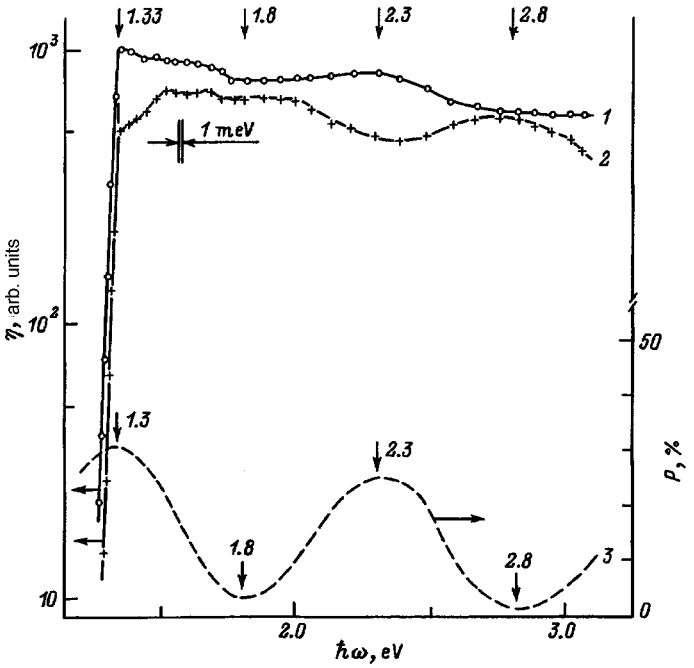

FIG. 4. Spectral variations in the relative photoconversion quantum efficiency (*1* — **E** parallel to the plane of incidence, *2* — **E** perpendicular to the plane of incidence) and in the induced photopleochroism coefficient (*3*) of an ITO/InP structure. ($T=300$ K, $\Theta=70°$).

In conclusion, we note that these solar cells provide a maximum azimuthal photosensitivity of ≈ 80 mA/W·deg for $\Theta = 75–80°$. Thus, the induced photopleochroism of ITO/InP structures can be used in photoelectric polarimetric systems. On the other hand, it should also be noted that polarization photoelectric spectroscopy of ITO/InP solar cells may find applications in process control in the preparation of brightening coatings and for diagnostics of the quality of such coatings in fabricated structures.

[1] M. M. Koltun, *Optics and Metrology of Solar Cells* [in Russian], Nauka, Moscow (1985), 280 pp.
[2] V. M. Botnaryuk, L. S. Gagara, L. V. Gorchak *et al.*, Geliotekhnika **23**, 37 (1990).
[3] V. Botnariuc, L. Gagara, E. Negru *et al.*, Solar Energy in Romania **2**(1), 53 (1993).
[4] G. Check and A. Genis, Solid State Technol. **23**(1), 102 (1980).
[5] B. L. Sharma and R. K. Purokhit, *Semiconductor Heterojunctions*, Pergamon, Oxford (1974).
[6] A. V. Lunev, Yu. V. Rud', M. A. Tairov *et al.*, Izv. Vyssh. Uchebn. Zaved. Fiz. **31**(8), pp. 39–45 (1988).
[7] A. Milnes and D. Feucht, *Heterojunctions and Metal–Semiconductor Junctions*, Academic Press, New York (1972) [Russian trans., Mir, Moscow (1975), 432 pp.].
[8] V. I. Strikha and S. S. Kil'chitskaya, *Metal–Semiconductor Junction Solar Cells* [in Russian], St. Petersburg (1992), 136 pp.
[9] G. S. Landsberg, *Optics* [in Russian], Moscow (1976), 926 pp.
[10] I. S. Gorban', *Optics* [in Russian], Vishcha Shkola, Kiev (1979), 224 pp.
[11] Yu. V. Rud', Izv. Vyssh. Uchebn. Zaved. Fiz. **29**(8), pp. 68–86 (1986).
[12] S. G. Konnikov, D. Melebaev, V. Yu. Rud' *et al.*, Pis'ma Zh. Tekh. Fiz. **18**(12), 39 (1992) [Sov. Tech. Phys. Lett. **18**, 382 (1992)].
[13] S. G. Konnikov, D. Melebaev, V. Yu. Rud' *et al.*, Pis'ma Zh. Tekh. Fiz. **18**(24), 11 (1992) [Sov. Tech. Phys. Lett. **18**, 798 (1992)].
[14] S. G. Konnikov, V. Yu. Rud' and Yu. V. Rud', Jpn. J. Appl. Phys. **32**, 515 (1993).
[15] D. Melebaev, V. Yu. Rud', and Yu. V. Rud', Cryst. Res. Technol. **31**, 269 (1996).
[16] V. Yu. Rud' and Yu. V. Rud', in *Abstracts of the 3rd International Workshop: Expert Evaluation and Control of Compound Semiconductor Materials and Technologies*, Freiburg, Germany (1996), p. 31.
[17] V. Yu. Rud', Author's Abstract of Candidate's Dissertation [in Russian], St. Petersburg (1995), 19 pp.
[18] Yu. V. Zhilyaev, N. Nazarov, V. Yu. Rud' *et al.*, Fiz. Tekh. Poluprovodn. **27**, 1611 (1993) [Semiconductors **27**, 890 (1993)].
[19] Yu. V. Rud' and G. A. Medvedkin, Inventor's Certificate USSR No. 671634; Byull. Izobret., No. 41 (1980).
[20] G. A. Medvedkin and Yu. V. Rud', Phys. Status Solidi A **67**, 333 (1981).

Translated by D. H. McNeill

Simulation of the free molecular flow of vapor for laser isotope separation

R. I. Golyatina, A. N. Tkachev, and S. I. Yakovlenko

Institute of General Physics, Russian Academy of Sciences, 117942 Moscow, Russia
(Submitted October 24, 1996)
Zh. Tekh. Fiz. **68**, 77–81 (May 1998)

Vapor flows from a single channel (tube) and from a set of tubes are simulated in the free molecular motion approximation. The integrated characteristics (the fractions of transmitted, sticking, and reflected particles) and the angular distributions of the flux and flux density of the vapor are obtained. Calculations of the flux of atoms scattered as a result of single collisions in an atomic beam are performed. © *1998 American Institute of Physics.*
[S1063-7842(98)01405-6]

INTRODUCTION

The problem of obstruction of the collector during atomic vapor laser isotope separation (AVLIS) was considered in Refs. 1 and 2 (see, for example, Refs. 3–6). A more complete analysis calls for consideration of the properties of the vapor source which determine the density and velocity distribution of the atoms in the ionization zone (Fig. 1). Below we shall discuss in more detail a treatment of a vapor source in the form of a set of narrow channels (usually tubes). Such sources have been treated several times.[7–9] However, the problem of laser isotope separation has its own special features, which call for an additional analysis. Moreover, the method proposed in Refs. 1 and 2 for calculating the characteristics of a scattered atomic flux can be improved significantly.

FLOW FROM A SINGLE CHANNEL

Effective model. The free molecular propagation of atoms along a channel is considered, i.e., only their collisions with the walls of the tube are taken into account. In the code produced the scattering was assumed to be a mixture of diffuse and specular reflection. In addition, the possibility of absorption of particles on the walls was taken into account.

Specifically, the following situation was simulated. The bottom of a channel of length l, which had the form of either a cylindrical tube of diameter d or a tube of rectangular cross section (when a slit was simulated, one of the dimensions was taken fairly large) was assumed to be an emitting surface. The distribution of the particles emitted from the bottom of the channel with respect to their velocity v was taken in the form

$$f_T(v)=Cv_x \exp(-m(v-V)^2/2T),$$

$$\int dv f_T(v)=1, \quad -\infty<v_y,v_z<\infty \quad 0<v_x<\infty. \qquad (1)$$

Here the x axis is parallel to the tube axis, m is the mass of an atom, T is the temperature of the vapor in the bath, V is the mean flow velocity, and C is a normalization constant. When $V=0$, the distribution (1) corresponds to the Maxwellian distribution function in the volume serving as the source of particles (in the bath). The analogous distribution for $V=0$ and $T=T_w$, where T_w is the temperature of the walls, was used for diffusely reflected particles. In a certain sense such a reflection law is analogous to the familiar Lambert law in optics. In the general case it was assumed in simulating reflection that a particle can be reflected diffusely with a certain probability, can be reflected specularly with a certain probability, and can stick to the wall with a certain probability.

We note that consideration of the free molecular flow of atoms is confined to fairly low densities $N\ll 1/\sigma l$, where σ is the elastic collision cross section of the atoms.

Passage of atoms through a channel. In the case of diffuse reflection in a tube, the fraction k of particles passing through the tube decreases, as expected, when the length-to-diameter ratio l/d of the tube is large. For long tubes ($l/d>100$) k practically coincides with the asymptote $k\cong 4d/3l$, and over the entire range of l/d, including short tubes, it is approximated well (to within no less than 3%) by the simple dependence $k=(1+0.17\sqrt{x}+0.75x)^{-1}$, where $x\equiv l/d$.

In the case of absorbing walls, the dependence of the fraction of reflected particles on the relative length of the channel $l/\Delta l$ is of great interest (where Δl is the caliber, i.e., the smallest transverse dimension of the channel) is of great interest. One important situation should be noted: if the walls

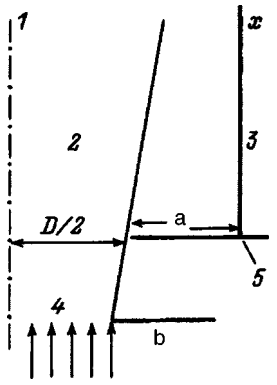

FIG. 1. Geometry of the problem of the formation of the vapor flux and ion extraction in laser isotope separation: *1* — symmetry axis, *2* — ionization zone, *3* — collector, *4* — vapor source, *5* — diaphragm, *6* — bath.

absorb particles with a certain probability $p<1$, then for a Maxwellian distribution of the particles in the volume in contact with the channel (where $V=0$), the fraction of reflected particles R is not negligibly small compared with the probability p even in the case of an infinitely long channel. It amounts to $R\cong 0.2p-0.3p$ for both square channels and planar slits (Fig. 2). This is natural. For a random velocity distribution and long channels, the greatest contribution to reflection is made by the part of the surface near the entrance to the channel; therefore, an increase in the channel length has practically no influence on the probability R of the reflection of an atom, although it strongly lowers the probability of its passage through the channel. At the same time, for long tubes the reflection coefficient R drops sharply as the directivity of the atomic flux increases, i.e., when $V\sqrt{m/2T}\gg 1$. This is also fully understandable. When the flux is directed, a large portion of the atoms collide with the wall far from the entrance to the channel. Hence the probability of the escape of particles in the backward direction is small, especially when the probability of diffuse scattering is low in comparison to absorption ($p\ll 1$).

Angular distribution of the atomic flux. The distribution of the atoms escaping from the end of a tube is usually characterized by the flux density distribution of the atoms with respect to the angle between the symmetry axis and the direction of their velocity. For practical utilization of the calculation results it is more convenient to tabulate the distribution of the flux density of the atoms $j(\rho)$ in a plane perpendicular to the symmetry axis as a function of the reduced distance to the tube axis $\rho=r/x_0=\tan\Theta$. Here r is the radius in the plane, x_0 is the distance from the end of the tube to the plane ($x_0\gg d$), and Θ is the angle between the tube axis and the direction to a selected point in the plane. In this case $2\pi\cdot j(\rho)\rho d\rho$ gives the probability that an atom will impinge on the ring $(\rho,\rho+d\rho)$.

As we know, as the ratio of the length of the tube to its diameter increases, the directivity of a certain fraction of the atomic flux increases (Fig. 3). However, there are several effects to which proper attention is usually not directed.

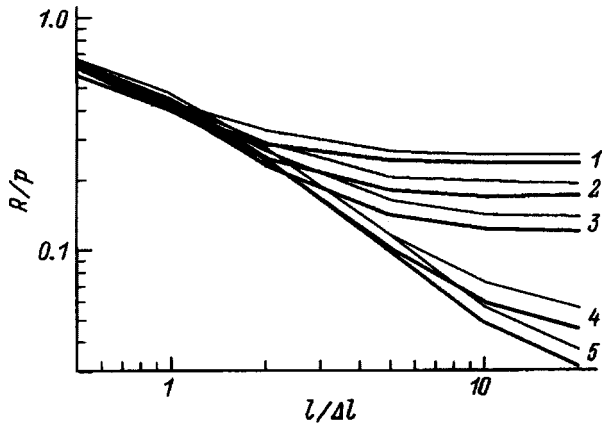

FIG. 2. Reflection of atoms from channels with absorbing walls (a planar slit). $v\sqrt{m/2T}$: *1* — 0, *2* — 1, *3* — 2, *4* — 5, *5* — 10 for $p=0.1$ (thick curves) and $p=0.3$ (thin curves). A ''blind'' channel is considered, i.e., it is assumed that the exit cross section of the channel absorbs particles with the same probability as its walls.

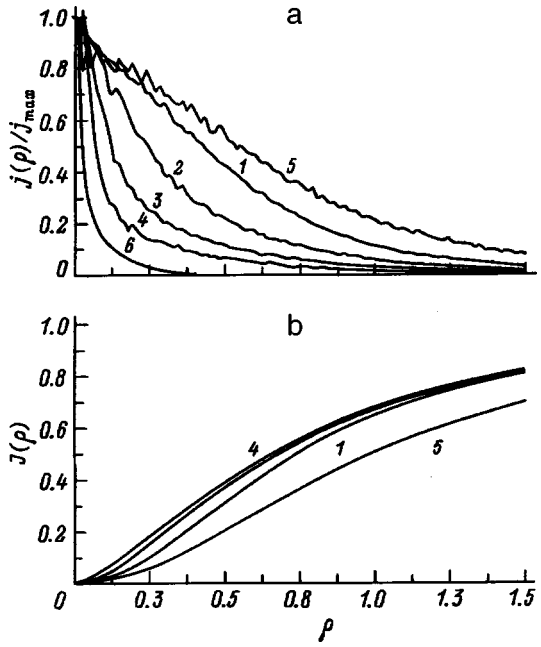

FIG. 3. Directivity of an atomic flux passing through a cylindrical tube: a — flux density distributions of the atoms in a plane perpendicular to the tube axis normalized to the maximum values; b — integrals of the flux density distributions; *1–4* — diffusely reflecting walls in the absence of absorption for $d/l=1$, 3.3, 10, 33; *5* — specularly reflecting walls for $d/l=33$. The atoms have a Maxwellian distribution before the entrance to the tube.

When the relative tube length l/d is increased, the fraction of particles passing through it without collisions decreases proportionally to the square of the reciprocal of the relative length $(d/l)^2$. At the same time, the total number of particles passing through the tube decreases only linearly, i.e., proportionally to d/l. This is because the contribution of the particles scattered by the walls predominates. The large contribution of the scattered particles causes the fraction of particles forming the ''pedestal'' of the peak of the angular distribution to increase as the relative length of the tube is increased. Therefore, when $r\sim x_0$ the probability $J(\rho)=\int_0^\rho 2\pi\cdot j(u)u du$ that atoms will impinge on the area within a circle of radius $r=\rho x_0$ is practically identical even for highly different values of l/d (Fig. 3b).

This fact contradicts the data in Ref. 8, according to which the flux at large angles relative to the axis is negligibly small (curve *6* in Fig. 3a, where $d/l=33$). Figure 4 is most instructive in this sense. The angle Θ_α, within which an appreciable fraction α of the flux of atoms passing through the tube is found, depends weakly on the relative length l/d. At the same time, the angle corresponding to half height of the distribution (curve *4*) depends significantly on the relative length of the tube. We note that our results differ strongly from the data in Ref. 9 (cf. curves *1* and *5*). Possibly the data presented in Ref. 9 was for twice the angle corresponding to half height of the distribution rather than for the angle within which half of all the particles escaping from the tube are found (as was stated in that paper[9]). This notion is indirectly confirmed by the fact that curve *6*, which was reconstructed from the data in Ref. 9, agrees fairly well with the dependence which we obtained (curve *4*).

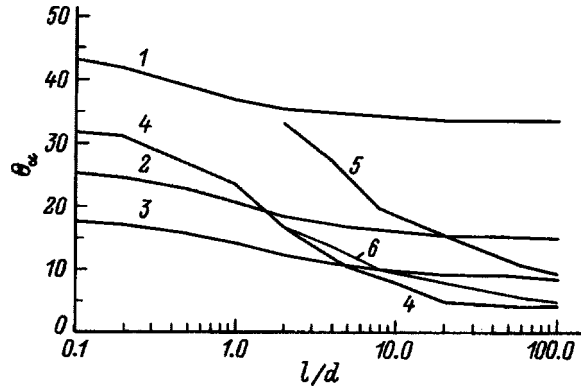

FIG. 4. Angles Θ_α within which the assigned fractions $\alpha=0.5$, 0.2, and 0.1 of particles escape from a tube (*1–3*).

In designing an ion-extraction system for laser isotope separation it is important to take into account the fact that the majority of the particles passing through long tubes are scattered at large angles, since particles scattered at large angles can obstruct a collector which is oriented parallel to the vapor flux and receives the ions extracted from the plasma (Fig. 1).

We also note that in the case of the specular reflection of particles by the walls the beam of particles escaping from a tube has an even greater spread of transverse velocities (curve *5* in Fig. 3a). This is because the particles entering the tube at large angles relative to its axis are not cut off in the case of specular reflection.

FLOW FROM A SET OF TUBES

Flow characteristics in an elongated source. The distribution of the total flux from a large set of tubes filling an elongated rectangle of the dimensions $\Delta L\times L$ is usually of interest. To ensure the maximum flow rate of the substance, the tubes are arranged as close as possible to one another. The total flux is obtained by summing the fluxes at a given point from all the tubes.

We wrote programs, which permit the calculation of the flux density distribution of atoms for any level of filling of the rectangle by tubes. Here we confine ourselves to consideration of only two variants: a) one row of tubes, and b) 20 rows of tubes. In both variants the length of the system of tubes was $L=1$, and the height of the tubes was $l=10$ mm. In the first variant we considered one row of 500 tubes with a diameter $d=2$ mm ($\Delta L=2$ mm). In the second variant we considered 2000×20 tubes with a diameter $d=0.5$ mm within a width $\Delta L=15$ mm. The coordinate system was positioned at the center of the rectangle formed by the tubes, the x axis, as before, being oriented to be parallel to the axes of the tubes, the y axis being parallel to the width of the rectangle, and the z axis being parallel to its length.

As expected, the distribution of the flux density from the system of tubes with respect to the z axis has a nearly rectangular shape (Fig. 5). On the other hand, almost the same distribution, which is defined by the expression

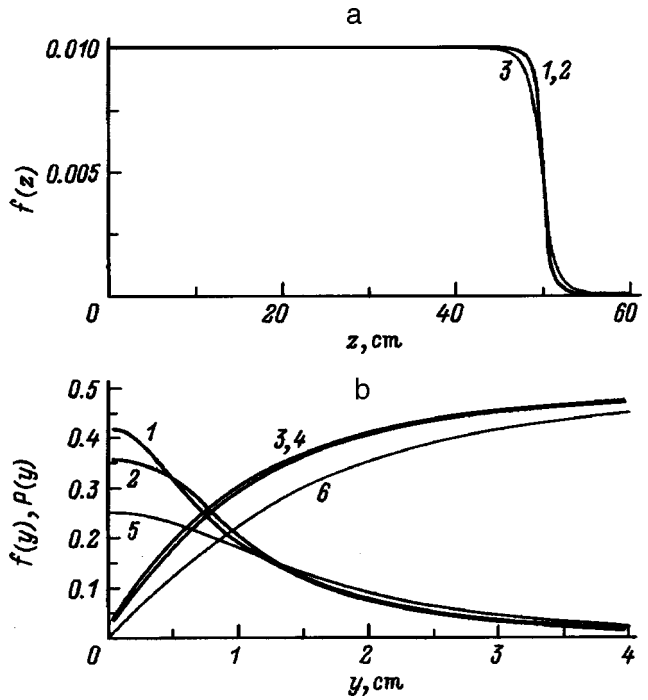

FIG. 5. Flux distribution of atoms passing through a set of parallel cylindrical tubes forming a rectangle of width ΔL and length L. Probability densities $f(z)$ and $f(y)$ that an atom will impinge on a unit of surface of the plane perpendicular to the axes of the tubes at a distance $x_0=20$ mm from the ends of the tubes. a — As a function of the distance to the symmetry plane (along the z axis) in the cross section passing through half of the width: *1, 2* — 1 and 20 rows of tubes, respectively; *3* — distribution of the equilibrium emission of atoms from an infinitely narrow, infinitely shallow slit. b — As a function of the distance to the symmetry plane (along the y axis) in the cross section passing through half of the length (in a transverse cross section): *1, 3* — one row of tubes; *2, 4* — 20 rows; *5, 6* — characteristics of the equilibrium emission of atoms from an infinitely narrow, infinitely shallow, and infinitely long slit. Curves *3, 4,* and *6* give the probability $P(y)$ that an atom will impinge on a band of width $0-y$.

$$f(z)=\frac{2x_0^3}{\pi L}\int_{-L/2}^{L/2}\frac{du}{[(u-z)^2+x_0^2]^2},$$

is produced by an infinitely narrow, infinitely shallow slit ($\Delta L\to 0$ and $l\to 0$, curve *3* in Fig. 5a) (the explicit expression for this integral is not presented because of its cumbersome nature).

In the case of many rows of tubes the distribution in the transverse direction along the y axis is somewhat more homogeneous than the distribution from a single row of tubes (curves *1* and *2* in Fig. 5b). However, the fraction of atoms scattered at large angles in the transverse direction is significant because of the effects mentioned above; therefore, the total probability $P(y)$ that an atom which has passed through a tube will impinge on a band of width y practically coincides for one and many rows of tubes (curves *3* and *4* in Fig. 5b). For comparison, we present the distributions

$$j(y)=\frac{1}{2x_0}\frac{1}{[1+(y/x_0)^2]^{3/2}},\qquad P(y)=\frac{1}{2}\frac{y}{\sqrt{y^2+x_0^2}},$$

which correspond to a source in the form of an infinitely

narrow, infinitely shallow, and infinitely long slit ($\Delta L \to 0$, $l \to 0$, and $L \to \infty$; curves *5* and *6* in Fig. 5b).

Neglect of the atom–atom collisions in the beams from different tubes imposes an additional constraint on the gas density at the end of the tubes $N \ll 1/\sigma \Delta L$. This simple *a priori* criterion possibly needs refinement, which can be done later on, if we can treat the problem with adequate consideration of the atom–atom collisions.

FLUXES IN THE WORKING ZONE

Simulation of the flux distribution without collisions. In Refs. 1 and 2 the distribution of the vapor density in the working zone was determined on the basis of direct simulation by calculating the time which test particles spend in a given cell in space. The method used in the present work is simpler and more exact.

In the free molecular flow regime, the analog of the optical law of the conservation of the value of the intensity along a beam in a transparent medium is known to hold: $f(\xi, v) = f(\xi + v\tau, v)$. Here f is the bulk distribution function of the particles with respect to the velocity vector v at an arbitrary point in space ξ, and τ is an arbitrary time interval. Therefore, after assigning a velocity grid at an arbitrary point in space and constructing the corresponding beams until they intersect with surfaces, which either emit particles or bound a volume, we can reconstruct the distribution function at any point in space. Then integrating the distribution function over the velocities, we obtain the particle density at the respective point.

Consideration of single collisions. As was shown in Refs. 1 and 2, in the zone of multiple ionization of a vapor its density should be small enough that the mean free path of the atoms would significantly exceed the transverse dimensions of the zone. However, single collisions must be considered in order to take into account the vapor flux in the region of the geometric shadow, which is usually created by the diaphragm protecting the collector from direct impingement of the atomic flux (see Fig. 1). In the present work the collision act was also simulated as in Refs. 1 and 2; however, the initial vapor density and the velocity distribution functions of the particles in the cell were calculated by the method described above.

Scattered flux. An expression for a uniform atomic flux of width D, which is infinite along the y and z axes and scattered in single collisions, was obtained in Refs. 1 and 2. It was assumed that the atoms move collinearly to the x axis and that the distribution with respect to the absolute value of the velocity is ''semi-Maxwellian:''

$$f_x(v) = 2(m/\pi T)^{1/2} \exp(-mv^2/2T),$$
$$-\infty < v_y, v_z < \infty, \quad 0 < v_x < \infty. \tag{2}$$

The expression for the flux density of the scattered particles as a function of the coordinate of a point lying at a height x above the diaphragm, which projects to a distance a on the vertical plane of the collector (Fig. 1), can be written in the form

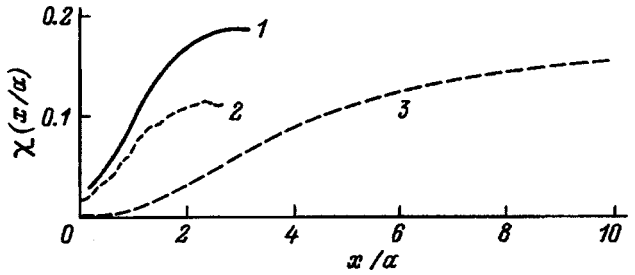

FIG. 6. Scattering of a flux due to single collisions (dependence of $\chi(x/a)$, which characterizes the probability density that an atom will impinge on a unit of surface of a plane parallel to the vapor flux, on the distance to the diaphragm). Distances to the symmetry axis, cm: *1* — 2, *2* — 4, *3* — theoretical dependence for a collinear particle flux.

$$F(x) = \sigma \sqrt{\frac{2T}{m}}\, DN^2 \chi(x/a). \tag{3}$$

Here $\chi(u)$ is a function which assigns the flux distribution with respect to the coordinate x. The approximation $\chi(u) = 0.018u^4/(1 + 1.62u^2 + 0.1u^4)$ can be used in the range $0 < u < 3$ to an accuracy no poorer than 3%.

The model of a collinear beam of atoms with a semi-Maxwellian velocity distribution makes it possible to sense the relationships between different quantities, but they must be tested by numerical calculations on the quantitative level. In fact, on the one hand, under real conditions an atomic beam has appreciable divergence, which leads to a significant increase in the number of scattered atoms impinging on the geometric shadow. On the other hand, the ''semi-Maxwellian'' distribution (2) overestimates the number of slow particles in comparison to (1).

Calculations of a scattered flux were performed for a source in the form of a planar slit with a width of 2 mm. The width of diaphragm was $D = 1$ cm (Fig. 1), the distance from the slit to the diaphragm was set equal to 2 cm, and the fluxes were reduced with respect to the two values $a = 1.5$ and 3.5 cm. The dependences obtained are presented in the form of (3), from which the $\chi(x/a)$ curves were calculated (Fig. 6). The simulation results are presented only for the region of the geometric shadow for forward flow.

As expected, when the atomic beam is not collinear, the scattered flux is no longer characterized by the universal function $\chi(x/a)$: different values of a have different χ. In addition, for a divergent flow the number of particles impinging on the region of the geometric shadow is significantly greater than in the case of a collinear flux, i.e., there is, so to speak, an effective decrease in the distance from the collector to the edge of the diaphragm a.

We note one more important fact. The scattered flux is proportional to the square of the vapor density in the ionization zone. This permits the determination of the mean vapor density in the ionization zone on the basis of numerical simulation results and data from measurements of the scattered flux density.

CONCLUSIONS

We regard the following as the most important results of the treatment performed.

1. A simple approximation, which describes the fraction of particles passing through a tube as a function of the ratio of the length of the tube to its diameter, has been obtained.

2. It is shown that, although the distribution of the particles escaping at an angle narrows somewhat as the ratio of the length of the tube to its diameter increases, the value of the angle within which an appreciable fraction of the particles is found varies very weakly.

3. It is shown that collisions in a divergent atomic flux lead to more effective obstruction of the region of the geometric shadow than does a collinear flux.

Calculations which take into account multiple collisions are needed to more accurately reveal the region of applicability of the free molecular motion approximation.

We thank V. A. Kuznetsov and A. Yu. Sapozhkov for some helpful discussions.

[1] S. A. Mayorov, A. N. Tkachev, and S. I. Yakovlenko, Laser Phys. **4**, 623 (1994).
[2] S. A. Maĭorov, A. N. Tkachev, and S. I. Yakovlenko, Mat. Model. **6** (9), 13 (1994).
[3] V. S. Letokhov, V. I. Mishin, and A. A. Puretzky, Prog. Quantum Electron. **5**, 139 (1977).
[4] S. K. Borisov, V. A. Mishin, and M. A. Kuz'mina, Prikl. Fiz., No. 1, 65 (1995).
[5] A. N. Tkachev and S. I. Yakovlenko, Kvantovaya Elektron. (Moscow) **20**, 1117 (1993) [Quantum Electron. **23**, 972 (1993)].
[6] A. N. Tkachev and S. I. Yakovlenko, Kvant. Elektron. (Moscow) **23**, 860 (1996).
[7] N. F. Ramsey, *Molecular Beams* (Clarendon Press, Oxford (1956); IL, Moscow (1960), 441 pp.).
[8] Yu. V. Zaĭtsev and A. A. Ovchinnikov, Zh. Tekh. Fiz. **50**, 2017 (1980) [Sov. Phys. Tech. Phys. **25**, 1176 (1980)].
[9] A. A. Tarasov and A. L. Tolstykh, Zh. Tekh. Fiz. **64**, 195 (1994) [Tech. Phys. **39**, 740 (1994)].

Translated by P. Shelnitz

Continuous frequency tuning of a picosecond neodymium-glass laser in the UV and VUV

R. A. Ganeev and T. Usmanov

Akadempribor Scientific and Production Association, Academy of Sciences of Uzbekistan, 700143 Tashkent, Uzbekistan

(Submitted October 24, 1996)
Zh. Tekh. Fiz. **68**, 82–89 (May 1998)

The results of an investigation of continuous frequency tuning of a neodymium laser in the UV and VUV ranges are reported. Generation of the sum frequency of second harmonic radiation and the radiation from a parametric light generator in the UV region (338–366 nm) is achieved. The optimal conditions for tuning UV radiation in the range 113.5–117.0 nm in third-harmonic generation processes in xenon and its mixtures with other gases are investigated. A third-harmonic generation efficiency of $\sim 5\times 10^{-4}$ and a tuning range >2600 cm^{-1} are obtained in the VUV range investigated. © *1998 American Institute of Physics.* [S1063-7842(98)01505-0]

INTRODUCTION

Sources of continuously tunable (in a range of hundreds of inverse centimeters) coherent UV and VUV radiation are needed for different problems of spectroscopy of atoms and molecules, biology, controlled thermonuclear fusion, laser isotope separation, nonlinear spectroscopy of high-lying states, laser chemistry, and others. Since the number of tunable radiation sources based on direct laser generation is still extremely small in these ranges, here methods of nonlinear-optical conversion of radiation from other, already quite well-developed regions of the spectrum are used. Progress in producing tunable UV and VUV radiation on the basis of nonresonant generation of harmonics and frequency mixing requires high-power laser systems with wavelength near 1 μm as well as the use of crystal parametric light generators (PLGs) and inert gases as the nonlinear media.

The high radiation intensities now achievable[1] from continuously tunable near-IR PLGs utilizing radiation from high-power wide-aperture neodymium-glass lasers[1] make possible the efficient conversion of such radiation into the UV range. Coherent tunable UV radiation can be obtained either by summing the frequencies of PLG radiation and the second harmonic of neodymium-glass lasers or by doubling the frequency of the second harmonic of PLG radiation.[2,3] The utilization of the advantages of cascade generation of harmonics in combination with the wide tuning range of PLGs has made it possible to produce by applying the first conversion scheme sources of high-power tunable UV radiation. The methods developed thus far for producing optimal beams in different channels[4,5] have led to even more efficient conversion of nanosecond pulses into the UV range.

Parametric light generators differ advantageously from other sources of frequency-tunable radiation (semiconductor, dye, and color-center lasers) by their high output energy and wide tuning range. Here the problems of the energy efficiency of picosecond PLGs and increasing the output energy of PLGs for further efficient conversion into the UV and VUV ranges remain important. From this standpoint it is necessary to investigate in detail the factors that limit the efficiency of conversion of radiation from a neodymium laser, one of the most suitable and well-developed sources of high-power picosecond radiation, into harmonics and parametric waves and to analyze the questions of narrowing the spectral line of parametric waves and decreasing the divergence of PLG radiation. In addition, the factors limiting the mixing of parametric waves and harmonics radiation must be analyzed.

The generation of VUV radiation which is tunable near $\lambda = 118.2$ nm (ninth harmonic of YAG laser radiation) was studied in Refs. 2, 6, and 7. However, the optimal conditions for third-harmonic generation (THG) in the range investigated have not been studied in detail. An important condition here is the existence of regions of anomalous dispersion, where efficient generation of the harmonics of focused radiation is possible, in the gases. Xenon was used as the nonlinear medium because the radiation of high-power pump sources falls into the anomalous dispersion regions of xenon. In Ref. 8 radiation generation in the range 117.6–119.2 nm was obtained and the conditions for THG in the mixture Xe:Ar were optimized.

The fact that xenon has regions of anomalous dispersion at shorter wavelengths makes it possible to produce continuously tunable VUV sources with a tuning range of several thousands of inverse centimeters. Optimization of the THG process in xenon and its mixtures with different buffer gases in this range, taking into account different limiting effects, and the creation of conditions for effective frequency conversion taking into account the influence of a number of experimental parameters on the phase matching of interacting waves (gas pressure and ratio, intensity and spectral characteristics of the pump radiation) are undoubtedly of interest both from the standpoint of understanding the peculiarities of this nonlinear optical process and from the practical standpoint (coverage of another section of the VUV spectrum and production of a wide-band picosecond source in this range).

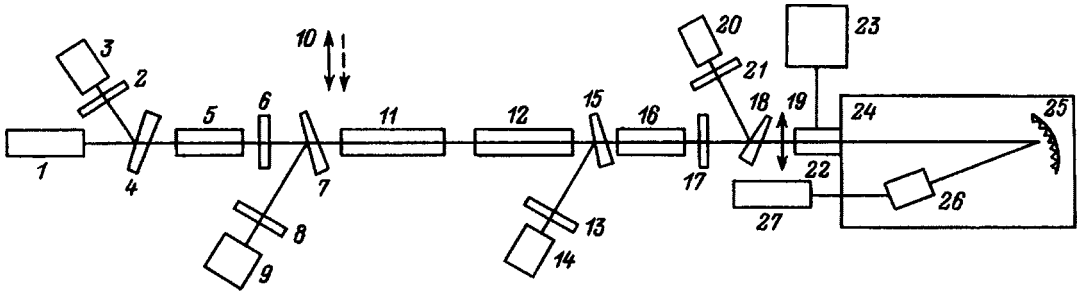

FIG. 1. Diagram of the experiments. *1* — Neodymium-glass laser; *2,6,8,13,17,21* — filters; *3,9,14,20* — FD-24K photodiodes; *4,7,15,18* — optical wedges; *5* — frequency-doubling crystal; *10*— cylindrical lens; *11,12* — parametric generator; *16* — frequency-mixing crystal; *19* — focusing lens; *22* — cell containing gases; *24* — VMR-2; *23* — auxiliary tank for mixing the gases; *25* — diffraction grating; *26* — VUV radiation detector; *27* — V4-17 pulsed voltmeter.

We report below the results of an investigation of parametric generation, summation of the frequencies of PLG radiation and the second-harmonic radiation in the UV region, optimization and development of sources of continuously tunable coherent radiation in the range 338–366 nm, and investigation on this basis of frequency conversion in the range 113.5–117.0 nm in xenon and its mixtures with other gases.

FREQUENCY TUNING OF NEODYMIUM LASER RADIATION IN THE UV REGION

Picosecond radiation was generated in a mode-locked neodymium phosphate glass laser ($\lambda = 1.054$ μm). The generated pulse train was fed into a system for selecting a single pulse. The selected pulse passed through a system for spatial filtering, image translation, and amplification. To compensate for the thermal birefringence during passage through the 20-mm in diameter terminal amplifiers, polarization rotators were inserted between these amplifiers. This decreased the relative fraction of depolarized radiation from 20% to 2%.[9] The output characteristics of the laser radiation were as follows: $\lambda = 1054.8$ nm, $\Delta\lambda = 0.3$ nm, $\tau = 7$ ps, and $E = 80$ mJ. The laser operated in the periodic-pulse mode with a repetition rate of 0.2 Hz. The radiation at all stages of frequency conversion was detected with calibrated FD-24K photodiodes.

This radiation was converted successively into a second harmonic and parametric waves in the IR range which were then mixed with the second harmonic in KDP crystals, as a result of which continuously tunable UV radiation was generated. The arrangement of the experiments on conversion of IR radiation into the UV and VUV ranges is displayed in Fig. 1.

The conversion of IR radiation in the second harmonic was accomplished in a type-I (*ooe* interaction) KDP crystal ($20\times20\times10$ mm). The conversion efficiency reached saturation ($\sim 44\%$) at $I \sim 10$ GW/cm^2. Further increases in the pump radiation intensity resulted in a small decrease in conversion efficiency (the radiation converted into the second harmonic ($\lambda = 527.4$ nm) was filtered out of the IR radiation and excited a superluminescence PLG, consisting of two nonlinear crystals cut for type-II interaction (*e-oe*). The latter crystals consisted of KDP crystals ($20\times20\times40$ mm generator crystal and $20\times20\times60$ mm amplifier crystal).

Preliminary experiments with a one-crystal PLG and a frequency-mixing crystal in both parallel and focused beams showed that the efficiency of this channel of conversion of IR waves into tunable UV radiation is low ($\eta \sim 5\%$), though in this case the spectrum was covered from 332 to 375 nm. The low efficiency was due to the mismatch of the spatial-spectral characteristics of the interacting waves in the frequency-mixing crystal. The use of one-crystal PLGs resulted in the generation of waves with a large spectral width and divergence and, correspondingly, a sharp decrease of the mixing efficiency in the UV region; it also limited the possibilities of further use of the generated radiation in subsequent frequency conversion processes.

Generation and amplification of parametric waves in the two-crystal scheme were accomplished in parallel beams. Frequency tuning was performed by synchronous rotation of the crystals *11* and *12*. The axes of the crystals were oriented so as to compensate for the aperture diaphragmatic effect. The distance between the crystals was chosen taking into account the amplification of parametric waves satisfying optimal mixing with second-harmonic radiation and was equal to 70 cm. The tuning range was equal to 870–1220 nm (Fig. 2a). The divergence of the PLG radiation was equal to 3 mrad. The maximum efficiency was equal to 30% at 14 GW/cm^2. The saturation pump intensity was equal to 12 GW/cm^2.

The radiation tunable in the IR region was mixed with second-harmonic radiation in a KDP frequency-mixing crystal *16* ($20\times20\times20$ mm), cut for type-II phase matching. Figure 3 shows the efficiency of conversion into tunable UV radiation as a function of the PLG radiation intensity and the intensity of the main radiation. The converted radiation, tunable in the range 338–366 nm (Fig. 2b), was filtered out of the IR and visible radiation and detected with a photodiode *20*.

We note that the width of the spectrum of the picosecond parametric radiation influences the process of efficient mixing with the second harmonic. The spectral width of synchronism during summation of the waves in the KDP frequency-mixing crystal *16* equals 0.4 nm, while the spectral width of the parametric waves was equal to 2 nm (Fig. 4). The narrowing of the spectral width of the parametric waves accompanying an increase in the separation between the crystals in the PLG results at the same time in lower

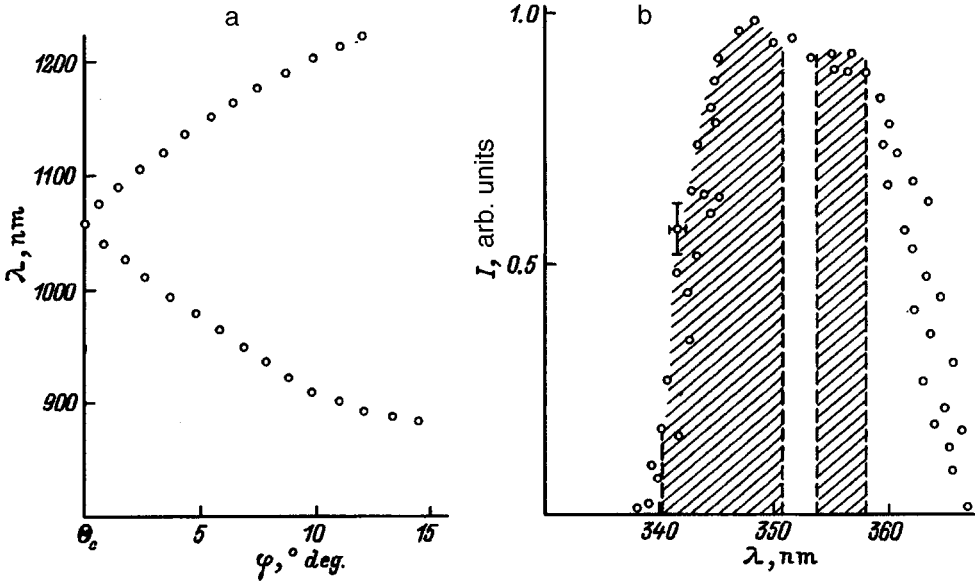

FIG. 2. Tuning characteristics. a — PLG with KDP crystals ($\lambda = 527.4$ nm, φ is the angle of detuning of the crystals from the degenerate regime); b — UV radiation (I is the relative radiation intensity). The regions of the UV spectrum where the third harmonic falls into the anomalous dispersion region of xenon are hatched.

efficiency of conversion into tunable IR radiation. Thus, optimization of the process of generation of tunable UV radiation consisted of finding an optimal ratio of the spectrum width and intensity of the tunable IR radiation. Efficient mixing here required, in addition to correspondence of the spectral-spatial characteristics of the second-harmonic and PLG waves, satisfaction of the Manley–Rowe relation. In our case this relation, according to which there should be one IR photon for each second-harmonic photon ($E_{GL}:E_{2\omega} \sim 1:2$), is not satisfied because the efficiency of the conversion of the main radiation into the PLG wave is too low on account of the large distance between the crystals. In addition, for the crystal lengths employed the effect of the group detuning of the pulses on the parametric conversion processes became large.

Conversion of focused radiation with wavelength $\lambda = 527.4$ nm into parametric waves in the two-crystal PLG and into UV radiation was investigated. The radiation in front of the generator crystal was focused with a cylindrical lens *10* ($f = 800$ mm) into the two-crystal PLG. The distance between the PLG crystals as well as the position of the frequency-mixing crystal were chosen so as to obtain the optimal parameters of the picosecond UV radiation. This worsened the divergence of the generated radiation, which made it impossible to obtain later high intensities of focused UV radiation (which are necessary for subsequent conversion into the VUV region of the spectrum).

The output energy of the picosecond UV pulses at wavelength $\lambda = 349$ nm was equal to 4 mJ with a spectrum width of 0.45 nm and a divergence of 1 mrad. The conversion efficiency can be further increased and the spectral and spatial characteristics of the tunable UV radiation can be improved by using schemes with separate formation of beams

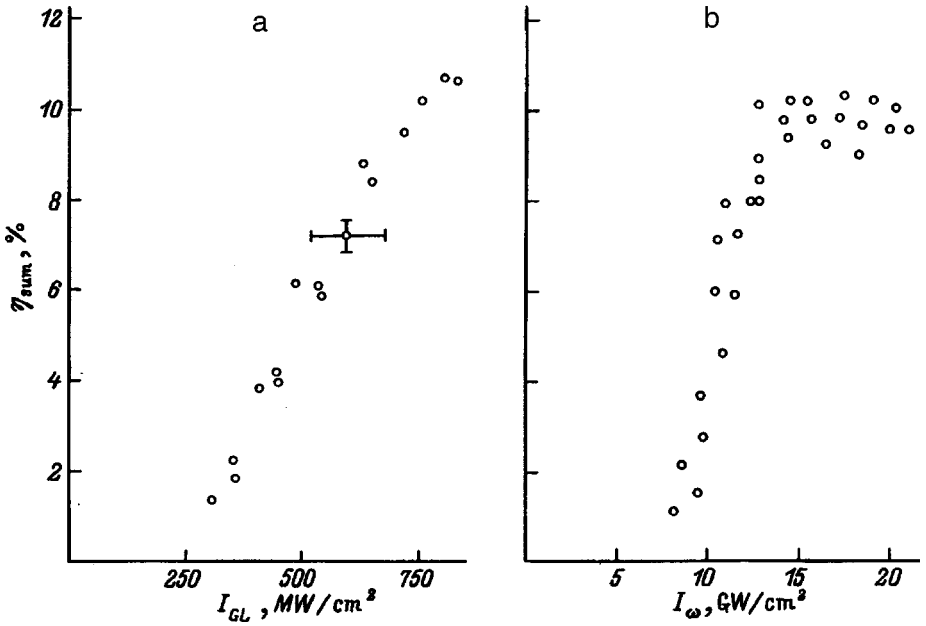

FIG. 3. Efficiency of conversion into the sum wave versus the intensity of PLG (a) and the intensity of the main radiation (b).

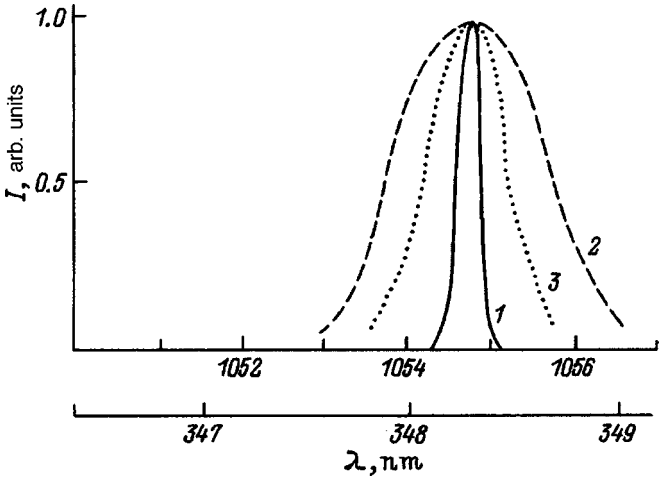

FIG. 4. Spectral distribution of the pulses. *1* — Pump pulse ($\lambda = 1054.8$ nm); *2* — PLG in the degenerate regime; *3* — UV radiation.

of the mixed waves in different independent channels as well as schemes with initial radiation for PLGs.[1,5,10]

GENERATION OF PICOSECOND VUV RADIATION ($113.5 < \lambda < 117.0$ nm)

Subsequent frequency conversion into the short-wavelength region of the spectrum was performed in gases, since they possess the highest transmittance in the region studied. Tunable UV radiation was focused (Fig. 1) after filtering out IR and visible range radiation with a quartz lens *21* ($f = 80$ mm) into a cell which contained the gases and was attached to a VMR-2 vacuum monochromator. The third harmonic of the pump radiation, tunable over the anomalous dispersion region of xenon, was generated in the cell. The generated VUV radiation was detected with a VÉU-6 electronic channel multiplier or a LPP-2 calibrated pyroelectric converter.[11] The signal from the detectors was fed into a V4-17 pulsed voltmeter. The wavelength of the pump radiation was registered with a STÉ-1 spectrograph.

The pump radiation parameters were as follows: tuning range 338–366 nm, pulse energy up to 4 mJ, pulse duration 7 ps, and spectral width 0.45 nm. The UV radiation intensity at the focal point of the lens ($f = 80$ mm) was equal to 5×10^{11} W/cm^2. The spatial distribution of the radiation was close to Gaussian. Xenon was used as the nonlinear medium, since the tripled frequency of the pump radiation covered several regions of anomalous dispersion (Fig. 2b) where synchronous generation of odd harmonics in focused beams is possible. Ultraviolet radiation tunable in the range 340.5–351 nm was used in the experiments. The experimental procedure was as follows. The pump radiation, tunable with a step of 0.2 nm, was converted into the range 113.5–117.0 nm. The influence of the xenon pressure and the ratio of the pressures of the nonlinear gas and the normal-dispersion buffer gas (argon and krypton) on the efficiency of conversion of the pump radiation into the third harmonic (TH) were investigated. The effect of the pump radiation intensity on the THG efficiency for different wavelengths of the converted radiation was also investigated.

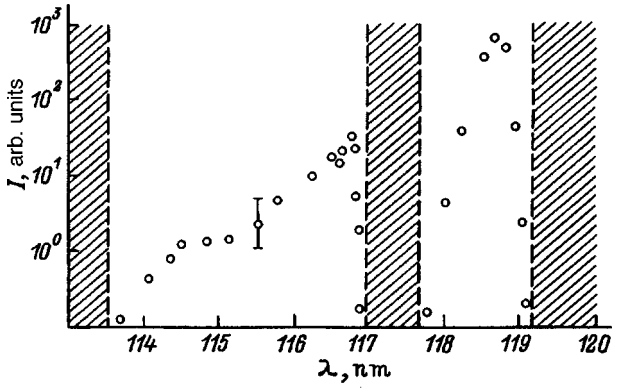

FIG. 5. Region of generation of VUV radiation in xenon (the regions of normal dispersion are hatched).

Figure 5 shows the range of wavelengths of the radiation that can be generated and the relative intensity of the radiation in that range. One can see that the energy of the generated radiation decreases as its wavelength decreases. The energy is highest near a resonance line of xenon (117.0 nm). At large wavelengths the frequency of the third harmonic of the converted radiation lay in the region of normal dispersion (117.0–117.6 nm). As a result of the focusing-induced phase shift of the interacting waves, the amplitude of the harmonic generated in this range in front of the waist of the Gaussian beam was completely compensated by the amplitude of the harmonic generated in the region behind the waist. For comparison, the results of Ref. 8 on the generation of radiation in the range 117.6–119.2 nm with comparable pump intensities are also presented here. We note that the conversion efficiency in this range was an order of magnitude higher, in good agreement with estimates of the oscillator strengths of the transitions $5p^6S - 7s[I1/2]$ ($\lambda = 117.0$ nm) and $5p^61S - 5d[I1/2]$ ($\lambda = 119.2$ nm) (the oscillator strengths are 0.0968 and 0.395, respectively).

The increase in the conversion efficiency with increasing wavelength in the range investigated occurs for two reasons. First, away from the Xe resonance line (117.0 nm) the nonlinear susceptibility of the medium decreases, which results in a decrease in the conversion efficiency. Second, the decrease in the generated radiation is due to a decrease in the pump intensity (in Fig. 2b the hatched region on the left-hand side is the spectral pumping range used in the experiment). The dependence of the efficiency of conversion into the third harmonic on the intensity of the UV radiation is quadratic in the entire experimental tuning range. The influence of the Kerr effect, self-focusing, and other limiting factors characteristic for the case of high ($> 5 \times 10^{12}$ W/cm^2) intensities[8,12] was very small in our case.

Conversion for the long- and short-wavelength regions of the spectrum of the pump pulse is optimized for different values of the xenon pressure. As the pressure of the nonlinear medium increases, the long-wavelength component of the pump radiation is converted first, after which the central part and finally the short-wavelength component are converted. The width of the spectrum of the generated VUV radiation was equal to 0.25 nm. Thus, the width of the radia-

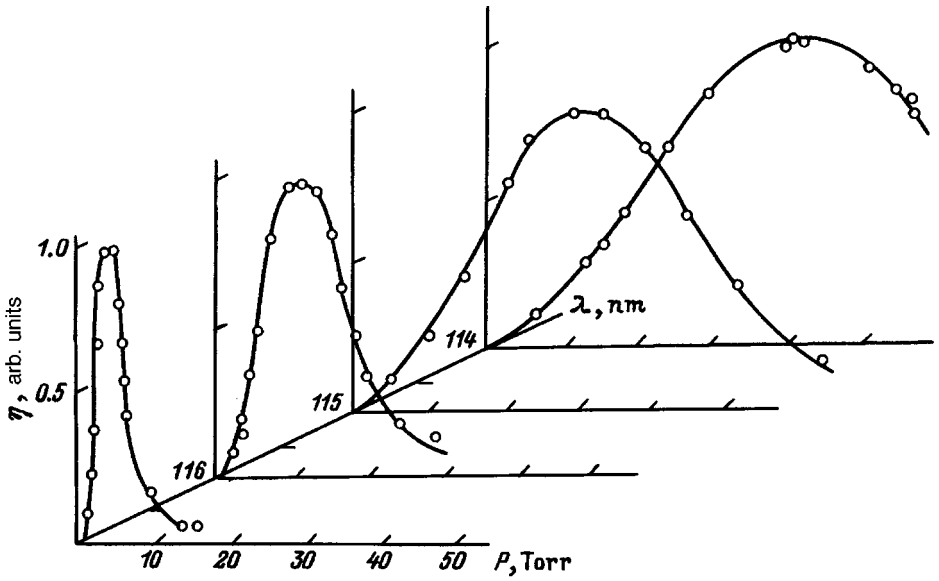

FIG. 6. Conversion efficiency versus xenon pressure for different wavelengths of the third harmonic ($I=5\times10^{11}$ W/cm^2).

tion spectrum decreased by almost a factor of 2 in the process of conversion into the third harmonic ($\Delta\lambda=0.45$, 0.25 nm). This is due to the dependence of the conversion efficiency on the radiation intensity. The ''wings'' of the spectral distribution of the pump radiation are converted with a much lower efficiency than the center. Taking account also of the fact that the optimal conditions of conversion (phase matching) are created for the central part of the spectral distribution of the pump, it is possible to achieve substantial discrimination in conversion of different sections of the spectral contour of the converted radiation.

We investigated the effect of gas pressure on conversion efficiency for different wavelengths of the generated radiation in the experimental region of anomalous dispersion of xenon (113.5–117.0 nm) with the pump radiation wavelength tuned from 340.5 to 351.0 nm (Fig. 6). For longer wavelengths the conversion maximum shifts in the direction of lower pressures. Thus, for $\lambda=114.2$ nm the optimal pressure at which maximum conversion is observed is $P_{\text{opt}}=38$ Torr, whereas for $\lambda=116.8$ nm one has $P_{\text{opt}}=3$ Torr. This is due to the fact that as the transition $5p^6\,{}^1S-7s[I1/2]$ ($\lambda=117.0$ nm) is approached, the phase detuning per atom increases and the number of particles of the nonlinear medium required to achieve optimal phase detuning, satisfying the condition $b\cdot\Delta k=-4$ (where b is the confocal parameter and Δk is the phase detuning between the harmonic and pump waves), is smaller.

The conversion efficiency can be increased by increasing the particle density of the nonlinear medium (since $\eta\sim N^2$, where N is the number of particles in the interaction zone). However, above a certain pressure (Fig. 6) conversion efficiency decreases because of departure from the optimal ratio between the pump and harmonic wave vectors (detuning of synchronism). To circumvent this difficulty a normal-dispersion gas is added to the anomalous-dispersion nonlinear medium. In this case one can choose the ratio of the gas pressures so as to obtain the optimum Δk for the mixture.

A great deal of attention was devoted to careful forced mixing of the components of the mixture. This was necessary in order to obtain stable conversion into a harmonic. Without careful mixing the likelihood that the ratio of the gas pressures would deviate from the optimal ratio in a microvolume near the focus, where conversion is especially efficient, increased. In the experiment the statistical variance of the intensity of the generated VUV radiation, other conditions being equal, increased and the maximum possible conversion efficiency for the given experimental conditions decreased (see also Refs. 13 and 14). As an example, Fig. 7a shows the function $\eta(R)$ (R is the ratio of the argon and xenon pressures) for the case when the gases mixed in a natural manner in a cell and the mixture was prepared in an auxiliary tank and then introduced into the gas cell. For the first case it is difficult to determine R_{opt} unequivocally, since the statistical variance of the results makes it possible to measure this quantity to within $R_p\pm4$, where R_p is the computed value of the optimal ratio of the partial argon and xenon pressures. For the case when an auxiliary tank with forced mixing was used, the experimentally obtained value equalled the computed value to within $R_p\pm0.5$.

Thus, for the case when the gas mixes naturally the position of the maximum and the behavior of the curve $\eta(R)$ were random. Maximum conversion is observed for $R=8-16$. The THG efficiency in a gas mixture does not reach the value that is possible for the given experimental conditions. As one can see from Fig. 7a, the mixture continues to remain nonuniform even after substantial time has passed. It is obvious that for the microvolume bounded by the waist zone, where the main conversion process occurs, the random deviation of R from the pressure ratio of Ar and Xe introduced into the cell was substantial, which will result in both a deviation of $\eta(R)$ from the expected dependence and large pulse-to-pulse fluctuations in the magnitude of the generated radiation (see the variance for the case of forced and natural mixing; each point corresponds to the average value over 10 shots). The obtained ratio ($R_{\text{opt}}=10.5$) was close to the optimal ratio of the Ar and Xe partial pressures for $\lambda=118.2$ nm with confocal parameter $b=6$ mm.[15]

Figure 7b shows the conversion into the third harmonic

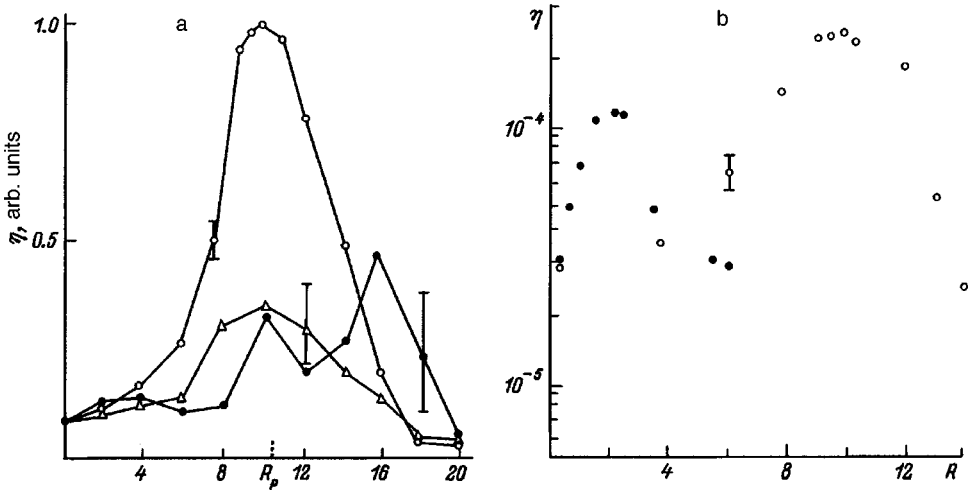

FIG. 7. a — Conversion efficiency versus $R=P_{Ar}:P_{Xe}$. $I=2\times10^{11}$ W/cm^2, confocal parameter $b=6$ mm; ○ — mixture prepared in an auxiliary tank; ●, △ — gases mixed in the cell (● and △ — results obtained 10 and 20 min, respectively, after the gases were introduced into the cell), $R_p=10.5$ — computed optimal pressure ratio for $\lambda=116.8$ nm. b — THG conversion efficiency versus R for different buffer gases: ● — mixture Kr:Xe, ○ — mixture Ar:Xe; $I=2\times10^{11}$ W/cm^2, $P_{Xe}=9$ Torr, $\lambda=116.8$ nm.

versus the parameter R for different buffer gases ($\lambda=116.8$ nm). Argon and krypton were used as the buffer gases. Other gases which are transparent in the experimental range of the spectrum require high pressures (hundreds and thousands Torr) to optimize the THG process. This results in breakdown phenomena even for relatively low pump intensities, so that these gases are undesirable. For both mixtures Ar–Xe and Kr–Xe the xenon pressure was equal to 9 Torr, i.e., three times higher than the optimal pressure for the case of THG in pure xenon. The THG efficiency for optimal values of R should be (since $\eta\sim N^2$) a factor of 9 higher than the maximum value of η in the case of conversion in pure xenon ($\eta=3\times10^{-5}$). Such an increase in η was obtained only in the mixture Ar–Xe. In the mixture Kr–Xe the efficiency increased only by a factor of 4. This discrepancy is evidently due to the fact that the addition of krypton changes (decreases) the susceptibility of the medium. The contribution of argon to the total third-order nonlinear susceptibility in the mixture is very small. The larger influence of krypton as compared with argon on the third-order nonlinear susceptibility, which is responsible for THG, is evidently due to the fact that the closest energy level in krypton ($\lambda=116.5$ nm) lies closer to the wavelength of the harmonic radiation than in argon ($\lambda=106.6$ nm). Incidently, this also explains the large (per atom) phase detuning in krypton as compared with argon, which results in lower values of R_{opt} for Kr. We note that a separate, exactly determined ratio between the buffer and nonlinear gas pressures is required for each region of the spectrum. Thus, the maximum conversion efficiency was observed for the mixture Ar:Xe with $R=9$ (for $\lambda=116.7$ nm) and 5 ($\lambda=115.5$ nm).

Krypton exhibits anomalous dispersion for $\lambda<116.5$ nm and could not be used as the normal-dispersion gas in our experiments in this region. As shown in Refs. 16–18, conditions of negative phase detuning ($\Delta k<0$), which are necessary for THG in krypton for VUV wavelengths less than the resonance line $\lambda=116.5$ nm, are realized in this region. As a result of this, the addition of krypton to xenon at $P=9$ Torr resulted in only a very small increase in THG efficiency for $\lambda<116.5$ nm.

The maximum conversion efficiency (5×10^{-4}) was obtained at the wavelength $\lambda=116.8$ nm with a xenon pressure of 25 Torr and $R=10$ ($I=4\times10^{11}$ W/cm^2). The tuning range was >2600 cm^{-1}.

CONCLUSION

We have presented the results of an investigation of continuous frequency tuning of neodymium laser radiation in the UV and VUV regions.

We investigated the parametric generation of light and summation of the second harmonic of the neodymium-glass laser radiation and the radiation from a PLG in the UV region. The operating regimes of one- and two-crystal PLGs were compared for the cases of nonlinear parametric conversion and mixing in focused and parallel beams. Generation was achieved in the range 338–366 nm. The regimes and optimal ratios of the spectrum width and intensity of the tunable radiation pulses were determined from the standpoint of further conversion into the VUV range. The output energy of the UV pulses near the degenerate regime of the PLG was equal to 4 mJ.

We investigated the conditions of optimal conversion of continuously tunable radiation in the range 113.5–117.0 nm, for which the dependences of the efficiency of conversion into the third harmonic on the pump wavelength and energy as well as on the ratio of the gas pressures. A comparison was made with the results on generation of continuously tunable radiation in a different anomalous dispersion region of xenon, 117.6–119.2 nm. It was observed that preliminary forced mixing of the working mixture was important in order to obtain the optimal ratio of the partial pressures in the frequency conversion zone. The maximum THG efficiency 5×10^{-4} in a mixture of gases in the range investigated and a tuning range <2600 cm^{-1} were obtained.

This work was supported in part by the International Science Fund (Grant No. RU 7000) and the Uzbek Fund for Fundamental Research.

[1] B. F. Bareĭka, I. A. Begishev, Sh. A. Burdulis *et al.*, Pis'ma Zh. Tekh. Fiz. **12**(3), 186 (1986) [Sov. Tech. Phys. Lett. **12**(2), 78 (1986)].
[2] A. H. Kung, Appl. Phys. Lett. **25**, 653 (1974).
[3] R. V. Danelyus, A. S. Piskarskas, V. A. Sirutkaĭtis *et al.*, *Parametric Light Generators and Picosecond Spectroscopy* [in Russian], Mokslas, Vilnius, 1983, p. 196.

[4] P. G. Kryukov, Yu. A. Matveets, D. N. Nikogosyan, and A. V. Sharkov, Kvantovaya Élektron. (Moscow) **5**, 2348 (1978) [Sov. J. Quantum Electron. **8**, 1319 (1978)].
[5] I. A. Begishev, A. A. Gulamov, E. A. Erofeev *et al.*, Kvantovaya Élektron. (Moscow) **17**, 971 (1990) [Sov. J. Quantum Electron. **20**, 889 (1990)]
[6] R. Mahon, T. J. Mcllrath, V. P. Myerscough, and D. W. Koopman, IEEE J. Quantum Electron. **QE-15**, 444 (1974).
[7] V. V. Korobkin, Yu. V. Korobkin, A. S. Markin, and P. P. Pashinin, Pis'ma Zh. Tekh. Fiz. **7**, 536 (1981) [Sov. Tech. Phys. Lett. **7**, 228 (1981)].
[8] R. A. Ganeev, V. V. Gorbushin, I. A. Kulagin, and T. Usmanov, Kvantovaya Élektron. (Moscow) **133**, 178 (1986) [Sov. J. Quantum Electron. **16**, 115 (1986)].
[9] R. A. Ganeev, V. V. Gorbushin, A. V. Zinov'ev *et al.*, Kvantovaya Élektron. (Moscow) **16**, 1816 (1989) [Sov. J. Quantum Electron. **19**, 1169 (1989)].
[10] I. A. Begishev, A. A. Gulamov, Sh. R. Kamalov *et al.*, Pis'ma Zh. Tekh. Fiz. **16**(24), 47 (1990) [Sov. Tech. Phys. Lett. **16**(12), 943 (1990)].
[11] R. A. Ganeev, V. V. Gorbushin, T. Usmanov, and S. T. Khudaĭberganov, Prib. Tekh. Éksp. No. **1**, 216–220 (1988).
[12] L. J. Zych and J. F. Young, IEEE J. Quantum Electron. **QE-14**, 147 (1978).
[13] A. H. Kung, J. F. Young, and S. E. Harris, Appl. Phys. Lett. **22**, 301 (1973).
[14] A. J. Cormier, W. Marculis, W. Sibbett, and J. R. Taylor, Opt. Commun. **48**, 61 (1983).
[15] R. A. Ganeev, I. A. Kulagin, I. A. Begishev *et al.*, Nonlinear Opt. **16**, 109 (1996).
[16] D. Cotter, Opt. Lett. **4**, 134 (1979).
[17] D. Cotter, Opt. Commun. **31**, 397 (1979).
[18] W. Zapka, D. Cotter, and U. Brackmann, Opt. Commun. **36**, 79 (1981).

Translated by M. E. Alferieff

Formation of x-ray beams with the aid of a tapered microcapillary

Yu. I. Dudchik, F. F. Komarov, and Ya. A. Konstantinov

A. N. Sevchenko Scientific-Research Institute of Applied Physical Problems, 220064 Minsk, Belarus
(Submitted January 20, 1997)
Zh. Tekh. Fiz. **68**, 90–93 (May 1998)

The possibility of obtaining x-ray microbeams with a prescribed intensity using a system containing a x-ray tube with a transmission thin-film anode and a tapered glass microcapillary is investigated. © *1998 American Institute of Physics.* [S1063-7842(98)01605-5]

X-ray waveguides in the form of glass microcapillaries 100–500 mm long and with channel diameters of 10–100 μm are a new component in x-ray technology.[1] X-ray beams can propagate directionally in a capillary channel, repeatedly reflecting from the channel walls at small glancing angles. The propagation direction of the x-rays can be changed by curving the capillary. A system containing a sufficiently large number of such capillaries (ordinarily, more than 100), curved and positioned so that one end of a capillary is points toward the x-ray source and the other toward the point of energy collection — the focal point — is actually a ''x-ray lens.''[2] Such a lens can focus 1–10 keV x-ray beams into a 5–10 μm spot. At the same time, a number of applications in microelectronics require obtaining intense x-ray microbeams with a focal spot of 1 μm and smaller. This problem can probably be solved with a one microcapillary, made in the form of a cone or possessing a parabolic channel profile in the direction of the channel axis. The x-ray optic characteristics of such systems have been simulated and investigated experimentally using synchrotron radiation sources.[3–6] On the other hand, wide application of such tapered microcapillaries may become possible only when a compact x-ray emitter based on a x-ray tube is used as the x-ray source. Work along these lines is reported in Refs. 7 and 8.

Our objective in the present work is to investigate the possibility of obtaining x-ray microbeams with prescribed intensity from a system containing as the x-ray optic component a tapered glass microcapillary and a x-ray tube as the radiation source.

Let us consider a system containing a point x-ray source and a tapered microcapillary. The source is placed on the capillary axis at a distance d from the entrance face (Fig. 1). The length of the capillary is L_c, the radius of the channel at the exit is R_c, and the cone angle is α_c. The radius of the capillary channel at the entrance is $R=R_c+L_c\sin\alpha_c$. The source emits photons with energy $\hbar\omega$. The photons propagate in the capillary channel, repeatedly reflecting from the channel walls, as shown in Fig. 1.

The dependence of the x-ray reflection coefficient R of a smooth surface of a material with permittivity $\varepsilon=1-\delta+i\gamma$ on the glancing angle θ is described by the well-known formula[1]

$$R=\frac{[\sqrt{2}x-(A+x^2+1)^{1/2}]^2+A-(x^2-1)}{[\sqrt{2}x+(A+x^2+1)^{1/2}]^2+A-(x^2-1)}, \qquad (1)$$

where $A=(x^2-1)+y^2$, $x=\theta/\theta_c$, $y=\gamma/\delta$, and $\theta_c=\delta^{1/2}$.

In the absence of absorption ($\gamma=0$) the x-rays will be completely reflected from the surface for grazing angles θ less than the critical angle θ_c of total external reflection.

Cylindrical microcapillaries ($\alpha_c=0$) can be used as collimators, making it possible to obtain diverging x-ray microbeams with the radius of the focal spot R_c and radiation cone angle $\theta<\theta_c$, where $\theta=R_c/d$. The length of a capillary L_c can be optimized on the basis of the specific value of the imaginary part of the permittivity γ.[1]

If the intensity of the point radiation source I_0 (photons/s $\cdot$ sr) is known, then the maximum intensity of the photon beam at a capillary exit equals (in the absence of absorption) $I_0\pi\theta_c^2$ and is obtained when the capillary is located at distance $d=R_c/\theta_c$ from the source. For a glass capillary with $R_c=1$ μm and 8 keV photons the parameter $d=270$ μm.

If a microfocus x-ray tube is used as the source of radiation, then because of the structural features of such devices it is impossible to position the capillary sufficiently close to the focal point of the tube. This distance (the distance from the tube focal point to the beryllium exit window for x-rays) for tubes with a massive anode equals 10–30 mm for tubes with a transmission thin-film (TTF) anode of 0.5–1 mm.[9] Therefore, to form a x-ray microbeam it makes sense to use instead of a cylindrical capillary a capillary shaped in the form of a cone whose length L_c and cone angle can be optimized for prescribed values of the exit radius R_c and source–capillary entrance distance d.

Figure 2 shows the computed dependence of the parameter T, characterizing the efficiency of the capillary, on the length of the capillary for different values of α_c. The parameter T is determined so as to be able to calculate the x-ray beam intensity I (photons/s) at the capillary exit for known intensity I_0 of the point source of radiation by means of the following expression:

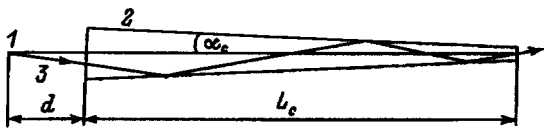

FIG. 1. Parameters of the system for obtaining x-ray microbeams. *1* — x-Ray source, *2* — microcapillary, *3* — x-ray beams.

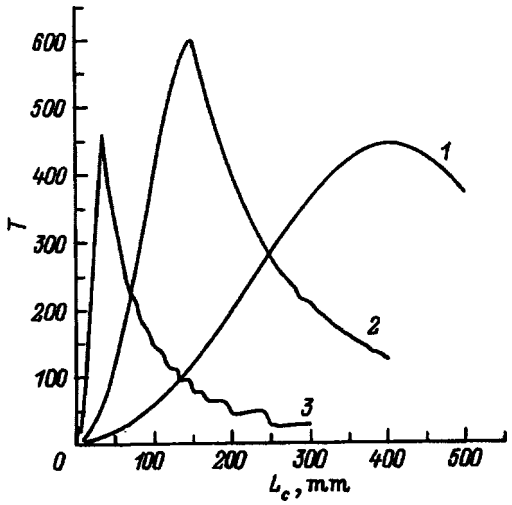

FIG. 2. The parameter T (Eq. (2)) versus microcapillary length L_c for different cone angles α_c, rad: *1* — 0.01, *2* — 0.03, *3* — 0.1.

$$I = I_0 T \frac{\pi R_c^2}{d^2}. \tag{2}$$

The values of the parameter T (Fig. 2) were obtained by simulating x-ray trajectories in a tapered glass capillary taking account of absorption of radiation on reflection according to Eq. (1). The calculations were performed for 8 keV photons; the values of d are indicated in Fig. 2. The values presented for the parameter T make it possible to estimate the photon flux through the exit opening of the capillary from a x-ray tube as a radiation source. If the working voltage U_a of the tube and the anode current i_a are given, then the number of characteristic photons of the anode material of the tube which are emitted by the tube into a solid angle $d\Omega$ per unit time t can be calculated according to the formula[9]

$$\frac{d^2N}{d\Omega dt} = C i_a \left(\frac{U_a}{U_q} - 1 \right)^{1.67}, \tag{3}$$

where C is the anode coefficient, which is known for a given material, and U_q is the ionization potential of the corresponding shell of the target atom.

The number of photons $d^2N/d\Omega dt$ emitted by the x-ray tube with a focal spot of area S_a is related with the intensity I_0 appearing in Eq. (2) as

$$I_0 = \frac{d^2N}{d\Omega dt} \frac{\pi R_c^2}{S_a}, \tag{4}$$

which reflects the impossibility of focusing radiation from a source into a spot smaller than the size of the source.

Analysis of the development of microfocus x-ray tubes with a TTF anode, specifically, tubes used in REIS-type apparatus,[10] shows that it is possible to fabricate tubes with the following parameters: $U_a = 40$ kV, $i_a = 0.5$ mA, and $S_a = 10 \times 10$ μm.

Table I shows the computed values of the number of photons I ($K\alpha$ series) at the exit of a system containing a tapered microcapillary with the indicated values of the radius R_c of the exit opening and a x-ray with a TTF and the above-indicated values of U_2, i_a, and S_a. The distance from the focal spot of the tube to the capillary entrance was assumed to be 5 mm. The capillary length and the cone angle were chosen so as to maximize the value of the parameter T (Fig. 2). The absorption of radiation in the anode material of the tube and in the beryllium window was neglected in the calculations. The estimates showed that taking account of these factors decreases I by a factor of 1.5–2.

TABLE I.

R_c, μm	α_c, mrad	L_c, mm	T	I, photons/s
0.15	0.01	110	50	80
0.5	0.02	120	20	4400
1	0.02	150	10	8800

Note: The distance from the tube focus to the capillary entrance is $d = 5$ mm; L_c is the length and α_c the cone angle of the capillary.

The results presented in Table I show that quite intense x-ray beams can be obtained with tapered microcapillaries. It should be noted that the values of the x-ray tube parameters employed in the calculations are not maximum admissible values. For example, according to Ref. 7, it is possible to fabricate microfocus x-ray tubes with a TTF anode such that the brightness of the tubes is only an order of magnitude smaller than that of a synchrotron source.

To perform experiments for investigation of the parameters of x-ray systems a series of microcapillary samples with a conical profile of the inner channel was prepared. The microcapillaries were obtained from commercial glass tubes by extrusion under the action of gravity on a load secured to the sample as the sample (capillary) is heated. The outer and inner diameters of the initial samples were equal to 3.7 and 0.8 mm, respectively. Tapered microcapillaries up to 30 mm long, with 300–100 μm entrance diameter and 1–20 μm exit diameter, were obtained. Typical profiles of the inner channel of the capillary are presented in Figs. 3a, b. The

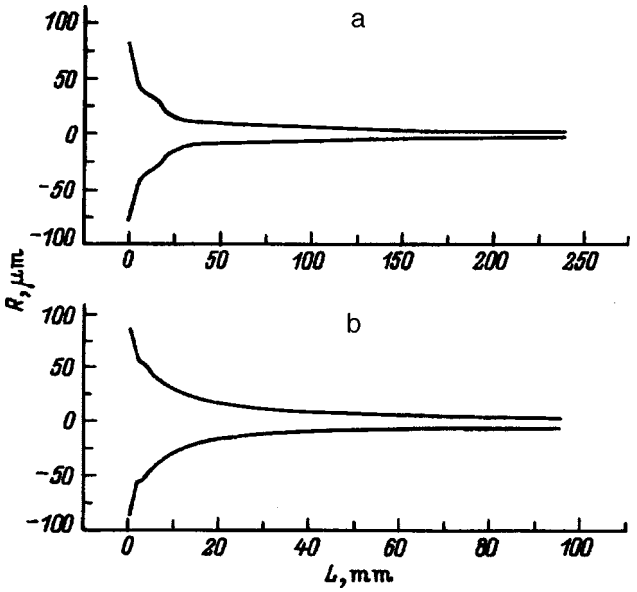

FIG. 3. Measured microcapillary profiles. L — distance along the capillary axis, R — distance in a perpendicular direction.

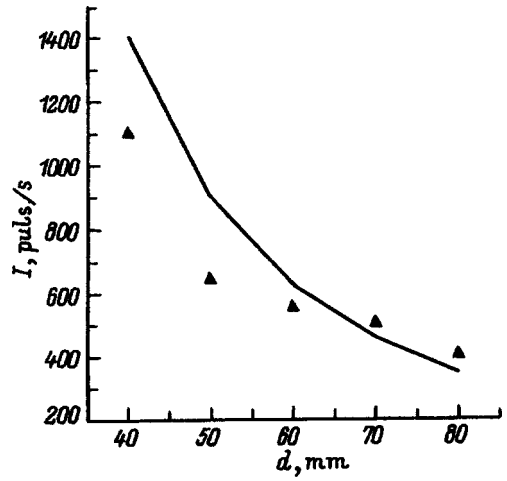

FIG. 4. Radiation intensity I at the microcapillary exit versus distance d between the focus of the x-ray tube and capillary. Curve — calculation; ▲ — experiment.

profiles were measured with an optical microscope.

A REIS-100 x-ray apparatus with a BS11 tube with a copper TTF anode was used to obtain x-ray microbeams. The voltage on the tube $U_a = 45$ kV, the current $i_a = 100$ μA, and the diameter of the focus of the tube was equal to 50 μm. The x-ray radiation was passed through a microcapillary with the inner-channel profile shown in Fig. 3b. The dependence of the beam intensity I at the capillary exit on the distance d between the tube focus and the capillary was measured. A detection unit from a DRON-2.0 diffractometer with a scintillation detector was used as the radiation detector. The results of the measurements are presented in Fig. 4. This figure also shows the computed values of the number of copper $K\alpha$ series photons which pass through the capillary. The number of photons $d^2N/d\Omega dt$ was taken to be 9 $\times 10^{10}$ photons/s·sr, the parameter T (Eq. (2)) was varied from 15 to 16 with the distance d varying within the limits indicated in Fig. 4. Despite the fact that photon absorption in the anode material and in the beryllium window, just as the bremsstrahlung photon flux, were neglected in the calculations, the order of magnitude agreement between the calculations and the experimental data makes it possible to conclude that the radiation in the capillary channel propagates in the waveguide regime, as shown in Fig. 1. It should also be noted that the relation (4) used in the calculations is approximate and can be refined only by numerical simulation of the x-ray trajectories from a source shifted relative to the axis of the x-ray optical system. This question as well as the spectral photon distribution at the capillary exit will be examined in a separate paper.

It can be concluded on the basis of our investigations that x-ray microbeams with intensity sufficient for practical applications can be obtained using x-ray optical systems based on microfocus x-ray tubes with a TTF anode and tapered glass microcapillaries.

[1] A. V. Vinogradov (ed.), *Reflection X-Ray Optics* [in Russian], Mashinostroenie, Leningrad, 1989, 463 pp.
[2] M. A. Kumakhov, Nucl. Instrum. Methods **48**, 283 (1990).
[3] V. I. Glebov, É. I. Denisov, and N. K. Zhevago, Zh. Tekh. Fiz. **61**(1), 125 (1991) [Sov. Phys. Tech. Phys. **36**, 1266 (1991)].
[4] D. J. Thiel, D. H. Bilderback, and A. Lewis, Rev. Sci. Instrum. **64**, 2872 (1993).
[5] D. X. Balaic and K. A. Nugent, Appl. Opt. **34**, 7263 (1995).
[6] D. H. Bilderback and D. J. Thiel, Rev. Sci. Instrum. **66**, 2059 (1995).
[7] N. Yamamoto and Y. Hosokava, Jpn. J. Appl. Phys. **27**, L2203 (1988).
[8] N. Yamamoto, Y. Homma, and S. Sakata, Mater. Res. Soc. Symp. Proc. **338**, 209 (1994).
[9] S. A. Ivanov and G. A. Shchukin, *X-Ray Tubes for Technical Applications* [in Russian], Énergoatomizdat, Leningrad, 1989, 200 pp.
[10] A. I. Borovskiĭ and G. A. Shchukin, Elektron. Promst., No. 5, 86 (1991).

Translated by M. E. Alferieff

Optical properties of a system of two coupled vertical microcavities

M. A. Kaliteevskiĭ

A. F. Ioffe Physicotechnical Institute, Russian Academy of Sciences, 194021 St. Petersburg, Russia
(Submitted February 25, 1997)
Zh. Tekh. Fiz. **68**, 94–97 (May 1998)

The interaction of two localized optical states in a structure consisting of a system of two coupled vertical microcavities is studied. It is shown that the interaction of two localized optical modes in coupled microcavities cause the modes to split. The optical properties of a system of coupled microcavities and the dispersion relations for the characteristic optical modes of the system are analyzed. © *1998 American Institute of Physics.* [S1063-7842(98)01705-X]

INTRODUCTION

It is well known that if two oscillators of arbitrary nature with identical free-state resonance frequencies are coupled sufficiently strongly with one another, then such a system of coupled oscillators will possess two characteristic frequencies, the splitting between which will increase with the strength of the coupling interaction.

A manifestation of this effect, known as Rabi splitting, was discovered at the beginning of the 1990s in semiconductor systems in the course of a study of the interaction of localized optical modes with excitons in semiconductor microcavities with quantum wells.[1] This led to the appearance of a large number of both experimental[2,3] and theoretical[4–6] works on this subject.

The next step in investigations of the interaction of oscillators of different nature is to investigate the interaction of two localized photon states,[7] which can occur in coupled vertical microcavities.

The objective of the present work is to investigate theoretically the optical properties of a system of coupled microcavities as well as the dispersion relations for the characteristic optical modes of such systems under normal incidence of light.

DISPERSION RELATIONS

Figure 1 shows a diagram of a structure in which the interaction of localized photon states can occur. It consists of two microcavities sharing a common central Bragg reflector (BR). The cavities 1 and 2 are located on each side of the common reflector. The structure is bounded on the exterior sides by Bragg reflectors BR1 and BR2. The photon modes localized in cavities 1 and 2 can interact via tunneling through the common reflector.

The interaction will be most efficient in the case when the free-state characteristic frequencies ω_1 and ω_2 of cavities 1 and 2, determined under normal incidence of light by the equations

$$\mathrm{Arg}(R_1)+\mathrm{Arg}(r)+2\Phi_1=2\pi N, \tag{1a}$$

$$\mathrm{Arg}(R_2)+\mathrm{Arg}(r)+2\Phi_2=2\pi M, \tag{1b}$$

are equal to each other. Here N and M are integers; r is the amplitude reflection coefficient of the common reflector; $R_{1(2)}$ is the amplitude reflection coefficient of the outer mirror of the first (second) cavity; $\Phi_{1(2)}$ are the phases acquired by the light as it passes through the first (second) cavity, which are determined by the expression

$$\Phi_{1(2)}=n_{c1(2)}L_{1(2)}\omega_{1(2)}/c, \tag{1c}$$

where $n_{c1(2)}$ are the refractive indices of the cavities, $L_{1(2)}$ are the cavity thicknesses, $\omega_{1(2)}$ are the characteristic frequencies of the first (second) cavity, and c is the speed of light in vacuum.

According to the approach set forth in Ref. 5, the dispersion relation for the characteristic modes of the structure shown in Fig. 1 can be written in the form

$$(t^2-r^2)R_1R_2\ \exp(i(\Phi_1+\Phi_2))-\exp(-i(\Phi_1+\Phi_2))$$
$$+r(R_1\ \exp(i(\Phi_1-\Phi_2))+R_2\ \exp(i(\Phi_2-\Phi_1)))=0. \tag{2}$$

For a symmetric structure with $R_1=R_2=R$, $\Phi_1=\Phi_2=\Phi$, and $L_1=L_2=L$ one can rewrite Eq. (2) in the form

$$R^2(t^2-r^2)\exp(2i\Phi)+2Rt\ \exp(i\Phi)-1=0, \tag{3}$$

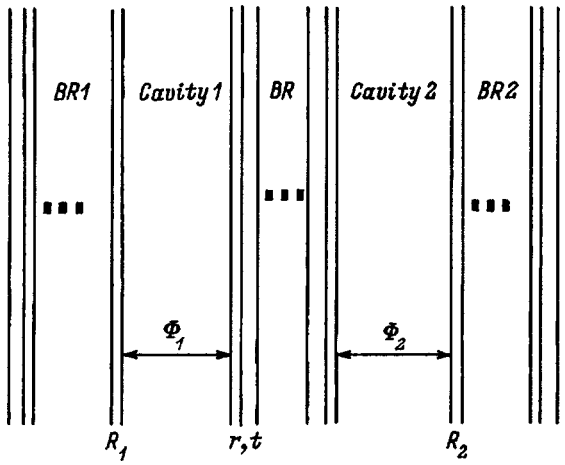

FIG. 1. Diagram of the structure.

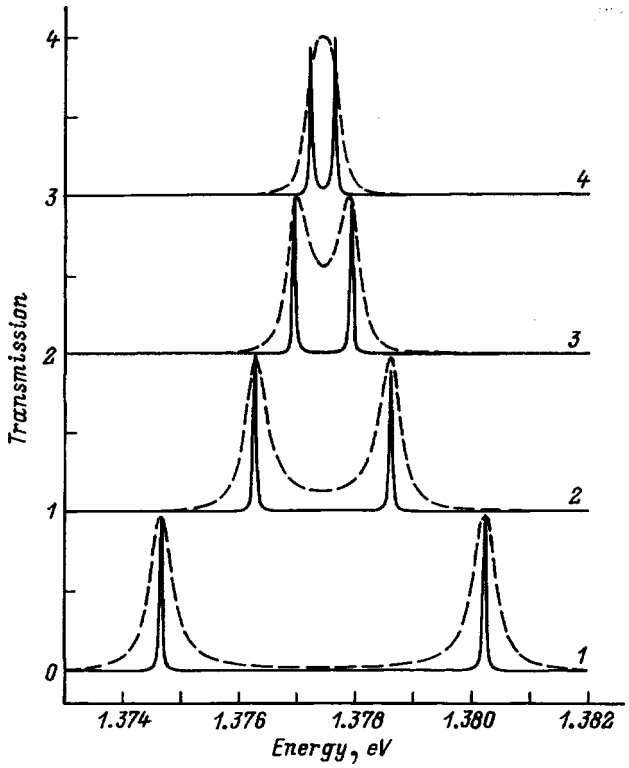

FIG. 2. Computed transmission spectra of coupled microcavities for different values of the reflection coefficient of the common reflector. *1* — $R=0.996$ ($P=12$), *2* — $R=0.999$ ($P=15$), *3* — $R=0.9995$ ($P=18$), *4* — $R=0.9999$ ($P=21$). Solid curves — structure side reflectors whose reflection coefficients equal 0.999; dashed curves — structure reflection with side reflectors whose reflection coefficients equal 0.95. The curves are shifted with respect to one another by one unit.

which can be represented as a product of two cofactors corresponding to two characteristic modes of the system of coupled cavities

$$[R(r+t)\exp(i(\Phi+\varphi))-1]\times[R(r-t)\exp(i(\Phi+\varphi))-1]=0, \tag{4}$$

where φ is the phase of the reflection coefficient of the exterior reflectors,[6] which satisfies the relation

$$\varphi\approx\frac{\pi n_1 n_2}{(n_2-n_1)n_c}\,\frac{\omega-\tilde{\omega}}{\tilde{\omega}}, \tag{5}$$

where n_1 and n_2 are the refractive indices of the cavity-forming layers, and $\tilde{\omega}$ is the Bragg interference frequency of the reflector.

It should also be noted[8] that near the Bragg interference frequency of the reflector the phases of the amplitude reflection and transmission coefficients differ by $\pi/2$ when the reflector contains an odd number of layers, i.e., in the case of the symmetric structure

$$\mathrm{Arg}\left(\frac{t}{r}\right)\approx\frac{\pi}{2}, \tag{6}$$

which becomes an exact equality at the Bragg interference frequency.

We shall assume that $t/r\ll 1$, i.e., the reflection coefficient of the common reflector is quite large. Substituting expressions (5) and (6) into Eq. (4), we obtain an equation for the mode splitting $\Delta\omega$

$$\Delta\omega\left(\frac{n_c L}{c}+\frac{2\pi n_1 n_2}{\tilde{\omega}(n_2-n_1)n_c}\right)\approx 2\,\frac{t}{r}. \tag{7}$$

If the Bragg interference frequency $\tilde{\omega}$ of the reflector equals the frequency ω_0 of the characteristic mode of a single microcavity, as determined by Eqs. (1), then Eq. (7) can be rewritten in the form

$$\Delta\omega\approx\frac{\omega_0|t|}{\pi\left(\dfrac{n_c L}{\lambda_0}+\dfrac{n_1 n_2}{(n_2-n_1)n_c}\right)}, \tag{8}$$

where $\lambda_0=2\pi c/\omega_0$ is the wavelength of light in vacuum, corresponding to the characteristic frequency of the microcavity.

OPTICAL PROPERTIES

Let us consider a symmetric system of two coupled microcavities with the following parameters: The refractive indices of both cavities $n_c=4$, the thicknesses of the cavities 1

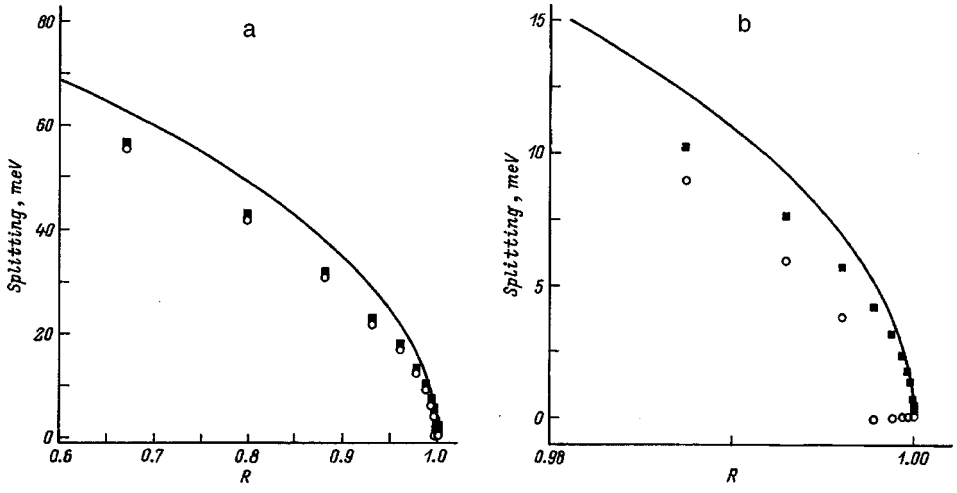

FIG. 3. Splitting of the modes in the spectrum as a function of the reflection coefficient of the common reflector with the reflection coefficients of the side reflectors equal to 0.999 (squares) and 0.95 (circles). The solid line shows the curve calculated from Eq. (8).

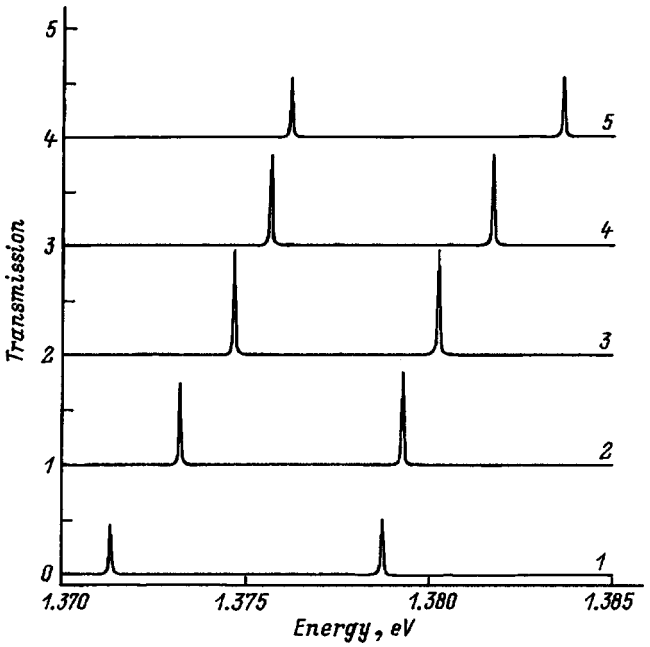

FIG. 4. Computed transmission spectra of coupled microcavities with the thickness of cavity 1 fixed at 225 nm and different values of the thickness of cavity 2. *1* — 227, *2* — 226, *3* — 225, *4* — 224, *5* — 223 nm; the layers in all three reflectors have the same thickness. The curves are shifted with respect to one another by one unit.

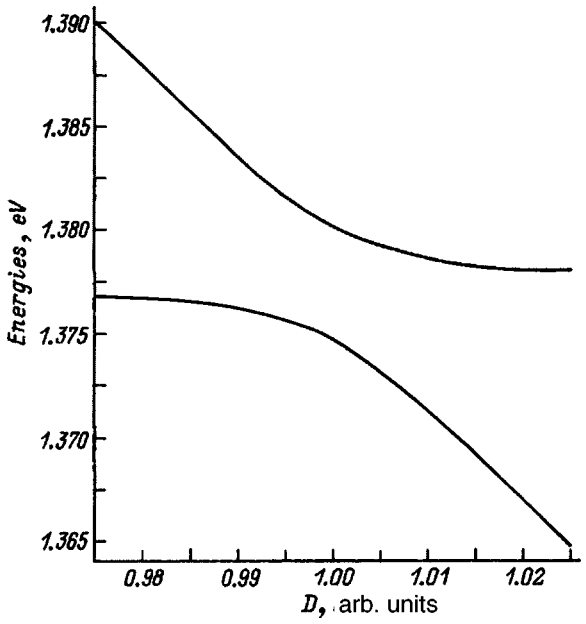

FIG. 5. Position of the characteristic optical modes of a system of two coupled microcavities as a function of the relative detuning of the cavities 1 and 2, determined with the aid of Eq. (1).

and 2 are 225 nm, the refractive indices of the reflector layers are $n_1=3$ and $n_2=4$, and the layers in the reflectors are 75 and 56.25 nm thick. For such a system the radiation wavelength corresponding to the characteristic modes of cavities 1 and 2 is $\lambda_0=900$ nm and $\tilde{\omega}=\omega_0$. Let the side reflectors consist of Q pairs of layers, and let the common reflector contain P layers with a refractive index of 3 which are separated by a $(P-1)$-th layer with a refractive index of 4.

Figure 2 shows light transmission spectra calculated by the transfer matrix method[9] for different values of the reflection coefficients of the common and side reflectors. One can see that as the reflection coefficient of the common reflector increases, the splitting of the peaks in the spectrum decreases, and in a strongly damped structure (side reflectors with lower reflection coefficients) increasing the reflection coefficient of the common reflector can cause the two peaks to merge into one peak corresponding to a transition from strong to weak coupling.

Figure 3a shows the splitting of the spectral features as a function of the reflection coefficient of the common reflector. For comparison, the solid line shows the curve determined by Eq. (8). Figure 3b shows the same dependences on a scale that makes it possible to see the transition from the strong to weak coupling. In all cases one can see the characteristic square-root dependence on the coupling parameter, which in this case is the transmission coefficient of the common reflector.

We shall now turn to the anticrossing modes in our system. Figure 4 shows a family of light transmission spectra of coupled microcavities whose thicknesses (and correspondingly the characteristic frequencies) differ somewhat. One can see that when the spectral position of one mode of the system changes, so does the position of the other mode, i.e., the modes are coupled. Analyzing the positions of the spectral features, one can see that they demonstrate anticrossing. It is also evident that the amplitudes of the peaks in the transmission spectra decrease with increasing detuning of the cavities.

Figure 5 shows the positions of the characteristic modes of the system, determined by Eq. (2), as functions of the relative detuning D of the cavities

$$D=\frac{\omega-\omega_0}{\omega_0}. \tag{9}$$

The curves have the well-known form of dispersion curves for coupled oscillators of various natures, viz., the anticrossing of modes. The positions of the resonance features in the spectra are virtually identical in this case to the solutions of Eq. (2).

The main results of this work are as follows. We have studied the interaction of localized photon states in a structure consisting of a system of two coupled microcavities, resulting in splitting of the optical modes of the system. An analytical expression was obtained for the splitting. The optical properties of the system were analyzed for normal incidence of light.

This work was supported by the Russian Fund for Fundamental Research (Grant No. 96-02-17836) and the Interdisciplinary Science and Technology Program ''Physics of Solid-State Nanostructures.''

I acknowledge A. V. Kovokin and E. L. Portnoĭ for helpful discussions.

[1] C. Weisbouch, M. Nishioka, A. Ishikava, and Y. Arakawa, Phys. Rev. Lett. **69**, 3314 (1992).
[2] R. Houdre, R. P. Stanley, and U. Oesterle, Phys. Rev. B **49**, 16761 (1994).

[3] J. Tignon, P. Voisin, and C. Delande, Phys. Rev. Lett. **74**, 3967 (1995).
[4] A. V. Kavokin and M. A. Kaliteevski, Solid State Commun. **95**, 859 (1995).
[5] E. L. Ivchenko, M. A. Kaliteevski, A. V. Kavokin, and N. A. Nesvihzskii, J. Opt. Soc. Am. B **13**, 1061 (1996).
[6] V. Savona, L. C. Andereani, P. Schwendimann, and A. Quatropani, Solid State Commun. **93**, 733 (1995).
[7] R. P. Stanley, R. Houdre, and U. Oesterle, Appl. Phys. Lett. **65**, 2093 (1994).
[8] M. A. Kaliteevskiĭ and A. V. Kavozhin, Fiz. Tverd. Tela (St. Petersburg) **37**, 2721 (1995) [Phys. Solid State **37**, 1497 (1995)].
[9] M. Born and E. Wolf, *Principles of Optics*, 4th ed. (Pergamon Press, New York, 1969; Nauka, Moscow, 1970, p. 77).

Translated by M. E. Alferieff

On the possibility of distributed associative writing of information by the superimposition of images (plurography)

A. A. Kal'nin and A. S. Nosov

St. Petersburg State Electrical Engineering University, 197376 St. Petersburg, Russia
(Submitted April 7, 1997)
Zh. Tekh. Fiz. **68**, 98–101 (May 1998)

An expository account is given for the principle of distributed associative writing of optical images by recording in a photosensitive medium the total signal from a set of superimposed images with a random spatial shift. The method preserves the basic characteristic qualities of the holographic method but does not require the use of sources of coherent or monochromatic radiation. The results of an experimental test of the method are presented. © *1998 American Institute of Physics.* [S1063-7842(98)01805-4]

PRINCIPLE OF THE METHOD

The proposed principle of distributed associative writing of information is to a certain extent a synthesis of the optical[1] and neural-net[2–4] methods of implementing an associative memory. It can be briefly described as a method for detecting self-similar images by repeated random superimpositions of the images and the selection of bright spots, which are associates of different parts of the complete image. The system of associates, each containing information from many parts of the image, that is recorded in this manner on a recording medium is a conditioned coded representation (plurogram) of the image.

Figure 1 elucidates the writing and reconstruction of a complete image according to its parts. Image *1*, for example, in the form of a luminous letter *A*, is reconstructed on a flat surface of a photosensitive material *3* with the aid of a plate *2* containing a set of randomly distributed pinholes of small diameter. The random superimpositions of the images arising in this peculiar sort of pinhole camera produce a complicated field of illuminance, some sections of which have a relatively high illumination intensity. The photosensitive material (or, more generally, the recording medium) has the property that, after exposure, traces (reflections) remain in the material only at locations where the exposure level is higher than a prescribed threshold value.[4] In other words, traces appear in the recording medium only at locations where bright superimpositions occur. When a contrast (threshold) type of positive photosensitive material is used, a trace of the symbol *A* appears in the form of many bright separate spots of various configurations against a black background.

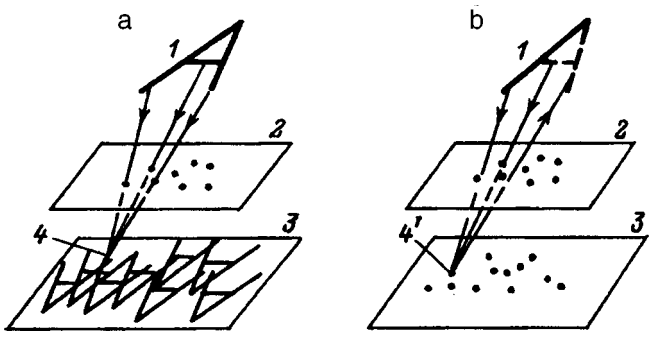

FIG. 1. Diagram elucidating the principle of coded writing of images by the plurography method. a — Multiplication of images of the symbol *A* (*1*) by a set of pinholes in an opaque plate (*2*) and the superimposition of the images on a photosensitive material (*3*) with the formation of bright spots (*4*, *4′*), b — the illuminance of a single reflection, an associate of the luminous parts of the symbol, produces upon reversal of the ray path, illumination in the absent part of the image.

Associative reconstruction of a complete image from a part of the image is elucidated in Fig. 1b. When a fragment of an image is demonstrated, images of part of the symbol *A* being demonstrated are superimposed on the plurogram *3*, just as during writing. In the process, the bright elements which were created as a result of the superimposition of the now present and absent (dashed) parts of the image *1* will with a certain probability be illuminated. Then there will appear a superimposition of conditioned images — the illuminated bright elements of the plurogram — but now in the plane of the initial partial symbol *A*. As a result of the selection of the bright associates at the writing stage, and in view of the reversibility of ray paths, there is a higher probability of bright superimpositions occurring within the contour of the initial image. By making a secondary selection of bright spots of illumination (for example, once again using a high-contrast photosensitive material), one can reconstruct the absent part (parts) of the image, element by element.

ELEMENTS OF THE THEORETICAL DESCRIPTION

We shall confine our attention here, for simplicity, to the writing and reconstruction of one-dimensional images, which are characterized by the coordinate dependence of the brightness $B(x)$ of the radiation from a strip of constant width b, for example, a set of luminous strips of different length (Fig. 2a).

Suppose that a plate with openings is located at a distance a from the image, and that the photosensitive layer is located at a distance h from the image. In this case an opening in the plate at a coordinate x_i (i is the number of the opening) will bring about the formation on the photosensi-

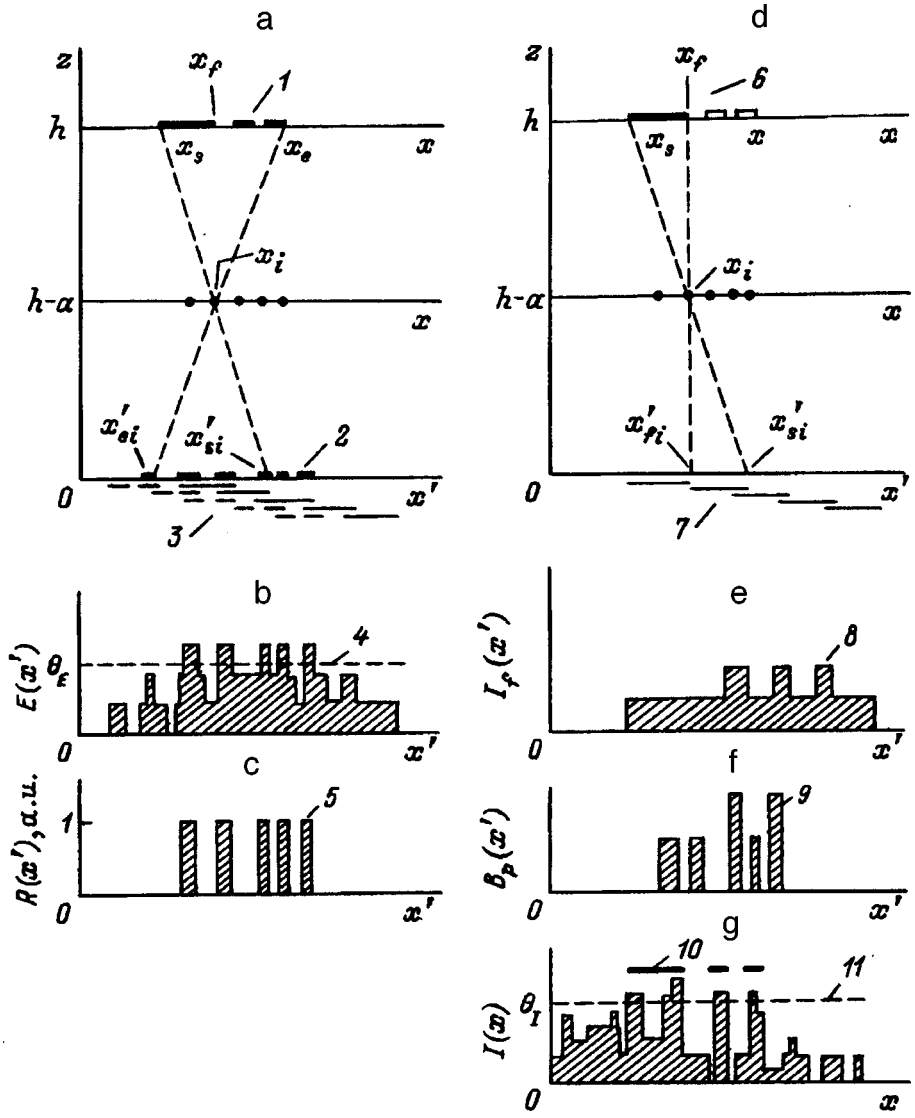

FIG. 2. Graphical illustration of distributed writing of a one-dimensional image (a–c) and its associative reconstruction (d–g). *1* — Image, *2* — elements of the plurogram, *3* — superimposition of inverted images, *4* — writing threshold, *5* — coded trace of the image (plurogram), *6* — part of the demonstrated image, *7* — superimpositions of partial inverted images, *8* — illuminance of the plurogram, *9* — brightness of the reflections of the plurogram, *10* — initial image, *11* — reconstruction threshold.

tive medium an inverted image of the original image $B(x)$, with the coordinate transformation given by the relation

$$x' = x + \frac{h}{a}(x_i - x), \tag{1}$$

where x and x' are, respectively, the coordinate of an element of the subject image and the coordinate corresponding to this element on the photosensitive recording medium.

If the total number of pinholes in the plate is n, then one will have a superimposition of n inverted images. The intensity $I(x')$ of the light incident on the recording medium is determined by the directional pattern of the radiation of the luminous elements of the image, the diameter d of an opening, and the distance between the image and the recording medium. Assuming that 1) the angle of formation α of the image elements through any opening i is small, 2) the diameter d of the openings is much greater than the wavelength λ in a wavelength band[1)] $\Delta\lambda$, and 3) the angular distribution of the radiation intensity is cosinusoidal, one can assume that the intensity of the light incident on the photosensitive material through one opening will be proportional to the brightness $B(x)$ of the light:

$$I(x') = \xi \cdot B(x), \tag{2}$$

where ξ is a coefficient of proportionality.

In this case the coordinate dependence of the intensity of the light incident on the photosensitive material will be due to the superimposition of n images:

$$I(x') = \xi \sum_{i=1}^{n} B[x_i - (x' - x_i)/(h/a - 1)]. \tag{3}$$

If the photosensitive recording medium possesses an accumulative property, then the accumulated dose is the exposure level $E(x',t)$

$$E(x',t) = I(x') \cdot t, \tag{4}$$

where t is the exposure time.

As we have said, only traces of bright signal superimpositions should remain on the recording medium. This makes it necessary to introduce a threshold exposure level θ_E (Fig. 2b). For definiteness, let us assume that a trace mark on the recording medium signifies the appearance of a region with a high reflection coefficient $R(x')$ for the incident light $I(x')$.

Then the writing of an image on the medium, with allowance for the accumulation–threshold property, can be represented as follows:

$$R(x')=\varkappa[E(x')-\theta_E], \quad \text{if} \quad E(x')-\theta_E\geqslant 0; \tag{5}$$

$$R(x')=0, \quad \text{if} \quad E(x')-\theta_E<0. \tag{6}$$

Here the coefficient $\varkappa$ depends on the properties of the photosensitive material. Expressions (5) and (6) are a coded record of the original image $B(x)$, i.e., a plurogram (Fig. 2c).

The reconstruction of a complete image from its parts occurs as a result of the illumination of some of the reflections of the plurogram, which were formed by superimposition of radiation from the present and absent parts of the original image. The part of the image that is present can also be a sampling of many fragments of the image. Here we bound the coordinates of the exitance of the object image by the interval $[x_s, x_f]$ with $x_s,\ x_f\in[x_s; x_e]$, where x_s and x_e are the limits of the complete image (Fig. 2d). In this case of presentation of a partial image, the illuminance $I_f(x')$ of the elements of the plurogram is given by expression (3), but the coordinates of the exitance of the original image $B(x)$ are limited by the length of the image fragment, i.e., $x\in[x_s; x_f]$. The illuminance of the reflections (Fig. 2e) produces a relief of the brightness distribution $B_p(x')$ on the recording medium,

$$B_p(x')=\beta I_f(x')R(x'), \tag{7}$$

where β is a coefficient of proportionality.

The conditioned image $B_p(x')$ which appears (Fig. 2f) is once again transformed into n superimpositions, but now in the plane of the original image:

$$I(x)=\xi'\sum_{i=1}^{n} B_p\left[x+\frac{h}{a}(x_i-x)\right], \tag{8}$$

where ξ' is a coefficient of proportionality relating the brightness of an element of the plurogram at the coordinate x' with the intensity of the light entering through a single opening in the plane of the original image at the coordinate x.

Repeated signal selection is possible, both with respect to the intensity $I(x)$ of the received radiation and with respect to the exposure level $E(x)=I(x)t$. Choosing the first option (Fig. 2g), we can write the reconstructed part of the image $I_r(x)$ in the form

$$I_r(x)=I(x)-\theta_I, \quad \text{if} \quad I(x)\geqslant\theta_I; \tag{9}$$

$$I_r(x)=0 \quad \text{if} \quad I(x)<\theta_I. \tag{10}$$

The selection of bright superimpositions of images according to a prescribed threshold at the writing stage means that light from many luminous parts of the subject image arrive in the region of the reflection that is formed. Since the ray paths are reversible when reconstruction is done through the openings through which the reflection was formed, in the image reconstruction stage the probability of superimpositions of light from the reflections of the trace is higher within the luminous regions of the original image than it is outside these regions. A secondary selection with respect to intensity performed at this stage will reveal the odds in favor of this.

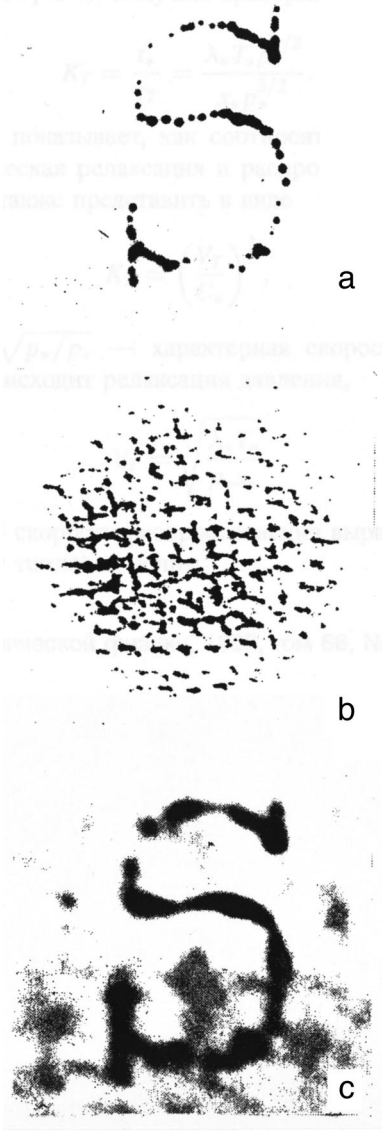

FIG. 3. Result of an experimental test of image writing and reconstruction by the plurography method. a — Luminous symbol, b — coded trace of the symbol, c — result of image reconstruction.

We note that a plate with openings is not the only method for producing superimposition of images. Moreover, it is not necessary to superimpose undistorted proportional images.

EXPERIMENTAL CONFIRMATION OF THE POSSIBILITY OF RECONSTRUCTING IMAGES FROM A PLUROGRAM

In the course of the investigations experiments were performed on writing and reconstruction of images by the method proposed above. For this, a luminous letter *S* in the form of a set of bright dots (Fig. 3a) was formed using a light source and a light mask. A plate with a 2×2 cm format, containing randomly distributed openings 0.2 mm in diameter and with a density of 60 cm^2, was placed midway between the image and the photosensitive material. The distance between the image and the photosensitive material was

$h = 24$ cm. The accumulation–threshold property of the recording medium was realized by using a special contrast photosensitive material with negative–positive inversion. Figure 3b shows the plurographic recording of the letter *S*.

The main difficulty arising in the experiments on associative reconstruction of the absent part of the image is a strong parasitic background which appears as a result of reflection of light from the ''black'' regions of the plurogram. For this reason, here we confine ourselves to demonstrating the reconstruction of the complete subject image using not reflected light but rather the light transmitted through a plurogram prepared on photographic film with a light-scattering interlayer. The result of image reconstruction using this conditioned coded representation (plurogram) and obtained with the aid of a special contrast photographic paper is shown in Fig. 3c.

In the experiments it was also possible to observe the reconstructed image visually on frosted glass placed at the same distance from the plurogram as the original image during writing. The image can be observed with acceptable sharpness when a portion of the plurogram is covered. This attests to the distributed nature of the recording.

As one can see from Fig. 3c, image reconstruction occurs against the background of random bright spots. Undoubtedly, a sharper threshold in the photorecording medium can lower this undesirable background. Another possibility is to use receiving systems with attractive properties.

The proposed method of signal recording supplements the earlier versions: structural reflection[5,6] and adaptive diffraction grating.[7]

In conclusion, we note that the limitations of this method must be investigated in detail in order to assess its technical value. First and foremost, it is necessary to take account of diffraction phenomena and to find the optimal values of the writing and reconstruction thresholds giving the best reconstructed image quality. In any case, the possibility of distributed associative writing without the use of sources of coherent radiation is in itself of methodological interest.

We express our deep appreciation to A. N. Pikhtin for a discussion of this work and for valuable remarks and to I. A. Mityureva for constructive discussions, which prompted this investigation. M. A. Koltok provided enormous assistance in performing this investigation, for which we are very grateful to her.

[1)]There exists an optimal diameter of the opening in a pinhole camera for obtaining maximum image resolution, equal to $0.95\sqrt{(h-a)\lambda}$.

[1] S. A. Akhmanov and M. A. Vorontsov (eds.), *New Physical Principles of Optical Information Processing* [in Russian], Nauka, Moscow, 1990, 400 pp.
[2] A. A. Frolov and I. P. Murav'ev, *Neural Models of Associative Memory* [in Russian], Nauka, Moscow, 1987, 160 pp.
[3] T. Kohonen, *Self-Organization and Associative Memory*, Springer-Verlag, New York, 1984, 255 pp.
[4] T. G. Bochkareva and I. A. Mityureva, Izv. St-Peterburg Gos. Élektron. Tekh. Univer., No. 435, 83 (1993).
[5] A. A. Kal'nin, in *Microelectronics and Semiconductor Devices* [in Russian], edited by A. A. Vasenkov and Ya. A. Fedotov, Radio i Svyaz', Moscow, 1989, No. 10, pp. 95–110.
[6] A. E. Drachev, A. A. Kal'nin, and V. V. Luchinin, Zh. Tekh. Fiz. **63**, 121 (1993) [Tech. Phys. **38**, 119 (1993)].
[7] A. A. Kal'nin and G. Shabbakh, Zh. Tekh. Fiz. **63**, 134 (1993) [Tech. Phys. **38**, 124 (1993)].

Translated by M. E. Alferieff

Experimental study of the temporal characteristics of a switch for topologically modulated signals

G. A. Kuzaev

Moscow State Institute of Electronics and Mathematics, 109028 Moscow, Russia
(Submitted February 5, 1996)
Zh. Tekh. Fiz. **68**, 102–104 (May 1998)

Aspects of an experimental study of the temporal characteristics of switches for topologically modulated signals are considered. A microwave resistive switch card serves as the experimental model. The clock frequency of the generator of topologically modulated pulses developed is chosen such that the ratio of the wavelength at the clock frequency to the dimensions of the standard switch card is equal to 10^4. It is concluded on the basis of the virtual absence of distortions of the input pulses switched by the device and the application of scaling to the experimental results that a switch of micron dimensions is effective for microsecond pulses, confirming the previously obtained theoretical data. © *1998 American Institute of Physics.* [S1063-7842(98)01905-9]

INTRODUCTION

One of the trends in microelectronics is to take into account the spatial features of the fields of electromagnetic signals in circuits with high clock frequencies and a high element packing density.[1–3] One of the ways to accomplish this is to use pulsed topological modulation, which was proposed in Ref. 4. The possibility of the subpicosecond switching of signals of a given type in different layers of an integrated circuit has been demonstrated, experimental models of switches for the microwave range have been developed and investigated experimentally, and the realization of quasineural operations when spatially nonuniform fields are superposed has been substantiated.[5–7] In the present work it is proposed that our main attention be focused on experimental investigations of the temporal characteristics of switches that were previously calculated only within theoretical models.[4–7]

EXPERIMENTAL MODEL OF THE SWITCH AND DETAILS OF THE INVESTIGATION

Let us briefly consider the features of topologically modulated signals and the methods used to process them. Digital information is contained in the spatial structure of the electromagnetic field lines, i.e., a topological scheme.[4,5] The discrete processing of such signals requires devices that are nonlinear with respect to the field topology. It is known from theoretical data that passive circuits can have such nonlinearity. The possibility of circumventing the physics of semiconductor effects permits the realization of ultrafast operations involving, for example, the spatial switching of signals in the bulk of an integrated circuit. Examples of such devices, which have been termed topological switches, were described in Refs. 5–7, which also present experimental data on the spatial separation of analog microwave signals. The object of the present work was to experimentally and theoretically investigate nonstationary switching process. For this purpose we used an experimental model of a resistive switch, which was previously investigated by experimental means in the microwave *S* band (Fig. 1).[7] It is fabricated on a Polikor ($\varepsilon = 9.6$) card with a thickness of 1 mm and has the form of an octupole (Fig. 1). Coupled strip transmission lines (*I*) of width 0.77 mm serve as the inputs (*1,2*), to which even or odd modes having fields with different spatial structures are supplied. The distance between the strips is equal to 0.18 mm. The temporal shape of the input signals is square or nearly so. When an even mode is supplied to the input, the conductors in the coupled transmission lines are charged equally, and the signal consequently reaches only output *II*. An odd mode, which has a different field topology, is reflected nearly entirely from output *II* and reaches output *III* along a 50-Ω strip line. Spatial switching of the signals is thereby accomplished. Film resistors with $R = 50\ \Omega$ are used for short-circuited conversion and for implementing the possibility of recording the voltage in the odd-mode regime.

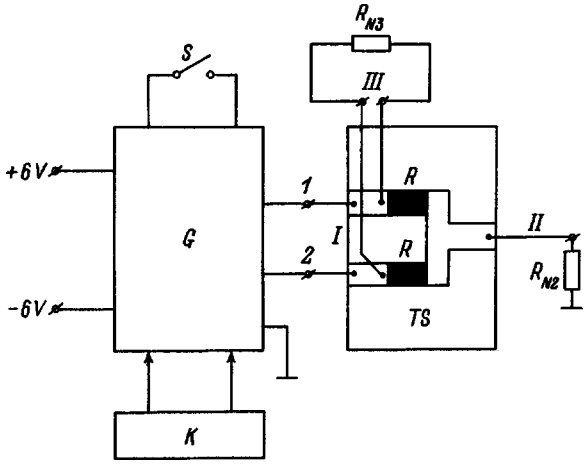

FIG. 1. Structural diagram of the experimental model for measuring the temporal characteristics of a resistive switch for topologically modulated signals: *G* — generator, *S* — switch for selecting the operating modes of the signal generator, *K* — correcting circuit, *TS* — resistive switch for topologically modulated signals, *R* — film resistors.

To test the operation of the switch in a nonstationary signal switching regime, we developed a signal generator, which permits the supply of even or odd modes to the input of the coupled strip transmission lines. A structural diagram of such a device is presented in Fig. 1 and consists of a signal generator G in a KR1533LN1 microcircuit, mounted elements, a correcting circuit K, a switch S for selecting the operating mode, the circuit card under investigation TS, and high-resistance loads R_{N2} and R_{N3}.

Correct selection of the clock frequency with consideration of the dimensions of the switch is important, since the results of the experimental investigations are to be used to draw a conclusion regarding the effectiveness of such a design fabricated according to a technology for very large scale integrated circuits (VLSIs). For example, the ratio of the wavelength λ_T at the clock frequency f_T to the characteristic dimensions d_e of the VLSI elements ($K_0=\lambda_T/d_e$) ranges from one to several powers of ten.[1–3] The experimental model of the switch investigated was fabricated using a hybrid microwave technology with dimensions of the order of several millimeters (Fig. 1). The distance d_e between input I and outputs II and III is 30 mm. Therefore, to correctly apply the scaling method,[2] the clock frequency f_T was selected such that $K_0=10^4$. This value is typical of the overwhelming majority of VLSIs.[1–3] Applying the principles of modern microelectronics, we can assert in a first approximation that the switching properties of the switch will be invariant against increases in the clock frequency up to the microwave range, if K_0 remains unchanged as the geometric dimensions of the switch are simultaneously reduced to micron values.

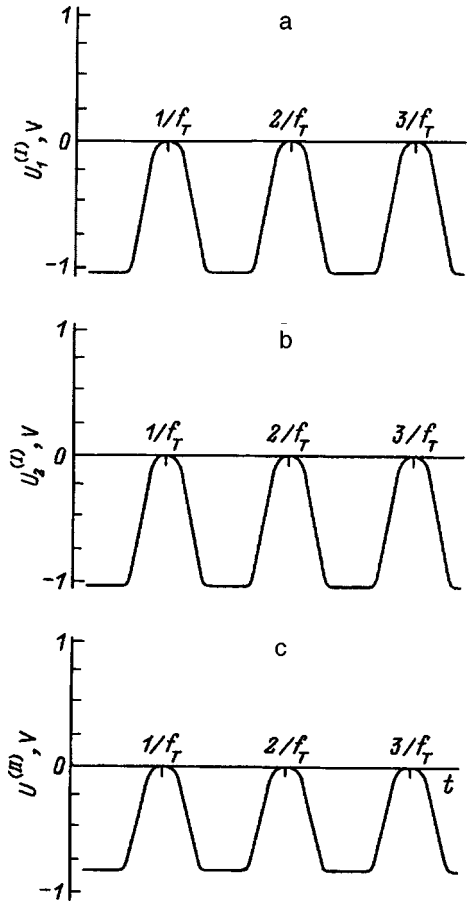

FIG. 2. Time dependences of the signals at input I and output II of the switch for topologically modulated signals: a — voltage at input terminal *1*; b — voltage at input terminal *2*; c — voltage at switch output II. The ratio of the wavelength λ_T at the clock frequency to the dimensions of the switch card $\lambda_T/d_e=10^4$, and the on–off time ratio of the pulses is 0.33.

RESULTS OF THE EXPERIMENTAL INVESTIGATIONS

The temporal characteristics of the experimental model developed were measured using an S1-99 oscillograph with a standard 1 MΩ input resistance. The error in the measurements of the signal shape does not exceed 5%. The free output of the instrument was also loaded with an equivalent 1 MΩ resistance during the measurements.

When a periodic sequence of pulses of the even mode was generated, their synchronism was virtually maintained at the input of the coupled strip transmission lines (Figs. 2a and 2b), and a signal which is somewhat diminished in amplitude because of the resistors R was fed into the high-resistance input of the oscillograph (Fig. 2c). In this case the signal at output III was suppressed by 30 dB . The final degree of suppression is governed primarily by the error in the generation of ''cophasal'' pulses of identical amplitude.

The generation of pulses of the odd mode had its own special features, since some asynchronism of the pulses of opposite polarity was observed due to the operation of the microcircuit. This led to the appearance of a pulse of the even mode at output II, whose duration was approximately equal to the asynchronism interval. To eliminate the error in the operation of the microcircuit in this regime, we developed a correcting circuit, whose parameters were adjusted experimentally. It made it possible to suppress pulses of short duration at output II by 27 dB. Greater synchronism of the pulses forming the odd mode is possible when a better integrated circuit is used.

CONCLUSIONS

Aspects of an experimental study of the temporal characteristics of switches for topologically modulated signals have been considered. A microwave resistive switch card served as the experimental model. The clock frequency of the generator of topologically modulated pulses developed was selected so that the ratio of the wavelength at the clock frequency to the dimensions of the standard switch card would be equal to 10^4. It has been concluded on the basis of the virtual absence of distortions of the input pulses switched by the device and the application of scaling to the experimental results that a switch of micron dimensions is effective for microsecond pulses, confirming the theoretical data previously obtained.[4–7]

We thank V. A. Gorlanov for his assistance in performing the experiments.

This work was partially financed by the Russian Fund for Fundamental Research (Grant No. 94-0204979-a).

[1] D. K. Ferry, L. A. Akers, and E. W. Greeneich, *Ultra Large Scale Integrated Microelectronics* [Prentice Hall, Englewood Cliffs, N.J. (1988); Mir, Moscow (1991), 327 pp.].
[2] Yu. V. Gulyaev, V. B. Sandomirskiĭ, and A. A. Sukhanov, Usp. Fiz. Nauk **144**, 475 (1984) [Sov. Phys. Usp. **27**, 868 (1984)].
[3] A. I. Shagurin and I. I. Korobkov, Mikroelektronika **23**(5), 76 (1994).
[4] G. A. Kuzaev, Zh. Tekh. Fiz. **65**(8), 205 (1995) [Tech. Phys. **40**, 863 (1995)].
[5] G. A. Kuzaev, Radiotekh. Elektron. **40**, 431 (1995).
[6] G. A. Kouzaev, in *Proceedings of the International Symposium on Electromagnetic Theory*, URSI, St. Petersburg (1995), pp. 584–586.
[7] V. I. Gvozdev, G. A. Kuzaev, and I. V. Nazarov, Mikroelektronika **24**(1), 29 (1995).

Translated by P. Shelnitz

Parametric interaction of volume magnetostatic waves in a ferrite film with spatiotemporal modulation of the magnetic field

A. F. Popkov

Zelenograd State Research Institute of Physical Problems, 103460 Moscow, Russia

Yu. K. Fetisov

Moscow Institute of Radio Engineering, Electronics, and Automation, 119137 Moscow, Russia

N. V. Ostrovskiĭ

Moscow Institute of Electronic Technology, 103498 Moscow, Russia

(Submitted March 4, 1996)
Zh. Tekh. Fiz. **68**, 105–112 (May 1998)

Effects of the resonant Bragg scattering of magnetostatic backward volume waves on the periodic structure of a conductive meander pattern with an alternating current are analyzed theoretically and compared with experiment. It is shown that unlike a static grating, a dynamic grating causes a frequency shift of the scattered wave. It is proposed that this phenomenon be utilized for effective control of the intermodal conversion of magnetostatic waves.
 [S1063-7842(98)02005-4]

INTRODUCTION

Long-wavelength magnetostatic spin waves (MSWs) propagating in yttrium-iron garnet (YIG) films are very sensitive to the conditions on the film surface and to the external magnetic field. This makes it possible to control the propagation of the waves by creating weak inhomogeneities on the film surface.

Static inhomogeneities can be formed, for example, by etching the film through a periodic mask,[1] by periodically varying the magnetization and anisotropy fields during implantation of the ferrite film,[2] by depositing a grating of conductive strips on the film surface,[3] or by placing a high-coercivity magnetic ribbon with a harmonic distribution of the magnetic field in it alongside the film.[4] When the conditions for spatial synchronism are satisfied, resonant Bragg scattering of an MSW on the static inhomogeneities accompanied by alteration of the wave number of the MSW takes place.

Dynamic inhomogeneity can be formed by depositing a conductor in the form of a meander pattern on the surface of a ferrite film and passing an alternating current through it.[5] The current flowing through the conductor creates spatiotemporal inhomogeneity of the magnetic field, which actually has the form of two magnetic-field waves traveling in opposite directions. If the amplitude of these waves is small compared with the homogeneous internal magnetic field in the film, an MSW will undergo inelastic scattering on the traveling waves when the phase synchronism conditions are satisfied. Unlike scattering on static inhomogeneities, in the present case not only the wave number, but also the frequency of the scattered MSW will be altered when the conditions for resonant Bragg scattering are satisfied. Similar phenomena appear when an MSW is scattered on a surface acoustic wave traveling in a film.[6] However, the periodic structures with a current considered in the present work permit achievement of complete interconversion of the MSW harmonics over considerably shorter interaction lengths, so that the influence of damping can be less significant in this case than in acoustomagnetic scattering.[7] In addition, the simplicity of the design of creating spatially periodic inhomogeneity using an alternating magnetic field is attractive.

The effects of the parametric interaction of MSWs have been analyzed only in reference to various static inhomogeneous structures and for the case of the scattering of MSWs on surface acoustic waves. The present work is the first detailed theoretical and experimental investigation of the Bragg scattering of magnetostatic backward volume waves (MSBVWs) in a YIG film with a conductive meander pattern deposited on its surface.

THEORY OF THE COLLINEAR SCATTERING OF MAGNETOSTATIC BACKWARD VOLUME WAVES

Let us consider a flat ferrite film of thickness d with a conductor in the form of a meander pattern positioned near its surface, as is shown in Fig. 1. We direct the x axis of a Cartesian coordinate system orthogonally to the plane of the film surface, placing the origin midway between the lower and upper surfaces. We assume that the meander pattern is unrestricted in aperture along the y axis, and its period Λ along the z axis significantly exceeds the film thickness d, so that the condition $\Lambda \gg d$ is satisfied. The external uniform magnetizing field H_0 is directed along the z axis parallel to the plane of the film. In this case magnetostatic backward volume waves can propagate along the field direction.

The structure of the magnetic fields and the dispersion equation for the MSBVWs in the case of a static external field (in the absence of a meander pattern) are found by

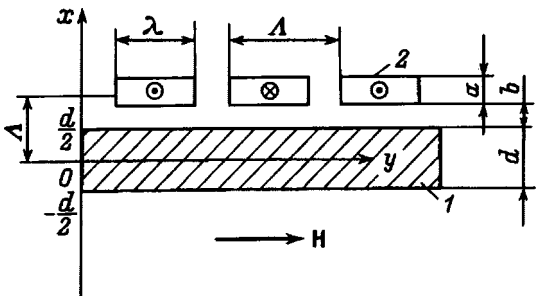

FIG. 1. Geometry of the structure investigated: *1* — ferrite (YIG) film, *2* — grating (meander pattern).

solving the linearized system of equations of motion of the magnetic moment **M** and the magnetostatic equations

$$\frac{d\mathbf{M}}{dt} = -\gamma[\mathbf{M}\times\mathbf{H}], \quad \text{curl } \mathbf{H}=0, \quad \text{div } \mathbf{B}=0, \tag{1}$$

where $\mathbf{B}=\mu_0(\mathbf{H}+\mathbf{M})$, $\mathbf{H}=\mathbf{H}_0+\mathbf{h}$, $\mathbf{H}_0$ is the constant magnetic field in the ferrite, $\mathbf{h}$ is the nonuniform demagnetizing field, μ_0 is the permeability of a vacuum, and γ is the magnetomechanical ratio.

The system of equations is supplemented by the boundary conditions for continuity of the normal component of the magnetic induction B_x and the tangent of the field component h_z at the film surfaces

$$B_x|_{x=\pm d/2}=\text{const}, \quad h_z|_{x=\pm d/2}=\text{const}. \tag{2}$$

The solution of this problem is well known.[8] If we introduce the scalar potential ψ for the magnetizing field $\mathbf{h}=-\nabla\psi$, the mode structure and the dispersion of the MSBVWs will be described for even modes by the following formulas:

$$\psi_n=\begin{cases} A_n\cos(\beta_n x)\exp[i(\omega_n t-kz)]+\text{c.c.}, & |x|<d/2, \\ A_n\cos(\beta_n d/2)\exp\big[i(\omega_n t-kz) \\ \quad -k(|x|-d/2)\big]+\text{c.c.}, & |x|\geqslant d/2, \end{cases} \tag{3}$$

where n is the mode number, ω_n is the frequency of the nth mode, A_n is its amplitude, k is the wave number,

$$\beta_n=\frac{|k|}{\sqrt{\chi_1^{(n)}-1}}, \quad \chi_1^{(n)}=\frac{\omega_H\omega_M}{\omega_n^2-\omega_H^2},$$

$$\omega_H=\gamma H, \quad \omega_M=\gamma M.$$

The dispersion equation has the form

$$\tan\left(\frac{\beta_n d}{2}\right)=-\frac{\beta_n}{k}. \tag{4}$$

For odd modes

$$\psi_n=\begin{cases} B_n\sin(\beta_n x)\exp[i(\omega_n t-kz)]+\text{c.c.}, & |x|<d/2, \\ B_n\sin(\beta_n d/2)\exp\big[i(\omega_n t-kz) \\ \quad -k(|x|-d/2)\big]+\text{c.c.}, & |x|\geqslant d/2, \end{cases} \tag{5}$$

Their dispersion equation has the form

$$\tan\left(\frac{\beta_n d}{2}\right)=\frac{\beta_n}{k}. \tag{6}$$

The characteristic features of the spectrum of these waves are the negative group velocity and the fact that it vanishes on the boundaries of the frequency range for their existence $\omega_H\leqslant\omega_n<\omega_0$, where $\omega_0=\sqrt{\omega_H(\omega_H+\omega_M)}$. The only exception is the fundamental zero-order odd mode, whose dispersion at the beginning of the spectrum has a linear character:

$$\omega^{(0)}(k)=\omega_0-V_g k+O((kd)^2),$$

where

$$V_g=\left.\frac{d\omega}{dk}\right|_{k=0}=\frac{\omega_0^2-\omega_H^2}{4\omega_0}d$$

is the group velocity of the fundamental mode at the beginning of the spectrum.

Because of the large group velocity, the fundamental mode is excited most efficiently by microstrip transducers and is damped more slowly as it propagates than are the higher modes.

As was shown in Ref. 8, the presence of a conductive grating near the surface of the ferrite film leads to interference effects due to the interaction of the signal and reflected harmonics of the MSWs. These effects are strong under the conditions of Bragg synchronism, for which condition $\omega(k)=\omega(K_0-k)$, where $K_0=2\pi/\Lambda$ is the wave number of the grating, holds. Passage of an alternating current $I=I_0\cos(\Omega t)$ with a frequency Ω through the meander pattern produces a standing wave, whose period is two times greater than the period of the static reflective grating. The conditions for scattering on this wave coincide with the conditions for Bragg diffraction on a meander pattern without a current only for double reflection processes with a zero total frequency shift. In the general case the synchronism conditions for scattering on static and dynamic gratings do not coincide. In order that they could be considered independent, the current modulation frequency Ω must exceed the width of the opacity band formed in the case of scattering on a static grating. Below we shall assume that this condition is satisfied.

We represent the magnetic field wave created by an alternating current in a meander pattern in the form of an expansion in a Fourier series

$$h(z,t)=\sum_n\sum_s h^{(n,s)}\exp[i(sK_n z-\Omega t)]+\text{c.c.}, \tag{7}$$

where $h^{(n,s)}=(h_x^{(n,s)}, 0, h_z^{(n,s)})$ is the amplitude of the nth Fourier harmonic, Ω is its frequency, $K_n=\pi n/\Lambda$, and the values $s=\pm 1$ correspond to propagation of the wave in directions parallel and antiparallel to the z axis, respectively.

Generally speaking, the amplitude of the first harmonic decreases exponentially with increasing distance from the meander pattern into the bulk of the film. However, if the film is sufficiently thin, and the condition $K_n d\ll 1$ holds, this dependence can be neglected in a first approximation.

With consideration of the magnetic shielding of the field within the film, the amplitudes of the harmonics are related to the current in the meander pattern by the following expression:

$$h_x^{(n,s)} = -\frac{ih_z^{(n,s)}}{1+\chi_\perp} = \frac{2aI_0\exp(-K_n b)}{\pi(1+\chi_\perp)}\sin\left(\frac{\pi n\lambda}{2\Lambda}\right)\sin^2\left(\frac{\pi n}{2}\right), \quad (8)$$

where a and λ are the thickness and width of the meander-coil transducer, b is the gap between the meander pattern and the film (Fig. 1), and $\chi_\perp = M/H$ is the static susceptibility of the film (Appendix A).

The general solution of the system of initial equations (1) should be sought, according to Floquet's theorem,[9] in the form

$$\psi = \sum_{m=-\infty}^{+\infty}\sum_{n=1}^{+\infty}\sum_{s}\psi_m^{(n,s)}\exp[im(sK_n z-\Omega t)] \times \exp[i(kz-\omega t)] + \text{c.c.} \quad (9)$$

It is a set of harmonics, which are shifted in frequency and wave number by the vector $(smK_n, m\Omega)$. In the zeroth approximation with respect to the amplitude of the variable magnetic field (or with respect to the small parameter $\varepsilon_n = \max|h^{(n,s)}|/H \ll 1$) the dependence of the amplitudes of the harmonics $\psi_m^{(n,s)}$ on the transverse coordinate x is given by formulas (3) and (5), in which it should be assumed that $\omega_m(k) = \omega(|smK_n + k|) + m\Omega$. The presence of a nonzero periodic field $h(x,t)$ leads to an interaction between the harmonics. In a first approximation with respect to ε_n the harmonics with the adjacent mode numbers $m=0$ and $m=\pm 1$ interact most strongly at the points where the corresponding dispersion curves $\omega_m(k)$ cross, i.e.,

$$\omega(k_s) = \omega(k) + s\Omega, \quad k_s = k + sK_n. \quad (10)$$

It follows from (10) that single and multiple forward scattering and backscattering of MSBVWs are possible, as is shown in Fig. 2. The dispersion curves of the MSBVWs in the figure were calculated using Eq. (4) for the fundamental mode and the values of the parameters corresponding to the experimental conditions presented below. It is seen that the character of the scattering of an original wave having the

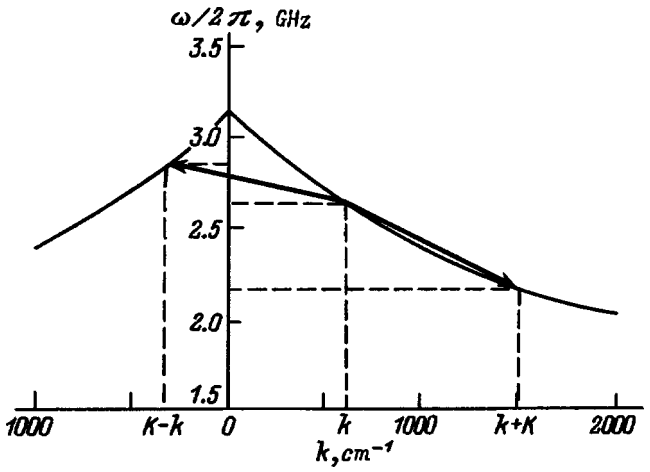

FIG. 2. Calculated scattering pattern of the fundamental magnetostatic volume mode for a modulation frequency $\Omega/2\pi = 30$ MHz and a meander-pattern period $\Lambda = 500$ μm.

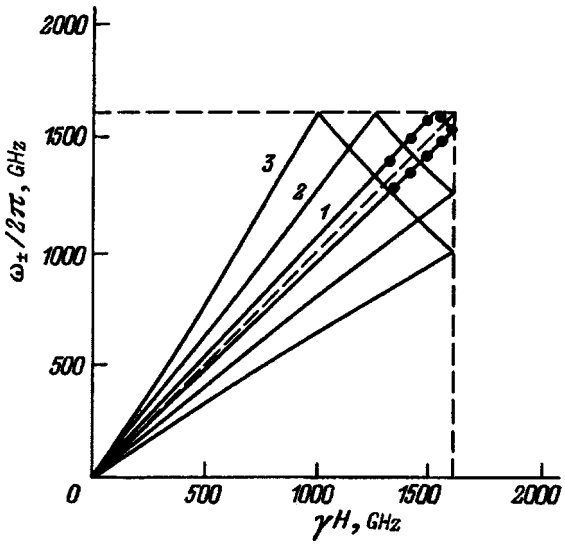

FIG. 3. Dependence of the frequencies of the scattered waves on the frequency of the signal wave for scattering on meandering conductors with various periods. Λ, μm: *1* — 500, *2* — 200, *3* — 100.

frequency ω and the wave number k depends on the wave number of the magnetic wave K. When $k > K$, only forward scattering (unidirectional scattering) of the original wave with an increase or decrease in the wave number accompanied by a decrease or increase in the frequency, respectively, is possible. When $k < K$, both forward scattering and backscattering (bidirectional scattering) accompanied by either a decrease or an increase in the frequency of the wave is possible. In the general case the frequencies of the scattered waves ω_+ and ω_- are located at different distances along the frequency scale from the frequency of the original wave ω.

Figure 3 presents calculated synchronism curves for the zero-order MSBVWs (1) in a YIG film with a thickness of 20 μm immersed in a field of intensity $H = 600$ Oe in the case of single scattering on a meander pattern with a period $\Lambda = 1000$ μm. Bidirectional scattering takes place in the frequency range $f > f_1$, and unidirectional scattering takes place in the frequency range $f < f_1$.

The bidirectional scattering of MSBVWs at small values of ε_n is described well by the coupling equations for the amplitudes of the envelopes of the synchronized harmonics. These equations are obtained by averaging the original equations (1) over the fast variables by the Bogoliubov–Mitropolsky method or by the singular perturbation method for media with spatiotemporal periodicity generalized to the case of bounded media.[10]

In the case of bidirectional scattering the coupling equations have the following form:

$$i\frac{\partial A_+}{\partial t} + iV_+\frac{\partial A_+}{\partial z} + \omega_B^+ A_- + i\delta\omega^+ A_- = 0,$$

$$i\frac{\partial A_-}{\partial t} - iV_-\frac{\partial A_-}{\partial z} + \omega_B^- A_+ + i\delta\omega^- A_+ = 0, \quad (11)$$

where $A_\pm$ are the amplitudes of the interacting harmonics,

$V_{\pm}=d\omega_{\pm}/dk$ are the group velocities, $\delta\omega_{\pm}$ are the linewidths of the interacting MSW harmonics, and $\omega_B^{\pm}$ are the coupling coefficients.

As the calculations show (Appendix B), the coupling coefficients for modes of identical symmetry have the form

$$\omega_{BB}^{s}=\frac{h^{(n,s)}}{M}\,\frac{2\beta_{-s}^{2}(k_{-s}-k_s)(\chi_1^{+}\chi_1^{-}+\chi_2^{+}\chi_2^{-})}{k_{-s}(\beta_s^2-\beta_{-s}^2)\left[1+\dfrac{k_s d}{2}\left(1+\dfrac{\beta_s^2}{k_s^2}\right)\right]\dfrac{\partial\chi_1^{s}}{\partial\omega}}, \tag{12}$$

where

$$\chi_1^{s}=\frac{\omega_H\omega_M}{\omega_s^2-\omega_H^2},\quad \chi_2^{s}=\frac{\omega_s\omega_M}{\omega_s^2-\omega_H^2},\quad \beta_s^2=\frac{k^2}{\chi_1^{s}-1},$$

$$\omega_s=\omega(k_s),\quad k_s=|k+sK_n|.$$

When modes of different symmetry interact, the (even-odd) coupling coefficients take the form

$$\omega_{BA}^{s}=\frac{ih^{(n,s)}}{M}\,\frac{2\beta_{-s}k_s}{\beta_s^2\left[1+\dfrac{k_s d}{2}\left(1+\dfrac{\beta_s^2}{k_s^2}\right)\right]\dfrac{\partial\chi_1^{+}}{\partial\omega}}$$

$$\times\left\{\frac{\omega_M}{\omega}(\chi_2^{s}+\chi_2^{-s})+\frac{\beta_s^2(k_{-s}-k_s)}{(\beta_s^2-\beta_{-s}^2)k_s}\right.$$

$$\left.\times\left[\left(\chi_1^{(\Omega=0)}\chi_1^{s}+\frac{\omega_M}{\omega_s}(\chi_2^{(\Omega=0)}+\chi_2^{-s})\right)\right]\right\}. \tag{13}$$

For meander patterns with a large period, for which $K_0 d=\pi d/\Lambda\ll 1$, Eqs. (12) and (13) are simplified, and when the conditions $\Omega/\omega\ll 1$ and $kd\ll 1$ are satisfied for the first-order modes, they take the following form

$$\omega_{BB}^{s}\simeq\frac{h_z^{(n,s)}}{M}\,\frac{\omega_M(\omega_H^2+\omega^2)}{2\omega_H\omega},\quad \omega_{AB}^{s}\simeq\frac{ih_x^{(n,s)}}{M}\,\frac{\omega_M^2}{\omega}\sqrt{\frac{kd}{2}}. \tag{14}$$

It follows from the formulas obtained that the coupling coefficient for bidirectional scattering at small wave numbers is maximal for modes of identical symmetry and depends weakly on the frequency, in contrast to the case of modes of different symmetry. The scattering efficiency, which is defined as

$$\eta=\left.\frac{A_-(z)}{A_+(0)}\right|_{z=L},$$

is found by solving Eqs. (12) with the boundary conditions

$$A_+(z)|_{z=0}=A_+(0),\quad A_-(z)|_{z=L}=0, \tag{15}$$

where L is the length of the meander pattern.

Setting $A_{\pm}=A_{\pm}\exp[i(\omega-\omega_{\pm})t]$, where $\omega_{\pm}$ are the frequencies of the synchronized MSBVWs [see Eq. (10)], for the amplitudes of the interacting harmonics, from the solution of the boundary-value problem we obtain the following expression for the scattering efficiency:

$$\eta=\left|\frac{A_-(L)}{A_+(0)}\right|=\left|\frac{(\alpha V_+-\Delta\omega-i\delta\omega_+)^2-\beta^2V_+^2}{\omega_B^{+}[\alpha V_+-\Delta\omega-i\delta\omega_++\beta V_++\cot(i\beta L)]}\right|. \tag{16}$$

Here

$$\alpha=\frac{\Delta\omega(V_--V_+)+i(V_-\delta\omega_+-V_+\delta\omega_-)}{2V_+V_-},$$

$$\beta=\frac{\{[\Delta\omega(V_++V_-)+i(V_+\delta\omega_-+V_-\delta\omega_+)]^2-4V_+V_-\omega_B^{+}\omega_B^{-}\}^{1/2}}{2V_+V_-},$$

$\Delta\omega=\omega-\omega_+$ is the detuning.

For single-mode scattering we can set $V_+=V_-=V$, $\delta\omega_+=\delta\omega_-=\delta\omega$, and $\omega_B^{+}=\omega_B^{-}=\omega_B$ to good accuracy in the case of $K_n d\ll 1$. Then, using Θ to denote $\sqrt{(\Delta\omega+i\delta\omega)^2-\omega_B^2}$, we obtain

$$\eta=\frac{\omega_B}{|\Delta\omega+i\delta\omega+i\Theta\,\cot(L\Theta/V)|}. \tag{17}$$

When the length of the grating is large and $L\Theta/V\gg 1$, this expression takes an even simpler form

$$\eta(L=\infty)\approx\frac{\omega_B}{|\Delta\omega+i\delta\omega+\Theta|}. \tag{18}$$

It is seen from (18) that for $\omega_B\gg\delta\omega$ the detuning relative to the mode synchronization frequency is determined by the half-width of the frequency splitting of the spectral curves, i.e., $\Delta\omega\approx\omega_B$, while for a weak interaction ($\omega_B\ll\delta\omega$) it is determined by the width of the MSW line, i.e., $\Delta\omega\approx\delta\omega$.

Let us now consider the case of the unidirectional scattering of MSBVWs. In this case the sign in front of the group velocity V_- in the second of the mode coupling equations (11) should be reversed. The boundary conditions for the amplitudes of the envelopes then take the form

$$A_+(z)|_{z=0}=A_+(0),\quad A_-(z)|_{z=0}=0. \tag{19}$$

The solution of the coupling equations with these boundary conditions gives the following expressions for the scattering efficiency:

$$\eta_1=\left|\frac{A_-(L)}{A_+(0)}\right|=\frac{\omega_B}{\xi|V_-|}\left|\sin(\xi L)\right|\exp\left(-\frac{\delta\omega L}{2V_{\text{mid}}}\right) \tag{20}$$

with a decrease in the wave number and

$$\eta_2=\left|\frac{A_+(L)}{A_+(0)}\right| =\left|\cos(\xi L)+i\frac{(|V_+|-|V_-|)(\Delta\omega+i\,\delta\omega)}{2|V_+V_-|\xi}\sin(\xi L)\right| \times\exp\left(-\frac{\delta\omega L}{2V_{\text{mid}}}\right) \tag{21}$$

with an increase in the wave number. Here

$$\xi=\frac{\sqrt{(|V_+|-|V_-|)^2(\Delta\omega+i\,\delta\omega)^2+4|V_+V_-|\omega_B^2}}{2|V_+V_-|},$$

$$V_{\text{av}}=\frac{2|V_+V_-|}{|V_+|+|V_-|}.$$

In the case of sufficiently large coupling coefficients, where $\omega_B\gg\delta\omega$, and a small difference between the group velocities of the interacting waves ($\Delta V\ll V$), it follows from (20) and (21) that

$$\eta_1=\sin(\xi L)\exp\left(-\frac{\delta\omega L}{2V}\right),$$

$$\eta_2=\cos(\xi L)\exp\left(-\frac{\delta\omega L}{2V}\right), \tag{22}$$

where it has been taken into account that $\xi\approx\omega_B/V$.

Formulas (22) show that when $L\omega_B\ll\pi/2$, maximum conversion is achieved at zero detuning ($\Delta\omega=0$). However, when $L\omega_B\approx\pi/2$, the suppression of unidirectional scattering is possible near the synchronization frequency, and a small detuning can promote an increase in the interconversion of the harmonics. Under the conditions of phase synchronism, where $\Delta\omega=0$, the conversion efficiency depends strongly on the group velocity of the MSWs. As the velocity decreases ($V\to0$), the amplitudes of the interacting waves not only decay, but also oscillate due to the decrease in the characteristic wave interaction length $L\sim V/\omega_B\to0$.

Double-scattering processes with a double frequency shift appearing at the points $\omega(k_s)=\omega(k)+2s\Omega$, where $k_s=|k+2sK_n|$, are characterized by significantly smaller scattering amplitudes, since their coupling coefficients are inversely proportional to the amplitude of the modulating field raised to the second power: $\omega_B^{(2)}\sim(h/H)^2$. Double scattering without a frequency shift is masked, in addition, by the Bragg scattering of MSWs without a frequency shift on the metallic grating of the meander pattern. The latter effect can be eliminated, in principle, by shielding the SHF field from the meandering conductor by metallizing the surface of the ferrite film using a thin insulating separating layer.

RESULTS OF EXPERIMENTAL INVESTIGATIONS

In the experimental investigations we used a YIG film of thickness $d=20$ μm with the saturation magnetization $4\pi M\simeq1750$ H and the ferromagnetic resonance linewidth $\Delta H=0.6$ Oe grown by liquid-phase epitaxy on a nonmagnetic substrate measuring 4×20 mm. The film was pressed against a Polikor substrate, on whose surface two broad-band microstrip transducers and a conductor in the form of a meander pattern between them were deposited by photolithography. The transducers, which had a width of 50 μm and a length of 4 mm, were placed at a distance $l=8$ mm from one another. Meander patterns with a conductor width of 50 μm, an aperture of 6 mm, a length of 7 mm, and various distances between the conductors $\Lambda=100$, 200, and 500 μm were used in the experiments. An alternating current with an amplitude up to $I_0=2$ A and a frequency $\Omega/2\pi=20-150$ MHz was passed through the meander pattern and created a modulating field with an amplitude up to 10 Oe in the film. The entire structure was immersed in a constant tangential external magnetic field $H=550$ Oe. A continuous SHF signal with a frequency in the range $\omega/2\pi=2-3.5$ and a power $P_{\text{in}}\leqslant1$ mW was supplied to the input transducer to excite MSBVWs in the ferrite film. The dependence of the power P_{out} (the amplitude–frequency characteristic) and the phase Φ (the phase–frequency characteristic) of the signal on the frequency under stationary conditions, as well as the spectra of the transmitted signal and the signal reflected from the input transducer upon modulation of the magnetic field, were recorded from the output transducer.

The propagation of MSBVWs in the frequency range from $\omega/2\pi=2.8$ to 3.15 GHz was observed in the structure described when the meander pattern between the transducers was absent. The minimum loss on the amplitude–frequency characteristic was $L=10\log(P_{\text{out}}/P_{\text{in}})\simeq-18$ dB. The measured upper cutoff frequency of the MSBVWs was equal to ~3.14 GHz, which agrees well with the theoretical value $\omega_0/2\pi=3.15$ GHz. When the meander pattern was introduced between the transducers, the upper cutoff frequency of the MSBVWs varied slightly, but the brokenness of the amplitude–frequency characteristic increased. Figure 4 shows portions of the amplitude–frequency characteristic and the phase–frequency characteristic for the structure containing the meander pattern with $\Lambda=500$ μm. The amplitude–frequency characteristic clearly exhibits three resonant dips with depths up to 20 dB and widths from 6 to 10 MHz at the ~3 dB level. The dips correspond to the Bragg reflection of MSBVWs from the conductor grating at frequencies whose wave number satisfy the condition $K\Lambda=\pi+2\pi N$, where $N=0,1,\ldots$. Discontinuities on the phase–frequency characteristic are also observed at these frequencies. A comparison of the $\omega(k)$ curve of the MSBVWs reconstructed from the phase–frequency characteristic with the calculated dispersion curve showed that the presence of the conductive meander pattern leads to some increase in the group frequency of the waves near the upper cutoff frequency of the range for MSBVWs and weakly influences the propagation of waves with $K\Lambda\leqslant1$. When the meander patterns with $\Lambda=200$ μm and especially $\Lambda=100$ μm were used, the brokenness of the amplitude–frequency characteristic increased further, and, in addition, the level of direct electromagnetic bridging of the gap between the input and output transducers increased sharply. Therefore, the measurements of the scattering of MSWs under nonstation-

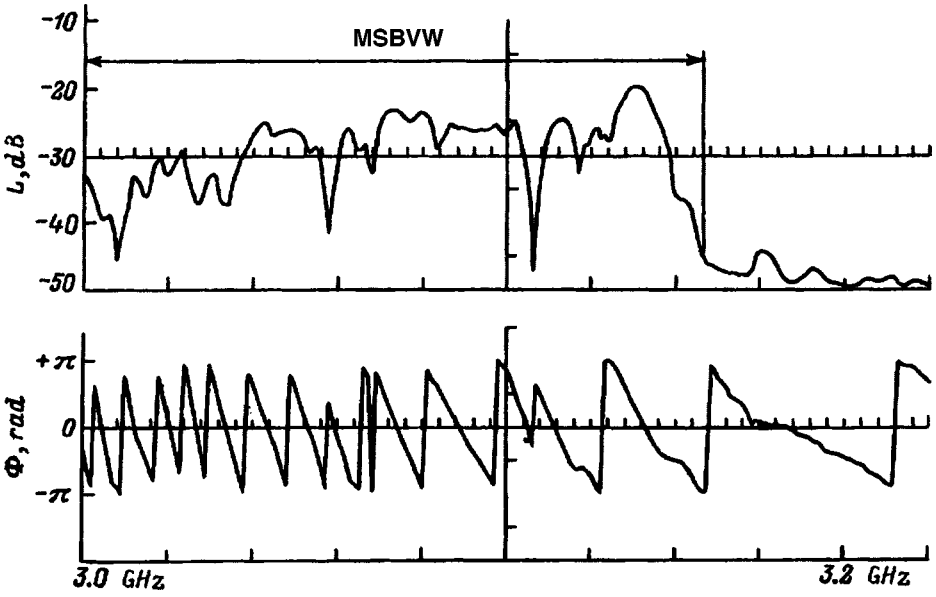

FIG. 4. Amplitude–frequency and phase–frequency characteristics of the transmitted magnetostatic volume waves in a structure with a meander pattern.

ary conditions were performed only with the meander pattern having $\Lambda = 500$ μm. Figure 5 presents the scattering efficiency of MSBVWs for the case corresponding to Fig. 2. Evaluation of the scattering efficiency from Eqs. (17)–(20) gives values which agree with experiment ($\eta \simeq 0.1$) for a current in the meander pattern $I_0 \sim 0.01$ A, which creates a nonuniform modulation field with an amplitude $h_s \sim 0.5$ Oe.

We note that similar MSW scattering phenomena in response to spatiotemporal modulation of a magnetic field are also characteristic of magnetostatic forward volume waves (MSFVWs) propagating in normally magnetized ferrite films. In this case, however, the sign of the group velocity of the MSFVWs coincides with the sign of the phase velocity; therefore, the frequency shift of the scattered wave is opposite to the shift in the case of MSBVWs, in which these signs are different.

The phenomena considered can be utilized to selectively generate higher modes of MSBVWs by means of their parametric interaction under phase synchronization conditions. In the case of strong coupling ($\omega_B \gg \delta\omega$), the efficiency of unidirectional conversion is specified at the synchronism point by (21). The efficiency maximum is achieved when

$$\tan\left(\frac{L\omega_B}{V}\right) = \rho,$$

where $\rho = 2\omega_B/\delta\omega \gg 1$, and it equals

$$\eta_{\max} = \frac{\rho}{\sqrt{1+\rho^2}} \exp(-\rho^{-1}\arctan(\rho)) \approx 100\%.$$

Thus, practically complete mode conversion can be obtained at an interaction length $L \sim \pi V/2\omega_B$, which amounts to $L \sim 1$ mm when the field modulation depth $h \approx 10$ Oe.

This work was carried out in part with the support of the International Science Foundation and the Russian Government (Grant No. M6Q300).

APPENDIX A

The distribution of the field is found from the magnetostatic equations

$$\text{curl } \mathbf{H} = \mathbf{j}, \tag{A1}$$

$$\text{div}(\mathbf{H} + \mathbf{M}) = 0, \tag{A2}$$

where $j = a\,\delta(x-\Delta)\Sigma J_n \cos(K_n + \varphi_n)$ is the current in the meander pattern, a is the thickness of the meander pattern, $\Delta = d/2 + b + a/2$ is the distance from the midplane of the ferrite film (the coordinate origin) to the midplane of the meander pattern (Fig. 1), J_n is the amplitude of the current density, and $\delta(x)$ is a Dirac delta function.

We introduce the magnetic potential defined by the relation $\mathbf{h} = \nabla\psi$. Integration over a small vicinity near the meander pattern gives the boundary conditions

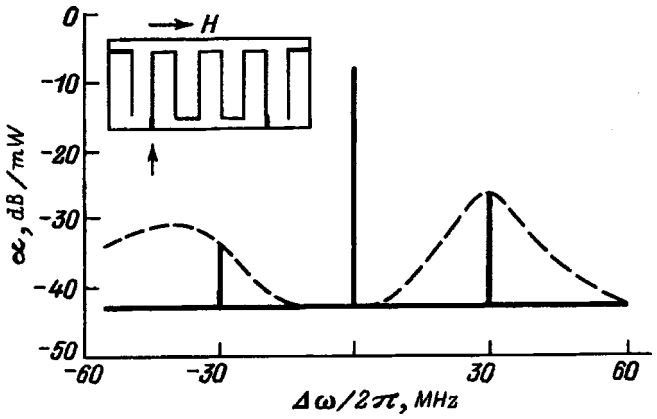

FIG. 5. Experimental dependence of the intensity of the transmitted and scattered MSBVWs in a meander pattern.

$$\left.\frac{\partial\psi}{\partial x}\right|_{x=\Delta-0}=\left.\frac{\partial\psi}{\partial x}\right|_{x=\Delta+0}+a\sum_n J_n\cos(K_nz+\varphi_n),$$

$$\left.\frac{\partial\psi}{\partial z}\right|_{x=\Delta-0}=\text{const}. \tag{A3}$$

The boundary conditions on the film-vacuum boundary are

$$\left.\frac{\partial\psi}{\partial x}\right|_{x=d/2+0}=(1+\chi_\perp)\left.\frac{\partial\psi}{\partial x}\right|_{x=d/2-0},$$

$$\left.\frac{\partial\psi}{\partial z}\right|_{x=d/2\pm0}=\text{const}, \tag{A4}$$

where $\chi_\perp=M/H$ is the static susceptibility.

Similar conditions should hold on the other boundary.

The solution of Eqs. (A1) and (A2) for the potential is sought in the form $\psi=\Sigma A_n(x)\cos(K_nz+\varphi_n)$. In this case the equations for the amplitudes in the vacuum have the form

$$\frac{d^2A_n}{dx^2}-K_n^2A_n=0, \tag{A5}$$

and the equations for the amplitudes in the film have the form

$$\frac{d^2A_n}{dx^2}(1+\chi_\perp)-K_n^2A_n=0. \tag{A6}$$

The solution of these equations under conditions (A3) and (A4) have the following form

$$\psi=a\sum_n J_n\cos(K_nz+\varphi_n)\exp(-K_nb)\times\frac{\cosh[\mu K_n(x+d/2)]+\mu\sinh[\mu K_n(x+d/2)]}{\cosh(\mu K_nd)+\mu(1+\chi_\perp/2)\sinh(\mu K_nd)}, \tag{A7}$$

where $\mu=1/\sqrt{1+\chi_\perp}$, and b is the gap between the film and the meander pattern.

Taking into account that $h_x=\partial\psi/\partial x$ and $h_z=\partial\psi/\partial z$, in the approximation $K_nd\ll1$ we obtain formula (8) from (A7).

APPENDIX B

Let us derive the coupling equations of parametrically interacting MSBVWs on a traveling magnetic wave of the form $h^{(n)}=(h_x^{(n)},0,h_z^{(n)})\exp[i(K_nz-\Omega t)]$. Because of the small value of the pumping amplitude $(h/H\ll1)$, we shall seek a solution in the form of two adjacent harmonics of the series (1), for which synchronism conditions of the form $\omega_+(k_-)=\omega_-(|k_+-K_n|)+s\Omega$, where $k_-=|k_+-K_n|$, hold.

In the zeroth approximation the amplitudes of the interacting harmonics are described by Eqs. (3)–(5). In this case

$$m_{x,s}^{(0)}=-\chi_1^s\frac{\partial\psi_s^{(0)}}{\partial x}, \tag{B1}$$

$$m_{y,s}^{(0)}=-i\chi_2^s\frac{\partial\psi_s^{(0)}}{\partial x}. \tag{B2}$$

For the first-order approximation, the following relations can be obtained from the Landau–Lifshitz equation with consideration of the weak temporal and spatial dependence of the amplitude of the interacting harmonics, whose slow variation is specified by the small parameters $\Delta\omega/\omega\sim\Delta k/k_s\sim h/H\ll1$, where $\Delta\omega$ and Δk are the detunings of the frequency and wave number, respectively:

$$m_{x,s}^{(1)}=-\chi_1^s\frac{\partial g_s^{(1)}}{\partial x}-i\frac{\partial\chi_1}{\partial\omega}\frac{\partial^2\psi_s^{(0)}}{\partial x\partial\tau}+i\chi_2^sh_s^{(n)}\times\frac{m_{y,-s}^{(0)}}{M}+\chi_1^s\frac{m_{x,s}^{(0)}}{M}h_z^{(n)}+\chi_1^{s\Omega}h_x^{(n),\Omega=0}, \tag{B3}$$

$$m_{y,s}^{(1)}=-i\chi_2^s\frac{\partial g_s^{(1)}}{\partial x}+i\chi_2^sh_z^{(n)}\frac{m_{x,-s}^{(0)}}{M}-\chi_1h_z^{(n)}\times\frac{m_{y,-s}^{(0)}}{M}+\frac{\partial\chi_2}{\partial\omega}\frac{\partial^2\psi_s^{(0)}}{\partial x\partial\tau},-i\chi_2^{s\Omega}h_x^{(n),\Omega=0}, \tag{B4}$$

$$m_{z,s}^{(1)}=i\frac{\gamma}{\omega}h_x^{(n)}m_{y,-s}^{(0)}, \tag{B5}$$

where g is a correction to the amplitude of the potential from the zeroth approximation $(\psi=\psi^{(0)}+g)$.

The equation for the corrected potential within the magnetic film follows from the magnetostatic equations and has the form

$$(1-\chi_1^s)\frac{\partial^2g^{(1)}}{\partial x^2}-k_+^2g^{(1)}=i\frac{k_+^2}{1-\chi_1^s}\frac{\partial\chi_1}{\partial\omega}\frac{\partial\psi_s^{(0)}}{\partial\tau}-2ik_s\frac{\partial\psi_s^{(0)}}{\partial z}+\frac{(\chi_2^-\chi_2^++\chi_1^-\chi_1^+)}{M}\frac{\partial^2\psi_s^{(0)}}{\partial x^2}-\frac{\omega_M}{\omega}k_sh_x^{(n)}(\chi_2^{-s}+\chi_2^{s\Omega})\frac{\partial\psi_{-s}^{(0)}}{\partial x}. \tag{B6}$$

The equation for the potential outside the film has the form

$$\frac{\partial^2g^{(1)}}{\partial x^2}-k_s^2g^{(1)}=-2ik_s\frac{\partial\psi_s^{(0)}}{\partial z}. \tag{B7}$$

The boundary conditions for the correction to the first-order approximation have the form

$$\left.\frac{\partial g^{(1)}}{\partial x}+m_x^{(1)}\right|_{x=\pm d/2\mp0}=\left.\frac{\partial g^{(1)}}{\partial x}\right|_{x=\pm d/2\pm0}, \tag{B8}$$

$$g^{(1)}|_{x=\pm d/2\mp0}=g^{(1)}|_{x=\pm d/2\pm0},\quad g^{(1)}(x=\pm\infty)=0.$$

The solution of the system of differential equations (B6) and (B7) with the boundary conditions (B8) leads to an inhomogeneous linear system of algebraic equations with a zero determinant, because the frequencies and wave numbers satisfy the dispersion equation for the modes of the zeroth approximation. The conditions for solvability of this system are the coupling equations (11) sought for slow variation of the wave amplitudes.

[1] C. G. Sykes, J. D. Adam, and J. N. Collins, Appl. Phys. Lett. **29**, 388 (1978).

[2] V. É. Babenko, A. M. Mednikov, Yu. K. Milyaev *et al.*, Zh. Tekh. Fiz. **56**, 2039 (1986) [Sov. Phys. Tech. Phys. **31**, 1221 (1986)].
[3] J. M. Owens, J. N. Collins, C. V. Smith *et al.*, Appl. Phys. Lett. **31**, 781 (1977).
[4] A. V. Voronenko and S. V. Gerus, Pis'ma Zh. Tekh. Fiz. **10**, 746 (1984) [Sov. Tech. Phys. Lett. **10**, 313 (1984)].
[5] A. N. Myasoedov and Yu. K. Fetisov, Zh. Tekh. Fiz. **59**(6), 133 (1989) [Sov. Phys. Tech. Phys. **34**, 666 (1989)].
[6] A. M. Mednikov, A. F. Popkov, V. I. Anisimkin *et al.*, JETP Lett. **33**, 632 (1981).
[7] Yu. V. Gulyaev, R. G. Kryshtal', A. V. Medved' *et al.*, Pis'ma Zh. Tekh. Fiz. **12**, 552 (1986) [Sov. Tech. Phys. Lett. **12**, 226 (1986)].
[8] R. W. Damon and J. R. Eshbach, J. Phys. Chem. Solids **19**, 308 (1961).
[9] V. A. Rabinovich, A. A. Vasserman, V. I. Nedostup, and L. S. Veksler, *Thermophysical Properties of Neon, Argon, Krypton, and Xenon* (Hemisphere, Berlin–New York, 1988; Nauka, Moscow, 1984).
[10] A. H. Nayfeh, *Perturbation Methods* [Wiley, New York (1973); Mir, Moscow (1976)].

Translated by P. Shelnitz

Influence of substitutions on the magnetic anisotropy of Gd-containing magnetooptic iron garnet films

V. V. Randoshkin, V. I. Kozlov, V. Yu. Mochar, N. V. Vasil'eva, and V. V. Voronov

Joint Self-Supporting Laboratory of Magneto-Optoelectronics, Institute of General Physics of the Russian Academy of Sciences at the Mordovian State University, 43000 Saransk, Russia
(Submitted August 20, 1996; resubmitted January 20, 1997)
Zh. Tekh. Fiz. **68**, 113–116 (May 1998)

The properties of magnetooptical films of the system $(Bi,Gd,Ln)_3(Fe,M)_5O_{12}$, where Ln = Lu or La and M = Ga or Al, grown by liquid-phase epitaxy on $Nd_3Ga_3O_{12}$ substrates oriented along (100), along (110), and close to (111), are investigated by x-ray and ferromagnetic resonance methods. © *1998 American Institute of Physics.* [S1063-7842(98)02105-9]

Bismuth-containing iron garnet single-crystal (IGSC) films containing Cd^{3+} ions are used in various magnetooptical devices.[1,2] These films are customarily grown on (111) oriented substrates.[1–5] Our present objective is to investigate magnetic anisotropy in the case of Bi-containing IGSC films whose orientation deviates from (111) and to analyze how they are influenced by ions substituted for Cd^{3+} and Fe^{3+}. In particular, we seek to determine whether Gd^{3+} ions paired with Bi^{3+} ions contribute to orthorhombic magnetic anisotropy.

Bismuth-containing IGSC films of the system $(Bi,Gd,Ln)_3(Fe,M)_5O_{12}$, where Ln=Lu or La, and M=Ga or Al, were grown by liquid-phase epitaxy from a supercooled $PbO–Bi_2O_3–B_2O_3$ fluxed melt on variously oriented $Nd_3Ga_5O_{12}$ substrates. The crystallographic orientation of the Bi-containing IGSC films (basal plane, angle Θ, and the deviation of the plane of the film from it) were monitored on a DRON-2.0 diffractometer within 0.1° error limits.

The mismatch of the film and substrate lattice parameters $\delta a/a$, measured in the direction of the normal to the plane of the film [$\delta a/a=(a_f-a_s)/a_s$, where a_f is the lattice parameter of the film and a_s is the lattice parameter of the substrate], was determined by a standard method from rocking curves measured on a two-crystal x-ray spectrometer. The spectrometer was assembled from a DRON-3M diffractometer and a monochromator unit utilizing a perfect Ge crystal and the (333) reflection. To identify peaks originating from the film and from the substrate, the rocking curves were recorded for two reflection orders, and the intensity ratio of the peaks was compared. The mismatch was calculated from the equation[6]

$$\delta a/a=-\Delta\vartheta\ \cot\ \vartheta, \tag{1}$$

which follows from Bragg's law. Here ϑ is the Bragg angle, and $\Delta\vartheta$ is the angular distance between peaks originating from the film and from the substrate. The values of Θ and $\delta a/a$ are given in Table I.

For films of the system $(Bi,Gd)_3Fe_5O_{12}$ the concentrations of bismuth X_{Bi} and gadolinium X_{Gd} can be determined from data in Table 9.4 of Ref. 7, taking into account only the mismatch of the film and substrate lattice parameters [the bismuth contribution is assumed to be equal to $\Delta a/\Delta X$ (pm per formula unit)]. For Bi-containing IGSC films of the system $(Bi,Gd,Ln)_3Fe_5O_{12}$ it is necessary, in addition, to take into account the contents of rare-earth elements in the mixture and their distribution coefficients.[8] When the composition of the film includes a nonmagnetic M^{3+} ion, it is impossible to determine the chemical composition of Bi-containing IGSC films from $\delta a/a$ data and the composition of the raw mixture, because the distribution coefficient of the M^{3+} ion is highly dependent on the film growth rate. The values of X_{Bi}, X_{Gd}, and X_{Ln} are given in Table I.

For films of the system $(Bi,Gd)_3Fe_5O_{12}$ the saturation magnetization $4\pi M_s$ can be determined from data in Table 9.3 of Ref. 7 on the assumption that in the system $(Bi,Ln)_xGd_{3-x}Fe_5O_{12}$ the value of $4\pi M_s$ increases linearly with x from the value corresponding to $Gd_3Fe_5O_{12}$ to the value corresponding to the hypothetical garnet $Bi_3Fe_5O_{12}$. The saturation magnetization for the latter is assumed to be the same as for $Lu_3Fe_5O_{12}$. The values of $4\pi M_s$ so determined are given in Table I.

The magnetic anisotropy parameters were investigated by the ferromagnetic resonance method at a frequency of 9.34 GHz. The resonance fields were recorded with the external magnetic field oriented perpendicular to the plane of the film (H_p, perpendicular resonance) and parallel to it (H_{in}, parallel or in-plane resonance), along with the corresponding ferromagnetic resonance linewidths $2\Delta H_p$ and $2\Delta H_{in}$. To determine the in-plane anisotropy of the film, the field was recorded as a function of the azimuth angle, $H_{in}(\varphi)$, in parallel resonance. The results of the ferromagnetic resonance measurements are given in Table I, where $H_{in\,min}$ and $H_{in\,max}$ are the minimum and maximum values of the resonance field in parallel resonance, respectively, and δH_{in} is the difference between these values.

Inasmuch as Bi-containing IGSC films of the system $(Bi,Gd,Ln)_3(Fe,M)_5O_{12}$ do not containing fast-relaxing magnetic ions, and as the gyromagnetic ratio of the slow-relaxing Gd^{3+} and Fe^{3+} ions is identical and equal to $\gamma_0=1.76\times10^7\mathrm{Oe}^{-1}\mathrm{s}^{-1}$, we have the following expression for them in accordance with the Wangsness equation,[2,9]

$$\gamma=\frac{M_{Gd}+M_{Fe}}{M_{Gd}/\gamma_{Gd}+M_{Fe}/\gamma_{Fe}} \tag{2}$$

TABLE I. Parameters of Bi-containing films of the system $(Bi,Gd,Ln)_3(Fe,M)_5O_{12}$ (f.u. = formula unit).

	Sample No.							
Sample	1	2	3	4	5	6	7	8
Ln	–	–	Lu	–	–	–	Lu	–
M	–	–	–	–	–	Ga	Ga	Al
X_{Bi}, f.u.	0.61	0.61	1.56	0.04	0.20	...	...	...
X_{Gd}, f.u.	2.39	2.29	0.86	2.96	2.80	...	...	...
X_{Ln}, f.u.	–	–	0.58	–	–	...	...	–
Orientation	(100)	(110)	(110)	(111)	(111)	(111)	(111)	(111)
Θ, deg	2.3	1.6	1.0	1.4	2.6	6.5	0.8	4.75
$\delta a/a \cdot 10^4$	0.0	0.0	−32.0	−50.0	−40.0	−3.4	+7.0	−13.0
$H_{in\ min}$, Oe	3250	2300	2550	2820	2950	3770	4720	3650
$H_{in\ max}$, Oe	3540	3480	3220	2850	3020	5170	4935	4000
δH_{in}, Oe	350	1180	670	30	70	1400	215	350
$2\Delta H_{in}$, Oe	87	70	35	87	210	870	240	360
H_p, Oe	3540	4200	4300	3800	3710	2000	50	1530
$2\Delta H_n$, Oe	60	40	52	87	280	1200	240	810
H_{eff}, Oe	−207	−870	−970	−470	−380	1330	3280	1800
$4\pi M_s$, G	415	415	1300	80	180	...	...	...

the effective value of the gyromagnetic ratio γ is equal to γ_0 (at least far from the point of compensation of the magnetic moment). Here M_{Gd} is the total magnetic moment of the Gd^{3+} ions in the dodecahedral sublattice of the garnet structure, and M_{Fe} is the total magnetic moment of the Fe^{3+} ions in the tetrahedral and octahedral sublattices. This fact, in contrast with Refs. 10 and 11, can be used to determine the effective magnetic anisotropy field H_{eff} from perpendicular resonance data alone, for which the resonance ratio can be written as

$$\omega/\gamma = H_{eff} + H_p, \tag{3}$$

where ω is the angular frequency of ferromagnetic resonance.

The fact that the Gd^{3+} and Fe^{3+} exhibit identical dynamical behavior confirms the results of investigations near the point of compensation of the angular momentum.[11–13] In particular, when Gd^{3+} ions are introduced into the composition of Bi-containing IGSC films, there is a drop in the necessary level of replacement of iron by nonmagnetic ions required to ensure compensation of the angular momentum. The values of H_{eff} are given in Table I.

We find that (100)-oriented $(Bi,Gd)_3Fe_5O_{12}$ films (sample 1 in Table I) are characterized by the occurrence of four equivalent maxima of the $H_{in}(\varphi)$ curve (Fig. 1), whose positions correspond to axes of the (100) type. The value of δH_{in} is relatively small in this case (see Table I). A comparison of the values of $4\pi H_s$ and H_{eff} in Table I leads to the conclusion that the magnetic anisotropy in these films is associated with demagnetizing fields.

In Bi-containing IGSC films of the same composition but with (110) orientation (sample 2 in Table I) the in-plane magnetic anisotropy of the film is more than three times the value in (100)-oriented films (cf. the values of δH_{in} in Table I). Here the curve representing the azimuthal dependence of the resonance field in parallel resonance (Fig. 2) is observed to have only two peaks, as is characteristic of films with orthorhombic magnetic anisotropy. The effective anisotropy field for these films is also not very strong. The introduction of Lu into films with this orientation (sample 3 in Table I) causes both the ferromagnetic resonance linewidth and the in-plane anisotropy of the film to decrease. Here the effective anisotropy field H_{eff} changes very slightly, and the $H_{in}(\varphi)$ curve has the form shown in Fig. 2.

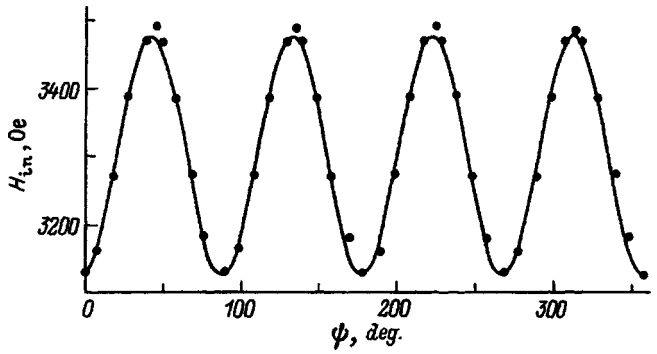

FIG. 1. Graph of the resonance field $H_{in}(\varphi)$ versus azimuth angle in parallel resonance for (100)-oriented Bi-containing iron garnet single-crystal of composition $(Bi,Gd)_3Fe_5O_{12}$.

The $H_{in}(\varphi)$ curve for $(Bi,Gd)_3Fe_5O_{12}$ films oriented close to, but not exactly along (111) (samples 4 and 5 in Table I) has a complex form in the plane of the film. For sample 4, which has the lowest (of those investigated) anisotropy in the plane of the film and a relatively small deviation Θ from the basal orientation of the film (see Table I), the $H_{in}(\varphi)$ curve has six peaks (Fig. 3), as is typical of the cubic crystallographic anisotropy of (111)-oriented films. However, because of the nonzero angle Θ, these maxima have different amplitudes. We note that the Bi concentration in this sample is minuscule (see Table I). The value of δH_{in} increases as Θ increases (sample 5 in Table I), where two of the six peaks of the $H_{in}(\varphi)$ curve become less pronounced. The effective anisotropy field for both samples 4 and 5 is not very great. As in the case of (110)-oriented films, the addition of Lu to Bi-containing IGSC films does not produce any significant changes in the magnetic anisotropy parameters.

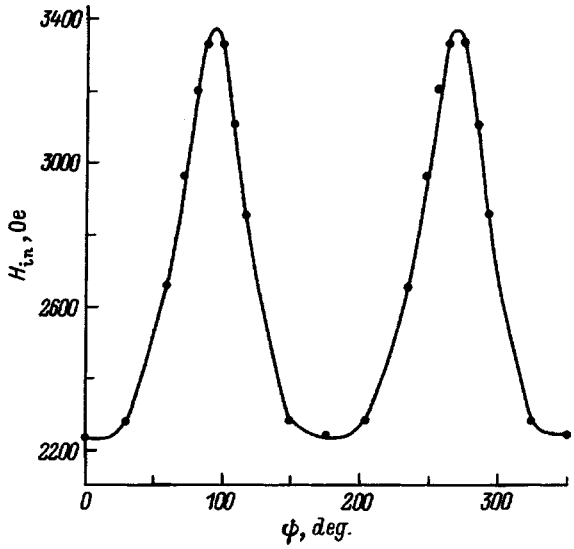

FIG. 2. The same as in Fig. 1 for the (110) orientation.

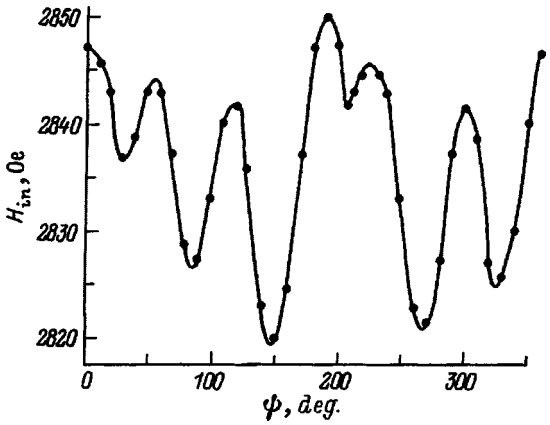

FIG. 3. The same as in Fig. 1 for an orientation close to (111) ($\Theta = 1.4°$).

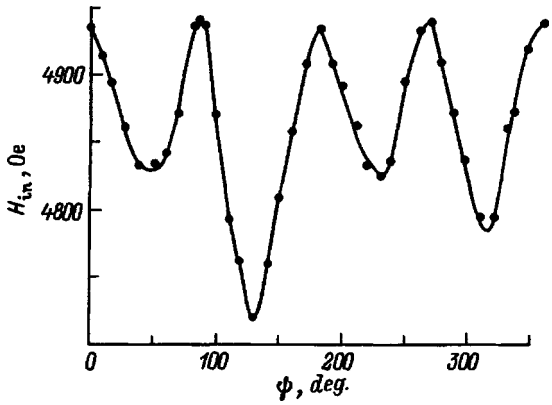

FIG. 5. The same as in Fig. 1 for Bi-containing IGSC films of composition $(Bi,Gd,Lu)_3(Fe,Ga)_5O_{12}$ with an orientation close to (111) ($\Theta = 0.8°$).

The addition of Ga to films of $(Bi,Gd)_3Fe_5O_{12}$ (sample 6) and $(Bi,Gd,Lu)_3Fe_5O_{12}$ (sample 7) induces fairly strong uniaxial magnetic anisotropy. As a consequence, the resonance field associated with perpendicular resonance becomes weaker than for parallel resonance. The field-azimuth curve $H_{in}(\varphi)$ for sample 6 has two broad maxima with a 180° period (as in Fig. 2), where the prominent features associated with cubic anisotropy are scarcely discernible. The same curve for sample 7 reveals four essentially equidistant peaks (Fig. 5). The stronger anisotropy in the plane for sample 6 relative to sample 7 is attributable to the more pronounced deviation of the substrate orientation from the (111) plane (cf. the values of Θ in Table I). We note that for these samples, since $\delta a/a$ has the opposite sign, the magnetostriction mechanism gives the opposite contribution to uniaxial magnetic anisotropy. The higher value of H_{eff} for sample 7 leads to the conclusion that the contribution of the magnetostriction mechanism to uniaxial magnetic anisotropy is positive for tensile stresses ($\delta a/a > 0$) and is negative for compressive stresses ($\delta a/a < 0$).

The introduction of Ga (sample 6) leads to considerable broadening of the ferromagnetic resonance line (see the ferromagnetic resonance linewidths $2\Delta H_p$ and $2\Delta H_{in}$ in Table I). However, despite the stronger uniaxial magnetic anisotropy, for the Bi-containing IGSC film doped with Lu (sample 7), the ferromagnetic resonance line (see Table I). It could be that this result is due to the smaller lattice misfit of the film and substrate.

The addition of Al to (111)-oriented $(Bi,Gd)_3Fe_5O_{12}$ films (sample 8 in Table I) also produces a fairly high uniaxial magnetic anisotropy (see the value of H_{eff} in Table I). The field-azimuth curve $H_{in}(\varphi)$, as in the case of Ga-containing films, is in the form of two maxima with a 180° period, superimposed with narrower, weaker peaks (Fig. 6). The addition of La to Bi-containing IGSC films to reduce the mismatch of the film and substrate lattice parameters and a change in the orientation of the substrate (sample 9 in Table I) does not yield any significant change in the profile of the $H_{in}(\varphi)$ curve, despite stronger in-plane anisotropy and weaker uniaxial magnetic anisotropy than for sample 8 (cf. the values of δH_{in} and H_{eff} in Table I).

All the investigated Bi-containing IGSC films have in common the property that the ferromagnetic resonance linewidth in parallel resonance is at most less than or equal to the linewidth in perpendicular resonance (cf. the values of $2\Delta H_p$ and $2\Delta H_{in}$ in Table I).

In summary, we have shown the following in our investigation of bismuth-containing iron garnet single-crystal films of the system $(Bi,Gd,Ln)_3(Fe,M)_5O_{12}$.

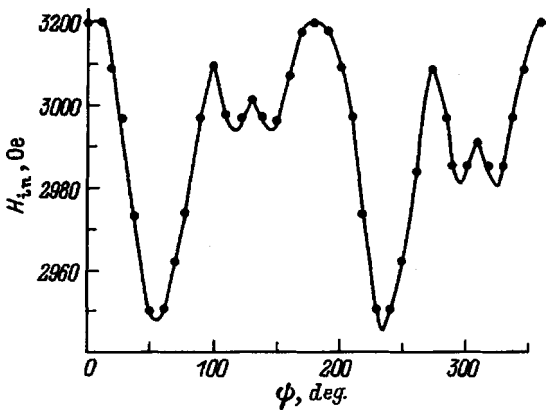

FIG. 4. The same as in Fig. 1 for Bi-containing IGSC films of composition $(Bi,Gd,Lu)_3Fe_5O_{12}$ with an orientation close to (111) ($\Theta = 2.6°$).

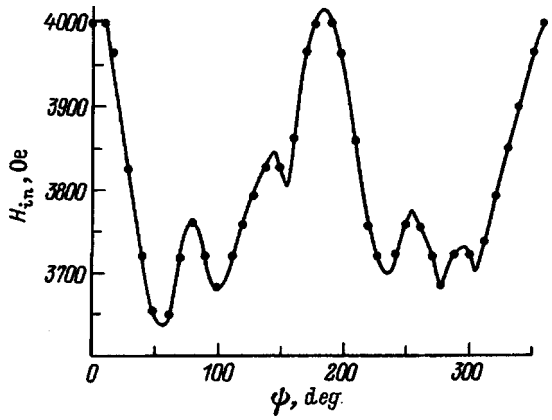

FIG. 6. The same as in Fig. 1 for Bi-containing IGSC films of composition $(Bi,Gd)_3(Fe,Al)_5O_{12}$ with an orientation close to (111) ($\Theta = 4.75°$).

1. Orthorhombic magnetic anisotropy is induced during the epitaxial growth of iron garnet films containing only Gd^{3+} and Bi^{3+} ions in the dodecahedral sublattice with (110) orientation and also with a deviation of the plane of the film from the (111) orientation.

2. The addition of Ga or Al to Bi-containing IGSC films produces fairly strong uniaxial magnetic anisotropy, but in the absence of substituents for Fe the magnetization vectors are oriented in the plane of the film.

3. The azimuthal dependence of the resonance field for Bi-containing IGSC films of the system $(Bi,Gd)_3Fe_5O_{12}$ reflects crystallographic magnetic anisotropy: For the (110) orientation the profile of the field-azimuth curve has two maxima with a 180° period, in the (100) orientation it has four equivalent maxima, and with a deviation of the film orientation from the (111) plane the number of strong maxima changes (from 6 to 2) as the angle Θ varies.

4. The introduction of substituents (Lu, La, Ga, Al) leads to the broadening and merging of adjacent maxima of the field-azimuth curve.

[1] A. K. Zvezdin and V. A. Kotov, *Magnetooptics of Thin Films* [in Russian] (Nauka, Moscow, 1988), 192 pp.
[2] V. V. Randoshkin and A. Ya. Chervonenkis, *Applied Magnetooptics* [in Russian] (Énergoatomizdat, Moscow, 1990), 420 pp.
[3] P. Hansen, H. Heitman, and K. Witter, Phys. Rev. B **23**, 6085 (1981).
[4] P. Hansen, K. Witter, and W. Tolksdorf, Phys. Rev. B **27**, 4375 (1983).
[5] P. Hansen, W. Tolksdorf, K. Witter, and J. M. Robertson, IEEE Trans. Magn. **MAG-20**, 1099 (1984).
[6] S. S. Gorelik, Yu. A. Skakov, and L. N. Rastorguev, *X-Ray and Electron-Optical Analysis* [in Russian] (Izd. MISiS, Moscow, 1994).
[7] *Magnetic Bubble Elements and Devices* [in Russian], edited by N. N. Evtikhiev and B. N. Naumov (Radio i Svyaz', Moscow, 1987), 488 pp.
[8] V. V. Randoshkin, V. I. Chani, and A. I. Tsvetkova, Pis'ma Zh. Tekh. Fiz. **13**, 839 (1987) [Sov. Tech. Phys. Lett. **13**, 348 (1987)].
[9] R. K. Wangsness, Phys. Rev. **91**, 1085 (1953).
[10] K. Gangulee and R. J. Kobliska, J. Appl. Phys. **51**, 3333 (1980).
[11] N. A. Loginov, M. V. Logunov, and V. V. Randoshkin, Fiz. Tverd. Tela (Leningrad) **31**(10), 58 (1989) [Sov. Phys. Solid State **31**, 1684 (1989)].
[12] V. V. Randoshkin and V. B. Sigachev, JETP Lett. **42**, 41 (1985).
[13] V. V. Randoshkin, *Magnetooptic Iron Garnet Films and Their Applications* [in Russian], Vol. 35 of Transactions of the Institute of General Physics of the Russian Academy of Sciences (Nauka, Moscow, 1992), pp. 49–107.

Translated by James S. Wood

Repetitive hydrogen pellet injector utilizing a screw extruder

I. V. Viniar, S. V. Skoblikov, and P. Yu. Koblents

St. Petersburg State Technical University, 195251 St. Petersburg, Russia
(Submitted April 30, 1997)
Zh. Tekh. Fiz. **68**, 117–120 (May 1998)

A new injector for the continuous formation of an unlimited supply of fuel pellets and their injection into the plasma of fusion reactors is described. A solid hydrogen rod of length in excess of 50 m has been extruded at an average rate of 20 mm/s, and more than a thousand pellets of diameter 2 mm have been formed from it in continuous operation at frequencies of 1 Hz and 2 Hz and have been accelerated to 0.6–0.8 km/s. © *1998 American Institute of Physics.* [S1063-7842(98)02205-3]

INTRODUCTION

One of the techniques for delivering fuel into the plasma of a fusion reactor is to inject macroscopic pellets of solidified hydrogen isotopes. Large-scale thermonuclear fusion facilities are equipped with injectors that continuously shoot fuel pellets into the plasma at a frequency from 1 Hz to 40 Hz (Refs. 1 and 2). However, the continuous operating time of the injector is limited by its content of prefrozen fuel from which the pellets are formed, and after a few minutes there is a required downtime while a new batch of fuel is frozen. The problem is not solved by increasing the extruder volume, because the mass of tritium in the injector must be minimal. It has been proposed that continuous, prolonged pellet injection might be achieved by using two or more extruders in the injector, where they would operate alternately to form pellets.[2,3] This approach adds to the complexity of the structure and increases the quantity of fuel contained in the injector, a feature that is unacceptable when working with tritium. The simpler and more promising method of continuous ''gaseous'' extrusion of thermonuclear fuel[4] incurs increased risk due to the high pressure of the gaseous (and potentially explosive) hydrogen isotopes used in the technological cycle.

Here we describe a solid hydrogen extrusion technique using a single screw extruder, along with an injector configuration that is serviceable for solving the problem of continuous, prolonged, reliable formation of fuel pellets for reactor injection.

DESCRIPTION OF THE EXTRUSION TECHNIQUE AND THE INJECTOR STRUCTURE

The proposed continuous extrusion technique is based on the well-known screw extrusion technique used for plastics,[5] where a channeled rotating worm screw delivers solid particles of a working medium (plastics, elastomers, etc.) to the exit orifice, through which the material is forced under the influence of the resulting compression and heating of the material. The extruder of the fuel injector differs from this setup in that it operates at a temperature of approximately 10 K and is supplied with a gas, which progresses along the screw channel and, in so doing, is converted initially into liquid and then into ice. This process is feasible by virtue of the fact that a temperature interval of only 5–10 K exists between the liquid and solid plastic states of the hydrogen isotopes. It is a well-known fact that the extrusion of transparent solid hydrogen ice suitable for the formation of a durable pellet requires that it be compressed to 5–20 MPa (Refs. 1–4), an operation that leads to large heat release and can also induce melting and extrusion instability. Consequently, the feasibility of achieving a stable extrusion regime by screw rotation needs to be tested experimentally. For this purpose we have designed and built an injector, whose schematic configuration and general appearance are shown in Fig. 1. Its main components are a high-vacuum chamber *1*, which houses the extruder *2* with an open-cycle heat exchanger *3* and a screw *4* which is driven from outside the chamber by a motor *5*, a valve *6* for admission of the driver gas, an electromagnetic drive *7* used to deliver pellets into the barrel *8*, and a diagnostic chamber *9*. The exit orifice of the extruder is connected to a transparent observation chamber *10* equipped with a vacuum pump *11*, which has a linear scale for visual observation and measurement of the length of the solid hydrogen rod. The main injector evacuation system is not shown in Fig. 1. The extruder has a length of 150 mm and comprises a cylindrical chamber of inner diameter of 12 mm with a helical heat-exchanger channel cut into its outer surface. Two semiconductor temperature sensors are placed in the upper and lower parts of the extruder. A 30-W heater is coiled around the length of the extruder. The extruder and the barrel are separated by a gap to thermally insulate the extruder from the barrel, which is not cooled by the helium flow.

During the operation of the injector hydrogen is delivered continuously into the extruder, which is cooled by helium flowing from a Dewar flask. The helium flow is regulated by a vapor-pressure stabilization system inside the Dewar and by a flow regulator at the exit from the injector chamber; these control devices are not shown in Fig. 1. Driven by the motor, the screw turns inside the extruder chamber, and the hydrogen moving along the helical screw channel gradually freezes and is forced out through an orifice of diameter 2 mm into the chamber for visual observation. The electromagnetic drive advances a thin-walled tube, which cuts off part of the extruded rod and enters the barrel.

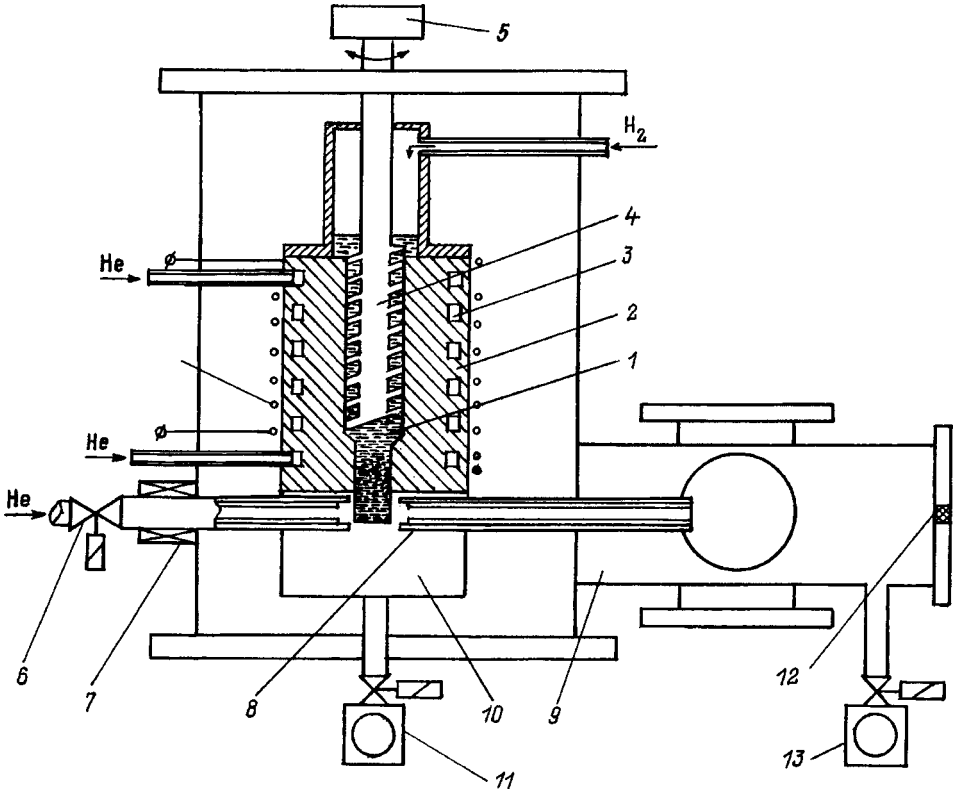

FIG. 1. Diagram of the fuel pellet injector with screw extruder.

A brief moment later (0.05–0.1 s) the valve admits compressed gas, which accelerates the pellet in the barrel and fires it into the diagnostic chamber. The pellet breaks a light beam and strikes a microphone *12*, which is attached to the flange of the chamber. These signals are used to measure the velocity of the pellet, and it is photographed in flash illumination with a duration of 0.1 μs. After striking the microphone, the pellet evaporates and together with the driver gas is removed from the chamber by a vacuum pump *13*. The cycle is then repeated.

EXPERIMENTAL RESULTS

In the first stage we concentrated mainly on obtaining a stable extrusion regime. The extruder temperature was held constant in the interval 10–13 K by regulating the helium flow (up to 10 liters/h) and the heater power. The fluctuations of the temperature from the set value did not exceed 0.5 K. Before the start of extrusion hydrogen at a pressure of less than 0.1 MPa was admitted into the extruder and frozen in it. The worm screw was rotated both by the motor and by hand at a rate of 10–80 rpm. A solid hydrogen rod appeared in the observation chamber 2–10 s after the start of rotation of the screw. Its characteristic form is shown in Fig. 2 for various extruder temperatures. Clearly, the higher the temperature of the rod, the more it is bent. In the event that extrusion is stopped, after 5–10 s the cylindrical rod acquires a conical shape as a result of sublimation of the hydrogen in vacuum. A transparent appearance is indicative of a high-quality solid hydrogen rod.

The extrusion rate was calculated from the time for the tip of the rod to traverse a scale of length 6 cm with five-millimeter divisions, which was attached to the wall of the observation chamber. The most stable extrusion regime was maintained when the screw turned at a speed of 15 rpm. The dependence of the extrusion rate on the temperature of the hydrogen rod in this regime is shown in Fig. 3. When the screw rotation speed was increased above 30 rpm, the extrusion rate scarcely increased at all and even decreased with time, eventually to zero, most likely because of strong heating of the hydrogen in the extruder chamber and a reduction

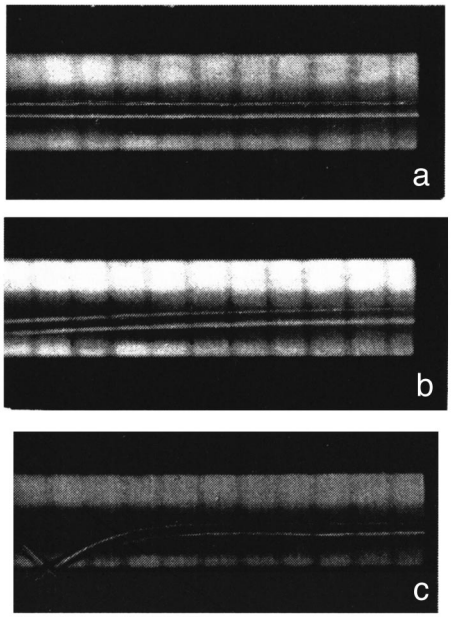

FIG. 2. Solid hydrogen rods extruded at various temperatures. a) 10 K b) 11 K; c) 12 K.

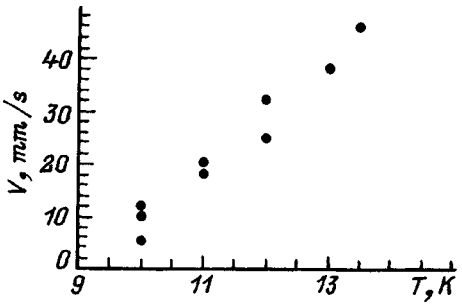

FIG. 3. Extrusion rate V versus temperature of the hydrogen rod T at a screw rotation speed of 15 rpm.

in the resulting compression. Nonetheless, an acceptable extrusion rate of 2–4 cm/s for the formation of pellets at a temperature of 10–12 K and frequency up to 10 Hz was maintained continuously for more than 30 min until the solid hydrogen filled up the volume of the observation chamber. Following its evacuation, the extruder was gradually restored with the start of rotation of the screw. During this entire time a hydrogen rod having a length of more than 50 m was extruded and, with allowance for cutting waste, could have been used to produce more than 12 000 pellets with a characteristic diameter of 2 mm. At most 5 cm^3 of solid hydrogen, amounting to fewer than 800 pellets, occupied the interior of the extruder at any given time. This result attests to the high efficiency and appeal of such an injector for reactor refueling, because the mass of tritium in the injector would be less than 2 g.

The objective of the second stage was to demonstrate the possibility of forming and accelerating a pellet intact in continuous operation, and also to photograph it. Once the rod appeared in the observation chamber, the electromagnetic drive unit quickly pushed the thin-walled tube toward it and, thereby cutting off part of the rod, transferred the shaped pellet in the barrel, which had a diameter 2.4 mm. Next, compressed helium at a pressure of 2–4 MPa was admitted from the pulse-actuated valve and accelerated the pellet in the barrel. At a time 0.05 s after the shot, the drive returned the tube to its original position, and the hydrogen rod continued to be forced into the observation chamber without delay or visible loss of quality of the ice. It was thus successfully confirmed that the driver gas has scarcely any influence on the stability or rate of extrusion. In the first experiments shots were fired at frequencies of 1 Hz, 1.5 Hz, and 2 Hz. More than a thousand pellets were formed and accelerated to 0.6–0.8 km/s without interruption. The flash lamp permitted only every third pellet to be photographed. All the photographed pellets were free of visible traces of damage and had the characteristic form shown in Fig. 4.

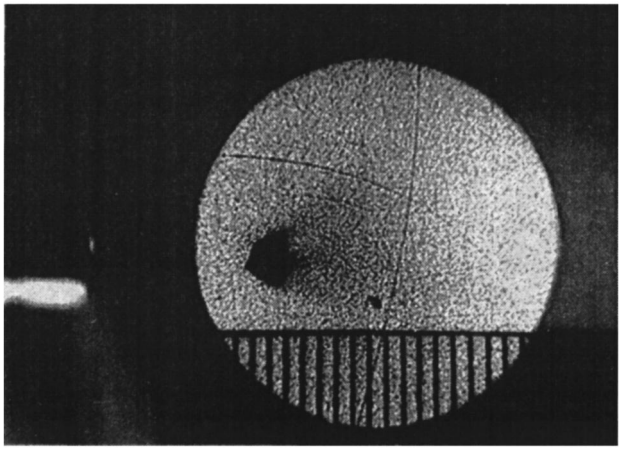

FIG. 4. Series of hydrogen pellets injected at a frequency of 1 MHz and velocity of 0.7 km/s.

Preparations are currently underway for the injection of particles at frequencies up to 10 Hz from a mixture of deuterium with hydrogen and for photographing every particle with a view toward determining the reliability in long-term injection.

CONCLUSION

The proposed and experimentally tested technique for the formation of macroscopic fuel pellets using a screw extruder can be used in principle to solve the problem of building a reliable system for refueling the plasma of fusion reactors in continuous, long-term operation. One extruder of this type meets all present-day requirements of the fuel injection system for reactors of the International Thermonuclear Experimental Reactor (ITER) type in regard to pellet formation, and it is distinguished by exceptional simplicity and reliability as well as a low reserve of hydrogen isotopes in the injector. An increase in the extrusion rate can be expected after the completion of mathematical modeling and experiments currently in progress.

The authors are indebted to B. V. Kuteev for support and valuable discussions and to V. G. Kapralov for furnishing a number of the electronic units.

[1] S. L. Milora, W. A. Houlberg, L. L. Lenguel, and V. Mertens, Nucl. Fusion **35**, 657 (1995).
[2] S. K. Combs, Rev. Sci. Instrum. **64**, No. 1679 (1993).
[3] B. V. Kuteev, I. V. Viniar, V. Yu. Sergeev *et al.*, Fusion Technol. **26**, 642 (1994).
[4] I. V. Vinyar, B. V. Kuteev, S. V. Skoblikov *et al.*, Zh. Tekh. Fiz. **65**(7), 167 (1995) [Tech. Phys. **40**, 723 (1995)].
[5] D. D. Ryabinin and Yu. E. Lukach, *Screw Machines for the Processing of Plastics and Rubber Mixtures* [in Russian] (Mashinostroenie, Moscow, 1965), 363 pp.

Translated by James S. Wood

Pentagonal two-loop ring interferometer

A. R. Agachev, A. B. Balakin, G. N. Buĭnov, S. L. Buchinskaya, R. A. Daishev, G. V. Kisun'ko, V. A. Komissaruk, S. V. Mavrin, Z. G. Murzakhanov, R. A. Rafikov, A. F. Skochilov, V. A. Cheredilin, and Yu. P. Chugunov

Kazan State University, 420008 Kazan, Russia
(Submitted May 5, 1997)
Zh. Tekh. Fiz. **68**, 121–125 (May 1998)

Results of work on the assembly and adjustment of an original pentagonal, two-loop interferometer are reported; the interferometer is a passive version of a compact laser gravitational wave detector. It is shown that the correlative automatic noise-compensation system developed for the project is capable of lowering the phase noise level in the resultant signal channel of the detector by two orders of magnitude. © *1998 American Institute of Physics.* [S1063-7842(98)02305-8]

INTRODUCTION

Projects geared to the fundamental objective of building an inventory of precision instrumentation for the measurement of extremely small signals, such as a signal representing the influence of a gravitational-wave field on the frequency-phase response characteristics of optical radiation, have been in progress since September of 1995 in the Kazan Joint Experimental Laboratory of Gravitational Optics Research (the Dulkyn Science Center of Gravitational-Wave Research and the Scientific-Industrial Association of Applied Optics).[1,2] The essential concept underlying this work is to create two optical channels in an instrument, with information about the useful signal being stored in only one of the channels, while the noise processes in both channels are correlated.

Here we give the results of work on the assembly and adjustment of a pentagonal, double-loop ring interferometer, which is a passive version of a compact laser gravitational-wave detector,[1] along with the results of testing a newly developed correlative automatic noise-compensation system.

The experiments were performed in a special-purpose cabin situated in a buried laboratory at a depth of 12 m from the zero mark, based on considerations of minimizing the influence of background vibrations and simplifying the temperature stabilization problem. The experimental cabin was placed in a buried diffraction-gratings laboratory (BDGL), which is a specially designed facility. The walls and floor of the laboratory are situated in an all-metal vessel, which rests on a sand cushion and is hydraulically isolated around the walls. The laboratory has a subfloor engineering service compartment with a depth of 2 m from the floor to provide for the installation of equipment foundations along with auxiliary equipment required for supplying electrical power to the main equipment and for electrical communications. The walls of the BDGL are lined with marble slabs to ensure further protection against dust. The experimental cabin consists of two enclosures, one housed inside the other. All extremely sensitive equipment, including the new pentagonal interferometer, is mounted on a special foundation in the inner compartment, and the foundation, in turn is vibration-isolated from the base of the compartment. The foundation comprises a 100-tonne reinforced concrete block, which is vibration-isolated by means of railroad-type coil springs. The equipment is further vibration-isolated by means of special vibration mounts. A three-stage thermal stabilization system is provided to establish the necessary temperature conditions. The first stage is implemented by a conditioner, which heats up the airflow circulated through the BDGL for ventilation and maintains a stable temperature within 0.5 °C limits (0.25 °C from the specified nominal value). The second and third stages are created by a specially designed autonomous temperature stabilization system. The second stage stabilizes the temperature in the outer compartment of the cabin within tenths of a degree from the nominal value, and the third stage does the same for the inner compartment within hundredths of a degree.

OPTICAL SYSTEM OF THE PENTAGONAL RING INTERFEROMETER

The optical system of the passive version of the pentagonal ring interferometer is shown in Fig. 1 and includes: *1*) the laser source; *2,12*) beam-splitting cubes; *3,11,13*) total-internal-reflecting (TIR) prisms; *4,8,10*) the interferometer mirrors; *5,9*) hologram diffraction gratings (with a carrier spatial frequency of 1767.8 lines/mm); *6,7*) polarizing prisms in the signal branch of the interferometer; *14*) a polarizing prism, which spatially separates the interference patterns; PD_{11}, PD_{12}, PD_{21}, PD_{22}) photodetectors. The optical elements *4,5,8,9,10* are situated at the vertices of a regular pentagon.

The light source was a frequency-stabilized LGN-302 laser operating at a wavelength of 0.6382μm, whose light polarization plane forms a 45° angle with the plane of the figure, this configuration being equivalent to the presence of two beams of equal intensity with mutually orthogonal azimuths of polarization (TE and TM). The solid lines in Fig. 1 correspond to the TE-polarized beam, and the dashed lines correspond to the TM-polarized beam.

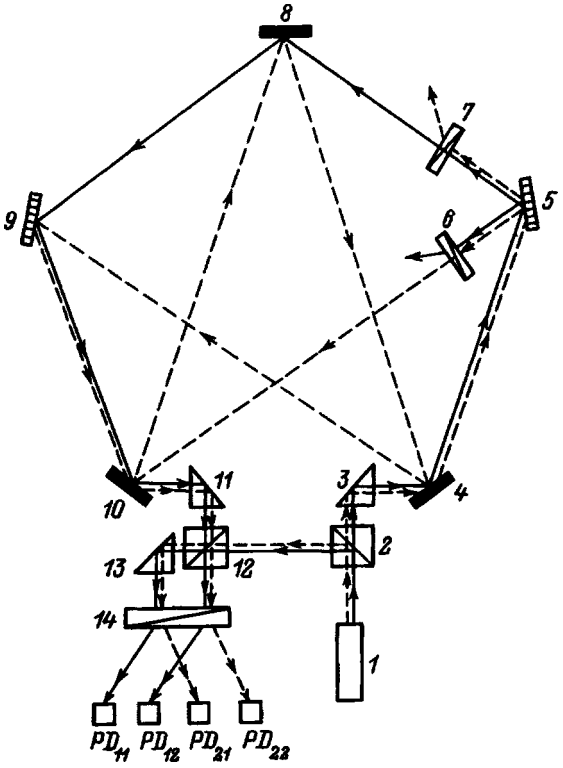

FIG. 1. Optical schematic of the pentagonal interferometer.

The interferometer operates as follows. The beam-splitting cube *2* divides the primary laser beam into two beams: The reflected beam serves as the reference beam, while the TIR prism *3* directs the transmitted beam into the pentagonal interferometer. The transmitted beam, in turn, is split into two beams by the hologram diffraction gratings *5* and *9*. The first beam propagates around the outer contour of the figure formed by the ray path; it is reflected from both gratings in the zeroth diffraction order and, because of the polarizing prism *7*, contains only the TE component of the laser output. The second beam is diffracted in the first order by the grating *5* and, after passing through the polarizing prism *6*, contains only the TM component of the primary laser beam; it is then reflected in succession from the mirrors *10*, *8*, and *4* and is incident on the grating *9*, where it is also diffracted in the first order and then converges in unison with the first beam. The TIR prism *11* extracts both the TE-polarized beam and the TM-polarized beam from the pentagonal interferometer and directs them onto the beam-splitting cube *12*, where they interfere with the TE-polarized and TM-polarized reference beams reflected from the beam-splitting cube 2. Two of the four interference patterns produced by this process (two from each of the two exit faces of the beam-splitting cube *12* are sent directly to the polarizing prism *14*, and the other two are directed onto it by the beam-splitting prism 13. The polarizing prism 14 provides full spatial separation of the interference patterns, which are recorded directly by the photodetectors PD_{11}, PD_{12}, PD_{21}, and PD_{22}.

It is evident from the optical schematic in Fig. 1 that the beam from the laser *1* (apart from inevitable losses of the TE-polarized and TM-polarized beams in the polarizing prisms *6* and *7* when they leak outside their own loops) is fully utilized to obtain information about the changes in phase of the optical radiation in the outer and inner loops of the pentagonal interferometer.

The photodetectors PD_{11} and PD_{12} are used to record the mutually coupled interference patterns associated with interference between the TE beams, and the photodetectors PD_{21} and PD_{22} are used to record the coupled interference patterns of the TM modes. The pentagonal double-loop interferometer is adjusted so that bands of infinite width will be observed in all four patterns. In reality, owing to divergence of the laser radiation and a significant difference in the optical paths in the reference and signal branches of the interferometer, the bands are observed in the form of rings, as is typical of interference between two spherical fronts having close radii of curvature.

The initial phases in the interference patterns can be established independently by varying the path length of the light transmitted through the elements *6* and *7* (by tilting them very slightly, on the order of a few minutes of angle, relative to the optical axis).

PROCESSING OF THE INTERFERENCE PATTERNS

In accordance with the optical schematic in Fig. 1, four waves are incident on two mutually orthogonal faces of the beam-splitting cube *12*: Two signal waves, one TE-polarized and the other TM-polarized (from the outer and inner loops, respectively) with complex amplitudes $A_1\exp(i\Phi_{1A})$ and $B_1\exp(i\Phi_{1B})$, are incident on one face, and two references waves, one TE and one TM with respective amplitudes $A_0\exp(i\Phi_{0A})$ and $B_0\exp(i\Phi_{0B})$, are incident on the other face. The interference of like-polarized beams at the beam-splitting layer inside the cube produces four interference patterns (two on each of the exit faces of the cube), in which the intensity distribution is described by the expressions

$$I_{11,12}=|R_{TE}|^2A_{0,1}^2+|T_{TE}|^2A_{1,0}^2 +2|R_{TE}||T_{TE}|A_0A_1\cos(\Delta\Phi_{TE}\pm\Gamma_{TE}),$$
$$I_{21,22}=|R_{TM}|^2B_{0,1}^2+|T_{TM}|^2B_{1,0}^2 +2|R_{TM}||T_{TM}|B_0B_1\cos(\Delta\Phi_{TM}\pm\Gamma_{TM}). \quad (1)$$

Here $R_{TE}=|R_{TE}|\exp(i\Gamma_{AR})$ and $R_{TM}=|R_{TM}|\exp(i\Gamma_{BR})$ are the reflection coefficients, and $T_{TE}=|T_{TE}|\exp(i\Gamma_{AT})$ and $T_{TM}=|T_{TM}|\exp(i\Gamma_{BT})$ are the transmission coefficients of the beam-splitting layer inside the cube, respectively; $\Gamma_{TE}=\Gamma_{AT}-\Gamma_{AR}$, $\Gamma_{TM}=\Gamma_{BT}-\Gamma_{BR}$, $\Delta\Phi_{TE}=\Phi_{1A}-\Phi_{0A}$, and $\Delta\Phi_{TM}=\Phi_{1B}-\Phi_{0B}$.

If light is not absorbed or scattered in the beam-splitting layer (i.e., if the latter is a homogeneous dielectric layer or a multilayer interference coating), then $\Gamma_{TE,TM}=\pi/2$. In this case the maxima of $I_{11,21}$ and the minima of $I_{12,22}$ are attained for the same value of the phase difference $\Delta\Phi_{TE,TM}$. If absorption is present in the layer, we have $\Gamma_{TE,TM}=\pi/2+\Gamma_{A,B}$, so that the maxima of $I_{11,21}$ and the minima of $I_{12,22}$ are separated by a phase shift equal to $2\Gamma_{A,B}$.

After the spatial separation of all four interference patterns (Fig. 1) the variations of the intensities I_{k1} and I_{k2} as a

result of variations of the phase difference $\Delta\Phi_{TE,TM}(t) = \Delta\Phi^0_{TE,TM} + \delta_{1,2}(t)$ are recorded by the photodetectors PD_{k1} and PD_{k2}. The voltages $U_{k1}(t) = \beta_{k1} I_{k1}$ and $U_{k2}(t) = \beta_{k2}(t)$ from the photodetector outputs ($\beta_{k1,2}$ denotes the conversion efficiencies of the photodiodes) are sent to a subtraction circuit, which generates the difference voltages $U_1(t) = U_{11}(t) - U_{12}(t)$ and $U_2(t) = U_{21}(t) - U_{22}(t)$.

The wave amplitudes $U_{k1}(t)$ and $U_{k2}(t)$ are determined by varying the initial phase difference $\Delta\Phi^0_{TE,TM}$ from zero to 2π:

$$\Delta U_{11,12} = U^{\max}_{11,12} - U^{\min}_{11,12} = 4|R_{TE}||T_{TE}|A_0 A_1 \beta_{11,12},$$

$$\Delta U_{21,22} = U^{\max}_{21,22} - U^{\min}_{21,22} = 4|R_{TM}||T_{TM}|B_0 B_1 \beta_{21,22}; \quad (2)$$

these results are then used to determine the normalization factors $\Delta U_k = (\Delta U_{k1} + U_{k2})/2$.

For small phase variations $|\delta_{1,2}(t)| \ll 1$ we obtain the following expressions for the difference voltages:

$$U_1(t) = U^0_1 + 2|R_{TE}||T_{TE}|A_0 A_1[\beta_{11}\cos(\Delta\Phi^0_{TE} - \Gamma_A) + \beta_{12}\cos(\Delta\Phi^0_{TE} + \Gamma_A)]\delta_1(t),$$

$$U_2(t) = U^0_2 + 2|R_{TM}||T_{TM}|B_0 B_1[\beta_{11}\cos(\Delta\Phi^0_{TM} - \Gamma_B) + \beta_{22}\cos(\Delta\Phi^0_{TM} + \Gamma_B)]\delta_2(t), \quad (3)$$

where

$$U^0_1 = \beta_{11} I^0_{11} - \beta_{12} I^0_{12} + 2|R_{TE}||T_{TE}|A_0 A_1 \times [\beta_{11}\sin(\Delta\Phi^0_{TE} - \Gamma_A) + \beta_{12}\sin(\Delta\Phi^0_{TE} + \Gamma_A)],$$

$$U^0_2 = \beta_{21} I^0_{21} - \beta_{22} I^0_{22} + 2|R_{TM}||T_{TM}|B_0 B_1 \times [\beta_{21}\sin(\Delta\Phi^0_{TM} - \Gamma_B) + \beta_{22}\sin(\Delta\Phi^0_{TM} + \Gamma_B)],$$

$$I^0_{11,12} = |R_{TE}|^2 A^2_{0,1} + |T_{TE}|^2 A^2_{1,0},$$

$$I^0_{21,22} = |R_{TM}|^2 B^2_{0,1} + |T_{TM}|^2 B^2_{1,0}.$$

Establishing the initial phase differences $\Delta\Phi^0_{TE,TM}$ by setting the quantities $U^0_{1,2}$ equal to zero, we obtain the normalized difference voltages

$$u_1(t) = \frac{U_1(t)}{\Delta U_1} = u_{10}\delta_1(t),$$

$$u_2(t) = \frac{U_2(t)}{\Delta U_2} = u_{20}\delta_2(t), \quad (4)$$

where the dimensionless quantities $u_{10,20} \sim 1$ are defined by the equation

$$u_{10,20} = \frac{\beta_{11,21}\cos(\Delta\Phi^0_{TE,TM} - \Gamma_{A,B}) + \beta_{12,22}\cos(\Delta\Phi^0_{TE,TM} + \Gamma_{A,B})}{\beta_{11,21} + \beta_{12,22}}.$$

The values of $u_{1,2}(t)$ are fed into a correlative automatic noise-compensation (CANC) system, which is implemented in a computerized analog-to-digital converter (ADC) configuration. A resultant signal $U_\Sigma(t)$ is generated at the output of the CANC system:

$$U_\Sigma(t) = u_1(t) - u_2(t)\frac{\overline{u_1(t)u_2(t)}}{\overline{u^2_2(t)}}, \quad (5)$$

where the overbar denotes time averaging. If the quantities $u_1(t)$ and $u_2(t)$ are completely correlated, i.e., if $u_2(t) = \text{const} \cdot u_1(t)$, the resultant signal $U_\Sigma(t) = 0$.

We have run a mathematical simulation of the CANC system, demonstrating the possibility of separating a weak useful signal contained in $u_1(t)$ from correlated noise for a signal-to-noise ratio of the order of 10^{-6}.

EXPERIMENTAL RESULTS

The pentagonal interferometer shown schematically in Fig. 1 has been assembled and adjusted on a polished, thick (10 cm), circular glass plate of diameter 65 cm; the pentagon has a side of 30 cm. To eliminate phase fluctuations during propagation of the laser beams around the outer and inner loops of the pentagonal interferometer under the influence of air currents and local temperature variations in the working zone, the optical system of the interferometer is covered with a protective hood in the form of a welded cylindrical structure made of D-16 alloy. Four separate interference patterns with the desired adjustment either to infinitely wide bands or to bands of finite width are obtained in the plane of the photodetectors.

The recording system includes two identical channels (reference and measurement). Each channel consists of a remote unit containing two photodiodes and two side-by-side photocurrent-to-voltage converters located directly on the interferometer, plus a differential amplifier unit with a power source; the latter unit is situated next to the computer. The remote unit and the differential amplifier unit are connected by a cable, which carries the supply voltage to the remote unit and returns the information signals to the differential amplifier.

The photocurrent induced in a photodiode is sent to the input of a current-to-voltage converter (CVC). The converter has a high input impedance, which is necessary for operation with a photodiode, and a low output impedance, which helps to minimize the influence of the long cable on the signal transmitted to the differential amplifier. When the pair of converters of one channel is adjusted so that the constant components of the useful signal are equal at their outputs, the differential amplifier suppresses both the constant component of the signal and in-phase noise induced in the cable. On the other hand, the difference signal from two arms of the

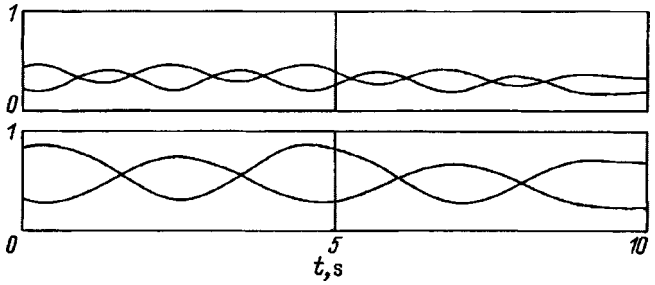

FIG. 2. Photodetector signals (in arbitrary units).

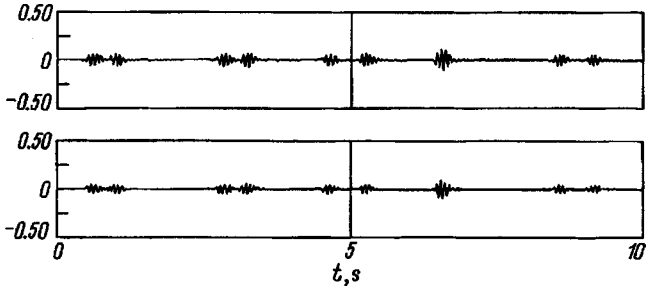

FIG. 3. Variations of $u_1(t)$ and $u_2(t)$ when the interferometer is subjected to a mechanical disturbance.

interferometer is amplified so as to match the peak-to-peak amplitude of the differential amplifier output voltage with the input voltage range of the ADC at the maximum noise level affecting the interferometer. The optical detectors are PD-256 diodes; from a batch of 30 photodetectors we have selected four having minimum internal noise and minimum spread of the monochromatic current sensitivity at the laser wavelength of 0.6328 nm.

The current-to-voltage converter is assembled from a 140UD24 pulse-stabilized, ultrahigh-precision, operational amplifier, which is designed for the construction of extremely stable dc amplifiers and operation with high-resistance signal sources. When the assembled CVC operates in conjunction with a selected photodiode, it has an internal noise level no higher than 45μV, which corresponds to a dynamic range in excess of 100 dB on the part of the remote unit.

The differential amplifier is assembled as an instrumentation amplifier utilizing three operational amplifiers, each of which is a 140UD25 precision amplifier with an ultralow input noise voltage. The assembled differential amplifier has an internal noise level no higher than 30μV, which corresponds to a dynamic range of at least 112 dB. The suppression of the in-phase component of the signal is 94 dB in the frequency band from 0 to 100 Hz.

The light polarization azimuths in the two interference patterns recorded by the photodetectors PD_{11} and PD_{12} are orthogonal to the light polarization azimuths in the interference patterns recorded by PD_{21} and PD_{22}.

Figure 2 shows experimental plots of the light intensities in the interference patterns versus time as the initial phase differences are varied. The signals from the photodetectors PD_{11} and PD_{12} are shown in the upper graph, and those from PD_{21} and PD_{22} are shown in the lower graph.

If the interferometer mirrors are affected by mechanical disturbances of any kind, the phases in the inner and outer loops vary synchronously. We have investigated various types of mechanical, acoustical, and temperature disturbances acting on the pentagonal interferometer. In every case we observed synchronous variation of the quantities $u_1(t)$

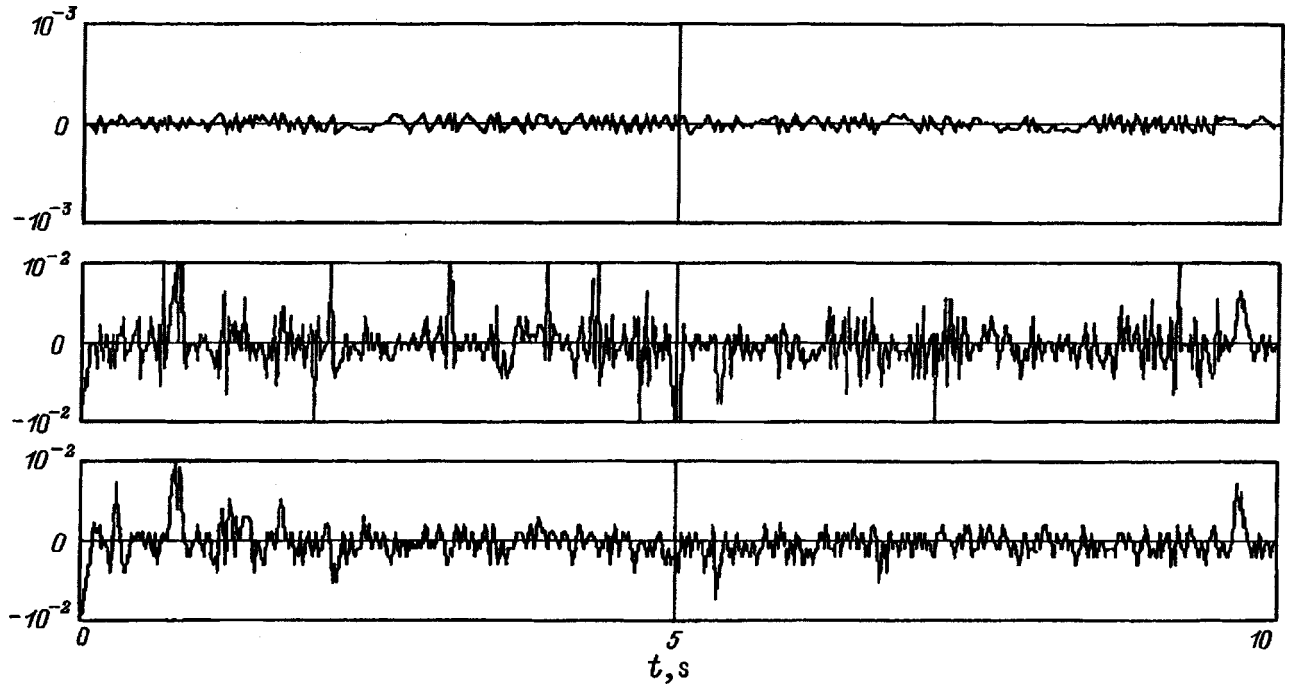

FIG. 4. Experimental results of operation of the correlative automatic noise-compensation (CANC) system.

and $u_2(t)$, as illustrated in Fig. 3, which shows the time variations of $u_1(t)$ in the upper part and of $u_2(t)$ in the upper part for the case when the base of the interferometer is subjected to a mechanical (shock) disturbance.

The newly developed CANC system has been tested in a real experiment, with the protective hood in place over the pentagonal interferometer. A phase modulator placed between the beam-splitting cubes *2* and *12* in the reference beam automatically maintained the value of $u_2(t)$ close to zero, inducing correlated phase variations in both channels.

Figure 4 shows the experimental results of operating the CANC system. The second and third traces show the phase variations in the inner and outer loops of the pentagonal interferometer [$u_1(t)$ and $u_2(t)$], and the first trace shows the result of correlation processing [$U_\Sigma(t)$]. It is evident from the figure that the phase noise in both channels, having an amplitude from 0.5×10^{-2}rad to 10^{-2}rad, is reduced to 10^{-4}rad, i.e., by almost two orders of magnitude, as a result of correlation processing. The remaining uncorrelated noise is mainly attributable to fluctuations of the air density under the protective hood in the parts of the outer and inner interferometer loops that are not common paths of light propagation. This noise can be eliminated by placing the pentagonal interferometer in a vacuum chamber.

CONCLUSION

As part of the Dulkyn Project for the detection of periodic gravitational radiation in the Joint Experimental Laboratory, an original interferometer representing a passive version of a compact gravitational-wave detector has been assembled and adjusted, resulting in the development of a procedure for the adjustment of a pentagonal, two-loop optical cavity with reflective diffraction elements and for testing the correlation of noise-induced phase distortions due to oscillations of the interferometer mirrors. Phase noise has been successfully reduced (to the level of 10^{-4}rad) in the resultant signal channel of the detector by means of a newly developed correlative automatic noise-compensation (CANC) system. The staff of the Joint Experimental Laboratory for Gravitational Optics Research is currently working on the design of an active version of the compact pentagonal gravitational-wave detector.

[1] A. B. Balakin, G. V. Kisun'ko, Z. G. Murzakhanov, and A. F. Skochilov, Dokl. Akad. Nauk **346**, 39 (1996) [Phys. Dokl. **41**, 19 (1996)].
[2] A. R. Agachev *et al.*, Pis'ma Zh. Tekh. Fiz. **20**(22), 27 (1994) [Tech. Phys. Lett. **20**, 901 (1994)].

Translated by James S. Wood

BRIEF COMMUNICATIONS

Choosing the amplitude interval for a proportional counter at a low signal level

P. S. Antsiferov

Institute of Spectroscopy, Russian Academy of Sciences, 142092 Troitsk, Moscow Region, Russia
(Submitted April 22, 1996; resubmitted January 16, 1997)
Zh. Tekh. Fiz. **68**, 126–127 (May 1998)

A procedure is described for choosing the optimum pulse amplitude interval for a proportional counter when the useful signal level is comparable with the natural background level. It is shown that the optimum interval for counter pulses having a Gaussian amplitude distribution function corresponds to 1.4σ. The application of the procedure is demonstrated in a test example with processing of the iron K_α x-ray spectrum. © *1998 American Institute of Physics.* [S1063-7842(98)02405-2]

Here we discuss an optimal — from the standpoint of signal-to-noise ratio (SNR) — signal-processing procedure for an x-ray proportional counter. The need for such a procedure arises, for example, in experiments on the x-ray spectra of multiply charged ions generated in an electron-beam trap, where the proportional counter detects the output signal of an x-ray monochromator.[1,2] If the counting rate is comparable with the background-level counting rate of the instrument, the latter being associated with cosmic rays as a rule,[3] an additional continuous spectral background is recorded as the monochromator scans a spectral line. This background is punctuated by Poisson fluctuations, and if the amplitude of the line is commensurate with, or lower than the magnitude of such fluctuations, spectral information is lost. Let $i(E_0,A)$ be the amplitude response function of the counter for photons of energy E_0 (E_0 is determined by the monochromator; A is the instantaneous amplitude of the counter pulse). Here we submit the problem of how to choose the requisite amplitude interval A_1-A_2 in which to accept and count the counter pulses so as to maximize the SNR in the resulting spectrum.

The variance of the background noise is proportional to $(N_n)^{1/2}$, where N_n is the average number of noise pulses at the spectral point in question. When the width of the distribution $f(E_0,A)$ is considerably smaller than the amplitude A_0 at which f attains a maximum, we can assume that $N_n \sim |A_2-A_1|$. On the other hand, the number of detected counter pulses associated with the useful signal is proportional to the quantity S:

$$S=\int_{A_1}^{A_2} f(E_0,A)\,dA. \tag{1}$$

In the case $S \leqslant N_n$, therefore, the SNR is proportional to the quantity R:

$$R=S/\sqrt{N_n}. \tag{2}$$

The condition of maximum R yields the system of equations

$$2f(E_0,A_2)(A_2-A_1)=\int_{A_1}^{A_2} f(E_0,A)\,dA,$$

$$2f(E_0,A_1)(A_2-A_1)=\int_{A_1}^{A_2} f(E_0,A)\,dA. \tag{3}$$

If the amplitude response function is symmetrical with maximum $A_0 \sim E_0$ (as is usually the case for $E_0 > 1\,\text{keV}$), the issue becomes the selection of a symmetrical interval $A_0 \pm \Delta A$, where ΔA is given by the equation

$$4f(E_0,A_0+\Delta A)=\int_{A_0-\Delta A}^{A_0+\Delta A} f(E_0,A)\,dA. \tag{4}$$

Numerical calculations for f having a Gaussian profile with average A_0 and standard deviation σ give $\Delta A = 1.4\sigma$.

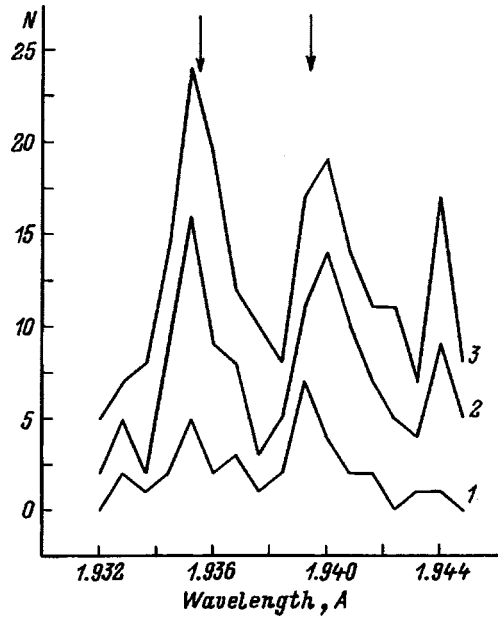

FIG. 1. Spectrogram of the iron $K_{\alpha 1,2}$ doublet, obtained at a low signal level. Amplitude intervals chosen for the counter pulses: *1*) $\Delta A = 0.5\sigma$; *2*) $\Delta A = 1.4\sigma$; *3*) $\Delta A = 3\sigma$.

TABLE I.

Background level, photons/div		Amplitude interval $\Delta A=0.5\sigma$	$\Delta A=1.4\sigma$	$\Delta A=3\sigma$
		0.4	3.7	7.5
$K_{\alpha 1}$	σ_L/L	0.94	0.79	0.82
$K_{\alpha 1}$	σ_W/W	0.6	0.47	0.57
$K_{\alpha 2}$	σ_L/L	0.83	0.79	0.97
$K_{\alpha 2}$	σ_W/W	0.58	0.48	0.55

To illustrate the procedure, we have performed a test experiment, using an x-ray monochromator[2] to record the spectrum of the iron $K_{\alpha 1,2}$ doublet ($\lambda \cong 1.94$ Å) excited in an x-ray tube. The radiation intensity of the tube was specifically reduced to a level such that the counting rate used in the monochromator of the SRM 19 x-ray proportional counter would be of the same order as its noise level. The amplitude response function of the counter to the iron K_α photon energy was determined in a separate calibration measurement with the ratio σ/A_0 equal to 0.12. Figure 1 shows spectrograms corresponding to the counter pulse amplitudes chosen for monochromator scanning from the intervals $\Delta A=0.5\sigma$, $\Delta A=1.4\sigma$, and $\Delta A=3\sigma$. Clearly, increasing ΔA from 1.4σ to 3σ causes the background to increase without changing the signal amplitudes in the lines themselves. The spectrograms were processed by the maximum-likelihood method,[4] which was used to approximate the experimental data by a sum of two Lorentzian profiles: $L/[(\lambda-\lambda_0)^2+(W/2)^2]$. The background level, the positions of the centers, the heights of the maxima L, and the widths W of both lines were determined, along with the standard deviations of these parameters. The representative characteristics for our purposes are the relative standard deviations σ_L/L and σ_W/W, which are shown in Table I together with the measured background level. The relative standard deviations are a minimum for $\Delta A=1.4\sigma$, demonstrating the adequacy of the given procedure for choosing the proper interval of pulse amplitudes for the x-ray proportional counter.

The author is grateful to K. N. Koshelev for valuable discussions and assistance with the study.

This work has received support from Grant No. 95-02-05810a of the Russian Fund for Fundamental Research (RFFI).

[1] P. S. Antsiferov and V. G. Movshev, Z. Phys. D **21**, Suppl., pp. 317–318 (1991).
[2] P. S. Antsiferov, Zh. Tekh. Fiz. **65**(5), 168 (1995) [Tech. Phys. **40**, 499 (1995)].
[3] E. Fünfert and H. Neuert, *Zählröhre und Szintillationzähler: Messmethoden für die Strahlung der künstlichen und natürlich-radioaktiven Substanzen* (*Radiation and Scintillation Counters: Radiation Measurement Techniques for Synthetic and Naturally Radioactive Substances*), 2nd ed. (G. Braun, Karlruhe, 1959; Gos. Izd. Lit. Obl. At. Nauki Tekh., Moscow, 1961).
[4] L. Janossy, *Theory and Practice of the Evaluation of Measurements* (Clarendon Press, Oxford, 1965; Mir, Moscow, 1965).

Translated by James S. Wood

Solving elastic plane problems involving the effect of Lorentz forces on conductors carrying a uniform current

E. A. Devyatkin

Institute of Problems in Mechanics, Russian Academy of Sciences, 117526 Moscow, Russia
(Submitted September 12, 1997)
Zh. Tekh. Fiz. **68**, 128–129 (May 1998)

It is shown that the solution of the first fundamental problem of the linear theory of elasticity in regard to the effect of the Lorentz force on a long conductor carrying a uniform longitudinal current in a magnetic field having an *a priori* unknown distribution can be reduced to the solution of homogeneous equations. © *1998 American Institute of Physics.* [S1063-7842(98)02505-7]

In calculations of the stress state of conductors under the influence of Lorentz forces the magnetic field in the region occupied by the currents is calculated (if not already known), along with the spatial distribution of the body forces. The standard method for solving the first fundamental problem of the linear theory of elasticity is to find a particular solution of the inhomogeneous equations and to reduce them to homogeneous equations. The determination of a particular solution in the general case of a conductor of complex configuration or a complex distribution of the external field (or both) can pose a none too simple, if not unsolvable problem. However, for the planar problem of Lorentz forces acting on a long conductor of arbitrary cross section with a uniform current flowing along it, the Maxwell stress tensor can be used to find a particular solution of the inhomogeneous equations without having to calculate the fields. A procedure for finding such a solution is set forth below.

We consider a long, nonferromagnetic, linearly elastic, isotropic, homogeneous conductor carrying a current of density **j** uniformly distributed over its cross section; it resides in a magnetic field with an induction **B**. Let the z axis of a Cartesian coordinate system xyz be directed parallel to the generatrix of the conductor surface, let its transverse cross section be a simply connected region with boundary Γ, and let the external magnetic field $\mathbf{B}_a$, like the field $\mathbf{B}_j$ of the conductor currents, be independent of the coordinate z, i.e., $\mathbf{B}_a=\mathbf{B}_a(x,y)$ and $\mathbf{B}_j=\mathbf{B}_j(x,y)$. Consequently, the Lorentz force acting on the conductor, $\mathbf{f}=\mathbf{j}\times\mathbf{B}$ ($\mathbf{B}=\mathbf{B}_a+\mathbf{B}_j$), is also independent of z. We assume that the conductor is in a plane strain state and that an external load **P** is applied to its lateral surface, equalizing the body forces **f** (unless they are self-equalizing).

The equilibrium and compatibility equations and the boundary conditions for the given situation have the form[1]

$$\sigma_{ij,j}=f_j=0,\ \ \triangle\sigma_{jj}=-\frac{1}{1-\nu}\,\mathrm{div}\mathbf{f}\quad (i,j=x,y), \tag{1}$$

$$P_i=\sigma_{ij}n_j\ \ \text{for } x,y\in\Gamma. \tag{2}$$

Here summation over repeated subscripts is implied, $\triangle$ is the Laplacian operator, ν is Poisson's ratio, and n_j denotes the components of the unit outward normal vector **n** to the surface of the conductor. The comma in the expression $\sigma_{ij,j}$ signifies differentiation with respect to the coordinate following it. For plane strain we have $\sigma_{zz}=\nu(\sigma_{xx}+\sigma_{yy})$.

The Maxwell stress tensor S_{ij} for a nonferromagnetic medium can be written in the form[2]

$$S_{ij}=\mu_0^{-1}\left(B_iB_j-\delta_{ij}\frac{B^2}{2}\right), \tag{3}$$

where δ_{ij} is the Kronecker delta, and μ_0 is the magnetic permeability of free space.

The tensor S_{ij} satisfies the equilibrium equations ($S_{ij,j}=f_i$) and in general does not satisfy the compatibility equation, because, generally speaking, div $\mathbf{f}\neq 0$. Using Maxwell's equation for nonferromagnetic conductors curl $\mathbf{B}=\mu_0 j$, we obtain div $\mathbf{f}=\mathbf{B}\cdot$curl $\mathbf{j}-\mu_0 j^2$. If $j=$const, then div $\mathbf{f}=-\mu_0 j^2$. We seek a solution of Eqs. (1) in the form $\sigma_{ij}=\tilde{\sigma}_{ij}-S_{ij}$. In the compatibility equation we have $\sigma_{jj}=\sigma_{xx}+\sigma_{yy}=\tilde{\sigma}_{xx}-S_{xx}+\tilde{\sigma}_{yy}-S_{yy}=\tilde{\sigma}_{xx}+\tilde{\sigma}_{yy}$, since[1)] $S_{xx}=-S_{yy}=(B_x^2-B_y^2)/(2\mu_0)$. For the stresses $\tilde{\sigma}_{ij}$ we then obtain from (1) equilibrium equations without body forces and a compatibility equation with a constant right-hand side:

$$\tilde{\sigma}_{ij,j}=0,\quad \triangle\tilde{\sigma}_{jj}=\frac{\mu_0 j^2}{1-\nu}. \tag{4}$$

The boundary conditions (2) now assume the form

$$P_i+S_{ij}n_j=\tilde{\sigma}_{ij}n_j\ \ \text{for}\ \ x,y\in\Gamma. \tag{5}$$

For the longitudinal stresses we have $\tilde{\sigma}_{zz}=\nu(\tilde{\sigma}_{xx}+\tilde{\sigma}_{yy})$.

If for problem (4), (5) we introduce Airy's function φ, which is related to the stress components $\tilde{\sigma}_{ij}$ by the equations $\tilde{\sigma}_{xx}=\varphi_{,yy}$, $\tilde{\sigma}_{yy}=\varphi_{,xx}$, and $\tilde{\sigma}_{xy}=\varphi_{,xy}$, the equilibrium equations are then satisfied, and from the compatibility equation we obtain the inhomogeneous equation with a constant right-hand side

$$\triangle\triangle\varphi=\frac{\mu_0 j^2}{1-\nu}. \tag{6}$$

The solutions of Eq. (6) are well known in application to problems in the static bending of plates (see, e.g., Ref. 3 and the literature cited therein), where its right side represents the distribution of the density of the external force acting on the plate. Choosing a particular solution $\varphi^{(0)}$ of Eq. (6) corre-

sponding to stresses $\tilde{\sigma}_{ij}^{(0)}$ and writing the solution of the basic problem (1), (2) in the form $\sigma_{ij}=\tilde{\sigma}_{ij}+\tilde{\sigma}_{ij}^{(0)}-S_{ij}$, for the stresses $\tilde{\sigma}_{ij}$ we have equilibrium and compatibility equations without body forces (i.e., their stress function is biharmonic) and boundary conditions in the form

$$P_i+(S_{ij}-\tilde{\sigma}_{ij}^{(0)})n_j=\tilde{\sigma}_{ij}n_i \quad \text{for} \quad x,y\in\Gamma. \tag{7}$$

Thus the initial inhomogeneous problem for any magnetic field distribution satisfying Maxwell's equations for nonferromagnetic conductors can be reduced to the case in which volume forces are absent. For $B_a \gg B_j$ one can assume that $\mathbf{f}=\mathbf{j}\times\mathbf{B}_a$. Consequently, div $\mathbf{f}=0$ (since inside the conductor $j=\text{const}$, curl $\mathbf{B}_a=0$), and in this case the tensor $-S_{ij}$ is a solution of equations (1). In the case of a known external field one does not need to calculate the field $\mathbf{B}_j$ in all regions of the conductor in order to determine the stress at a point in the conductor where $\mathbf{B}_j=0$; it is sufficient to know the values on the boundary.

If we require that the components of the tensor $\tilde{\sigma}_{ij}^{(0)}$ normal and tangential to the boundary Γ be equal to zero at the boundary, the form of the boundary conditions (7) is simplified. A suitable candidate for such a particular solution of Eq. (6) for a conductor of radius R is the function $\varphi^{(0)}=\mu_0 j^2(r^2-R^2)^2/[64(1-\nu)]$ ($r^2=x^2+y^2$) (Refs. 1 and 4) used in the problem of the transverse bending of an edge-clamped circular plate under the influence of a load distributed uniformly on it. The corresponding stress components in polar coordinates are $\tilde{\sigma}_{rr}^{(0)}=\mu_0 j^2(r^2-R^2)/[16(1-\nu)]$, $\tilde{\sigma}_{\Theta\Theta}^{(0)}=\mu_0 j^2(3r^2-R^2)/[16(1-\nu)]$, $\tilde{\sigma}_{r\Theta}^{(0)}=0$. At the boundary we have $\tilde{\sigma}_{rr}^{(0)}(R)=0$, $\tilde{\sigma}_{r\Theta}^{(0)}\equiv 0$, and the boundary conditions assume the form $\tilde{\sigma}_{rr}(R)=P_r(R)+S_{rr}(R)$, $\tilde{\sigma}_{r\Theta}(R)=P_\Theta(R)+S_{r\Theta}(R)$. Using this solution, we can readily determine the stresses in a circular conductor when the current flowing along it interacts with its self-magnetic field ($\mathbf{P}=0$, $\mathbf{B}_a=0$). The field of the current has only a circular component and in the conductor is equal to $B_j=\mu_0 jr/2$. We write the solution of the problem in the form $\sigma_{rr}=\tilde{\sigma}_{rr}+\tilde{\sigma}_{rr}^{(0)}-S_{rr}$, $\sigma_{\Theta\Theta}=\tilde{\sigma}_{\Theta\Theta}+\tilde{\sigma}_{\Theta\Theta}^{(0)}-S_{\Theta\Theta}$, $\sigma_{r\Theta}=\tilde{\sigma}_{r\Theta}-S_{r\Theta}$. The diagonal elements of the Maxwell stress tensor are equal to the energy densities of the magnetic field $W=-S_{rr}=S_{\Theta\Theta}=B_j^2/(2\mu_0)$, and $S_{r\Theta}=0$. The solution $\tilde{\sigma}_{ij}$ (where $i,j=r,\Theta$) must satisfy the equilibrium and compatibility equations without body forces and boundary conditions with a uniformly distributed pressure $\tilde{\sigma}_{rr}(R)=S_{rr}(R)=W(R)$, $\tilde{\sigma}_{r\Theta}(R)=0$. Such a solution is $\tilde{\sigma}_{rr}(R)=\tilde{\sigma}_{\Theta\Theta}=-W(R)$, $\tilde{\sigma}_{r\Theta}=0$ (Refs. 1 and 4), i.e., we have a constant hydrostatic pressure (the so-called hydrostatic solution). We finally obtain $\sigma_{rr}=\mu_0 j^2(3-2\nu)\times(R^2-r^2)/[16(1-\nu)]$, $\sigma_{\Theta\Theta}=-\mu_0 j^2[(3-2\nu)R^2-(1+2\nu)r^2]/[16(1-\nu)]$, $\sigma_{r\Theta}=0$, which coincides with the solution obtained in Ref. 5. This example is analogous to the familiar rotating cylinder problem, in which the inertial term also depends linearly on r (see, e.g., Ref. 4).

The results can be applied to the solution of planar elasticity problem by numerical methods and to the solution of inverse problems.

[1)] We assume without loss of generality that the magnetic field does not have a longitudinal component ($B_{az}=0$).

[1] Yu. A. Amenzade, *Theory of Elasticity* [in Russian] (Vysshaya Shkola, Moscow, 1976, 272 pp.).
[2] L. D. Landau and E. M. Lifshitz, *Electrodynamics of Continuous Media*, 2nd ed., Pergamon, Press, Oxford–New York (1984); Nauka, Moscow (1982), 620 pp.
[3] L. V. Kantorovich and V. I. Krylow, *Approximate Methods of Higher Analysis* [Wiley, New York, 1964; 5th ed., Fizmatgiz, Moscow, 1962, 708 pp.].
[4] A. E. H. Love, *A Treatise on the Mathematical Theory of Elasticity*, 4th ed. (Cambridge University Press, Cambridge; Macmillan, London (1927); reprint, Dover, New York (1944); ONTI, Moscow-Leningrad (1935), 674 pp.
[5] A. A. Kuznetsov, Zh. Tekh. Fiz. **30**, 589 (1960) [Sov. Phys. Tech. Phys. **5**, 552 (1960)].

Translated by James S. Wood

Influence of relaxation on the profile of a nonlinear acoustic pulse

G. T. Adamashvili

Iv. Dzhavakhishvili Tbilisi State University, 380028 Tbilisi, Georgia
(Submitted September 12, 1997)
Zh. Tekh. Fiz. **68**, 130–131 (May 1998)

The influence of transverse relaxation on a nonlinear acoustic wave generated in the presence of the acoustic self-induced transparency (SIT) phenomenon is investigated. An explicit analytical equation for the profile of the nonlinear acoustic wave is derived by a perturbation theory developed on the basis of the inverse scattering problem. This equation provides a possible means for investigating experimentally the profile of an acoustic SIT pulse with allowance for relaxation effects, so that these results can be used to construct new types of acoustoelectronic devices. © *1998 American Institute of Physics.* [S1063-7842(98)02605-1]

The acoustic self-induced transparency (SIT) phenomenon refers to the enhancement of the acoustic transmission of a resonant medium under the influence of an acoustic pulse whose intensity exceeds a threshold value and whose duration is shorter than the irreversible relaxation time. Such a pulse is characterized by a long delay time in the medium and distortion of its profile.[1] A model in which the irreversible relaxation times are assumed to be indefinitely large[2] is often used in the theoretical investigation of acoustic self-induced transparency. The influence of relaxation effects on a nonlinear acoustic SIT pulse has been analyzed[3] by a perturbation theory developed on the basis of the inverse scattering method. This method utilizes the auxiliary Zakharov–Shabat spectral problem.[4] In Ref. 3 the influence of relaxation effects on the discrete spectrum of scattering data of the Zakharov–Shabat problem has been investigated, and the variations of the velocity, amplitude, instantaneous frequency, and phase of the relaxation-induced nonlinear acoustic wave has been calculated. It has been proved[5] that allowance for transverse scattering in the presence of inhomogeneous spectral line broadening leads to the excitation of a continuous spectrum of scattering data, and this phenomenon changes the profile of a nonlinear optical wave. The same result is equally valid for an acoustic pulse generated in the presence of acoustic self-induced transparency. The objective of the present study is to derive explicit analytical equations for the profile of an acoustic SIT wave with transverse relaxation effects taken into account.

To provide a simple model that can be used to investigate the influence of transverse relaxation on a nonlinear wave profile, we consider a nonmetallic, diamagnetic crystal of cubic symmetry containing a small concentration of paramagnetic impurities with an effective spin $S=1/2$. We assume that a transversely polarized acoustic pulse of frequency ω, wave vector $\mathbf{k}$, and duration T propagates along one of the fourfold axes (the z axis). A static magnetic field $\mathbf{H}_0$ is applied in the same direction. We also assume that the pulse exists in resonance with the paramagnetic impurities. We consider the criterion of coherent interaction of the pulse with the medium to be satisfied: $T \ll T_{1,2}$, $\omega T \gg 1$ (Refs. 1 and 2), where T_1 and T_2 are the longitudinal and transverse relaxation times of the paramagnetic impurities. In this situation acoustic self-induced transparency can be described by a system comprising the Bloch equations and a wave equation, which for slow variables ρ^+ and q has the form

$$\frac{\partial \rho^+}{\partial \tau}=i\Delta\omega\rho^+-2r\langle S^z\rangle-\frac{\rho^+}{T_2},\quad \frac{\partial\langle S^z\rangle}{\partial\tau}=r\rho^--q\rho^+,$$

$$\frac{\partial q}{\partial z}=\varkappa\int_{-\infty}^{+\infty}g(\Delta\omega)\rho^-(\Delta\omega)d\Delta\omega,\quad \varkappa=\frac{L^2n\omega}{8\rho v^3\hbar}. \qquad (1)$$

The quantities $\rho^\pm$, r, and q are determined from the relations

$$\langle S^\pm\rangle=\pm i\rho^\pm\exp[\pm i(\omega t-kz)],\quad q=-r^*=-\frac{L}{2\hbar}\mathcal{E}^-,$$

$$\varepsilon^\pm=\varepsilon_{xz}\pm i\varepsilon_{yz}=\mathcal{E}^\pm\exp[\pm i(\omega t-kz)],$$

$$L=\beta H_0F_{xzxz},$$

$$F_{xzxz}=F_{yzyz},\quad \tau=t-(z/v),\quad \Delta\omega=\omega_0-\omega,$$

where ε_{xz}, ε_{yz}, and F_{xzxz} are the components of the strain and spin–phonon coupling tensors, $\langle S^{\pm,z}\rangle$ are the average values of the operator variables $S^{\pm,z}$, β is the Bohr magneton, v is the sound velocity at the point $z=0$, ω_0 is the resonance frequency of the paramagnetic impurities, $\hbar$ is Planck's constant, $g(\Delta\omega)$ is the normalized inhomogeneous broadening function of the spectral line of electron-acoustic resonance, ρ is the density of the crystal, and n is the number of paramagnetic impurities per unit volume.

The system of equations (1) is valid when the longitudinal relaxation time is much longer than the transverse relaxation, assuming here that $T_1\to\infty$. To determine the profile of the nonlinear acoustic SIT wave, it is necessary to first determine the explicit form of the continuous spectrum (the ''reflection coefficient'') R of the auxiliary Zakharov–Shabat spectral problem, taking transverse relaxation into account. Following the scheme proposed in Ref. 5, we find that in the simplest case, where a pulse having the profile of an acoustic SIT soliton is transmitted into the medium, the reflection coefficient $R(z=0)=0$, whereupon the explicit equation for

the profile of the nonlinear acoustic SIT wave, taking transverse relaxation into account, assumes the form

$$q=-4\eta b\frac{\exp[-2(\eta+i\xi)\tau]}{z}+\frac{T}{T_2}\frac{4\pi^2\eta_0^2 n\exp[i(\beta_0-2\xi\tau)]}{3z^2}\times\left\{\frac{\langle f(\xi)\rangle(z-2)^2}{iB-8\pi\eta C}\left[\exp\left(i\frac{B}{8\pi\eta}z\right)-\exp(Cz)\right]-\frac{4\langle f(\xi)\rangle^*\exp\left[4\eta(\tau_0-\tau)+\frac{Bz}{4\pi\eta}\right]}{iB+8\pi\eta C^*}\times\left[\exp\left(-i\frac{B}{8\pi\eta}z\right)-\exp(C^*z)\right]\right\}, \quad (2)$$

where

$$\langle f(\xi)\rangle=8\varkappa\times\int\frac{2\xi^2+2\xi\xi_1-4\xi\xi_1^*-3(\xi_1-\xi_1^*)\Delta\omega}{(2\xi-\Delta\omega)(2\xi_1-\Delta\omega)(2\xi_1^*-\Delta\omega)}\times g(\Delta\omega)d\Delta\omega.$$

The quantities ξ, ξ_1, β_0, b, and η are the essence of the discrete spectrum of scattering data of the auxiliary spectral problem. They are defined together with B and C in Ref. 5. Making use of the fact that $\mathrm{Re}C<0$ and $B\sim O(\eta^2T_2^{*2})$, we readily obtain the asymptotic form of q in the limit $z\to\infty$:

$$q(z,\tau)=-2i\eta_0\exp[i(\beta_0-2\xi\tau)]\mathrm{sech}[2\eta(\tau_0-\tau)]-\frac{T}{T_2}\frac{\pi n\eta\langle f(\xi_0)\rangle}{6C(\xi_0)}\{1-2\,\mathrm{sech}^2[2\eta_0(\tau-\tau_0)]\}\times\exp[i(\beta_0-2\xi_0\tau)],$$

where ξ_0 and η_0 are the values of ξ and η at $z=0$.

The quantities $(4\eta_0\hbar)/L$, $1/(2\eta_0)$, $\omega-2\xi_0$, and τ_0 are the amplitude, width, instantaneous frequency, and delay time of the pulse, respectively. The explicit form of the nonlinear wave is simplified in special cases, for example, when the spectral line has a Lorentzian profile:

$$q=-2i\eta_0\exp[i(\beta_0-2\xi\tau)]\mathrm{sech}[2\eta(\tau-\tau_0)]+\frac{T}{T_2}i\pi\eta_0\{1-\mathrm{sech}^2[2\eta_0(\tau-\tau_0)]\}\times\exp[i(\beta_0-2\xi_0\tau)].$$

It is evident from Eqs. (2)–(4) that the inclusion of transverse relaxation effects, as expected, alters the profile of the nonlinear acoustic SIT wave, and these corrections are of the order of T/T_2. Consequently, the allowance for effects of excitation of a continuous spectrum yields a contribution to the nonlinear profile of the same order as the contribution of the discrete spectrum to the amplitude, width, instantaneous frequency, and delay time of the pulse.[5]

We have investigated in detail the case in which a pulse in the form of an acoustic SIT soliton is transmitted into the medium. We note that Eq. (2) can be used to obtain the explicit form of the nonlinear wave when a pulse of arbitrary (with area close to 2π) profile is transmitted into the medium. The explicit equations (2)–(4) obtained here for the profile of an acoustic SIT pulse, combined with the results of Ref. 5, where the influence of transverse relaxation on the amplitude, width, instantaneous frequency, and delay time of the pulse is described, can be used to formulate a total picture of the influence of transverse relaxation on the acoustic self-induced transparency phenomenon.

[1] N. Shiren, Phys. Rev. B **2**, 2471 (1971).
[2] G. T. Adamashvili, Phys. Lett. A **86**, 487 (1981).
[3] G. T. Adamashvili, Phys. Lett. A **95**, 439 (1983).
[4] S. P. Novikov, S. V. Manakov, L. P. Pitaevskiĭ, and V. E. Zakharov, *Theory of Solitons: The Inverse Scattering Method* (Consultants Bureau, New York, 1984; Nauka, Moscow, 1980, 400 pp.).
[5] G. T. Adamashvili, Teor. Mat. Fiz. **75**, 371 (1988).

Translated by James S. Wood

Harmonic generation in microinhomogeneous composites

M. A. Satanin, A. A. Snarskiĭ, K. V. Slichenko, and I. V. Bezsudnov

National Technical University, 252056 Kiev, Ukraine
(Submitted April 3, 1997)
Zh. Tekh. Fiz. **68**, 132–134 (May 1998)

The influence of the microstructure of slightly nonlinear composites on the nonlinear response is investigated. The third-harmonic amplitude is expressed in terms of the fourth moment of the current and the local value of the nonlinear sensitivity tensor of the composite. The general structure of the effective sensitivity tensor is analyzed. The possibility of measuring the components of the tensor experimentally is discussed. © *1998 American Institute of Physics.* [S1063-7842(98)02705-6]

The investigation of nonlinear phenomena in composites can yield important information about the microscopic structure of materials.[1] Several authors[2,3] have commented on the nonuniversality of the nonlinear behavior of systems in the critical region and the sensitivity of the critical indices to the microgeometry of a random medium. Recently a profound interrelationship has been observed between the nonlinear conductivity, the $1/f$ noise factor, and third-harmonic generation[3–8] in slightly nonlinear media. It has been found that these quantities can be expressed in terms of correlation functions of the electric field $\langle e^4 \rangle$ and the current $\langle j^4 \rangle$. The study of the behavior of the higher moments and their divergences can provide additional information on the structure of composites.[9] The most practical method for the investigation of nonlinear properties lies in the generation and measurement of the third harmonic. At the present time an expression for the third-harmonic amplitude is known only for a locally isotropic random medium.[3,8]

In this paper we derive a general expression for the third-harmonic amplitude, taking into account the local microstructure of the composite. As an example, we consider a composite consisting of microscopic particles of carbon dissolved in a polymer. The crystallographic axes of the polycrystals are randomly oriented in this system. There are also numerous well-known examples involving real textured films and bulk samples whose constituent microcomponents have a highly preferred orientation of the axes.[1] We are interested in nonlinear effects in such a substance, harmonic generation in particular. In the linear approximation the field and the current are related by the equation

$$e_\alpha = \rho_{\alpha\beta} j_\beta, \tag{1}$$

where $\rho_{\alpha\beta}$ is the local resistance tensor of the composite.

Summation over repeated indices is tacitly understood unless stated otherwise. The components of the tensor $\rho_{\alpha\beta}$ (laboratory coordinate system) can be expressed in terms of the corresponding components in a moving coordinate system, $\rho_{\alpha\beta} = u_{\alpha\gamma}\rho^0_{\gamma\delta}u_{\delta\beta}$, where $u_{\alpha\gamma}$ is a rotation matrix. Whatever the type of texture, we model it by selecting the appropriate distribution of angles describing the rotation matrix $u_{\alpha\gamma}$.

The current and the field obey the equations

$$\operatorname{div} \mathbf{j} = 0, \quad \operatorname{curl} \mathbf{e} = 0. \tag{2}$$

The electric field and the current vary randomly from one point to another in the composite. We introduce their averages over the volume of the system and with respect to the orientations of the microcrystallites:

$$\mathbf{E} = \langle \mathbf{e} \rangle, \quad \mathbf{J} = \langle \mathbf{j} \rangle. \tag{3}$$

The effective resistance for the macroscopic system is an isotropic tensor $\rho^e_{\alpha\beta} = \rho^e \delta_{\alpha\beta}$. The quantity ρ^e is defined by the relation

$$\mathbf{E} = \rho^e \mathbf{J} \tag{4}$$

or by the energy relation

$$\rho^e \mathbf{J}^2 = \langle \rho_{\alpha\beta} j_\alpha j_\beta \rangle. \tag{5}$$

These definitions are equivalent for macroscopic systems.

We now discuss briefly how to describe a nonlinear composite. The physical mechanisms of nonlinearity depend significantly on the material of the microcrystallites. If the microcrystallites represent a metal or a highly doped semiconductor, the electron-temperature approximation can be used. But if the microcrystallites represent a wide-gap dielectric or a lightly doped semiconductor, it is necessary to take into account the activation mechanism underlying the field dependence of the current in these microstructures.

We confine the present study to the weak nonlinearity approximation. In this case each of the above-indicated models reduces to inclusion of the cubic term in the expansion

$$e_\alpha = \rho_{\alpha\beta} j_\beta + k_{\alpha\beta\gamma\delta} j_\beta j_\delta, \tag{6}$$

where $k_{\alpha\beta\gamma\delta}$ is the local nonlinear resistance tensor.

The number of components of the tensor depends on the spatial symmetry of the microcrystal. The number is readily calculated to be 10 for the tetragonal system, possibly 4 for the cubic system, and 11 for the hexagonal system.

Let the sample be connected into an external circuit in such a way that the components of the average current vary according to the law $J_\alpha = J^0_\alpha \cos(\omega_\alpha t)$ (summation over α does not apply here). The local currents also vary with time according to the harmonic law $j_\alpha = j^0_\alpha \cos(\omega_\alpha t)$ (again no summation over α). We obtain a relation between the local

temperature variation due to heating of the electron gas and the local nonlinear resistance tensor. We generalize an expression derived previously[8] for a locally isotropic medium. Forming the balance equation, we obtain

$$\delta T=\frac{1}{\Lambda}\rho_{\alpha\beta}j_\alpha j_\beta, \tag{7}$$

where Λ is the coefficient of heat transfer from electrons to the lattice.

The local variation of the resistance with local variation of the temperature

$$\delta\rho_{\alpha\beta}=\frac{\partial\rho_{\alpha\beta}}{\partial T}\delta T$$

can be written in the form

$$\delta\rho_{\alpha\beta}=h\frac{\partial\rho_{\alpha\beta}}{\partial T}\rho_{\gamma\delta}j_\gamma j_\delta, \tag{8}$$

where $h=1/\Lambda$.

On the other hand, it follows from Eq. (1) that

$$e_\alpha=(\rho_{\alpha\beta}+\delta\rho_{\alpha\beta})j_\beta. \tag{9}$$

Substituting Eq. (8) into (9) and comparing with (6), we find

$$k_{\alpha\beta\gamma\delta}=h\frac{\partial\rho_{\alpha\beta}}{\partial T}\rho_{\gamma\delta}. \tag{10}$$

It should be noted that the nonlinear term in Eq. (6) can have a more general significance than (10), which has been obtained on the basis of a temperature model. Consequently, the local variation of the resistance for a locally anisotropic medium can be written in the form

$$\delta\rho_{\alpha\beta}=k_{\alpha\beta\gamma\delta}j_\gamma j_\delta. \tag{11}$$

Invoking Cohn's theorem,[10] we write the variation of the effective resistance

$$\delta\rho^e\mathbf{J}^2=\langle\delta\rho_{\gamma\delta}j_\gamma j_\delta\rangle. \tag{12}$$

Substituting Eq. (11) into (12), we obtain

$$\delta\rho^e\mathbf{J}^2=\langle k_{\alpha\beta\gamma\delta}j_\alpha j_\beta j_\gamma j_\delta\rangle. \tag{13}$$

Making use of Eq. (13) and the relation

$$E_\nu=(\rho^e+\delta\rho^e)J_\nu, \tag{14}$$

we can write the field correction induced by the weak nonlinearity of the medium:

$$\delta E_\nu=(\langle k_{\alpha\beta\gamma\delta}j_\alpha j_\beta j_\gamma j_\delta\rangle/\mathbf{J}^4)\mathbf{J}^2J_\nu. \tag{15}$$

As mentioned above, this type of relation is valid beyond the temperature model. It also holds in cases where the nonlinearity has a different origin. For example, the nonlinearity can be attributable to a dependence of the electron scattering cross section on the electric field, the influence of the Lorentz force on the carrier paths, etc.

In the locally isotropic case, when

$$k_{\alpha\beta\gamma\delta}=k_s\delta_{\alpha\beta}\delta_{\gamma\delta} \tag{16}$$

and the external current and local currents vary harmonically, Eq. (15) can be used to express the third-harmonic amplitude in the form

$$B_{3\omega}=\langle k_s(j^0)^4\rangle/\langle j^0\rangle^4. \tag{17}$$

Equation (17) coincides with the result of Ref. 8.

It is evident from Eq. (15) that in the first nonlinearity approximation the response function is characterized by a correlation function of the form

$$K=\langle k_{\alpha\beta\gamma\delta}j_\alpha j_\beta j_\gamma j_\delta\rangle/\mathbf{J}^4. \tag{18}$$

Averaging over the positions and orientations of the microcrystallites, we write Eq. (18) in the form

$$K=k^e_{\alpha\beta\gamma\delta}n_\alpha n_\beta n_\gamma n_\delta, \tag{19}$$

where n is a unit vector, which depends on the direction of the average current and the time, $n=\langle j\rangle/|\langle j\rangle|$.

The number of independent components of the effective nonlinear conductivity tensor $k^e_{\alpha\beta\gamma\delta}$ depends on the symmetry of the system. For simplicity we consider only two-dimensional systems, for example, textured films or model systems such as those discussed in Ref. 3. A totally isotropic film is characterized by three independent components $k^e_{xxxx}=k^e_{yyyy}$, $k^e_{xxyy}=k^e_{yyxx}$, $k^e_{xyyx}=k^e_{yxxy}$, and $k^e_{xyxy}=k^e_{yxyx}$, because the additional relation $k^e_{xxxx}=k^e_{xxyy}+k^e_{xyxy}+k^e_{xyyx}$ holds in this case. Consequently, for an isotropic film the correlation function can be written in the form

$$K=k^e_{xxxx}, \tag{20}$$

i.e., harmonic generation is characterized by a single constant $k^e_s=k^e_{xxxx}$, and the third-harmonic amplitude is given by Eq. (17). We note at once that for a texture with hexagonal symmetry the expression for the correlation function coincides with the expression for an isotropic medium.

We now consider the case in which the spatial distribution is homogeneous, and the angular distribution is nonisotropic. The simplest example of this situation can be achieved as described in Ref. 3. Square dielectric inclusions are formed in a conducting matrix. The centers of the inclusions are distributed with equal probability over the plane of the film, and all the squares have the same orientation. For such a medium the tensor $k^e_{\alpha\beta\gamma\delta}$ has four independent components $k^e_{xxxx}=k^e_{yyyy}$, $k^e_{xxyy}=k^e_{yyxx}$, $k^e_{xyyx}=k^e_{yxxy}$, and $k^e_{xyxy}=k^e_{yxyx}$, and the correlation function can be written in the form

$$K=k^e_{xxxx}(n_x^4+n_y^4)+2(k^e_{xxyy}+k^e_{xyxy}+k^e_{xyyx})n_x^2n_y^2. \tag{21}$$

It is useful to transform (21) as follows:

$$K=k^e_s+2k^e_qn_x^2n_y^2, \tag{22}$$

where $k^e_s=k^e_{xxxx}$, and $k^e_q=(k^e_{xxyy}+k^e_{xyxy}+k^e_{xyyx}+k^e_{xxxx})$.

It is evident from Eqs. (17) and (22) that the third-harmonic amplitude depends on the microgeometry of the composite. It is important to note that information on the microgeometry can be obtained by measuring the macroscopic characteristics of the system.

As an example, we discuss a method that can be used to obtain information about the microgeometry of a texture with local cubic symmetry. If the microcomponents of the texture have a nonisotropic distribution, information about it can be extracted by measuring the third harmonic. According to Eqs. (15) and (22), the third-harmonic amplitude can be

expressed in terms of a correlation function involving a combination of four currents and the nonlinear resistance tensor. It is evident form Eq. (22) that the amplitude will contain information about the coefficient k_q. To extract this information, we assume that the external current has two projections onto the coordinate axes. Let the oscillation frequencies of the components be ω_x and ω_y. For this case we substitute Eq. (22) into the response expression (15). It is readily perceived that the response function also contains a combination-frequency mode in addition to the $3\omega_x$ and $3\omega_y$ harmonics. For example, the components of the current along the x axis contain harmonics at the combination frequencies $3\omega_x \pm \omega_y$, etc. The amplitudes of these modes are proportional to the coefficient k_q.

To summarize, the nonlinear response contains additional information about the microgeometry of a random medium. We have shown here that information about a texture can be obtained by measuring a macroscopic characteristic of the system: the third-harmonic amplitude. The predicted functional relations can be tested both on textured films and on model systems.[3] Additional information can be acquired by virtue of the dependence of the amplitude on an external magnetic field. A magnetic field can redistribute the currents in the structure and alter the asymptotic behavior of the fields in the approach to singularities. The higher moments of the field and current are found to be very sensitive to a magnetic field, so that additional information about the microstructure of composites can be extracted by studying the generation of harmonics in a magnetic field. A detailed investigation of the behavior of higher harmonics in a magnetic field is planned.

[1] *Proceedings of the Third International Conference on Electrical Transport and Optical Properties of Inhomogeneous Media*, Physica A **207** (1994).
[2] L. De Arcangelis, S. Reder, and A. Coniglio, Phys. Rev. B **34**, 4656 (1986).
[3] M. A. Dubson, Y. C. Hui, M. B. Wiessman, and J. C. Garland, Phys. Rev. B **39**, 6807 (1986).
[4] A. Aharony, Phys. Rev. Lett. **58**, 2726 (1987).
[5] D. Stroud and P. M. Hui, Phys. Rev. B **37**, 8719 (1988).
[6] D. J. Bergman, Phys. Rev. B **39**, 4548 (1989).
[7] O. Levy and D. J. Bergman, Phys. Rev. B **50**, 3652 (1994).
[8] A. A. Snarskiĭ, Pis'ma Zh. Tekh. Fiz. **21**(1), 3 (1995) [Tech. Phys. Lett. **21**, 1 (1995)].
[9] A. M. Dykhne, V. V. Zosimov, and S. F. Rybak, Dokl. Akad. Nauk **345**, 467 (1995) [Phys. Dokl. **40**, 613 (1995)].
[10] P. Penfield Jr., R. Spence, and S. Duinker, *Tellegen's Ţheorem and Electrical Networks* [MIT Press, Cambridge, Mass., 1970; Énergiya, Moscow, 1974].

Translated by James S. Wood

Regulation of the output energy of a backward-wave linear accelerator by the duration of the rf power pulse

V. V. Kozlyuk

Institute of Chemical Kinetics and Combustion, Siberian Branch of the Russian Academy of Sciences, 630090 Novosibirsk, Russia

(Submitted March 5, 1997)
Zh. Tekh. Fiz. **68**, 135–137 (May 1998)

The problems of regulating the output energy of the accelerated beam of a backward-wave linear proton accelerator over a wide range without altering the beam intensity are investigated. The proton energy is regulated by adjusting the duration of the rf power pulse delivered to the accelerator and by regulating the delay time between the instant of injection and the instant at which the leading edge of the rf pulse arrives at the output end of the accelerator. The method is tested on the interdigital-type accelerating section of length 1.25 m of a linear proton accelerator. It is shown experimentally that the electron beam energy at the accelerator output can be varied approximately threefold without any appreciable sacrifice of the beam intensity by varying the duration of the rf pulse in the given accelerator section. [S1063-7842(98)02805-0]

A useful asset to a linear accelerator functioning as a source of ionizing radiation is the capability of regulating the output energy of the accelerated beam while maintaining a constant beam current.[1] The implementation of such regulation is fairly simple to achieve in multisection resonance machines by tilting individual sections of the accelerator.[2] In application to single-section, traveling-wave linear accelerators energy regulation is achieved by varying the input power, frequency, or phase of the rf power supply.[1,3] However, this technique produces only a slight change in the output energy in the first case, a sharp drop in the accelerated beam current in the second case, and division of the linear accelerator into at least two sections, adding to the structural complexity of the accelerator itself, in the third case.

In the present article we discuss a procedure for regulating the output energy of a backward-wave linear accelerator in such a way as to maintain a constant accelerated beam current.

We consider the interaction of beam-current and rf power pulses in the accelerating section of a backward-wave linear accelerator. In accordance with the scheme of particle acceleration in a backward-wave field,[4] we initially deliver to the accelerating structure an rf power that propagates in the direction of the injector. At the instant when the leading edge of the rf pulse appears at the output of the accelerating system, we activate particle injection. It is clear that the opposing motion of the particles and the wave significantly reduces their interaction time T in comparison with what it would be in any other circumstance. The time T is expressed by the equation[5]

$$T = l\,\frac{V_g + V}{V_g \cdot V}, \tag{1}$$

where l is the spatial particle–wave interaction length, V is the velocity of synchronous beam particles, averaged over the length l, and V_g is the group velocity of the rf power, averaged over the length l.

If we choose $l < L$, the particle energy $W(l)$ is lower than the output energy of the accelerator. It is given by the expression

$$W(l) = e\int_0^1 E(z)\,dz, \tag{2}$$

where e is the electron charge, z is the longitudinal coordinate, and $E(z)$ is the accelerating field in the section.

We set the duration T_p of the rf power pulses equal to T, whereupon beam-wave interaction takes place only in part of the section. Since injection is initiated at the instant of arrival of the leading edge of the rf power pulse at the output of the accelerating system, particle acceleration is initiated from the first cells of the section. The bunching and energy buildup of particles take place in this part of the accelerating system. The accelerator output energy is lower than the energy that could be attained over the entire length of the section. Consequently, by varying the duration T, in effect, we vary the length of the accelerating system beginning at the injection end, wherein the wave interacts with the beam, and therefore vary the output particle energy as well.

It is important to note that the energies of accelerated particles situated at the beginning and end of the injection pulse differ on account of the difference in the duration of their interaction with the oncoming stream of rf power pulses. Particles situated in the vicinity of the leading edge of the beam current are accelerated during a time period equal to the duration of the rf power pulse. Consequently, they build up the maximum energy. But here rf power is extracted from the accelerating system. Subsequent particles no longer interact with this part of the rf pulse and therefore accumulate less energy. Particles situated in the zone of the trailing

TABLE I.

T, ns	V, m/s	V_g, m/s	l, mm	W, MeV	W, eV	W_{exp}, eV
160	1.38×10^7	1.58×10^7	1252	1.9	1035	1040
140	1.3×10^7	1.55×10^7	1064	1.49	812	880
120	1.22×10^7	1.51×10^7	884	1.14	621	670
100	1.1×10^7	1.46×10^7	714	0.89	485	500
80	1.06×10^7	1.43×10^7	561	0.7	381	390

edge of the beam current are accelerated for a time period equal to the duration of the rf pulse minus the injection pulse. Consequently, they build up the lowest energy of all particles in the pulse. To diminish this energy difference, it is necessary to use the shortest possible injection current pulses. However, an energy difference in the beam-current pulse is a fundamentally unavoidable drawback of the given technique for regulating the output energy of a linear accelerator. If we make $l>L$, the rf power fills up the entire accelerating system throughout the total time of acceleration of the beam-current pulses. The particle energy becomes equal to the accelerator output energy W_0 and no longer increases with any further increase in the duration T. The beam is accelerated as in the conventional accelerator operating regime.

If the beam-current pulses are injected before the leading edge of the rf pulses reach the output of the accelerating system, these pulses meet inside the section, where wave-particle synchronism is generally lacking. As a result of the loss of synchronism the beam is not accelerated, and any discussion of regulating the output energy is meaningless under the circumstances.

The pulse durations T required to regulate the accelerator energy are usually of the order of hundreds or even tens of nanoseconds. The generation of such pulses at a high rf power level is not a simple engineering problem. The difficulty can be circumvented by increasing the duration T_{p} of the rf pulses to microsecond values. In this case injection does not take place at the instant of arrival of the leading edge of the rf pulses at the output of the accelerating system, but after a finite delay time τ. As mentioned above, the accumulation of energy by particles in the accelerating system is proportional to T. In the given situation $T=T_{\text{p}}-\tau$, and this time can be regulated by varying the duration T_{p} of the rf power pulses or by varying the injection delay time τ.

The technique has been tested experimentally by electronic simulation on the interdigital-type accelerating system of a backward-wave linear proton accelerator. The length of the system is 1.25 m, the initial energy is 385 keV (210 eV), and the final energy is $W_0=1.9$MeV (1035 eV). The theoretical-design pulsed rf power delivered to the accelerating system is 180 kW (54 mW). The figures in parentheses give the values of the parameters of the pulsed electronic model used to represent the proton accelerator in testing the technique. The duration of the injection current pulses was 10 ns, and the accelerated beam current had a value in the interval $10-12\mu$A. The duration T of the rf pulses was regulated in the range 80–160 ns. The rf power pulses had a trapezoidal profile with leading and trailing

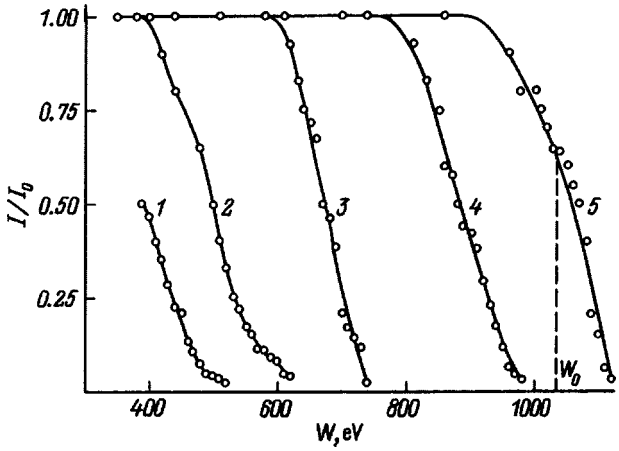

FIG. 1. Relative beam current versus beam energy for various rf power pulse durations. *1*) $T=80$ns; *2*) 100 ns; *3*) 120 ns; *4*) 140 ns; *5*) 160 ns; I_0 denotes the accelerated beam current.

edges of duration 10–15 ns each. Particles were injected into the section at the instant when the leading edge of the rf power pulse reached the output of accelerating system. The error of this synchronization, allowing for the finite spread of the leading edges of the beam-current and rf power pulses, did not exceed 20 ns. The pulsed beam currents were measured by means of a secondary-electron multiplier,[6] and the particle energy was measured by the retarding-potential method.[7]

Table I shows the results of direct measurements and the results of calculations of the output energy of the linear accelerator section. The accelerator output energy (2) was calculated on the basis of Eq. (1) and the results of previously reported[8] measurements of prototype resonance models of accelerating systems.

In the table W MeV denotes the calculated values of the output particle energy of the linear proton accelerator, W eV represents the scaled values of the same energies for the electronic model, and W_{exp} is the measured output energy of the linear accelerator section on the electronic model. A comparison of the last two columns reveals good agreement between the calculated and measured output energies of the linear accelerator. Figure 1 shows delay curves of the relative value of the beam current for the rf power pulse durations given in the table. It is evident that the output particle energy decreases from 1040 eV to 380 eV as T is decreased from 160 ns to 80 ns. The beam current does not vary more than 10% in this case.

In closing, it can be concluded that the output particle energy of a backward-wave linear accelerator can be regulated in such a way as to maintain a constant accelerated beam current. The feasibility of regulating the beam output current while maintaining a constant beam output energy has been demonstrated previously[9] in a similar structure. Consequently, independent control of the output values of the beam energy and current is achieved in the method of backward-wave acceleration of charged particles, thereby extending the possible applications of the method in radiation studies.

[1] Yu. S. Ryabukhin and A. V. Shal'nov, *Accelerated Beams and Their Applications* [in Russian] (Atomizdat, Moscow, 1980), 192 pp.
[2] *Linear Ion Accelerators* [in Russian], Vol. 1, edited by B. P. Murin (Atomizdat, Moscow, 1978), 260 pp.
[3] G. I. Zhileĭko, *High-Voltage Electron Beams* [in Russian] (Énergiya, Moscow, 1968), 240 pp.
[4] A. S. Bogomolov, Dokl. Akad. Nauk SSSR **208**, 1328 (1973) [Sov. Phys. Dokl. **18**, 152 (1973)].
[5] V. V. Kozlyuk, Inventor's Certificate No. 1711349 (USSR) [in Russian]; Byull. Izobret., No. 5 (1992).
[6] A. N. Borisenko, V. V. Kozlyuk, and V. V. Perov, Prib. Tekh. Eksp. No. 2, pp. 133–135 (1988).
[7] F. R. Shul'man and S. A. Fridrikhov, *Secondary-Emission Methods in Solid State Research* [in Russian] (Nauka, Moscow, 1977), 552 pp.
[8] V. V. Perov, V. M. Pavlov, and V. V. Kozlyuk, Vopr. At. Nauki Tekh. Ser. Tekh. Fiz. Éksp. (Kharkov), No. 1/3, 7 (1979).
[9] V. V. Kozlyuk and V. V. Perov, in *Proceedings of the Twelfth All-Union Seminar on Linear Charged-Particle Accelerators* [in Russian] (Kharkov, 1991), p. 116.

Translated by James S. Wood

Experimental study of the resonance reflection of a plane electromagnetic wave from a wide-spaced strip grating

S. N. Vorob'ev

Radioastronomy Institute, Academy of Sciences of Ukraine, 310002 Kharkov, Ukraine

I. K. Kuzmichev

Institute of Radiophysics and Electronics, National Academy of Sciences of Ukraine, 310085 Kharkov, Ukraine

(Submitted April 15, 1996)
Zh. Tekh. Fiz. **68**, 138–140 (May 1998)

The resonance reflection of a plane electromagnetic wave from a diffraction grating consisting of wide-spaced, thin, tilted metal strips is confirmed and investigated experimentally. Good agreement is obtained between the experimental results and published theoretical data. © *1998 American Institute of Physics.* [S1063-7842(98)02905-5]

Electromagnetic fields scattered by gratings of identical thin metal strips have properties that qualify such structures for successful applications in antenna technology and microwave devices. The uses of strip gratings as selective elements are quite diverse.[1–5] In particular, a grating of tilted metal strips can be used as a directional coupler or semitransparent screen with an adjustable separation level, which can range essentially from zero to one, depending on the ratio between the width of the strips, their tilt angle relative to the plane of the grating, and the period of the latter. The reflection of waves from the grating has a distinct resonance character, because it is caused by interference interaction of the fields in the zones between the strips.

The phenomenon of total resonance reflection of a TE-polarized plane wave from a wide-spaced tilted-strip grating has been discovered on the basis of a rigorous solution of the problem of electromagnetic wave diffraction by a periodic grating[6] and has been further investigated in a subsequent paper.[7] The objective of the present study is to test experimentally the existence of such resonances in real equidistant gratings and to assess the accuracy of agreement of the theoretical results with the practical data. These results can then be used to evaluate the validity of the assumptions underlying the mathematical model of the grating (ideal conductivity and infinitely thin strips) and eventually, working in the resonance reflection regime, to design complex electrodynamic systems operating in the millimeter wavelength range.

Total-reflection resonance in an infinite periodic grating is interpreted as a phenomenon in which a plane wave normally incident on the grating excites two normal modes of the structure, which propagate along the grating (i.e., in the direction perpendicular to the edges of the strips) in opposite directions to each other. Consequently, a high-Q standing-wave regime is established in the vicinity of the grating, thereby rendering the grating ''insensitive'' to the incident field exciting the normal modes of the structure. In other words, a grating with wide-spaced strips behaves like a perfectly reflecting screen for such a plane wave.[7]

It follows from an earlier numerical analysis[7] that a grating consisting of seven elements with parameters $d/l=0.25$ and $\psi=45°$ ($2d$ is the strip width, l is the period of the grating, and ψ is the strip tilt angle relative to the normal to the plane of the grating) reflects $\sim 80\%$ of the energy of the incident wave, i.e., the modulus of the field reflection coefficient is $|\Gamma|\approx 0.9$. We recall that a necessary condition for the total resonance reflection regime is that the wave spectrum of the periodic grating contain only one, fundamental propagating mode. This condition corresponds to the presence of a single dominant lobe in the directivity pattern of the reflected field for a bounded structure.

For the experimental work a grating was fabricated with parameters $2d=1.835$ mm, $l=3.67$ mm, and $\psi=45°$; the copper-foil strips had a thickness of 0.3 mm (the ratio d/l and the angle ψ coincide with the above-cited data from Ref. 7), and the number of strips was 12 (the grating is illustrated in Fig. 1). This structure comprises a fairly wide-spaced grating (where the open spacing of two strips exceeds the visible width of one strip) without waveguide regions between adjacent strips.[6,7] The number of strips in the grat-

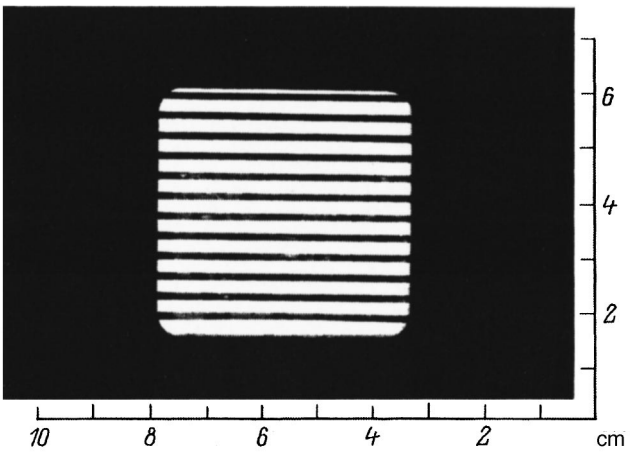

FIG. 1. Wide-spaced tilted-strip grating. The mounting in which the strips are set is coated with an absorbing shield to prevent multiple reflections.

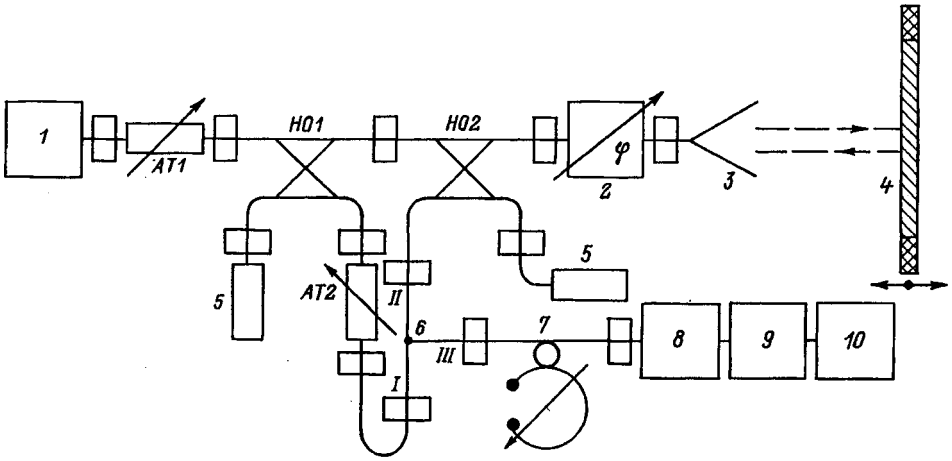

FIG. 2. Block diagram of the experimental and measurement apparatus. *1) G4-142 rf signal generator; 2)* phase shifter; *3*) horn antenna; *4*) baffle containing the investigated grating; *5*) matched load; *6*) three-way E-junction; *7*) wavemeter; *8*) detector section; *9*) measurement amplifier; *10*) oscilloscope; *AT1*) decoupling attenuator; *AT2*) polarization attenuator; *H01,HO2*) directional couplers.

ing was chosen on the basis of the following considerations. First, an equidistant structure with more than ten elements is equivalent, in terms of its electrodynamic characteristics, to an infinite periodic grating within relative error limits $\delta \sim 1\%$ (if the criterion given in Ref. 8 is used to estimate the degree of correspondence), in contrast with a seven-element grating, for which it has been shown[7] that $\delta \sim 12\%$. Hence, the resonance reflection regime on a 12-strip grating is sharper than for a seven-element grating. Moreover, radiation along the grating, which is parasitic in our case, decreases when the number of elements in the structure is increased.[7,8] Second, if such a grating is placed, say, in an open resonator in which the fundamental TEM_{00q} modes exists, the field ''spot'' must ''illuminate'' at least three strips of the structure to excite resonance reflection in the grating. We note that when one of the higher modes (TEM_{20q} or especially TEM_{40q}) is present in the open resonator, the distribution of fields in the plane of the grating greatly exceeds the dimensions of the field spot of the fundamental mode of such a system. Third, it is desirable to investigate a grating of small dimensions (and, accordingly, one without too many strips) if it is to be used subsequently as a constituent element of an electrodynamic system.

The measurements were carried out in the wavelength range $\lambda = 4.0 - 4.6$ mm. A block diagram of the measurement apparatus is shown in Fig. 2. A 50×50 mm grating (Fig. 1) situated in an absorbing baffle is capable of being shifted in the direction perpendicular to the irradiating antenna. The signal reflected from the investigated grating is sent through a phase shifter and a directional coupler *2* (*H02*) to arms *II* and *III* of a three-way E-junction and into the receiving section, which consists of a detector, a measurement amplifier, and an oscilloscope. A wavemeter is included in the receiving section to monitor the frequency of the G4-142 signal generator. The signal on the oscilloscope screen varies sinusoidally as the baffle containing the grating is shifted (Fig. 2) (this effect is associated with reflection from the grating). Repeated reflections from the antenna (a pyramidal horn in this case) and various bodies encountered in its radiation field are eliminated by shielding with absorbent coatings.

The experimental procedure is as follows. The baffle containing the grating is shifted and positioned in such a way as to maximize the reflected signal in arm *III* of the E-junction. The two signals in arm *III* of the E-junction (one reflected from the grating and transmitted into arm *II* of the E-junction, the other a reference signal from the oscillator in arm *I* of the E-junction) are then balanced by means of the second attenuator (*AT2*) and a phase shifter, whereupon the readings of *AT2*, being equal to a_1, are recorded. The next step is to calibrate the measurement apparatus. The investigated grating is replaced by a perfectly reflecting copper sheet, and again the E-junction is balanced by means of the phase shifter and *AT2*, whose readings now have the value a_2. As a result, the modulus of the field reflection coefficient $|\Gamma|$ of the investigated grating is readily calculated from the equation[3,9] $|\Gamma| = 10^{a/20}$, where $a = a_2 - a_1$.

Figure 3 shows the measured values of the reflection coefficient $|\Gamma|$ as a function of the dimensionless frequency parameter $\kappa = l/\lambda$. The small-scale oscillations of the experimentally recorded graph of $|\Gamma(\kappa)|$ (the dots in Fig. 3 represent the measured values of $|\Gamma|$) are most likely induced by unmanageable multiple reflections from objects at some distance from the experimental apparatus. The averaged $|\Gamma(\kappa)|$

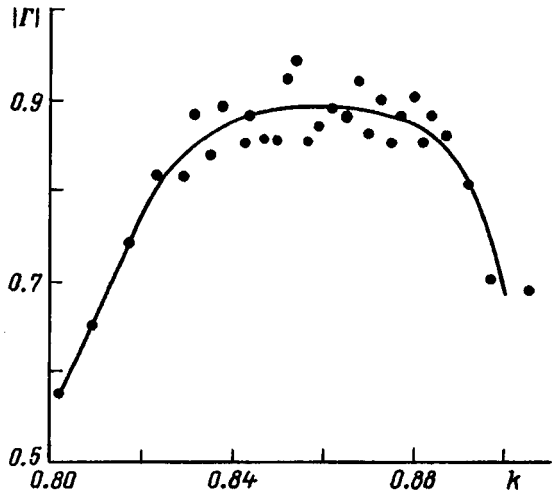

FIG. 3. Modulus of the reflection coefficient $|\Gamma|$ versus frequency parameter κ.

curve, which closely approximates the true dependence, is represented by the solid curve in Fig. 3; it follows from an analysis of this curve that resonance wave reflection occurs in the grating in the frequency interval $\kappa_{\text{refl}}=0.85-0.87$. The measured value of the frequency $\kappa_{\text{refl}}=0.86$ agrees with the value obtained theoretically in Ref. 7 (the discrepancy is less than 5% with allowance for the shift of the calculated value of κ_{refl} for a grating with a large number of strips).

Consequently, the mathematical model of the grating and the wave-scattering processes in it adequately represents the prevalent conditions of the experiment, and the well-known assumptions of the mathematical model can be regarded as validated. The rigorous electrodynamic method used to solve the boundary-value problem in Ref. 7 and the careful execution of the experiment have resulted in good agreement between the calculated and measured physical characteristics of the resonance wave reflection effect.

We note in conclusion that the results of the study offer possibilities for the construction of electrodynamic systems, specifically on the basis of an open resonator, in which a wide-spaced tilted-strip grating (specially positioned in the resonator cavity) functions as a selective control element. The method set forth in Refs. 7 and 8 can be used to perform a preliminary numerical analysis of the wave diffraction processes in such a microwave system, significantly diminishing the volume of subsequent experimental research.

The authors are deeply grateful to S. L. Prosvirnin for steadfast support throughout the course of the study and also for valuable suggestions and remarks tendered in a discussion of the results.

[1] V. P. Shestopalov, L. N. Litvinenko, S. A. Masalov, and V. G. Sologub, *Diffraction of Waves by Gratings* [in Russian], (Izd. KhGU, Kharkov, 1973), 287 pp.
[2] M. Ando and K. Takei, IEEE Trans. Antennas Propag. **AP-35**, 367 (1987).
[3] V. P. Androsov and I. K. Kuz'michev, IRÉ AN Ukr. SSR Preprint No. 355 [in Russian] (Institute of Radiophysics and Electronics, National Academy of Sciences of Ukraine, Kharkov, 1987), 14 pp.
[4] S. S. H. Naqvi and N. C. Gallagher, J. Opt. Soc. Am. A **7**, 1723 (1990).
[5] B. Gimeno, J. L. Cruz, E. A. Navarro, and V. Such, J. Electromagn. Waves Appl. **7**, 1201 (1993).
[6] S. N. Vorob'ev, L. N. Litvinenko, and S. L. Prosvirnin, ZhVVM **26**, 894 (1986).
[7] S. N. Vorob'ev and S. L. Prosvirnin, Zh. Tekh. Fiz. **58**, 458 (1988) [Sov. Phys. Tech. Phys. **33**, 276 (1988)].
[8] S. N. Vorob'ev, Radiotekh. Élektron. **32**, 687 (1987).
[9] Z. Frait and C. E. Patton, Rev. Sci. Instrum. **51**, No. 1092 (1980).

Translated by James S. Wood

Nondestructive deep-level diagnostic method for semi-insulating materials

É. A. Il'ichev

F. V. Lukin State Scientific-Research Institute of Physics Problems, 103460 Moscow, Russia
(Submitted July 18, 1996; resubmitted June 3, 1997)
Zh. Tekh. Fiz. **68**, 141–143 (May 1998)

An original nondestructive method for the local deep-level diagnostics of semi-insulating materials is discussed. The method, called deep-level relaxation optoelectronic spectroscopy (DLROS), is based on the contactless recording of relaxation processes of the electron-hole and trap systems. It can be used to determine the type, energy, and capture cross section of deep energy centers and to establish their distribution in a wafer for integrated-circuit applications. The DLROS method is effective for the production input, interim (between operations), and output monitoring of substrates and GaAs structures. Unlike DLTS, it does not require the fabrication of measurement electrodes on samples. © *1998 American Institute of Physics.* [S1063-7842(98)03005-0]

The widespread application of gallium arsenide and its solid solutions in information technology is hindered by the appreciable variance of the parameters of active integrated circuit elements at different points of the wafer[1] and the virtual impossibility of managing the variations of their threshold characteristics in the presence of light and heat disturbances.[2,3] These difficulties are assumed to be attributable to the sensitivity of the stoichiometric composition of binary systems to technological factors affecting the material during the growth of ingots and epitaxial structures or during technological operations involved in the production of wafers and devices.[4–6] A fundamental distinction of gallium arsenide materials and technologies is the decisive influence of both background-type and specially introduced deep-level energy centers on the parameters of devices and circuits.[7,8] This influence stems from the need to monitor the trap parameters in semi-insulating substrates and device structures in the course of integrated circuit fabrication. Conventional methods for measuring the trap parameters in semiconductors (e.g., deep-level transient spectroscopy — DLTS) are ineffective in studies of semi-insulating materials, because they require the formation of barrier and ohmic contacts on samples, which introduces large distortions in the spectrum of interface energy states in III–V systems. Existing nondestructive diagnostic techniques based on impurity light absorption yield scant information, are time-consuming, and are ill-suited to investigations of device structures running through the technological cycle.

Here we discuss our previously proposed[9] DLROS (deep-level relaxation optoelectronic spectroscopy) method for the local nondestructive diagnostics of trap parameters in semi-insulating materials. It can be used to measure the relaxation times of the electron-hole and trap systems in semiconducting and semi-insulating materials, to determine the type and energetics of deep centers, and to estimate trap densities and capture cross sections. In samples whose trap density N_t is lower than the density of free equilibrium carriers n_0 the method can be used to estimate n_0 and to determine the type of conductivity of the material. The DLROS method entails the contactless recording of relaxation processes of the electron-hole and trap systems in the presence of periodic photoexcitation and quasiequilibrium variation of the sample temperature. The diagnostic technique is rendered nondestructive by placing the heated sample between the plates of a capacitor and irradiating the diagnostic target zone through one of the capacitor plates with electromagnetic radiation having a periodically varying amplitude and a quantum energy equal to (or greater than) the energy width of the bandgap. The in-plane localization of the diagnostics is governed by the dimensions of the light probe, and the in-depth localization depends on the effective diffusion length. The physical phenomena on which the method is based are associated with generation-recombination processes in the irradiated zone of the sample and the formation of a diffusion-drift potential. The light incident on the sample penetrates to a depth α^{-1} (α is the light absorption coefficient), and in the course of diffusion and drift in the field of the surface-layer contact potential difference nonequilibrium carriers propagate into the depth of the sample, substantially altering the pattern of equilibrium population of deep centers over the Debye shielding length and producing a space charge in the indicated zone. This process changes the character of the potential distribution near the surface, and the periodic variation of the illuminance of the probed zone of the sample therefore induces a periodic variation of the photopotential, setting the stage for the application of capacitative recording methods.

The signal recording and processing methods can differ, depending on the specific attributes of the class of materials under investigation. For the diagnostics of semi-insulating materials in the system GaAs–AlAs the method of measuring the current induced in the external circuit of the measurement capacitor by the periodic variations of the photopotential, which exhibit a pulsed behavior, in the light-probed zone of the sample yields sufficient information, and its implementation is simple. The information signal is pro-

cessed by analyzing the temperature dependence of the instrument-generated function

$$\tilde{I}(T) \approx \frac{I_0 \tau(T)\{1-\exp[-t/\tau(t)]\}}{t},$$

where $\tau(T)$ is the potential relaxation time, t is the running time, and T is the instantaneous temperature of the sample.

It is easily shown that the indicated function $\tilde{I}(T)$ has a maximum on the temperature scale when the photopotential relaxation time $\tau(T)$ (carrier lifetime at a trap) is equal to the delay time t^* between light pulses if the pulse duration is much shorter than t^*. Since the carrier lifetime at a center τ_i, its energy E_i^*, and the sample temperature are bound by the relation $\tau_i = \tau_{0i}\exp(E_i^*/kT)$ in the case of a monoenergetic center or discrete, noninteracting energy centers, knowledge of the temperatures T_i^* of the corresponding maxima of the function $I_i(T)$ for two or more delay times t_i^* is sufficient for determining the energy of the centers

$$E_t = k\frac{T_i^* T_{i+1}^*}{T_{i+1}^* - T_i^*}\ln\left(\frac{t_{i+1}^*}{t_i^*}\right)$$

and calculating their capture cross sections.

In measuring the density of deep levels, it is necessary to establish the following relation between the impedance of the measurement capacitor Z_c, the input impedance of the measurement amplifier Z_{in}, the leakage impedance, and the bulk impedance of the sample Z_n: $Z_c \gg Z_n \gg Z_{\text{in}}$. It is readily verified that these impedance relations are always satisfied for conducting and semi-insulating materials in the system GaAs–AlAs at excitation pulse repetition rates of 10^2-10^6 Hz when the gap between the sample and the semitransparent capacitor plate is greater than 0.1 mm, and the characteristic dimension of the light probe is smaller than 5 mm. In this case the following relation holds between the photo-emf U_φ and the input voltage of the measurement amplifier U_{in}:

$$U_\varphi = U_{\text{in}}\frac{(R_{\text{in}}C_{\text{in}}\omega+1)}{C_s\omega R_{\text{in}}},$$

where ω is the angular frequency of the periodic light signal, R_{in} is the amplifier input resistance, C_{in} is the amplifier input capacitance, and C_s is the capacitance of the measurement capacitor.

Making use of the fact that $t^* \gg \tau_s$ and $C_s \ll C_r$ (where τ_s is the time constant of the measurement system, and C_r is the leakage capacitance), we obtain the following relation between the photopotential U_φ and the variation of the trap population ΔN_t from an analysis of the dependence of the current through the sample on the variations of the photopotential:

$$U_\varphi \approx \frac{q\Delta N_t \Delta x^2 \tau}{\alpha C_s},$$

where Δx is the minimum dimension of the light probe, and q is the elementary charge.

From this result we obtain an expression for the maximum variation of the carrier density at traps:

$$\Delta N_t \approx \frac{U_{\text{in}}(R_{\text{in}}C_{\text{in}}\omega+1)\alpha}{R_{\text{in}}\omega q \Delta x^2 \tau}.$$

Consequently, by increasing the irradiation intensity until the photopotential is a maximum and recording the photopotential relaxation time τ and the amplifier input voltage U_{in}, we obtain the approximate (lower bound) density of deep levels.

The method can be used to estimate n_0 in cases when the density of equilibrium free carriers n_0 is greater than the trap density. The recorded quantity in this case is the threshold excitation intensity at which the photopotential relaxation time begins to depend on the intensity with which the probed zone of the sample is ''pumped'' by light. This dependence is caused by the transition from a linear to a quadratic recombination mechanism once the nonequilibrium carrier density Δn becomes equal to the equilibrium carrier density n_0. It is readily shown that in this case the equilibrium density obeys the relation

$$n_0 \approx \frac{p^*\beta\tau}{\hbar\nu\alpha^{-1}\Delta x^2},$$

where p^* is the threshold irradiation power, β is the quantum efficiency, τ is the photopotential relaxation time, $\hbar\nu$ is the photon energy, α is the light absorption coefficient of the material, Δx is the linear dimension of the light probe.

We note that n_0 can be also be estimated (for $n_0 > N_t$) by analyzing the behavior of the function $\tilde{I}(T)$; in this case the role of the characteristic energy is taken by the Fermi energy, which permits the free-carrier density n_0 to be calculated. Measurements of n_0 using calculations based on a change of the recombination mechanism and on an analysis of the temperature dependence of $\tilde{I}(T)$ give consistent results.

The efficiency of the DLROS method in application to the local diagnostics of semi-insulating materials in III–V systems has been demonstrated[10–12] in examples of experimental investigations of the deep-level parameters of industrial ingots of semi-insulating gallium arsenide grown at various levels of doping with elemental chromium and the relationship of the electrophysical parameters of GaAs integrated circuits designed for a specific functional application to the parameters of deep trapping levels and device structures. In particular, a relation has been established between the parameters of deep trapping levels and buffer layers that exhibit backgating and sidegating; the factors responsible for the high-temperature limit on the performance of GaAs integrated circuits have been determined; and the influence of elastic stresses both on the distribution of deep centers in a wafer and (in some cases) on the deep-center energetics has been investigated.[12] Thus, the DLROS method is effective to use in the input-monitoring stages during the production of ingots and device structures for GaAs integrated circuits and also for interim monitoring between operations. The method is useful for the investigation of generation-recombination processes in compensated materials and processes of gettering of impurities by defects, for example, local elastic stresses.

[1] H. Ch. Alt, H. Schink, and G. Rackeiser, in *Fifth Conference on Semi-Insulating III–V Materials*, Chap. 1 (Malmö, Sweden, 1988), pp. 512–520.
[2] T. J. Drummond, W. Kopp, R. Fischer *et al.*, IEEE Trans. Electron Devices **ED-30**, 1806 (1983).
[3] A. J. Valoits, G. Y. Robinson, K. Lee, and M. S. Shur, J. Vac. Sci. Technol. B **1**, 190 (1983).
[4] E. L. Vinogradov, A. G. D'yachenko, É. A. Il'ichev *et al.*, Mikroélektronika **20**, 137 (1991).
[5] H. C. Gatos, J. Lagowski, and T. E. Kazior, Jpn. J. Appl. Phys. **22**, 11 (1983).
[6] M. G. Mil'vidskiĭ, *Semiconductor Materials in Modern Electronics* [in Russian], (Nauka, Moscow, 1986), p. 143.
[7] V. A. Gergel', É. A. Il'ichev, A. I. Luk'yanchenko, and É. A. Poltoratskiĭ, Fiz. Tekh. Poluprovodn. **26**, 794 (1992) [Sov. Phys. Semicond. **26**, 445 (1992)].
[8] É. A. Il'ichev, V. A. Onishchenko, É. A. Poltoratskiĭ *et al.*, in *Digests of the Russian Conference on Microelectronics, ''Mikroélektronika-94''* [in Russian], Chap. 2 (Zvenigorod, 1994), pp. 387–388.
[9] É. A. Il'ichev and A. I. Luk'yanchenko, Inventor's Certificate No. 2079853 [in Russian], Byull. Izobret., No. 9714 (1997).
[10] É. A. Il'ichev, É. A. Poltoratskiĭ, G. S. Rychkov, and V. I. Khaĭnovskiĭ, in *Proceedings of the Second International Scientific-Technical Conference on Microelectronics and Information Science* [in Russian], No. 2 (Zelenograd, 1997), pp. 251–257.
[11] E. A. Il'ichev, É. A. Poltoratskiĭ, G. S. Rychkov, and V. I. Khaĭnovskiĭ, Mikroélektronika **25**, 363 (1996).
[12] É. A. Il'ichev and M. F. Stupak, Élektron. Promst., No. 2, pp. 3–11 (1996).

Translated by James S. Wood